THÈSE POUR OBTENIR LE GRADE DE DOCTEUR DE L'UNIVERSITÉ DE MONTPELLIER

Spécialité: Électronique

École doctorale: Information, Structures, Systèmes (I2S)

Unité de recherche: Institut d'Électronique et des Systèmes - UMR 5214

Single-mode interband cascade lasers for petrochemical process monitoring

Présentée par Jordan FORDYCE

le 08 décembre 2023

Sous la direction de Laurent CERUTTI,

Tomasz PIWONSKI et

et Liam O'FAOLAIN

Devant le jury composé de

Thierry TALIERCIO, Professeur, CNRS,IES - Université de Montpellier	Examinateur
Frédéric GRILLOT, Professeur, Sup Télécom Paris	Rapporteur
Marc SOREL, Professeur, University of Glasgow	Rapporteur
Robert WEIH, Ingénieur de recherche, Société nanoplus	Examinateur
Tomasz PIWONSKI, Chercheur, CAPPA - Munster Technological University	Co-encadrant de thèse
Liam O'FAOLAIN, Professeur, CAPPA - Munster Technological University	Co-directeur de thèse
Laurent CERUTTI, Maitre de Conférences, CNRS,IES - Université de Montpellier	Directeur de thèse

SINGLE-MODE INTERBAND CASCADE LASERS FOR PETROCHEMICAL PROCESS MONITORING

Jordan A. M. Fordyce



A thesis submitted for a double doctoral degree at Munster Technological University

Supervisor: Dr. Laurent Cerutti

Co-Supervisor: Dr. Tomasz Piwonski

Co-Supervisor: Dr. Liam O'Faolain

08/12/2023

Thesis prepared in association with:




UNIVERSITÉ
DE MONTPELLIER


MTU
Ollscoil Teicneolaíochta na Mumhan
Munster Technological University

Contents

List of Tables v

List of Figures vii

Glossary xv

Acknowledgments xvii

1 Introduction 1

2 Fundamentals of mid-infrared semiconductor lasers 5

2.1 Introduction to laser principles . . . 6

2.1.1 Stimulated emission and gain . . . 6

2.1.2 Population inversion and pumping . . . 7

2.1.3 Optical cavities . . . 9

2.1.4 Electro-optical characteristics of a semiconductor laser . . . 11

2.2 Mid-infrared semiconductor materials . . . 13

2.2.1 Fundamental opto-electronics . . . 13

2.2.2 Active regions with QWs . . . 16

2.2.3 Challenges for mid-infrared range emission . . . 17

2.2.4 III-V-Sb lasers . . . 19

2.2.5 ICL active region . . . 22

2.3 Techniques for single-mode emission . . . 24

2.3.1 DFB and DBR devices . . . 25

2.3.2 Slotted waveguides . . . 27

2.3.3 Vernier-tuned devices . . . 29

2.4 State-of-the art single-mode ICLs and slotted lasers . . . 32

2.4.1 Single-mode Lasers . . . 33

2.4.2 Vernier tuned Lasers . . . 33
2.5 Gas sensing using spectroscopic techniques . . . 34
2.5.1 Tunable laser absorption spectroscopy . . . 34
2.5.2 Quartz-enhanced photoacoustic spectroscopy . . . 35

3 Microfabrication of Fabry-Perot ICLs 37
3.1 ICL Design for 3.3 µm emission . . . 38
3.2 ICL epitaxy . . . 41
3.2.1 Growth and characterization techniques . . . 41
3.2.2 Growth of type-II W-QWs and characterization . . . 43
3.2.3 Growth of AlSb/InAs SL cladding and characterization . . . 45
3.2.4 Growth of a complete ICL structure . . . 45
3.3 Lithography for FP ICLs . . . 46
3.3.1 Fundamentals of photolithographic processes . . . 47
3.3.2 FP ICL process . . . 51
3.4 Electro-optical characterization of FP ICLs . . . 55
3.4.1 Pulsed mode and CW performance . . . 55
3.4.2 Wavelength Tunability Measurements . . . 57

4 First development of single-mode slotted ICLs 61
4.1 Modelling slotted waveguides . . . 61
4.1.1 Design concepts for ICL slotted waveguides . . . 62
4.1.2 Slotted waveguide mask design for multiple wavelengths . . . 66
4.2 Slotted laser process development . . . 68
4.2.1 Photolithography development on GaSb . . . 70
4.2.2 Dry etching optimization on ICL material . . . 72
4.2.3 Slotted ICL fabrication . . . 74
4.3 Slotted ICL Performance . . . 75
4.3.1 Comparison to FP ICL Performance . . . 76
4.3.2 Dependence on etch depth . . . 77
4.3.3 Wavelength tunability . . . 78

5 Improvement of slotted ICL fabrication and performance 83
5.1 Second iteration of slotted ICLs . . . 83
5.1.1 Slot process optimization . . . 84
5.1.2 Initial dry etching process . . . 85
5.1.3 Dry etching optimization for wing reduction . . . 86
5.1.4 Second slotted ICL fabrication . . . 88
5.1.5 Performance of second iteration slotted ICLs . . . 90
5.2 Third iteration of slotted ICLs . . . 91
5.2.1 Photolithography changes . . . 92

5.2.2 Initial dry etching process . . . 92
5.2.3 High temperature etching gas study . . . 93
5.2.4 Third slotted ICL fabrication . . . 95
5.2.5 Performance of third iteration slotted ICLs . . . 100

6 Towards Widely Tunable ICLs **105**
6.1 Modelling slotted waveguides for Vernier tuning . . . 105
6.1.1 Design objectives for Vernier tuning . . . 106
6.1.2 Slotted waveguide simulations for Vernier tuned ICLs . . . 107
6.2 SVT ICL Mask Design . . . 109
6.3 Multi-section Laser Fabrication . . . 113
6.4 SVT ICL performance . . . 115
6.4.1 Isolation trench test section . . . 115
6.4.2 FP ICL test section . . . 116
6.4.3 Two-section slotted ICLs . . . 117
6.4.4 SVT ICL section . . . 119

7 Conclusion **123**

List of Publications **129**

Bibliography **131**

A1 Characterization of ICL structures **143**

A2 Laser microfabrication **145**

A3 DFB cross comparison study **151**

A4 Slotted ICL performance **155**

A5 SVT ICL Process and Performance **159**

List of Tables

3.1 Dry etching recipe parameters 52

4.1 Dry etching recipes that were explored to optimize the etch profile of the slots. The flow rates are given in sccm, the pressure is in mTorr, and the etch rate is in nm/min. 72
4.2 Final dry etching recipes used in the slotted interband cascade laser (ICL) fabrication. . . 74

5.1 The dry etching recipes studied to minimize wing formation. 87
5.2 Dry etching parameter comparison for the recipes used to explore different gas compositions, etch temperatures, and pressures. The flow rates are given in sccm, the pressure is in mTorr, and the etch rate is in nm/min. 93
5.3 Dry etching recipes that were explored to optimize the etch profile of the mesa at 220 °C. The flow rates are given in sccm, the pressure is in mTorr, and the etch rate is in nm/min. 94
5.4 Summary of epi-up single-mode behaviour for 8 µm wide devices with respect to slot dimensions in the LP study. The side mode suppression ratio (SMSR) is the max value measured and given in dB, the tuning refers to the electrical tuning in nm/mA, and the CSMR is the continuous single-mode wavelength range in nm. 103

6.1 Design iterations implemented for the slot period combination designated B in order to meet the organization constraints and consequences of the adjustments. 111
6.2 Design iterations implemented for the mirror combination designated C in order to meet the organization constraints and consequences of the adjustments. 112

7.1 Summary of electro-optical parameters of the best slotted ICLs from each process run mounted epi-up. **Note: n_{eff} for C1665 was calculated from a distributed feedback (DFB) fabrication.* 125

2 Summary of the FP ICL characterization for the growths and their subsequent use in the investigation of slotted waveguides. 144
3 Calculated refractive indices 144

4 SU-8 Recipe optimized for vertical sidewalls for the slot definition. 147

5 Summary of the design parameters and calculations implemented for the first development of SVT ICLs 3. 160

List of Figures

1.1 Absorption line strength of various gases in the mid-infrared (MIR) spectral range[1, 2]. . 2

2.1 *A:* Radiative transitions in the electronic states of an atom. *B:* Transitions between different conduction and valence band states of a solid semiconductor. 6

2.2 *A:* Optical pumping schemes for two, three, and four level laser schemes. *B:* Pumping via current injection into energy bands (versus the wave vector) of a semiconductor. The different energy levels are likened to the occupied/unoccupied states. 8

2.3 *A:* Passive Fabry-Perot (FP) (Plane - Parallel) resonator and the optical cavity modes formed between the mirrors. *B:* The Fabry-Perot laser (active) resonator, with gain material placed between cleaved facets (mirrors). The cavity modes that fall within the gain bandwidth of the material are supported. 9

2.4 An example power-current-voltage (PIV) sketch of performance typical to ICLs, highlighting important figures of merit. 12

2.5 Illustration to highlight the difference between direct and indirect band gap materials. . . 14

2.6 Illustration of interband vs intersubband transitions. 15

2.7 Three different types of semiconductor heterojunctions. From *Left* to *Right*: Type I (straddling), Type II (staggered), and Type III (broken). 17

2.8 Quantum well configurations for the type-II class 17

2.9 Different types of recombination processes in the valence band for the Auger processes. . 18

2.10 Band gap energy/wavelength as a function of lattice constant for several semiconductors, adapted from[2] 19

2.11 Sketch of the quantum well (QW) and heterojunction configuration for *A:* a diode laser, *B:* a quantum cascade laser (QCL), and *C:* an ICL. 20

2.12 Threshold current densities of MIR lasers, adapted from [3]. 21

2.13 Schematic of cascaded QWs. 22

2.14 One stage of the ICL active region including the W-quantum well (W-QW), hole injector, semimetallic interface and electron injector. The wave function of the carriers is shown in the conduction band (CB) and valence band (VB) throughout the stage in blue and orange for electrons or in green and purple for holes. . . . 23
2.15 Two stages of the ICL active region are drawn with the energy levels highlighted. As well, the material used for the QWs is labelled. . . . 24
2.16 A schematic representing the different types of waveguide designs that can achieve single-mode emission. *A:* DFB waveguide, *B:* Slotted waveguide, and *C:* distributed Bragg reflector (DBR) section. . . . 25
2.17 *A:* Reflections along the propagation direction of a square grating. *B:* Reflectivity as a function of the detuning from the Bragg wavelength. Images adapted from [4]. . . . 26
2.18 A schematic representing the DFB design incorporating lateral metal gratings. . . . 27
2.19 Schematic representing different slotted waveguides. *A:* A single section slotted waveguide has slots, with t_E and d_s, placed along the length of the gain section with period d. *B:* A two section slotted waveguide has the slots separated from an additional gain section by an isolation trench with with w_t. . . . 28
2.20 Illustration of a slot interacting with the fundamental lasing mode to create interference. . 29
2.21 A schematic illustrating possible configurations for Vernier tuned lasers. *A:* Two DFB sections (waveguide 1 and 2) are separated by a gain section. *B:* Two slotted sections are separated by a phase and gain section. The phase section is attached to waveguide 1. . . . 29
2.22 The S_{FSR} from two single-mode sections as well as their superimposed output at one λ_{Bragg}. 31
2.23 A scheme depicting the criteria for making single-mode lasers, from Eqn. 2.41, and how the cavity modes should be overlapped with the reflectivity peaks of the slots. When the cavity modes are red, they are likely to lase while when they are peach they are likely suppressed. 32
2.24 A scheme illustrating absorption spectroscopy through a gas cell [5]. . . . 35
2.25 A scheme illustrating quartz-enhanced photoacoustic spectroscopy (QEPAS) absorption spectroscopy through a gas cell with a tuning fork [6]. . . . 35

3.1 Schematic of a full ICL structure. . . . 38
3.2 The refractive index of each layer in an ICL are plotted along with the mode intensity of the TE_0. . . . 39
3.3 *A:* Threshold current and power densities are plotted with the number of stages for broad area ICLs (2 mmx150 µm. *B:* The total EDQE and EDQE per stage is plotted for the same broad area ICLs. Lasers are operated in pulsed mode and have $\lambda \approx$3.6 µm. Both figures are adapted from [7]. . . . 40
3.4 Sketch of the UHV chamber used to grow the full ICL structure . . . 42
3.5 *A:* W-QW structure and characterization used to calibrate the growth parameters for the active region. *B:* PL curves from W-QW strucutres grown at four different growth temperatures. *C:* HR-XRD of the W-QW structure grown at 435 °C. . . . 44
3.6 XRD characterization of the cladding growth parameters. . . . 45
3.7 HR-XRD characterization of a full ICL growth. . . . 46

3.8 Steps involved in a photolithography process. 47
3.9 The top row shows Scanning electron microscope (SEM) images of the substrate with the mask before etching and the bottom row shows SEM images of the substrate after etching and mask removal. This allows a comparison of the etching profile achieved with Ar on different substrates. 49
3.10 The top row shows SEM images of the substrate with the mask before etching and the bottom row shows SEM images of the substrate after etching and mask removal. This allows a comparison of the etching profile achieved with BCl_3 on different substrates. . . 50
3.11 The top row shows SEM images of the substrate with the mask before etching and the bottom row shows SEM images of the substrate after etching and mask removal. This allows a comparison of the etching profile achieved with Cl_2 on different substrates. . . . 50
3.12 Photolithography process steps for fabricating FP ICLs. 51
3.13 Exposed photoresist forming the etching mask for the laser ridges. 52
3.14 Optical monitoring signal used to observe the etch progression for the mesa. 53
3.15 Exposed photoresist forming the contact windows on top of the laser ridges. 53
3.16 ICL facet after cleavage for a 10 µm ridge. 55
3.17 Characteristics of FP ICLs measured in pulsed mode and in continuous-wave (CW). The main plot depicts the PIV performance in pulsed mode and the inset plot illustrates the spectra measured in pulsed mode and in CW. 56
3.18 PI measurements of a 8 µmx1.6 mm device measured in CW at different heatsink temperatures. 57
3.19 CW spectra of a 8 µmx1.6 mm ICL. 58
3.20 Two different FP ICLs are presented that were used to investigate the tuning properties of the material. *A:* Selected CW spectra of FP ICL for the current tuning with the heat sink set to T =20 °C. *B:* Spectra for the temperature tuning with the current set to I =114 mA. . . 58

4.1 *A:* The refractive index and mode intensity is plotted for each layer in an ICL. *B:* The cross section of a typical ICL is shown with the slotted waveguide along the length of the cavity. *C:* The simulation parameters of the slotted waveguide are labelled on the features in the waveguide, highlighting the constraints placed on their size. 63
4.2 *A:* Schematic illustrating how single-mode vs multi-mode emission can be realized with respect to the width of emission and S_{FSR}. *B:* The reflectivity spectra from different slot widths appropriate for fabrication with photolithography. 64
4.3 *A:* The simulated R is shown with respect to t_E for $\lambda \approx$3.3 µm. *B:* The full width half max (FWHM) of R is plotted as a function of t_E. 64
4.4 *A:* The simulated response for R is plotted as N is varied. *B:* The change in the FWHM of R is plotted as a function of N at $\lambda \approx$3.3 µm. 65
4.5 *A:* A plot of C_{FSR} as a function of the cavity length.*B:* An illustration representing multi-mode vs single-mode emission as C_{FSR} changes. 66
4.6 The reflectivity peaks for the short period slots, d =6.68 µm, and the long period slots, d =13.1 µm, are plotted the pulsed emission from FP ICLs fabricated on four of the growths. The different colours represent the different slot width combinations possible. 67

4.7 A: The dependence of the reflectivity strength (R) and the reflectivty peak FWHM is shown with respect to the number of slots. The cavity mode spacing, C_{FSR} is also plotted with the simulated FWHM while changing the total length (equivalently, N). B: The dependence of R and the FWHM are shown with respect to t_E. 68

4.8 Simulations of slot patterns with d =13.1 µm and 6.68 µm are shown for a FP laser measured at T =20 °C in CW mode with injected current I =100 mA and 130 mA. 69

4.9 A general overview of the steps involved in the technological process fabricating a slotted ICL. The box for defining the slots is blue, highlighting that it is the new addition to the FP ICL fabrication. The main steps that are required to define the slots are expanded in orange boxes. 69

4.10 Deposition of two potential photoresists that could be used to transfer the slot pattern to the hard mask. *A:* AZ1505 and *B:* AZ1518. 71

4.11 Comparison of dry etching in ICL material and in GaSb. *A:* Shows the vertical photoresist mask from SU8 photolithography. *B:* Shows the dry etching process in GaSb material with the etching mask still on.*C:* Depicts the dry etching process in ICL material, with the etching mask removed. 71

4.12 Altering parameters of the FP ICL dry etching recipe. *A:* Etch mask *B:* Recipe 1 (FP ICL) with hard mask *C:* Recipe 2 *D:* Recipe 3 *E:* Recipe 4 *F:* Recipe 5 *G:* Recipe 6 *H:* Recipe 7 73

4.13 Slots and mesa profiles at various stages of the process. *A:* Shows the slot openings in the etch mask. *B:* Shows the slots after etching the cladding layer, with the hard mask still on the sample. *C:* Shows a cross section of the slots in the ridge before metallization. *D:* Shows the cross section of the mesa after metallization. *E:* Shows the slots after metallization. *F:* Shows a close up of the slot after the process is complete. 75

4.14 PIV curves of a FP ICL and slotted ICL are shown at 20 °C in CW operation for lasers with a 8 µm wide mesa. The FP ICL has a length of 1.6 mm while the slotted ICL has a length of 1.8 mm. The slots were etched with t_E =1.0 µm. 76

4.15 Comparison of the spectra between the FP and slotted ICL in CW at their I_{max} currents and heatsink temperatures of *A:* 27 °C and *B:* 21 °C. 77

4.16 The spectra for slotted ICLs with different etch depths are presented at conditions were single-mode emission was observed. 78

4.17 The temperature dependence of the PI curves a slotted ICL are shown in CW operation for lasers with a 8 µm wide mesa and a length of 1.8 mm with the IV curves shown in the inset figure. The slots have t_E =1.0 µm. 79

4.18 The emission of a slotted ICL with t_E =0.8 µm over a series of different operating conditions.*A:* The temperature is fixed at 20 °C and I is varied from below I_{max} to I_{max} and above I_{max}. *B:* The current is fixed at I_{max} for the temperatures between 13 °C to 20 °C. 79

4.19 *A:* The spectra for the slotted ICL at 20 °C and $I = I_{max}$ is plotted. *B:* The wavelength tuning for $I_{Th} < I < I_{max}$ at two different temperatures is plotted for when single-mode emission was achieved. 80

5.1 SEM images comparing slot etching on ICL samples. *A:* Slot recipe 1, taken from a cross section of a cleaved 100 µm ridge. *B:* N+ recipe, taken from a slot test section. 85

5.2 SEM images comparing mesa etching on ICL samples. *A:* Slot recipe 1, taken from a cross section of a 8 µm ridge. *B:* N+ recipe, taken from a mesa test ridge. 85

5.3 SEM images comparing slot-mesa layouts. *A:* Slot lengths are the same size as the mesa width. *B:* Slot lengths are larger than the mesa widths. 86

5.4 SEM images from the mesa cross section and slots > mesa width profiles are shown, from top to bottom. *A:* Effects of recipe 2, decreasing the pressure, are depicted. *B:* Effects of recipe 3, increasing the Cl_2 flow rate, are depicted. *C:* Effects of recipe 4, increasing the pressure, are depicted. 87

5.5 SEM images comparing the wings after ultrasonication. *A:* Sample etched with N+ recipe. *B:* Sample etched with R4. 88

5.6 Summary of process 2 for the second iteration of slotted ICLs. 88

5.7 SEM images highlighting key features of the process. *A:* Hard mask opening after slot photolithography. *B:* Slot dry etch with hard mask on sample. *C:* Hard mask openings after mesa photolithography. *D:* Mesa dry etch, with wings before sonication. *E:* Wings after sonication. *F:* Cross section of the final device after electroplating. 90

5.8 PIV characteristics of a slotted ICL and reference FP ICL for L =1200 µm, w =6.6 µm at 10 °C. 91

5.9 SEM images from the dry etching tests showing the profile on ICL material after being etched with *A:* UMV2 *B:* HTTYN and *C:* GATYN. 93

5.10 Dry etching recipe variations on ICL samples, with the hard mask left on. *A:* Reference sample using HTTYN. *B:* Etch using V1. *C:* Etch using V2. *D:* Etch using V3. *E:* Etch using V4. *F:* Etch using V5. 95

5.11 Summary of process 3 for the third iteration of slotted ICLs. 96

5.12 SEM images looking at the quality of the slot definition during the fabrication. *A:* Slot pattern etched into the Si_3N_4 layer. *B:* Slots etched into the cladding layer with vertical sidewalls. 96

5.13 SEM images illustrating the etching profile during the fabrication. *A:* Vertical profile of the mesa etch from an alignment marker. *B:* Slot and mesa etching from a 10 µm mesa after Si_3N_4 mask removal. *C:* Slot after the mesa etch and removal of the Si_3N_4 mask. 97

5.14 SEM images of slotted ICLs from process 3. *A:* Cross section of a LP1 slot. Inset is a zoomed out view of the slot spacing from a cleaved 100 µm ridge. *B:* Cross section of a LP2 slot. *C:* Cross section of a LP3 slot. Cross sections are shown for *D:* LP1 mesa width 8 µm, *E:* LP2 mesa width 20 µm, and *F:* LP3 mesa width 12 µm. 99

5.15 Evaluation of the fabricated slotted waveguide parameters. *A:* The expected vs measured dimensions are summarized from the LP samples. Plot *(i)* shows d_s, plot *(ii)* shows t_E, and plot *(iii)* shows N for a device with length 1.8 mm. *B:* SEM images from a zoomed out view of the slot spacing from a cleaved 100 µm ridge on the LP samples. 100

5.16 *A:* PIV characteristics from the LP samples mounted epi-up in CW mode are shown at 15 °C for devices with a ridge width of 8 µm and length of 1.6 mm. *B:* The temperature dependence of the PI curves from LP1 are shown. 101

5.17 The spectra for the highest SMSR from LP1 and LP2 mounted in the epi-up configuration with dimensions 8 µmx1.6 mm operated in CW mode. *A:* LP1 is shown at 23 °C and 85 mA. *B:* LP2 is shown at 25 °C at 70 mA. 102

5.18 Summary of the emission measured from the LP2 laser mounted in the epi-up configuration with dimensions 8 µmx1.2 mm operating in CW at 17 °C. *A:* Selected spectra over the current tuning range between 89 mA to 103 mA. *B:* Summary of the electrical tuning achieved including *(i)* the wavelength of single-mode emission, *(ii)* the SMSR, and *(iii)* the instantaneous tuning. 103

6.1 A schematic illustrating the general design for the slotted Vernier tuned ICL. Two slotted sections are separated by a phase and gain section with isolation trenches. The total device length is defined by cleaved facets with AR coatings. 107

6.2 *A:* The slot reflectivity peak spacing is shown for different simulated slot periods for t_E =1.8 µm and $N = 7$. *B:* The mean reflectivity strength of different slot periods was simulated with respect to the number of slots with t_E =1.8 µm. 108

6.3 Simulations depicting different slotted waveguide configurations. *A:* Resulting S_{FSR} combinations for M1 with d =181 µm and M2 with d =251 µm. *B:* Resulting S_{FSR} combinations for M2 and M3 with d =294 µm. 108

6.4 *A:* The simulated S_{FSR} used to calculate the FWHM as N is changed for t_E =1.5 µm and d =294 µm. *B:* The reflectivity strength as a function of t_E, until ≈100 nm before the separate confinement layer (SCL), as N is increased for d =181 µm. 109

6.5 The slotted Vernier tuned (SVT) photolithography mask layout with the mesa ridges. The purple boxes represent the groupings of the different designs. The different iterations are labelled as well. The red lines and numbers represent the cleave lines and the order. The green boxes represent the devices that are not SVT; the isolation slot test section, the FP laser test section, and the two section slotted ICLs. 113

6.6 Overview of the SVT ICL process. 114

6.7 The ion etch mask layout with respect to the SVT ICL device layers. 114

6.8 *A:* An SEM image depicting an isolation trenches after fabrication. *B:* An overview image of the SVT sample before cleaving. 115

6.9 The resistance measurements for the isolation trenches. *A:* The measurements from SVT1 are shown as the slot width increases. *B:* The measurements are shown as the etch depth increases, i.e. for SVT1 and SVT3. 116

6.10 The spectra and PIV from the FP ICL test section are shown for L=3000 µm (w=8 µm) and uncoated facets. *A:* The PIV characteristics are presented for all the FP ICLs of the section. *B:* The spectra are presented for two of the lasers well above threshold. 117

6.11 Electro-optical characteristics from the two-section slotted ICL test lasers mounted epi-up in CW mode. *A:* The PIV curves for each section pumped independently are shown at 10 °C in CW. *B:* The spectra are shown for the slotted ICLs at 15.5 °C with the slots pumped (ON) and not pumped (OFF) with the FP ICL spectra plotted for comparison. 118
6.12 The PIV from the SVT ICL fabricated with the B4 design with each section pumped individually is shown at 10 °C in CW mode, as measured out of the facet on the M1 slot section. *A:* The M1 slot section and the phase section are presented. *B:* The gain section and the M2 slot section are presented. 119
6.13 The spectral emission after tuning the M2 slotted section with currents of 40 mA, 60 mA, 80 mA, and 100 mA. The other sections had fixed currents with the M1 slots at 120 mA, the phase at 0 mA, and the gain at 100 mA at a heat sink temperature of 14.5 °C. 120
6.14 *A:* The spectral emission after tuning the Phase section with currents of 15 mA, 45 mA, and 60 mA. The other sections had fixed currents with I_{M1} =0 mA, I_{Gain} =120 mA, and I_{M2} =120 mA at a heat sink temperature of 14.5 °C. *B:* The spectra for the I_{Phase} =45 mA measurement plotted in the log scale to highlight the SMSR. 121

7.1 Overview of the steps and fabrication achievements from the three processes explored to fabricate single-section slotted ICLs. 124
7.2 PIV from the LP samples E802A, with LP1 t_E =0.8 µm, LP2 t_E =1.1 µm, LP3 t_E =1.0 µm, w =8 µm and L =1.6 mm. *A:* The etch series for the SICLs mounted epi-down. *B:* Comparison of the etch series mounted epi-up. Both measurements are shown for 15 °C The noise in the IV curve is just due to poor contact with the probe needle. 126
7.3 Summary of single-mode emission measured over I_{Gain} and I_{S2} currents at 14.5 °C. I_{Phase} and I_{S1} are not shown. *A:* The wavelengths measured for the given operating conditions. *B:* The corresponding SMSR for the given operating conditions. 127

4 Threshold current density measurements of various growths characterized for this project 143

5 *A:* Dry etching using the N+ recipe and a metal mask. *B:* Again, the original recipe but with the dielectric hard mask. The top row shows the mesa profile. The bottom row shows the slots after the masks should be removed. 148
6 SEM images from the mesa cross section, slots > mesa width, slots = mesa width, and slots < mesa width profiles are shown, from left to right. *A:* The resulting etching profiles and wings observed from the N+ recipe. *B:* The resulting etching profiles and wings after implementing recipe 1 and increasing the Ar flow rate. 149
7 A few different F-based dry etching recipes to open/remove the hard mask from Tyndall. *A* shows a SF_6 recipe, *B* shows the slot/mesa mask opening recipe in process 3 ($SF_6/C_4F_8/H_2$/He), and *C* shows the contact window opening recipe of process 3 (C_4F_8/He). 150

8 The materials used to make a performance comparison based on the DFB process developed at nanoplus. These were chosen because the SCLs were symmetric and the expected wavelength was similar. Both epitaxies represent an optimization for emission near λ =3.3 µm 152

9 *Left:* Resulting optical modes predicted for the different ICL structures and their refractive index profile. *Right:* Comparison of the FP ICL performance between material from N+ and UM, and to the UM FP process (FPP). Taken at 20 °C and I_{thr} ≈30 mA. 152
10 PIV measurements of DFB ICLs with uncoated facets and L =900 µm at T =10 °C. *Left:* The results from C1665 are presented and achieved I_{thr} ≈38 mA and P_{out} ≈4 mW. *Right:* The results from NICL120 are presented and achieved I_{thr} ≈21 mA and P_{out} ≈14 mW, though the rollover point was not reached yet. 153
11 *Left:* The laser with the best single-mode tuning range and SMSR. *Right:* The laser with the lowest threshold. 154

12 Summary of the emission measured from 8 µmx1.6 mm lasers mounted in the epi-down configuration. *A:* LP1 and *B:* LP3. 155
13 Summary of the emission measured from the devices mounted in the epi-down configuration. *Left:* LP1 performance is shown at 15 °C. *Middle:* LP2 performance is shown for an injected current of 130 mA as the temperature is changed. *Right:* LP3 performance is shown at 35 °C. 156
14 Summary of the emission measured from the devices mounted in the epi up configuration that lased. *Left:* LP1 performance is shown at 23 °C and 25 °C for a laser with L =1.6 mm, with some single mode emission observed. *Middle:* LP2 performance is shown for a laser with L =1.6 mm at 25 °C with an operating point for single mode emission. *Right:* LP2 performance is shown again for a laser with L =1.2 mm at 17 °C with a large tuning range of single mode emission. 157

15 The C_{FSR} is calculated for different values of n_g that are possible from the material. The range of lengths shown covers the single slot period up to the full facet to facet length of the different designs. The inset highlights the C_{FSR} from the range of the single slot periods implemented in the designs. 159
16 PIV characteristics from the two-section slotted ICL test lasers mounted epi-up in CW mode are shown at 10 °C for devices with a ridge width of 7 µm and length of 1.6 mm. *B:* The temperature dependence of the PI curves from LP1 are shown. 161
17 PIV characteristics from the two-section slotted ICL test lasers mounted epi-up in CW mode are shown at 10 °C for devices with a ridge width of 8 µm and length of 1.6 mm. *A:* Testing done in pulsed mode. *B:* Testing done in CW mode. 162
18 PIV and spectra from the two-section slotted ICL with both sections pumped. *A:* The PIV at in CW mode at 10 °C with I_{Slot} at 0 mA and 150 mA. *B:* The spectra are shown at 16 °C with I_{Gain} at 110 mA as I_{Slot} is increased between 0 mA to 125 mA. 162
19 The spectra measured from both outputs of the SVT ICL are shown as I_{M2} is increased with only the gain section pumped at 140 mA at 14.5 °C. 163

Glossary

QEPAS quartz-enhanced photoacoustic spectroscopy

MIR mid-infrared

VOC volatile organic compounds

ICL interband cascade laser

DFB distributed feedback

NIR near infrared

SMSR side mode suppression ratio

BSG binary superimposed gratings

SVT slotted Vernier tuned

DBR distributed Bragg reflector

QCL quantum cascade laser

CW continuous-wave

CB conduction band

VB valence band

FP Fabry-Perot

TEM transverse electro-magnetic

PIV power-current-voltage

QW quantum well

W-QW W-quantum well

SL superlattice

SRH Shockley-Read-Hall

MQW multiple quantum well

SMIF semi metallic interface

FWHM full width half max

HR high reflection

AR anti-reflection

SCL separate confinement layer

SOA semiconductor optical amplifier

TLAS tunable laser absorption spectroscopy

PECVD plasma enhanced chemical vapour deposition

SEM Scanning electron microscope

TEC thermo-electric cooler

Acknowledgments

Working in three different places over the course of the last three years means there is a long list of people to thank. I truly feel the expression "it takes a village" applies to doing a PhD abroad. Although I won't be able to thank everyone, please know all the help I received was deeply appreciated.

I would like to express my gratitude to my supervisors Dr. Laurent Cerutti, Dr. Tomasz Piwonski, and Dr. William Whelan-Curtin (Liam O'Faolain) for accepting me into the program and their guidance towards its successful completion. I learned a great deal from my time in this PhD and felt supported the entire way. Beginning in France: Daniel Diaz-Thomas you helped me get the project off the ground and I am very happy to have shared the clean room with you. Kumar Kinjalk it was a delight to share the office with you and be "the laser people". Moving to Ireland: Michael Dillane you get a special shout out for introducing me to the fun Tyndall people and for all the fun science chats. I want to thank Alan Hyde and Dan O'Connell for all the guidance they provided me in the clean room and helping me troubleshoot and brainstorm about the many challenges I faced. Finally, in Germany: I would like to thank the people at nanoplus, especially Robert Weih, Josephine Nauschutz, and Silke Kuhn, for inspiring me, calming me, and helping me get so much done in a short time.

Now to acknowledge the non-scientific support I received: the lunch time fight club, the Techno Teams, the people at Prana, the people at BJJ Cork, Anonymous A, La Birra Grande, the people at nanoplus... You are the village that made me feel like I had family so far away from home. I appreciate the patience, the whiskey evenings, the lunch time walks, learning more than I should about astrology, the nights at Kraken, the nights at the Brog... You kept my morale high, listened to me complain, and made sure I had so many experiences that have become my favourite memories. Thank you for being so consistently there for me. Special thanks go to Elena, Meig, and Erika who had to (got to?) deal more acutely with meltdowns. I am happy we have managed to keep the doors open no matter what country we've been in.

I would like to thank my family for understanding my wandering ways and giving me their support and encouragement. It's been challenging but I am grateful we have still been able to be there for the big moments. And last, but not least, I need to thank my mom, Sherry. Your support and wisdom was, and always will be, missed...

CHAPTER 1

Introduction

Photonics is an exciting field to be working in right now: currently sources and sensors are being developed with increasing sophistication for numerous applications. Microelectronic devices need to be replaced with photonic devices in order to reach the demand for increased speed and decreased size[8]. This creates an extensive list of research topics so that the photonic devices can deliver the same performance as their microelectronic predecessors. At the same time, photonics allows a different approach to be used in order to address certain problems. Using light for sensing and identification can be done optically using lasers and detectors, as opposed to with thermal or electrochemical methods. This leads to higher sensitivity, a better dynamic range, and increased speeds[9]. Laser sources and detectors need to be developed for free space communication, breath analysis, environmental sensing, industrial process monitoring, and food inspection, for example [10–14].

OPTAPHI is a European double doctorate training network involving optical sensing using advanced photo-induced effects which is achieved through the combination of novel laser sources with novel spectroscopic techniques for gas and liquid sensing [15]. The research from fourteen different projects in the network was grouped into three main work packages: environmental sensing, agri-food analysis, and industrial processing monitoring. This thesis is the work for project 3.5. Within the framework of the network, this novel laser source between 3 µm to 5 µm will replace the source in quartz-enhanced photoacoustic spectroscopy (QEPAS) detection, since the mid-infrared (MIR) spectral range is interesting for industrial process monitoring due to the presence of absorption lines from many different hydrocarbons, such as methane, ethane, and carbon dioxide, as well as from volatile organic compounds (VOC)[16] like chloroform. The absorption lines of various species are presented in Fig. 1.1. As well, it will help reduce the power requirements and overall size of the remote sensor because a GaSb based interband cascade laser (ICL) can be powered by a battery due to its efficient performance in this spectral range which allows these sources to be integrated in handheld devices or on unmanned aerial vehicles (UAVs), for example. Developing this type of source within the framework of the network will help optical sensors take part of the growing sensor market.

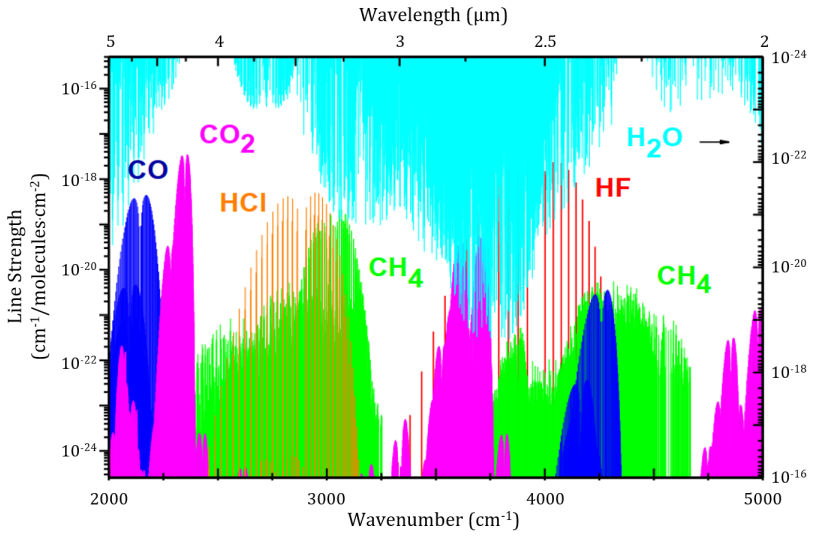

Figure 1.1: Absorption line strength of various gases in the MIR spectral range[1, 2].

Developing ICL technology into a practical gas sensing system requires single-mode emission. This already exists as a distributed feedback (DFB) ICL but is an expensive approach since it requires e-beam lithography. Other methods need regrowth steps, which are more complicated yet, or metallic gratings that reduce the total output power. In the near infrared (NIR) spectral range around 1.55 µm, single-mode lasers are fabricated using a slotted waveguide and achieve extremely high side mode suppression ratio (SMSR)s (>30 dB)[17]. This type of laser is fabricated using standard UV photolithography which leads to time and cost savings. Slotted waveguides are based on the same principles as DFB lasers, but the extended dimensions make them less complicated to fabricate. This waveguide design will be integrated onto ICLs for economical single-mode emission.

This motivates the integration of slotted waveguide technology with ICL architecture to develop an economical, low power single-mode laser source in the MIR. Correctly identifying a gas species present in a sample requires single-mode emission and tuning to match the absorption line, depending on the environmental conditions. Identifying multiple species is often done using multiplexing schemes with multiple lasers sources[18]. In order to offer a wider tuning range, multiple lasers are often packaged together - increasing costs and complexity. Increasing the tuning range possible with one laser source allows for the ability to detect multiple gas species with one sensor. Configurations that employ the Vernier tuning principle are seen in binary superimposed gratings (BSG), for example, that combine two DFB gratings and offer a wide tuning range but are not continuous[19]. Analogously, Vernier tuning is demonstrated using a combination of slotted waveguides at 1.55 µm where up to 50 nm of quasi-continuous tuning is achieved [20, 21]. Meanwhile, external cavity ICLs achieve a tuning range of 150 nm at 3.2 µm and 300 nm at 3.8 µm due to the broad gain bandwidth of the ICL active medium[22, 23]. Similar tuning ranges are expected to be within reach of slotted Vernier tuned (SVT) ICLs.

This work is the union of two different types of technology and a discussion of the challenges faced during the development of two devices: the slotted ICL and the SVT ICL. This is reflected in where the project was hosted to make use of the Université de Montpellier's expertise in ICLs and Munster Technological

University's expertise in slotted waveguides and Vernier tuned devices. Additionally, the company nanoplus hosted my secondment and offered their expertise and experience in ICL design and fabrication. Throughout this manuscript, I will describe the steps taken to merge slotted waveguides with ICLs by dividing my work into the following chapters:

- Chapter 2 is an introduction to the principles of laser physics and the fundamentals of semiconductor opto-electronics. The important concepts required to understand the design and challenges of devices emitting in the MIR will be covered.
- Chapter 3 outlines laser growth techniques, characterization, and how the material was characterized to design single-mode lasers. An additional section is added to compare the material performance to commercial single-mode designs; namely the DFB waveguide.
- Chapter 4 describes the design and performance of the first slotted ICL.
- Chapter 5 is devoted to the optimization of the process and improvement of the performance for slotted ICLs.
- Chapter 6 reports the current understand of extending this knowledge to a widely tunable device using the Vernier tuning concepts. The first design and performance is presented with suggestions for future work outlined.

CHAPTER 2

Fundamentals of mid-infrared semiconductor lasers

Lasers are a ubiquitous tool today for many areas such as communication, spectroscopy, imaging, surgery, and displays, to name a few. They were developed based on the work of theoretical physicists studying light-matter interaction in the late 19th century and on the work of microwave scientists who built the first maser (*microwave* amplification by stimulated emission of radiation), the predecessor to the laser (*light* amplification by stimulated emission of radiation), in the 1950s.

The journey begins with the work of Charles Fabry and Alfred Perot who created the first interferometer[24]. It continues with Albert Einstein who conceptualized the photoelectric effect and stimulated emission, as well as with Max Planck who posited that light is an energy quanta form of electromagnetic radiation[25, 26]. Their work was published in the late 19th century to early 1900s. It would take another 40 years until these concepts could be realized in Charles Townes' design of a maser[27]. During this same period, Alexander Prokhorov and Nikolai Basov took important steps in designing a pumping system and the idea of a three level maser[28]. Although the maser worked, many were skeptical these results could translate to shorter, visible wavelengths. Finally in May 1960, Theodore H. Maiman built the first laser, using synthetic pink ruby[29, 30].

Importantly for this thesis, semiconductor lasers were created in 1962 by Robert Hall with the first GaAs diode laser[31]. The basis for the sampled-grating distributed Bragg reflector (DBR) laser was then established from the invention of the differing multi-element mirror laser in 1988 by Larry Coldren[32]. Then in 1994, the same year as the first demonstration of a quantum cascade laser (QCL) by Jerome Faist, Rui Yang proposed the idea for an ICL[33, 34]. It took until 2008 for continuous-wave (CW) room temperature operation to first be reached by an ICL[35].

This chapter will introduce the main concepts of laser operation and semiconductor physics that are necessary to design and fabricate lasers in the mid-infrared range. The theoretical framework and state-of-the-art performance of devices available at the beginning of this thesis will be described, motivating the utility of this work.

2.1 Introduction to laser principles

Laser radiation is characterized by being coherent, directional, and bright. Coherence is an important property with two aspects: spatial and temporal. Spatial coherence means that between two points on the same wavefront, the phase difference remains the same as the wave propagates through space. Temporal coherence means that at one point the phase difference remains the same. To understand these basic properties in the context of semiconductor lasers, the building blocks of laser operation will be presented. In order to have lasing we must be able to create a population inversion (through pumping with current injection), have conditions for stimulated emission (exhibiting threshold behaviour), and create positive feedback (gain material placed in an optical cavity)[36]. The following subsections introduce the building blocks for understanding laser emission following the derivations and introductions of [36] and [37].

2.1.1 Stimulated emission and gain

Consider some atom or molecule with two energy levels, E_1 and E_2, with $E_2 > E_1$ where the first level is the ground state, as depicted in Fig. 2.1. If the atom is initially in the second level (excited state) it will eventually decay to the ground state (since $E_2 > E_1$) and the energy difference $E_2 - E_1$ will be released. This energy can be released by the atom in the form of electromagnetic radiation and can either be spontaneous or stimulated emission. The wavelength, λ_0, of the emitted radiation is given by:

$$E_2 - E_1 = \frac{hc}{\lambda_0} \tag{2.1}$$

where h is Planck's constant and c is the speed of light in vacuum. The energy can also be released through a non-radiative way, and go into kinetic energy of the atom, for example. When the atom releases a photon at a random time (arbitrary phase) and in any direction, this is called spontaneous emission.

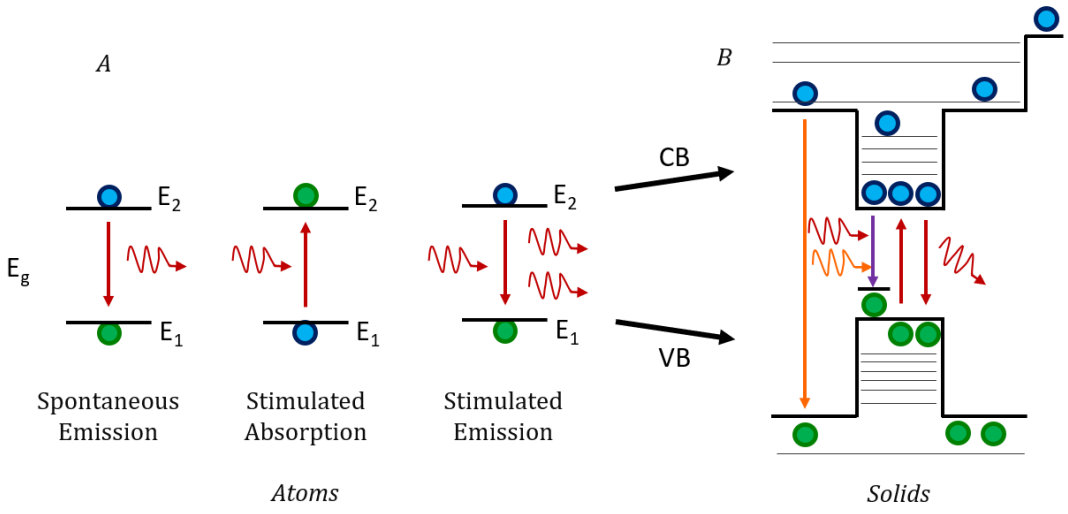

Figure 2.1: *A:* Radiative transitions in the electronic states of an atom. *B:* Transitions between different conduction and valence band states of a solid semiconductor.

Now consider a photon with wavelength λ_0 is incident on the material. If the atom is in the ground state, the photon can be absorbed and the atom will transition to the excited state. This is stimulated absorption. If the atom is in the excited state, the incoming photon can force the atom to transition into the ground state, releasing its own photon with wavelength λ_0 during the transition. Since this process is forced by the incoming photon, the emission is in phase to the initial photon and along the same direction. This is known as stimulated emission and it is the important gain mechanism that allows lasers to work. In fact, the ability for the rate of emission to be greater than the absorption of photons at a certain electron density leads to the signature threshold behaviour that will be used to evaluate the laser performance. The rate of laser transitions between energy levels is described by their Einstein coefficients of the material. These coefficients describe the rate of absorption or emission with respect to the incoming light at thermal equilibrium and are required when solving the rate equations for a material, the three different types of radiative transitions are shown in Fig. 2.1A.

To understand some of the fundamentals of lasers, it is useful to consider atomic levels and transitions. The allowed energy levels electrons can occupy are given by the solution to Schrodinger's equation for the electronic potential and are useful for describing the active species in gas and solid-state lasers. In semiconductors, the energy levels broaden into bands of levels because of the bonds formed to make the solid. This is illustrated in Fig. 2.1B. In crystalline material with N atoms chained together, the number of available vs filled states is split into the conduction band (CB) and valence band (VB). This will be introduced in Sec. 2.2, but it is noted here to show that at a high level, although there are many more energy states in the CB and VB of the material, the necessary states can be likened to E_2 and E_1 in order to understand the system to generate laser emission.

2.1.2 Population inversion and pumping

The rate equations for a material describe the rate that N atoms or molecules (per unit volume) make transitions at some time t to a given energy level. N_i describes the population of level E_i. At thermal equilibrium absorption dominates stimulated emission since, according to Boltzmann statistics, most of the population will be in the ground level. At thermal equilibrium the populations would be described by:

$$\frac{N_{2,e}}{N_{1,e}} = \frac{g_2}{g_1} e^{(-\frac{E_2-E_1}{k_B T})} \tag{2.2}$$

where $N_{i,e}$ is the population at thermal equilibrium, g_i is the degeneracy of that level, k_B is the Boltzmann constant, and T is the temperature.

If there is an incident wave of sufficient intensity (photons/s) at the wavelength λ_0, we would hope to be able to move most of the population up to the excited state before the atom can decay through a radiative or non-radiative process back to the ground state. This is depicted in Fig. 2.2. Radiative transitions happen between E_2 and E_1, where as non-radiative (and fast) transitions happen between E_3-E_2 and E_1-E_0. At thermal equilibrium $N_{2,e} < \frac{g_2}{g_1} N_{1,e}$ but when there is a flux of photons incident on the material, i.e. under non-equilibrium conditions, a population inversion can occur where $N_{2,e} > \frac{g_2}{g_1} N_{1,e}$ and the material will act as an amplifier. When this can be achieved the material is called an active material.

If the atom decays through spontaneous emission, the rate is actually proportional to the population in

the upper state:

$$(\frac{dN_2}{dt})_{sp} = -AN_2 \tag{2.3}$$

where the rate of spontaneous emission is denoted by A, first obtained by Einstein through thermodynamic considerations, and the lifetime would be denoted $\tau_{sp} = 1/A$.
Similarly for stimulated emission or absorption, the expression would be:

$$(\frac{dN_2}{dt})_{st} = -W_{21}N_2 \tag{2.4}$$

where W_{21} is the rate of stimulated emission and W_{12} is the rate of stimulated absorption. Unlike A, the coefficient W_{21} depends not only on the transition but also on the intensity of the incident wave. For a plane wave, for example, we could write $W_{21} = \sigma_{21}F$ where F is the flux and σ_{21} is the cross section.

In order to make a working laser, we need at least three levels in order to sustain a population inversion. This is because Einstein showed that for non-degenerate two level systems $W_{21} = W_{12}$ and $\sigma_{21} = \sigma_{12}$. Most lasers involve a four level system which balances the need to try and pool the electrons in the certain excited states with levels for pumping that have fast decay times and are separate from the levels involved in emission. These different systems are shown in Fig. 2.2A for optical pumping. The four level system is a bit more intuitive to understand for optical pumping schemes than it is for current injection, which is illustrated in Fig. 2.2B. In current injection, an external current supplied electrons to the CB of the material (and holes to the VB). The injected electrons create a population inversion by filling the higher states, up to E_3, so that the carriers are available to move to the optical transition level at E_2. The non-radiative transitions happen with one band as the unoccupied/occupied states shift, and the three or four level system can still be applied to the more complicated bands of a semiconductor. The ability to create a population inversion is part of the criteria to making a laser since this ensures that the rate of stimulated emission will be greater than the rate of absorption, and the threshold for lasing can be overcome as described in the previous section. The so-called transparency value describes the rate of pumping required to ensure the appropriate electron density is available for emission, accounting for losses and absorption.

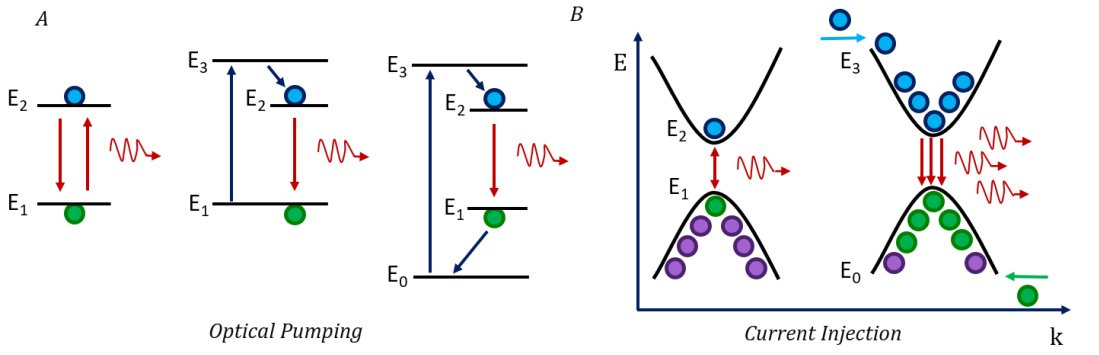

Figure 2.2: *A:* Optical pumping schemes for two, three, and four level laser schemes. *B:* Pumping via current injection into energy bands (versus the wave vector) of a semiconductor. The different energy levels are likened to the occupied/unoccupied states.

2.1.3 Optical cavities

Feedback that leads to amplification of stimulated emission is generated by placing the gain medium inside an optical cavity. The optical cavity also leads to the directional output lasers are well known for. An optical cavity is created by arranging mirrors so that the confined, reflected light forms a standing wave. The standing wave produces longitudinal modes along the direction the light travels that have different frequencies according to the separation of the mirrors. The amplification from the optical cavity is important for increasing the photon number, which leads to more stimulated emission. On each pass there are also losses from the mirrors and material, so an important metric to describing a cavity is the photon lifetime of that cavity mode. The cavity quality factor, Q factor, is the amount of energy stored vs the energy lost in one cycle of oscillator (or round trip). The Q factor is calculated from:

$$Q = \frac{\nu}{\Delta\nu_c} \tag{2.5}$$

where ν is the cavity resonance frequency, and $\Delta\nu_c$ is the mode's line width. A cavity is designed such that it has a large Q factor and incurs minimum losses in order to have a stable output beam with a small linewidth.

Different types of cavities are classified by the focal lengths of the mirrors and the distance between them. The different types include plane-parallel, spherical, confocal, hemispherical, and concave-convex. The most common type is the plane-parallel or FP cavity which consists of two opposing flat mirrors, as shown in Fig. 2.3A. The cavity modes are formed at positions based on the standing wave that can form between two mirrors separated by a distance, L. This arrangement is rarely used for free standing optics because of the difficulty in alignment but these problems are reduced for semiconductor lasers. For these

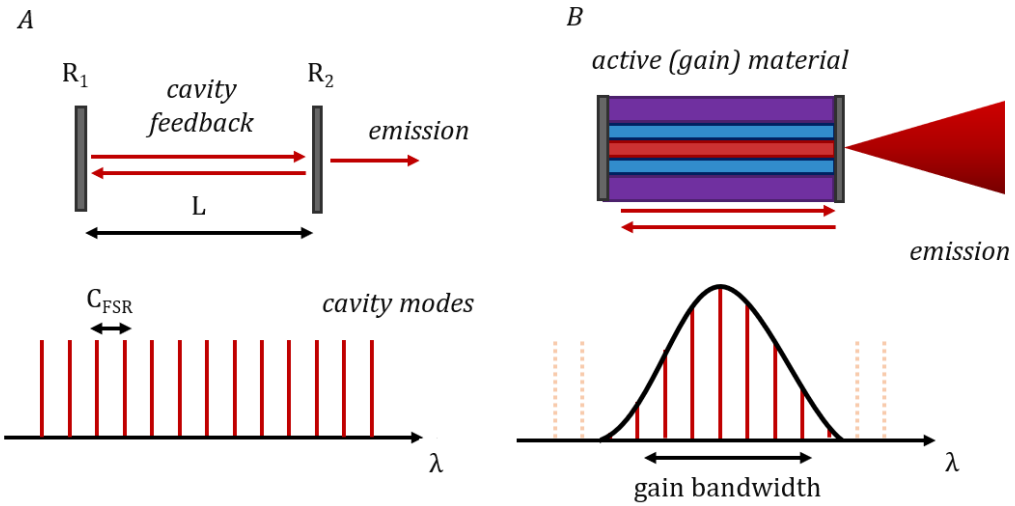

Figure 2.3: *A:* Passive Fabry-Perot (FP) (Plane - Parallel) resonator and the optical cavity modes formed between the mirrors. *B:* The Fabry-Perot laser (active) resonator, with gain material placed between cleaved facets (mirrors). The cavity modes that fall within the gain bandwidth of the material are supported.

lasers, reflective coatings or cleaved edges can be applied to the ends of a gain material, replacing the mirrors in a free space optics set up. Only certain geometries can produce a stable resonator and by using ray transfer matrices, the criterion for this stability can be describe by the two mirrors radii of curvature, M_{R1}, M_{R2} and the distance between them, L:

$$0 \leq (1 - \frac{L}{M_{R1}})(1 - \frac{L}{M_{R2}}) \leq 1 \tag{2.6}$$

The optical modes, ν, can be found by imposing the condition that the cavity length, L, be an integer number of a half wavelength. For a passive cavity, ν can be found using:

$$\nu = m\frac{c}{2L} \tag{2.7}$$

where m is a positive integer. Equivalently, this condition can be imposed on the phase shift of a plane wave after one round trip. Then the condition would become $2kL = 2\pi m$, where $k = 2\pi/\lambda$ is the wavevector. The free spectral range of the cavity, C_{FSR}, is the spacing between two successive modes and it is calculated by:

$$C_{FSR} = \frac{\lambda^2}{2n_g L} \tag{2.8}$$

where n_g is the group index of refraction, $n_g = n(\lambda) - \lambda\frac{\partial n}{\partial \lambda}$, including dispersion. In Fig. 2.3B, the effect of including gain material in a cavity is illustrated. The output is the convolution of cavity modes formed in a passive cavity with the gain of the material placed in the cavity. Some modes are amplified, while others are no longer supported as optical losses incurred. The total loss comes from the internal loss of the material and the mirror loss of the cavity. The mirror loss, α_m, is given by[38]:

$$\alpha_m = \frac{1}{2L} ln \frac{1}{R_1 R_2} \tag{2.9}$$

where R_i is the power reflectivity of the mirrors. This can be calculated using Fresnel's reflection equations for plane waves in the case of a facet, where there is a semiconductor-air interface:

$$R = \frac{(n-1)^2}{(n+1)^2} \tag{2.10}$$

where n is the index of refraction of the semiconductor. For the GaSb lasers, $n \approx 3.5$ so $R \approx 0.3$[4].
One property that comes from the gain medium being in a cavity is directionality. In order for the positive feedback to occur from the two mirrors, the beam must be propagating orthogonally to their plane in order to be sustained (the longitudinal modes). In part, what this indicates is that the beam divergence can be made diffraction limited meaning that the beam's divergence can be described by:

$$\theta_d = \frac{\beta\lambda}{D} \tag{2.11}$$

where D is the diameter of an aperture, λ is the wavelength, β is a numerical factor describing the shape of the amplitude distribution of the wave, and θ_d is the beam divergence. If the wave is only partially

spatially coherent, the divergence through the aperture will be larger than θ_d.
Being close to a diffraction limited beam means that a laser has the maximum power in the beam diameter. This leads to a high photon density in the beam and also allows for an extremely high intensity in the focal plane when the beam is focused which is an important feature exploited in many applications. The important metric that commonly quantifies the laser's directionality is the M^2 factor, which describes how diffraction limited a Gaussian beam is. The half angle beam divergence:

$$\theta = M^2 \frac{\lambda}{\pi \omega_0} \tag{2.12}$$

where ω_0 is the beam waist and λ is the wavelength in the medium. A perfectly diffraction limited beam would have $M^2 = 1$.
The longitudinal modes describe the standing wave between the two mirrors, along the z direction. The transverse modes describe the intensity distribution of the wave perpendicular to the optical axis (along the surface of the mirrors). These are created by the width of the cavity, and are described as transverse electro-magnetic (TEM) modes with two different indices for the number of nodes in x and y (TEM_{mn}). These modes are described by Hermite-Gaussian polynomials, where the basic TEM_{00} mode would be a Gaussian. The fundamental TEM_{00} is all that is desired in the devices considered in this thesis. For a symmetric dielectric slab waveguide, this thickness would be:

$$d < \frac{\lambda}{2\sqrt{n^2 - 1}} \tag{2.13}$$

where n is the index of refraction of the waveguide and 1 comes from the index of refraction of air. When the cavity is too large higher order modes can be supported and the consequence of this will be discussed in the design sections.

2.1.4 Electro-optical characteristics of a semiconductor laser

There are a number of metrics that are used to describe the performance of a laser, which come from the analysis of the power-current-voltage (PIV) measurements. An example of the PIV characteristics of a laser is sketched in Fig. 2.4, with the left axis showing the electrical properties from the IV measurements and the right axis showing the optical properties from the PI measurement. The current and voltage across the laser are measured using probes that are manually placed on the laser's metal contacts while the optical properties are measured at one end of the laser using a cooled photodetector, power meter, or spectrometer. During operation, the laser is placed on a heat sink that is cooled with a thermo-electric cooler (TEC). For operation, current injection can happen in CW mode or in pulsed mode. In pulsed mode, typically 1 µs pulses at a repetition rate of 10 kHz are applied to the device to avoid local heating.
The PIV metrics sketched in Fig. 2.4 include the threshold current I_{thr}, the voltage at threshold V_{thr}, the turn on voltage V_{OC}, the series resistance R_s, the slope efficiency dP/dI, and the current and power at the roll over point I_{Max}, P_{Max}. The threshold is marked by the abrupt knee in the PI curve and is a key metric for material performance, as it proves the laser design has gain that can overcome the material and cavity losses. This is I_{thr} or J_{thr} when we divide by the area (wxL) of the device to get the current density. V_{OC} is

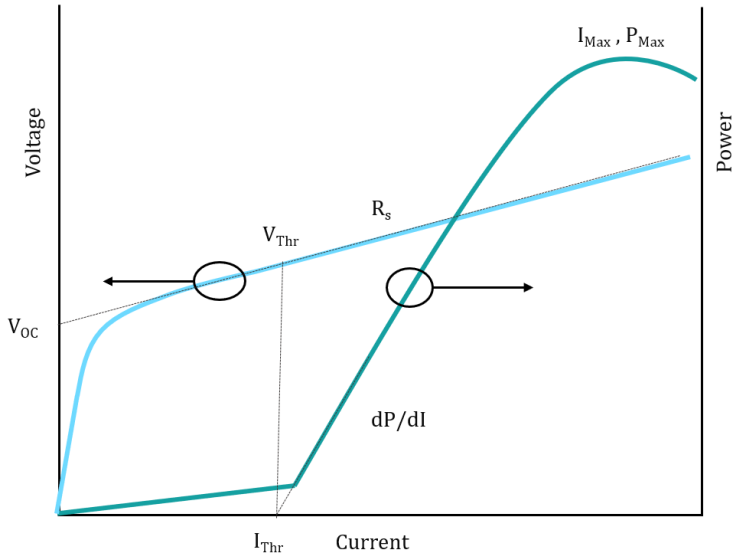

Figure 2.4: An example PIV sketch of performance typical to ICLs, highlighting important figures of merit.

the voltage that needs to be applied for the device to become conductive (similar to a normal diode). R_s is found from the slope at the IV curve and represents the material and contact resistance. It is an important metric for determining the quality of the fabrication and identifying self-heating issues. Another feature of the IV curve is the leakage current. Although it is not quantified, it is represented by the amount of current that flows for $V < V_{OC}$. dP/dI is the slope of the fit of the PI curve near the threshold and is measured to have an idea of the slope far from the roll over point, which is marked by the drop of power at I_{Max}, P_{Max}. It is a good indicator of the quality of the growth since it depends on the quantum efficiency, discussed below. The roll over point happens because of heating and gain saturation in the material. The P_{Max} achieved, especially when operating in CW mode, depends on the device dimensions, facet coating options, and mounting orientation. Facet coating helps to maximize the output of the laser since a high reflective coating can be applied to one side, nearly doubling the output instead of having the laser emitting from the two cavity ends. At the same time, the mounting orientation is important because the distance of the active region to the heat sink will affect the effectiveness of the cooling and the point of gain saturation. Between the threshold and rollover point, the output power can be calculated:

$$P = \eta_i \eta_d \frac{\alpha_{cav}}{\alpha_{cav} + \alpha_i} \frac{h\nu}{q} (I - I_{thr}) \tag{2.14}$$

where η_i is the internal quantum efficiency, η_d is the external quantum efficiency, α_{cav} are the cavity and facet losses, α_i is the internal losses, and q is the electron charge[39]. η_d can be found from the slope efficiency[37]:

$$\eta_d = \frac{q\lambda}{hc} \frac{dP}{dI} \tag{2.15}$$

η_d represents the ratio of injected carriers to the emitted photons while η_i represents the ratio of injected carriers to the photons generated by the material within the cavity, thought they might not necessarily

contribute to the output power[40]. An estimate of α_i and η_i can be extracted from the relation between the η_d and the cavity length, L, given by:

$$\eta_d = \frac{\eta_i}{(1 + \alpha_i L / ln(1/R))} \tag{2.16}$$

where R is the facet reflectivity (≈0.3 from Fresnel equations for an interface between air and semiconductor material with n_{eff} ≈3.5)[41]. The final cavity length represents a trade off between the losses that scale with length vs the gain that can be provided; a balance between low threshold current densities and high output powers. This relationship illustrates that threshold currents increase with shorter cavities since the mirror losses become larger.
An important parameter that indicates temperature stability is the characteristic temperature, T_0 of the laser. When T_0 is low, I_{thr} will increase and dP/dI will decrease with increasing operating temperature. A high T_0 indicates better thermal stability. At a given temperature, T_1:

$$I_{thr}(T) = I_{thr}(T_1) e^{\frac{T - T_1}{T_0}} \tag{2.17}$$

where $I_{thr}(T)$ is the threshold current at a given temperature, $T[K]$[39].
For this thesis, the main electro-optical characteristics of a laser considered are I_{thr}, P_{Max}, and C_{FSR}, though all elements of the device performance are important for optimizing the design.

2.2 Mid-infrared semiconductor materials

There is a large variety in the physical and operating parameters of lasers. When they are characterized by the physical state of the active material, we have the categories solid-state, liquid, or gas lasers. But, then if you refer to the wavelength of emission you have categories such as X-ray, UV, visible, or MIR lasers[36]. Although the active region of a semiconductor laser is in the solid-state, they are often not included in this category because the mechanisms for pumping are quite different and so solid-state lasers generally describe the active material who have ions introduced as an impurity in a transparent host material[36]. This thesis describes the work on a specific type of MIR semiconductor laser - the interband cascade laser. The topics discussed in this section will focus on semiconductor lasers that employ quantum well (QW)s in the active region. In the following sections, a brief review of some semiconductor physics will be introduced with a focus on materials and systems that are used to design devices that operate in the MIR wavelength range, 2 µm to 20 µm.

2.2.1 Fundamental opto-electronics

Semiconductor lasers require the active medium to be a direct gap material in order to allow photon emission. A direct band gap material is one in which the momentum, $\vec{k}$, of the electrons and holes is the same in the minimum of the CB and maximum of the VB. Optical transitions occur when the photon energy exceeds the band gap energy. Examples include GaAs and GaSb. When the $\vec{k}$ of the carriers in the CB and VB are different, optical transitions are hindered by the fact that there are no target states, meaning energy and momentum conservation can't be fulfilled, and this is called an indirect band gap. If

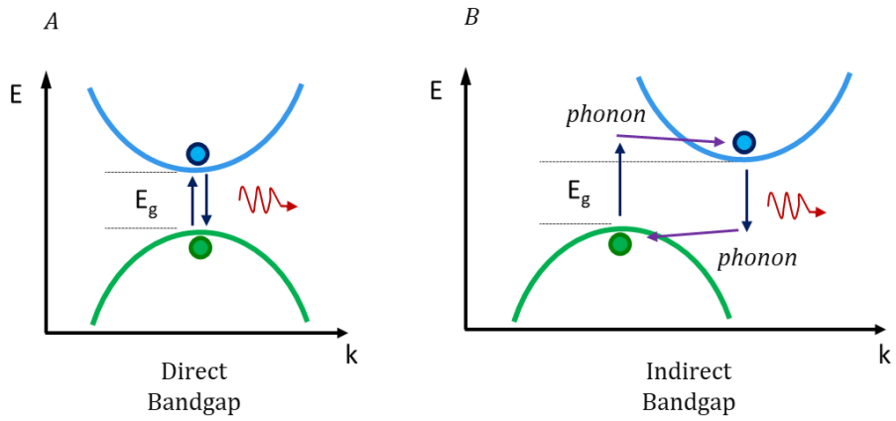

Figure 2.5: Illustration to highlight the difference between direct and indirect band gap materials.

phonons are emitted, the processes become possible but will occur at much lower rates, simply because more bodies are involved in the transition. The differences between the transitions are highlighted in Fig. 2.5. Many semiconductor lasers are based on III-V compounds, which are a combination of elements from the third and fifth groups of the periodic table.

The optical transitions involved in semiconductor lasers are either interband transitions, between the CB and VB, or intersubband transitions, between two different levels in the CB, as sketched in Fig. 2.6. In this thesis, we will only focus on interband transitions to understand ICLs.

For a semiconductor at 0 K the CB will be empty and the VB will be completely filled. Electrons can be raised to the CB via pumping and will then quickly drop to the lowest unoccupied level of that band. At the same time, electrons at the top of the VB relax and leave holes. The lowest unoccupied levels are represented by the quasi-Fermi levels E_{FC} and E_{FV} for the CB and VB, respectively. Light emission will then occur when the electrons drop down to fill the holes in the VB. In order for this to be part of a laser system, stimulated emission must occur. The condition for the incoming photon, with energy $h\nu$, to be amplified (instead of absorbed) is given by:

$$E_g \leq h\nu \leq E_{FC} - E_{FV} \tag{2.18}$$

This is intuitively understood from Fig. 2.6 since in order for the electron to undergo a transition between the quasi-Fermi levels, there must be empty states and so the photon energy may need to be slightly larger than E_g in order to accommodate this. Both E_{FC} and E_{FV} change depending on the intensity of the pumping because they depend on the population in the CB: E_{FC} increases with N while E_{FV} decreases. In order to satisfy Eqn. 2.18, there is a minimum electron density required that is called the transparency carrier density, N_{tr}, such that:

$$E_{FC}(N) - E_{FV}(N) = E_g \tag{2.19}$$

Once $N > N_{tr}$, the material will have net gain and can lase if this is sufficient to overcome the losses as described in Sec. 2.1.3.

A constant flow of carriers must be available to replenish those that recombine when they are converted into photons. This pumping must be done via an external energy source and can be done optically or

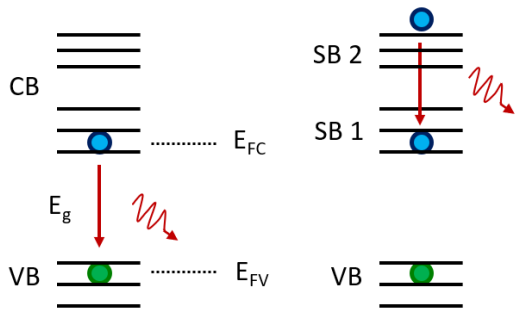

Figure 2.6: Illustration of interband vs intersubband transitions.

electrically. In a semiconductor the most convenient way is to electrically pump the active region directly with an electrical current (current injection). The carriers are confined to the active region, increasing the probability of recombination, by adding cladding layers to form a double heterostructure[42]. Diode lasers are formed by sandwiching the active material between p and n type materials whose band gap is larger than the active region so that light is not absorbed by these layers. The thickness of the active region plays an important role on the confinement and conditions at threshold. The dependence of the threshold current density on the active layer thickness, d, at threshold is given by:

$$J_{thr} \propto \frac{qd}{\eta_i \tau_r} N_{thr} \tag{2.20}$$

where τ_r is the radiative recombination time. η_i has already been defined as the internal quantum efficiency which means the fraction of the carriers that recombine radiatively in the active layer. For sufficiently large values of d, N_{thr} is almost the same as the N_{tr} and is therefore constant, leading to a linear relationship between J_{thr} and d. When d becomes sufficiently small the confinement of the active layer is less effective and the beam spreads over the surrounding layers. This leads to a minima in J_{thr} with respect to d. As well, we must define the threshold condition using spatially averaged values. If at this point we set the condition that the spatially averaged gain must equal the spatially averaged losses[36]:

$$\langle g \rangle L = \langle \alpha_a \rangle L + \langle \alpha_{c1} \rangle L + \langle \alpha_{c2} \rangle L + \gamma_m \tag{2.21}$$

where L is the length of the active medium, g is the gain, α_a is the losses of the active layer, $\alpha_{c1,2}$ are the losses of the cladding layers, and γ_m is the mirror loss. The term $\langle g \rangle L$ is defined as the modal gain and we introduce the beam confinement factor, Γ, to represent the fraction of the beam power that is actually in the active layer. Γ can be approximated using the normalized thickness of the active layer and cladding layers by the expression:

$$\Gamma \approx \frac{D^2}{2 + D^2} \tag{2.22}$$

where D, the normalized thickness, is calculated by:

$$D = 2\pi \frac{\sqrt{(n_1^2 - n_2^2)d}}{\lambda} \tag{2.23}$$

where n_i is the refractive index of the active region and cladding layers. Substituting this expression back into Eqn. 2.21 leads to an expression with the threshold carrier density, and subsequently threshold current density (Eqn. 2.20), that is inversely proportional to Γ. This explains the minima in J_{thr} with respect to d.

Returning to the idea of the double heterostructure, the cladding layers were important for carrier confinement, but the implications have to be considered for the optical cavity; optical confinement needs to be possible. Optically, a guiding structure can be made when the refractive index of the active layer is much larger than the surrounding cladding layers and cavity feedback will still be possible.

2.2.2 Active regions with QWs

If the thickness of the active layer is reduced to the point where the dimension is comparable to the de-Broglie wavelength, then a QW forms (thickness ≈10 nm). This reduces I_{thr} and improve the device efficiency[37]. Confinement occurs and leads to quantized energy levels for the carriers, similar to the electron energy levels in the infinite QW studied in basic quantum mechanics. Recall for the infinite square well of width a the energy levels are discretized as:

$$E_n = \frac{n^2\pi^2\hbar^2}{2ma^2} \tag{2.24}$$

where m is the mass of the electron and n is an integer. For an attractive potential there always exists a bound state in 1D and 2D but not in 3D. The carriers are confined by the QW and this confinement along one direction changes the density of states for the carriers. Recall, the 3D density of states is proportional to $\sqrt{E}$ and in comparison, the 2D density of states is a constant. So, the 2D density of states has a significant number of available states as well as guarantees a bound state for the carriers. In comparison to bulk, the QW confinement leads to a 2D density of states which means the number of available states, after an energy gap, is independent of the energy. This is important because the absorption and gain coefficients depend on the density of states and this directly impacts the transparency density required for lasing.

There are two classifications of QWs: type-I meaning the carriers are confined in the same material while in type-II the carriers are confined in different materials. The heterojunction offsets are further classified according to the band alignment, as shown in Fig. 2.7. Type I QWs have a type-I heterojunction offset, which is when the CB is higher than the VB. Type II QWs contains type-II heterojunction offsets, which is when the CB is higher than the VB, and type-III heterojunction offsets, which is when the VB is higher than the CB. In type-I QWs the overlap of the carrier wave function is very high; almost 100% since it is in the same material[3]. In order to improve wave function overlap for type-II QWs, more complex configurations have been developed, in order to still capitalize on the reduced band gap. So called superlattice (SL)s and W-quantum well (W-QW)s are used and they are pictured below [43, 44]. SLs are a periodic structure of QWs, with the thickness of <10 nm, meaning the neighbouring QWs can couple together. This means carriers can tunnel through these barriers, so a mini-band is formed due to the de-localization of the electronic states. This broadened emission spectrum means the density of states becomes 3D, so the gain that can be achieved is reduced[45]. In comparison, the W configuration

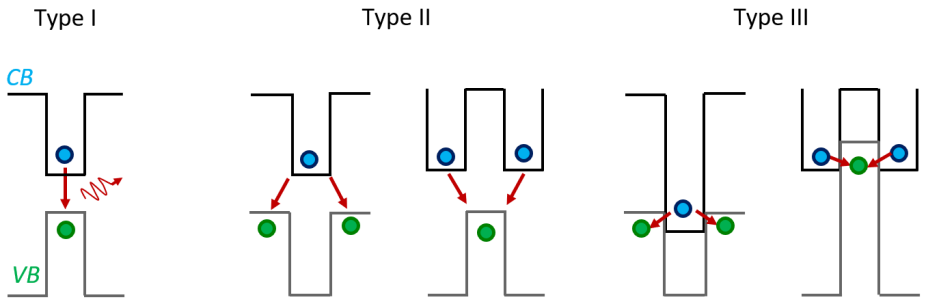

Figure 2.7: Three different types of semiconductor heterojunctions. From *Left* to *Right*: Type I (straddling), Type II (staggered), and Type III (broken).

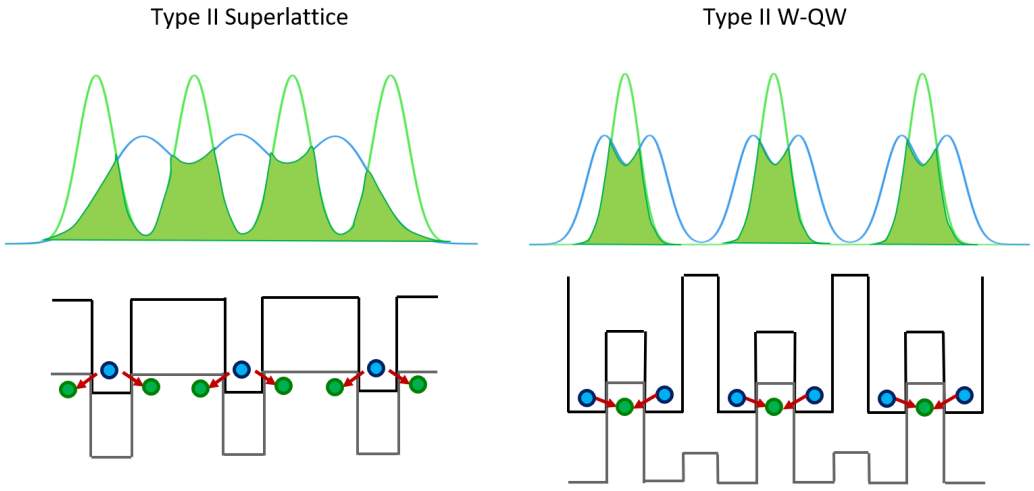

Figure 2.8: Quantum well configurations for the type-II class

introduces a barrier and this addition increases carrier overlap to up to 70%[44]. Since there are just two QWs, the 2D density of states can be preserved which reduces the carrier density at transparency and enhances the differential gain[3]. The W-QW configuration is important in reducing the Auger coefficient, an important challenge in designing MIR devices, and will be discussed in Sec. 2.2.5.

2.2.3 Challenges for mid-infrared range emission

There are several challenges faced in keeping a low threshold current density when designing a laser for the MIR range, since for these longer wavelengths there is a decreasing band gap between the CB and VB for interband transitions. Recombination processes that scale with wavelength, such as Auger and free carrier absorption, are an obstacle for laser design[46]. However, there are also some advantages to narrow band gap materials, which include less spontaneous emission and a lower carrier density required for population inversion.

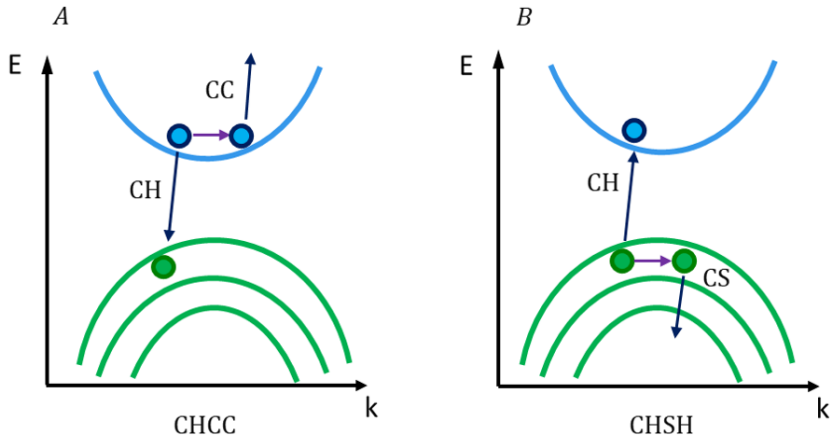

Figure 2.9: Different types of recombination processes in the valence band for the Auger processes.

The losses that make the MIR difficult to reach with a reasonable J_{thr} include four different types of losses [3]. These types of recombinations include Shockley-Read-Hall (SRH) recombnination, radiative recombination, Auger recombination, and carrier leakage. They have an additive effect to the current density[47]:

$$J = J_{SRH} + J_{rad} + J_A + J_L \tag{2.25}$$

The mechanism for J_{SRH} is the electron passing through a dopant/defect in the lattice and creating a phonon; nonradiative recombinations. J_{rad} refers to transitions that generate photons. J_L refers to the leakage current; referring to processes when injected carriers do not recombine in the QWs. J_A represents the Auger effect, which are non-radiative recombination processes that scale with the wavelength.
SRH recombinations involve interband gap defect states. In semiconductors, a defect is something that causes a break in the crystal symmetry which create a recombination center between the CB and VB. These can arise from impurity atoms (dopants) or crystal dislocations[48]. J_{SRH} scales linearly with the carrier density, n, and L, though it is only dominant at low n with respect to threshold: $J_{SRH} \propto AnL$. Radiative transitions are subject to the k selection rule and the rate is given by Fermi's Golden rule[49]. J_{rad} then scales linearly with n and the hole density p, as well as L: $J_{rad} \propto BnpL$.
The biggest problem with MIR device performance stems from Auger recombination. Auger processes mean the energy of an electron that recombines with a hole is transferred to a third carrier that finally dissipates the energy into a forth carrier. Since phonons are often involved, Auger processes not only deplete the carrier density but also heat the crystal[50]. The two main Auger processes that are considered are illustrated in Fig. 2.9, labelled CHCC and CHSH.
The CHCC mechanism involves an electron hole recombination between the **C**B and **H**eavy hole VB that excites a **C**B electron into a higher **C**B state. The CHSH mechanism involves an electron hole recombination between the **C**B and **H**eavy hole VB that excites electron from the **S**pin orbit VB into the **H**eavy hole VB[46]. To make a simple analytical relationship, since there are 3 carriers involved, this process scales with n^3 (if $n = p$), so that $J_A \propto Cn^3L$.

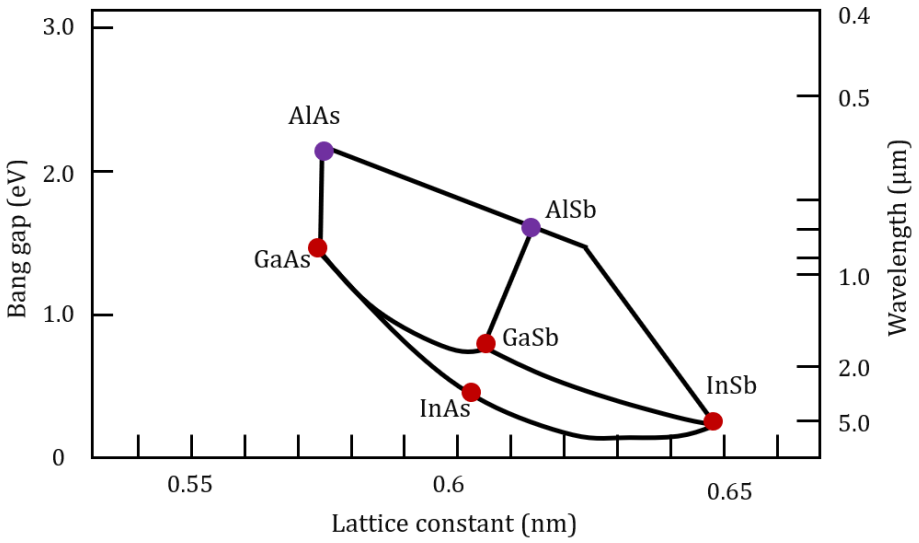

Figure 2.10: Band gap energy/wavelength as a function of lattice constant for several semiconductors, adapted from[2]

The coefficient for Auger recombination is given by[3]:

$$C = C_0 e^{-\frac{E_a}{k_B T}} \tag{2.26}$$

where k_B is the Boltzmann constant, T is the temperature, and E_a is the activation energy. The probability of Auger recombination is dependent on the matrix element for Coulomb interactions, and satisfying energy/momentum conservation rules. This sharply peaks for the lowest energy distribution of carriers, which results in E_a being dependent on the band gap. For CHCC processes, $E_a \propto E_g$ and the carrier masses[51]. The dependence of the Auger recombination rate on wavelength is then clear. For CHSH processes, there are two distinct regimes that depend on E_g with respect to the spin orbit splitting energy, Δ_{SO}. If $E_g > \Delta_{SO}$, then the activation energy for this process is scaled with the participating carrier masses and the proximity of E_g to Δ_{SO}. As the band gap grows larger than the spin orbit splitting, this process decreases. If $E_g < \Delta_{SO}$, then $E_a \propto \Delta_{SO} - E_g$[52].
Quantum confinement can lead to additional pathways for Auger recombination that are thresholdless, since they require no activation energy. This involves bound-unbound transitions between confined carriers in the QW and the continuum. Since this is a thresholdless transition, the Auger coefficient would only weakly depend on temperature; in contrast to the exponential coefficient for the activated pathways[53]. For MIR devices, Auger recombination is a critical challenge that needs to be addressed to minimize threshold current density and temperature sensitivity.

2.2.4 III-V-Sb lasers

Band gaps corresponding to MIR wavelengths are covered by the family of III-V materials that use antimonides. The III-V-Sb system refers to zinc-blend alloys that are approximately lattice matched to

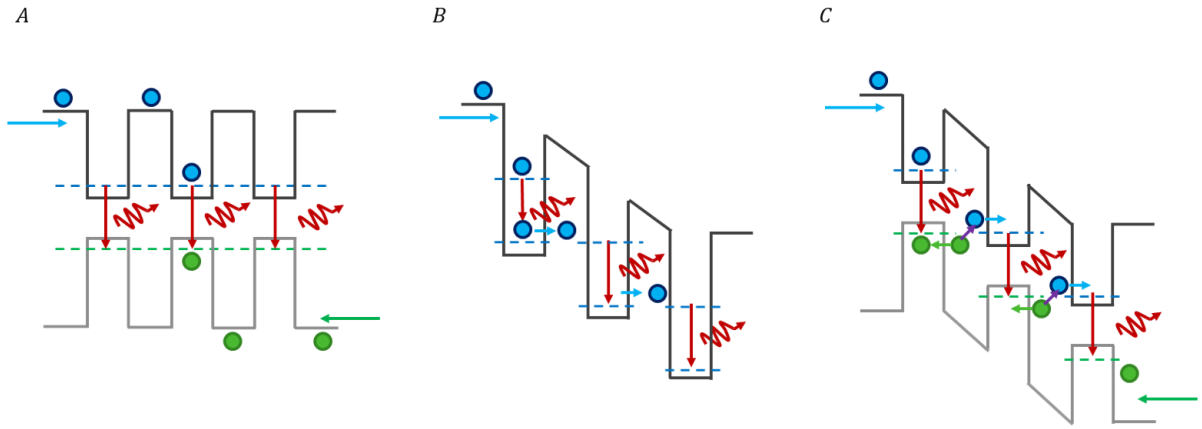

Figure 2.11: Sketch of the QW and heterojunction configuration for *A:* a diode laser, *B:* a QCL, and *C:* an ICL.

GaSb, which has a lattice constant, a =6.095Å[3]. This lattice constant can accommodate other III-V binary compounds as well as ternary or quarternary alloys, which is shown in Fig. 2.10[2, 54]. This shows a plot of the band gap (wavelength) vs lattice constant for the different III-V-Sb materials of interest around GaSb, highlighting the range of band alignments possible. The lines highlight how the lattice constant and band gap will change as we shift from one compound to another. AlAs and AlSb are in purple because they are indirect semiconductors.

The three main type of lasers that are used for the MIR include diode lasers, QCLs, and ICLs as illustrated in Fig. 2.11. Fig. 2.11A shows a multiple quantum well (MQW) diode laser where emission is generated by interband transitions and the electrons and holes are confined within the same material[37]. Fig. 2.11B shows a QCL where emission is generated by intersubband transitions and the electrons are recycled from the cascading of QWs[33]. Fig. 2.11C shows an ICL where emission is generated by interband transitions and the carriers are recycled by the cascaded architecture.

Threshold current densities of different devices measured near room temperature are presented in Fig. 2.12[3]. Emission in the lower end of the MIR range can be achieved with type-I diode lasers. Their performance tends to deteriorate with increasing wavelength and the output power and characteristic temperature drops[46, 55]. This deterioration can be attributed to Auger recombination and hole leakage due to VB offset[56]. Meanwhile, QCLs span most of the MIR spectral range, with room temperature emission beginning around 3 µm[57]. QCLs generate light via intersubband transitions in the CB, which immediately leads to a reduction in Auger recombination since no interband transitions are involved. This comes at the cost of various fabrication challenges to ensure the correction CB offset between layers, as well as high operating voltages due to the high number of QWs needed[58].

As illustrated by Fig. 2.12, beyond 3 µm type-II QW lasers begin to outperform the type-I QW lasers beyond 3 µm. Transitions can occur between two different materials, allowing transitions less than the band gap of the one material (Fig. 2.7, type-III heterojunctions)and allowing independent engineering for the spatially separated carriers[59]. This spatial separation (Fig. 2.7 type-I vs type-II QW) helps to reduce Auger recombination and radiative losses, but at the expense of reducing wavefunction overlap[60, 61]. The best type-II QW configuration to implement is the W-QW (Fig. 2.8). This benefits from the reduced

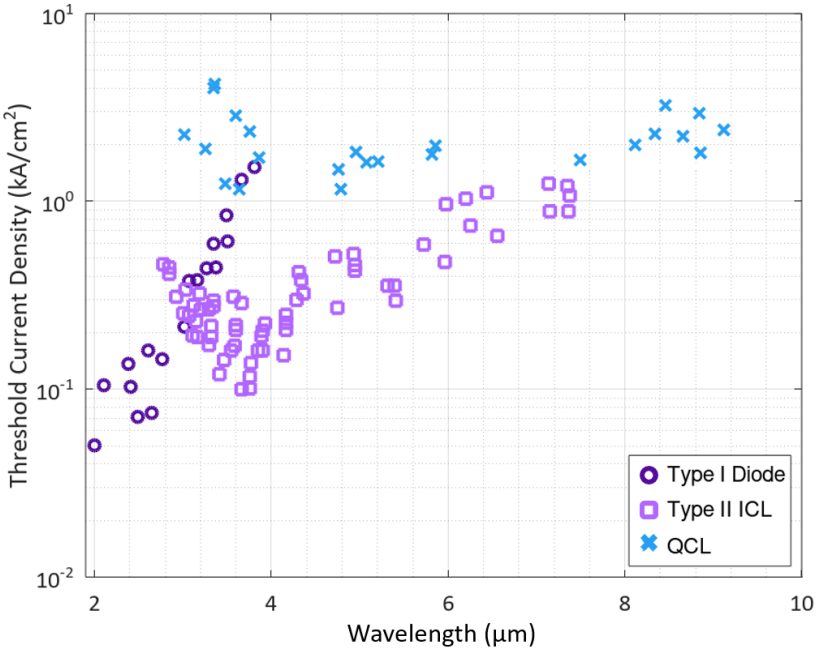

Figure 2.12: Threshold current densities of MIR lasers, adapted from [3].

Auger recombination but preserves the wavefunction overlap.
Besides choosing type-II interband material architectures to combat the higher Auger coefficient in the MIR, a cascaded QW architecture can be implemented to further improve laser performance above MQW diode lasers[62]. MQWs chained together behave a lot like resistors connected in parallel configuration. For each QW, carriers need to be supplied for emission to occur. If the QWs could be chained together in series, each carrier could pump multiple QWs[2]. Consider M different QWs, the threshold behaviour is described by the following equations:

$$V_{th} = M\frac{E_g + \Delta E}{q} \tag{2.27}$$

$$P_{th} = V_{th}I + RI^2 = M\frac{E_g + \Delta E}{q}J_{th}S + RJ_{th}^2S \tag{2.28}$$

where S is the surface area of the device and ΔE is accounting for the internal losses of the device. The threshold power scales with M and is therefore lower than the parallel configuration, which scales with M^2 (since $J_{th} \to MJ_{th}$ in the last term)[63].

Both QCLs and ICLs connect QWs in series and cascade them. Cascading refers to the bending of the bands via an external field to align the QWs under one another, so that the carriers will fall (cascade) into each subsequent QW so that each carrier can produce multiple photons, as illustrated in Fig. 2.13[62]. QCLs are a cascade of type-II QWs for intersubband transitions, while ICLs are a cascade of W-QW for interband transitions. Cascading offers reduced series resistance, uniform carrier injection and large band offsets which leads to lower threshold currents, as illustrated in the minima between 3 μm to 4 μm in Fig. 2.13, though is at the expense of higher operating voltages[64].

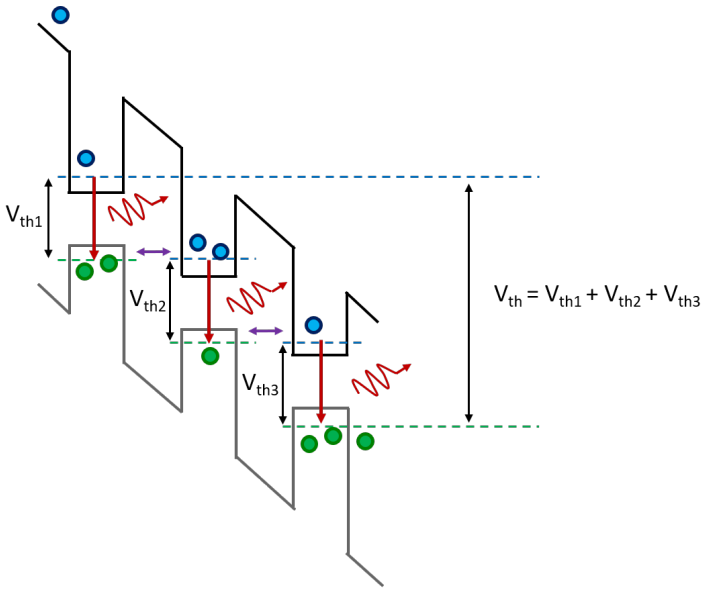

Figure 2.13: Schematic of cascaded QWs.

Utilizing cascaded W-QW has allowed the losses due to Auger recombination to be overcome and allow for efficient performing ICLs to be fabricated for the MIR[63]. Interband transitions are needed to avoid the difficulties creating a population inversion with the short phonon relaxation times experienced in intersubband transitions that are seen for QCLs[64]. ICLs also require fewer QWs to achieve positive gain. This leads to the overall lower operating power required with respect to QCLs.

2.2.5 ICL active region

The ICL active region is more complex than MQW diode lasers as it contains multiple repeated stages, not just QWs, in order to have room temperature operation in the MIR. The main components of one stage are: the W-QW, the hole injector, the semi metallic interface (SMIF), and the electron injector. This stage is then repeated 5-10 times to make up the entire active region[65]. An example of the band diagram of one ICL stage is shown below in Fig. 2.14. The wave functions of the electrons is drawn in blue and orange in green and purple for the holes throughout the stage.

The W-QW allows emission, the hole injector forces holes into the QW, and the electron injector efficiently dumps electrons into the next QW. The goal of each component is to quickly transport the carriers between QWs and then keep them in the QWs so that they can produce the maximum number of photons possible. The SMIF allows the carriers to be transported between the VB and CB because of the unique alignment of the bands between GaSb and InAs possible under an applied field[54]. The SMIF separates the GaSb/AlSb QWs from the InAs/AlSb QWs in the hole and electron injectors, respectively. When the thickness of this interface is optimized, large amounts of optical losses from free hole absorption can be avoided in comparison to alternative doped tunnel junction designs[66]. The alignment of each stage under applied bias is important as well, the separation must be sufficient to produce optical gain while also generating an internally generated equilibrium of the carrier densities. The separation of the stages is illustrated in Fig. 2.15, where two stages of the active region are sketched. The quantum ground state energies are

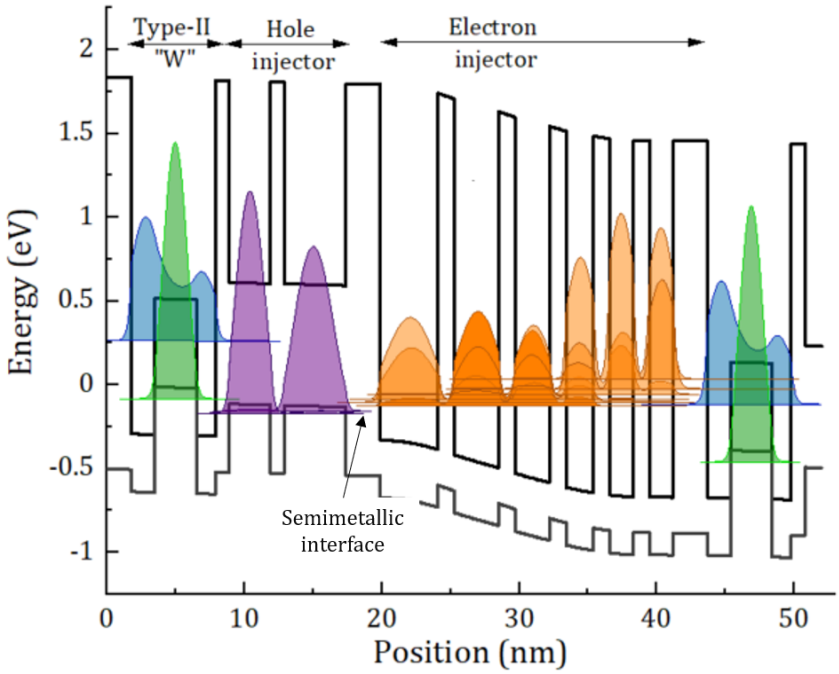

Figure 2.14: One stage of the ICL active region including the W-QW, hole injector, semimetallic interface and electron injector. The wave function of the carriers is shown in the CB and VB throughout the stage in blue and orange for electrons or in green and purple for holes.

highlighted in the QWs, drawn as black lines, and the material for the different layers is labelled. The optical gain must compensate the photon loss, which is a condition from Eqn. 2.18. Now, E_{FC} is in the CB of stage 2 and E_{FV} is in the VB of stage 1, for example, are at the same level (refer to Fig.2.14). The thickness and doping of the QWs in the electron/hole injectors are extremely important to balance in order to achieve the correct carrier density distribution by the SMIF[67]. If the QWs are too thick, there will be free carrier absorption while if they are too thin, the threshold voltage will be much higher than needed[65]. The creates one quasi-Fermi level on either side of the SMIF leading from/to the successive W-QWs[65].

The design goals of the hole and electron injectors are then to maintain this quasi-Fermi level while maximizing the fraction of injected carriers in the active states. The hole injector is the potential barrier that separates the InAs QWs in the W-QW from those in the electron injector. It is designed to prevent tunnelling across its width, which electrons can do via mid-gap defects. But, if it is too thick, holes won't be transported to the W-QW[68]. The electron injector is composed of varying thicknesses of InAs/AlSb QWs that form a mini-band and transport the electrons to the next active QW under an applied field. The varying thicknesses mean there is not an equal occupation probability, as suggested by the wavefunction shape of the electrons seen in Fig. 2.14. Doping of the electron injector is important to rebalancing the carriers at threshold. Without supplementing the carriers generated at the SMIF, there will be far greater holes than electrons. The AlSb barriers in the injectors are relatively thin to ensure the transport is not hindered.

In the previous sections, the general properties of the W-QW configuration were already discussed. The

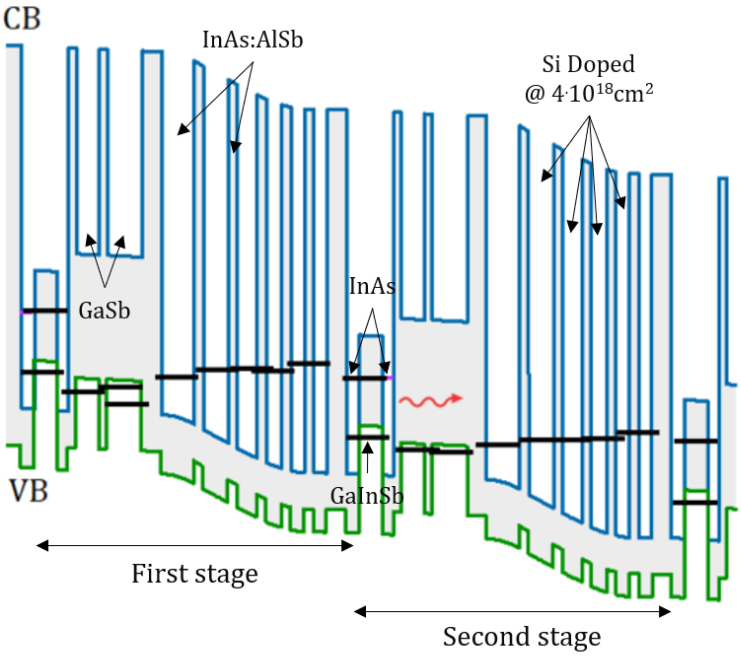

Figure 2.15: Two stages of the ICL active region are drawn with the energy levels highlighted. As well, the material used for the QWs is labelled.

W-QW design for an ICL has two InAs electron QWs surrounding a $Ga_{1-x}In_xSb$ alloy hole QW. The $Ga_{1-x}In_xSb$ contains $x = 30 - 35\%$ In (refer to Fig. 2.10) and results in a 2.5% compressive strain on the QW. The thickness is important in lowering the threshold current density, tuning the transition energy and minimizing the intersubband absorption, depending on which wavelength is being targeted[69]. The InAs W-QW thicknesses are used to select the desired laser emission wavelength.

2.3 Techniques for single-mode emission

Single-mode lasers evolve from the multi-mode FP laser scheme previously described in Sec. 2.1.3. We saw that a laser is created by the enhancement of optical cavity feedback from a gain medium. The output light contains resonator modes: longitudinal modes along the propagation direction and transverse modes perpendicular to this axis. Single-mode emission is achieved for a laser where only one of these resonator modes is supported. Higher order modes in the transverse direction can be suppressed by changing the width of the cavity but other methods are required to suppress unwanted longitudinal modes.
In general, this can be done by introducing defects into the laser cavity that alters the feedback between the facets[70]. These defects partially transmit and reflect light promoting constructive/destructive interference that results in the selective modification of the loss of longitudinal modes. These defects cause perturbations to the index of refraction of the top cladding, or more specifically the spatially averaged effective index of refraction, n_{eff}[71]. The general principle of producing interference by modulating n_{eff} can result in very different waveguide designs, some of which are depicted in Fig. 2.16[72].
Fig. 2.16 illustrates three of the different waveguide designs that will be discussed in this section: the

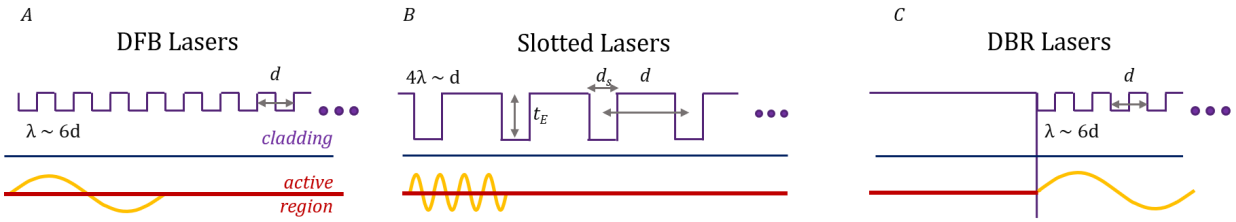

Figure 2.16: A schematic representing the different types of waveguide designs that can achieve single-mode emission. *A:* DFB waveguide, *B:* Slotted waveguide, and *C:* DBR section.

DFB laser, the slotted laser, and the DBR laser[4]. Although the focus of this thesis is on the design and fabrication of a slotted ICL, understanding the landscape of the various single-mode technologies is important. The relative size of the features of these designs is important: size of the grating/slots, desired emission wavelength, and length of the cavity. A DFB/DBR laser have a grating much smaller than the emission wavelength such that the accumulation of the light's diffraction from these features illicit feedback. For the DBR this can take the form of a grating, spatially separated from the active region, or a stack of alternating layers with different refractive indices. A slotted laser has larger features such that mode selection is caused by the refraction of light along the length of the waveguide. All of these designs couple forward and backward propagating waves through diffraction/refraction under the Bragg condition to achieve single-mode emission at the Bragg wavelength, λ_{Bragg}[73].

2.3.1 DFB and DBR devices

DFB and DBR lasers are similar in that their feedback effect is generated from sub-wavelength, periodic gratings or layers. Gratings are a period array of refractive index (or gain) variations[37]. For the forward and backward propagating beams around the cavity to couple at one wavelength, in accordance with Bragg's law, the grating period must be set such that:

$$m\lambda_{Bragg} = 2n_{eff}\Lambda_{grid} \tag{2.29}$$

where $m = 1,2,3,...$ is the order of diffraction and Λ_{grid} is the period of the grating. n_{eff} can be calculated between two different layers with indices of refraction, $n_{1,2}$, using:

$$n_{eff}^2 = \frac{(n_1^2 + n_2^2)}{2} \tag{2.30}$$

The propagation constant, β at this wavelength is defined as:

$$\beta = \frac{2\pi}{\lambda_{Bragg}} \tag{2.31}$$

The grating in the waveguide causes perturbations to n_{eff} from the contrast of cladding (high index material) and the air gaps (low index material). When these perturbations are small, coupled-wave analysis can be applied to describe the system [73]. The periodic perturbations to the refractive index

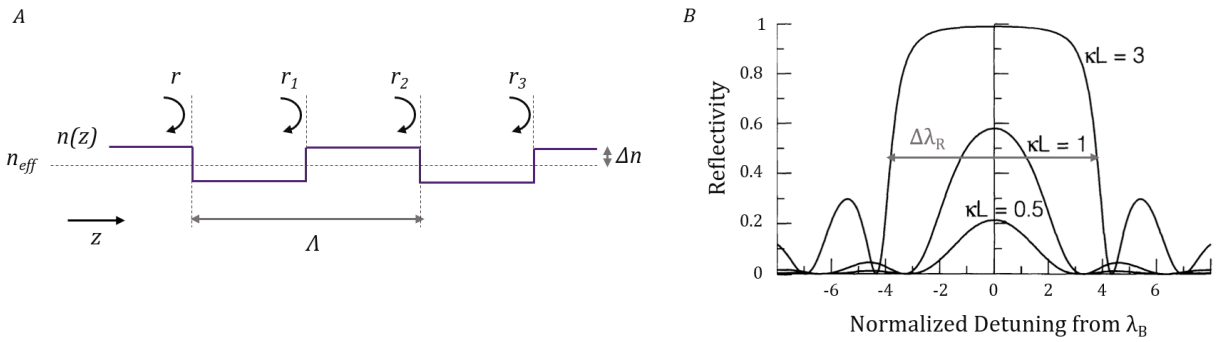

Figure 2.17: *A:* Reflections along the propagation direction of a square grating. *B:* Reflectivity as a function of the detuning from the Bragg wavelength. Images adapted from [4].

and/or the loss can be described:

$$n(z) = n + \Delta n \cos(2\beta z) \tag{2.32}$$

$$\alpha(z) = \alpha + \Delta\alpha \cos(2\beta z) \tag{2.33}$$

where Δn and $\Delta\alpha$ describe the difference between the high and low index materials[74]. An example of $n(z)$ is shown in Fig. 2.17A where the modulation is a square wave.

The coupling constant, κ, describes the strength of coupling between the forward and backward propagating waves and is given by:

$$\kappa = \frac{\pi\Delta n}{2n\Lambda_{grid}} + i\frac{\Delta\alpha}{2} \tag{2.34}$$

The normalized coupling coefficient, κL, describes the amount of feedback provided by the grating[4]. The detuning from β determines the bandwidth to this reflective response and can be described by the following equation:

$$\Delta\lambda_R = \frac{\lambda_{Bragg}^2 \kappa}{\pi n_{eff}} \tag{2.35}$$

The broadening of the reflectivity response is illustrated in Fig. 2.17B for different values of κL. Since there is a bandwidth associated with the response of the grating, the figure of merit for single-mode lasers is the SMSR, which is calculated from neighbouring modes:

$$SMSR = \log\left(\frac{S_N}{S_{N+1}}\right) \tag{2.36}$$

where S_N is the peak height of mode N. The design for the DFB assumes no end mirrors are present, since the feedback along the active region is sufficient for lasing. The facet reflectivity, R, influences the resonant wavelengths of the lasers as well and in the case that they are symmetric, $R_1 = R_2$, a minima in response occurs at λ_{Bragg} and instead side modes are supported[75]. The simplest solution to avoiding this is to enforce asymmetric facet reflectivity through high reflection (HR) and anti-reflection (AR) coatings, for example[76].

Fabrication of a DFB can be accomplished through many different means such as with a buried structure

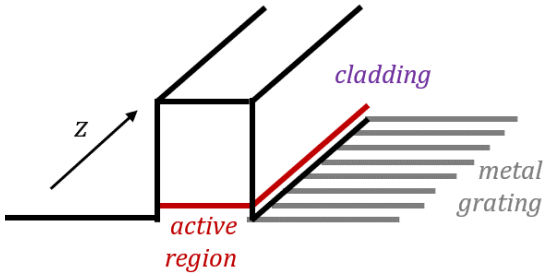

Figure 2.18: A schematic representing the DFB design incorporating lateral metal gratings.

near the active region, in the top cladding, or with lateral gratings [77–83]. A buried grating is fabricated by etching a grating into a waveguide layer close to the active region and then continuing the growth by covering this layer with the cladding and contacts. This is done in order to increase κ, but at the cost of fabrication complexity. When the grating is moved to the top or side of the waveguide, regrowth can be avoided but the coupling efficiency drops dramatically. Electron beam (e-beam) lithography needs to be used to define the grating, because of the sub-micrometer sizes.

For top cladding or lateral gratings, the periodic structure can alter the real and/or imaginary parts of n_{eff} for the device via two different methods: index (κ is real) or gain coupling (κ is imaginary). Top cladding gratings, as depicted in the schematic of Fig. 2.16, are fabricated in the cladding layer work with the principle of index coupling[84]. The use of metal in gratings results in gain coupling because the mode incurs losses by interacting with the imaginary component of the metals' refractive index[81]. Lateral metal gratings can be placed at the sides of the active region by etching a ridge waveguide to this layer, allowing the tail of the mode to interact with the grating as it propagates between facets. This type of design is depicted in Fig. 2.18.

In contrast, a DBR laser has the grating spatially separated from the active region and replaces the cleaved facet. This means the DBR is a passive section and its response to current and temperature changes (tuning) will be different from the active gain section. Passive means that there is no pumping required for the interference/filtering effect. The gain bandwidth of the active region will red-shift with temperature but the reflectivity response from a passive grating will not change. This affords them a broad tuning range with respect to DFBs, even if they suffer from complex fabrication due to the transition between active and passive sections. But, they are excellent designs when a broad range of tunability is desired. In contrast, for a DFB the grating and gain region experience similar responses to current and temperature changes. This limits the tuning range to the shift in the refractive index that can be induced in the material. DFBs are more simple to fabricate and they are better for single-mode emission, achieving high SMSRs.

2.3.2 Slotted waveguides

The distinction between slotted waveguides and DFBs is the size and geometry. When the defects changing the refractive index become large, the operating principles change. The interaction with the mode is stronger, so they act like reflective surfaces, as opposed to perturbations from scattering centers[85]. This starts to happen at the microscale, and then we refer to the defects as slots. Slotted lasers belong to the

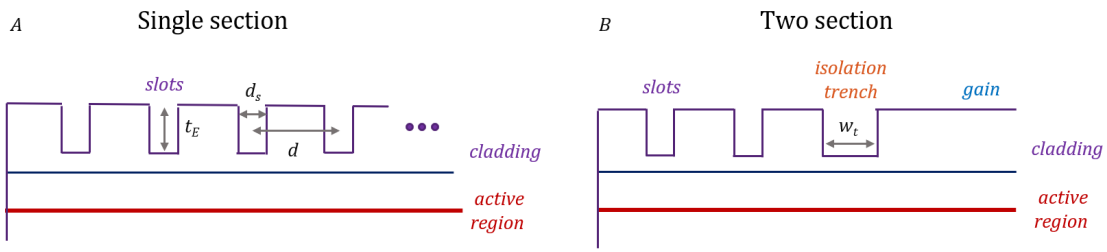

Figure 2.19: Schematic representing different slotted waveguides. *A:* A single section slotted waveguide has slots, with t_E and d_s, placed along the length of the gain section with period d. *B:* A two section slotted waveguide has the slots separated from an additional gain section by an isolation trench with with w_t.

group of active grating devices and they operate as previously described for DFBs, with a certain period selecting a λ_{Bragg}. The difference between slotted lasers and DFBs is that the periodic spacing is much greater than the wavelength which allows them to be fabricated using standard UV photolithography[21]. If Eqn. 2.29 is modified to include the diffraction order:

$$n\lambda_{Bragg} = 2n_{eff}d \tag{2.37}$$

where n is the grating order and we have relabelled Λ_{grid} as d here. DFBs and DBRs are typically first order gratings (low order gratings) whereas slotted waveguides are very high order gratings, $n > 20$[85]. The parameters that can be changed to address these concepts are slot spacing (d), slot width (d_s), etch depth (t_E), number of slots (N) and device length[20]. An illustration of the structure is shown in Fig. 2.19. In A slots are placed along the entire length of the active region while in B an additional gain section is added, separated from the slotted section by an isolation trench of width w_t. The isolation trench has $w_t >> d_s$ in order to provide electrical isolation >1 kΩ and allow each section to be independently pumped. Both configurations make use of one d and result in single-mode emission.

The reflective surfaces form inside the slots at the cladding air interface. d_s needs to ensure that the reflections from both sides of the slot are in phase with the optical feedback, accounting for π phase changes at the interfaces moving from slot to waveguide (low to high refractive indices). This occurs when d_s is integer multiples of a quarter of the desired wavelength (odd n). d will need to ensure integer multiples of half of the desired wavelength is supported (even n)[85]. We refer to the waveguide's reflective response as the slot FSR, S_{FSR}. Both the strength, R, and S_{FSR} is important to the design.
d is used to ensure the desired lasing wavelength is selected and with a S_{FSR} appropriate to the desired applicationg (high SMSR or tunability). The larger d, the narrower S_{FSR}, as expected based on the conversion between real space and frequency space. d_s can also be responsible for changing S_{FSR} if the edge to edge distance of between slots is fixed. Its main effect is on the strength of reflectivity, R, of the design. If we make a comparison to electrical signals, we can think of the "duty cycle" of waveguide, where the slot is defined to be the "off" state. Slotted lasers have a higher duty cycle than the DFBs presented in the previous section (though this is not a rule). Controlling both d and d_s allows easy control over this parameter.

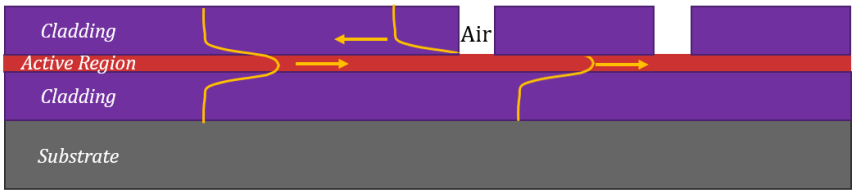

Figure 2.20: Illustration of a slot interacting with the fundamental lasing mode to create interference.

t_E changes R and the full width half max (FWHM) of the reflectivity peak. Etching is then a control parameter of the S_{FSR}, because it controls how much the slots will interact with the tail of the propagating mode. This is illustrated in Fig. 2.20. A mode propagating along a waveguide is not completely confined in the active region, as we know. Although the laser is designed to minimize mode interaction in the optical cladding because of losses, creating a top grating laser relies on the fact that the mode extends to the other layers. As the mode propagates along the laser and encounters a slot, most of the mode continues (is transmitted) unperturbed, to first order, while the tail is reflected[21]. The amount of the mode that is reflected is a function of the depth of the slot and the reflectivity should, therefore, have an exponential behaviour with respect to t_E[21]. To higher order, the mode will be slightly perturbed, which will shift the peak away from the slot slightly (towards the substrate).

2.3.3 Vernier-tuned devices

As single-mode emission evolves from FP lasers, single-mode tunability evolves from single-mode lasers. Broadband tunability can be achieved by designing a multi-section device whose emission profile depends on the interference of two single-mode waveguides. This concept exploits the Vernier tuning effect

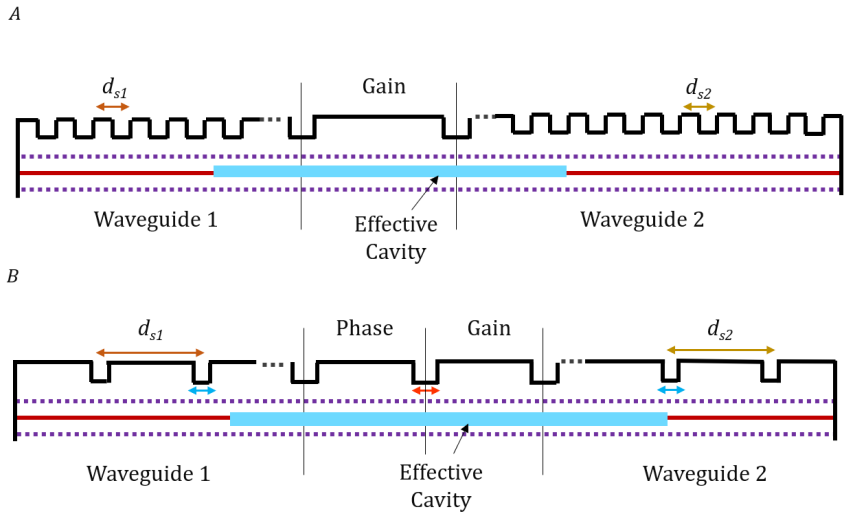

Figure 2.21: A schematic illustrating possible configurations for Vernier tuned lasers. *A:* Two DFB sections (waveguide 1 and 2) are separated by a gain section. *B:* Two slotted sections are separated by a phase and gain section. The phase section is attached to waveguide 1.

because it extends the continuous tuning range in a similar way to how a Vernier scale can increase the range and resolution for measurements by overlapping different increments[4].

$$\Delta\lambda = \frac{\lambda_{Bragg}^2}{2n_{eff}(d_{s2} - d_{s1})} \tag{2.38}$$

where d_{si} is the period of each single-mode waveguide section (with a unique S_{FSR}). Other configurations with more sections are possible, such as in Fig. 2.21B, where a phase section is added to waveguide 1. A phase section as $L = d_{s1}$ in order to provided extra control over S_{FSR1} to achieve more continuous tuning in the device.

Eqn. 2.38 is also subject to the properties of the gain material, such as the gain bandwidth and the maximum change in index of refraction. These properties can be measured from a single section's maximum tuning range, as it is determined by the amount one peak from the S_{FSR} can be shifted. This can be calculated from[21]:

$$\Delta\lambda_{shift} = \frac{\lambda_c \Delta n_{max}}{n_{eff}} \tag{2.39}$$

where $\Delta\lambda_{shift}$ is the continuous peak wavelength shift, λ_c is the tuning range centre wavelength, and Δn_{max} is the maximum change in n_{eff}. Referring to Eqn. 2.37 as well, wavelength changes can be elicited by changing the cavity length, the mode, or the refractive index[4]. The cavity length cannot be directly changed, but the mode and the refractive index can be changed through current injection and with temperature changes.

Figure 2.22 illustrates single-mode emission from two waveguides with different d. The dashed and dotted purple lines represent the $S_{FSR1,2}$ of each waveguide. The blue solid line represents the output from $S_{FSR1} x S_{FSR2}$. There is a peak where there is strong overlap between $S_{FSR1,2}$ and small peaks where there is weak overlap. Since the S_{FSR} is slightly different, this overlap only occurs at one wavelength and the other peaks destructively interfere.

Consider the 6 modes, L_{1-3}, M_{1-3}, from Figure 2.22. M_2 and L_2 overlap to begin, giving the single-mode in blue. Tuning can be implemented in a few different ways[17]:

- increasing the current (index of refraction) of each section, shifting the S_{FSR} by the same amount: M_2 and L_2 remain overlapped so that the single-mode shifts
- changing the current of each section such that L_1 and M_2 overlap: the single-mode overlap will happen at a different wavelength now
- changing the current of each section such that L_1 and M_1 overlap: the single-mode overlap happens at a different wavelength and with a the ability to shift the S_{FSR} as in the first point

Each S_{FSR} has a unique spacing, therefore it takes more (or less) current to shift the peaks from L_1 to L_2 versus M_1 to M_2. Instead of the tuning range being defined by the maximum shift between L_i (or M_i), the tuning range is extended because of the two scales allow $L_1 : M_3$ to be reached because of the Vernier effect.

The $\Delta\lambda$ that can be achieved is dependent on the electro-optical characteristic of the material such as the current range between I_{thr} and I_{max}. These parameters are determined by the length of each section

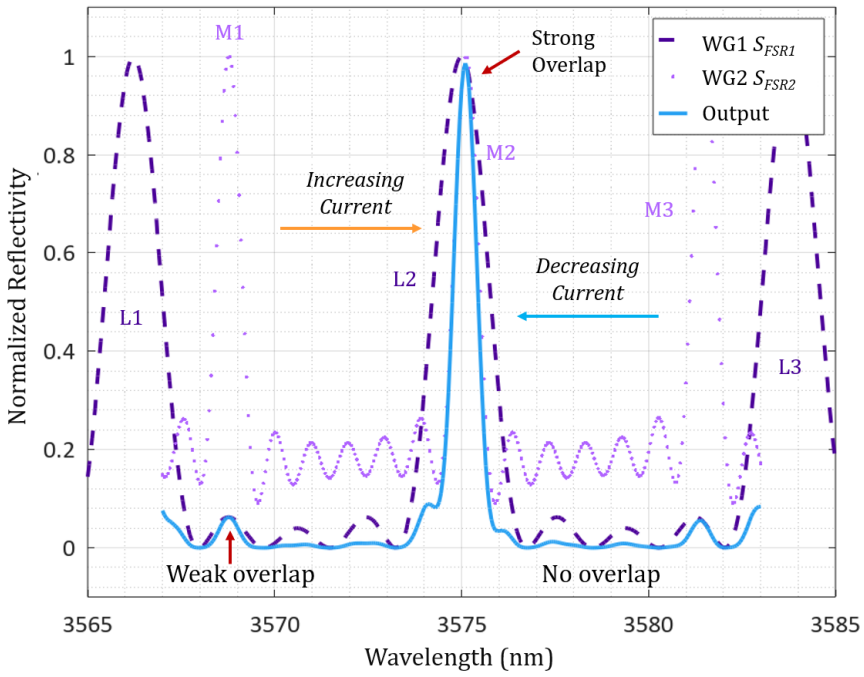

Figure 2.22: The S_{FSR} from two single-mode sections as well as their superimposed output at one λ_{Bragg}.

and the thermal cross talk between the sections[86]. Even with a design exploiting the Vernier effect, the tuning range is still very much dependent on the refractive index of the material and thus can be influenced by current injection, carrier, and thermal effects. The tuning range, T, is given by:

$$T = \frac{S_{FSR_{s1}} S_{FSR_{s2}}}{S_{FSR_{s1}} - S_{FSR_{s2}}} \tag{2.40}$$

where $S_{FSR_{s1}}$ and $S_{FSR_{s2}}$ represent the reflectivity peak spacing from two different slotted waveguides, s_1 and s_2. Single-mode lasers will have slightly different criteria now and must satisfy the following[21]:

$$\frac{1}{2} S_{FSR} > C_{FSR} > \frac{1}{2} FWHM \tag{2.41}$$

Fig. 2.23 depicts this equation by illustrating the consequences of this criteria on the cavity mode spacing and the slot reflectivity peak spacing. The top row shows the left hand side of the inequality, so the cavity modes are spaced such that only one overlaps with each slot reflectivity mode. The middle row shows what happens when this is not satisfied, and shows that while one cavity mode may overlap with the slot reflectivity peak, one of the slot peaks may be missed. The bottom row shows the right hand side of this inequality with single-mode or multi-mode criteria on the left and right hand side.

As the name suggestions, the gain section amplifies the cavity modes that will be transmitted into the slotted section before being reflected. This defines effective cavity length, L_{eff}, associated with this

penetration depth, d_{pen}. d_{pen} is defined by:

$$d_{pen} = \frac{N-1}{2} d \tag{2.42}$$

in the limit where the slot loss is under-compensated and the slot number is low[20][87]. The length for the cavity mode spacing, Eqn. 2.8, is then defined by the length of the gain section, phase section and d_{pen} in the two slotted waveguides, s_1 and s_2:

$$L_{eff} = L_g + L_p + d_{pen_{s1}} + d_{pen_{s2}} \tag{2.43}$$

2.4 State-of-the art single-mode ICLs and slotted lasers

The purpose of this work is two merge two technologies: ICLs and slotted waveguides. In order to understand the potential of such a device, the landscape of multiple laser architectures must be reviewed. ICLs have established their superiority within the 3 µm to 6 µm spectral range, exhibiting a threshold current density lower than 100 A cm^{-2}[88]. These lasers operate at high temperatures, surpassing 100 °C in CW, enabling them to output powers on the order of hundreds of mWs while maintaining low power consumption [65, 89]. Notably, recent research has demonstrated the potential to extend the emission wavelength beyond10 µm, albeit at low temperature conditions [90, 91]. Given the absence of slotted and SVT ICLs at the beginning of this thesis, we will briefly discuss state-of-the-art DFB ICLs as a starting

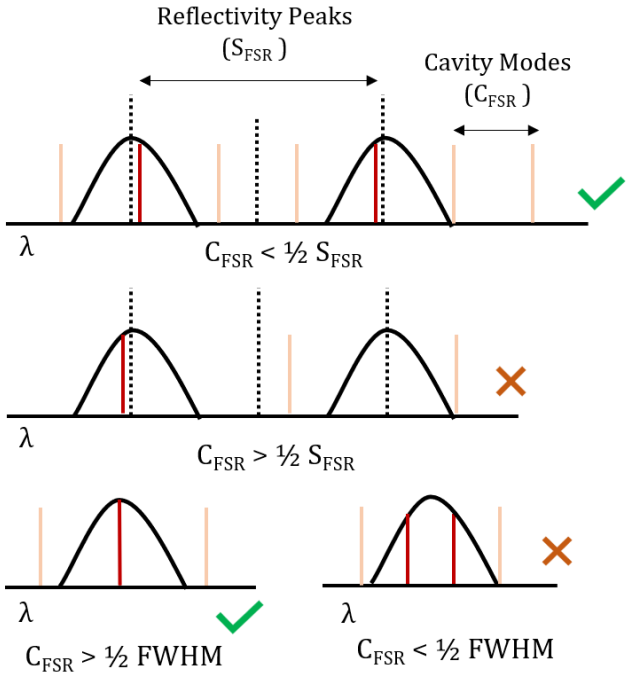

Figure 2.23: A scheme depicting the criteria for making single-mode lasers, from Eqn. 2.41, and how the cavity modes should be overlapped with the reflectivity peaks of the slots. When the cavity modes are red, they are likely to lase while when they are peach they are likely suppressed.

point for single-mode ICL emission. Additionally, we will present the performance of different ICL device configurations capable of broad wavelength tuning and lasers built on different material systems utilizing the Vernier tuning principle.

2.4.1 Single-mode Lasers

DFB ICLs are commercially available and already used in tunable laser absorption spectroscopy (TLAS) applications. The company nanoplus uses laterally coupled gratings for their DFBs and provides ICLs that emit between 2.7 µm to 7 µm [5, 92, 93]. A 2.4 mm long and 9.8 µm wide ridge device with as-cleaved facets achieved output powers around 10 mW at 25 °C into a single-mode at λ =3.4 µm in CW [81]. The SMSR is around 30 dB and a wavelength tuning range of around 22 nm[94]. The company Thorlabs[6] demonstrated longitudinally segmented DFB gratings can generate 42 mW at 3.3 µm with 30 dB at 25 °C for ridges with widths of 10 µm [95].
Other configurations of grating ICLs have been explored, mainly by the Naval Research Lab (NRL). They used corrugated waveguides to increase the output power by broadening the ridge and still select one mode, though it comes at the cost of increased the fabrication complexity. Their DFB ICL emitted 55 µW in CW mode into a single-mode at 3.7 µm at 25 °C[96]. They have also demonstrated DFB ICLs with Ge top cladding gratings operating in CW up to 80 °C. At 40 °C, for ridge widths of 7.4 µm and cavity lengths of 2 mm a device output over 27 mW with SMSR over 30 dB [97].
Meanwhile, at telecommunication wavelengths lasers using a slotted waveguide have achieved single-mode emission with SMSR >40 dB[20]. This slotted waveguide design involves no metal gratings and a section of a few periodically placed slots in the upper cladding layer. These lasers fabricated for emission around 1.55 µm use a different material structure; InP and AlGaInAs, and are MQW diode lasers. The device geometry is also quite different; typical laser lengths are around 250 µm for example[98]. As for DFBs, slotted lasers are also commercially available and they are fabricated by the company Eblana[99].
At longer wavelengths, using InP based QCL architecture, slotted waveguides have been implemented to achieve single-mode emission at 5.1 µm[100]. This laser design used two sections; a waveguide and gain section, and could operate between temperatures of 10 °C to 45 °C. Single-mode emission had an SMSR of 20 dB, peak power of 500 mW, and threshold current density of 2.4 $kA^3 cm^{-1}$.

2.4.2 Vernier tuned Lasers

SVT lasers have been fabricated on the InP material system as MQW diodes at λ =1.55 µm and as QCLs at λ =10 µm. This means the design has been demonstrated as effective at short and long wavelengths which is important since the dimensions of the slot geometry can increase substantially for longer wavelengths. Six section SVT MQW diode lasers using AlGaInAs materials were demonstrated at λ =1.55 µm with a wide, quasi-continuous tuning range of 55 nm and over 30 dB of SMSR. This design added semiconductor optical amplifier (SOA)s to the ends of the laser, which boosts the power with active gain stages and prevents any facet slot interference that could parasitically affect the waveguide feedback effect. The gain bandwidth of this material system is narrower than for ICLs, so 55 nm of tuning means an extremely efficient use of this bandwidth[101].
Three section SVT QCLs using InGaAs/InAlAs QWs were demonstrated at 10 µm with 420 nm of tuning

range and SMSR above 15 dB[102] This demonstrates that the slotted waveguides are more than capable of taking advantage of the broad gain bandwidth from different laser architectures and that longer lasers of up to 7 mm is possible. For this SVT QCL, only the slotted section is active and it was operated in a pulsed configuration.
BSG ICLs employ Vernier tuning by combining two DFB grating sections. They do offer a wide tuning range, but are not continuous. Discontinuous tuning of 158 nm was measured with 14 nm of mode hop free wavelength tuning observed[19]. These BSGs operated in CW mode up to 30 °C with output powers of 3.5 mW at room temperature for λ =3.7 µm.
A different approach to creating a broadband laser is to couple the laser with an external cavity (EC). Light is coupled from the laser to a cavity formed by the collimating lens/mirror and a diffraction grating. The wavelength selection is done by rotating this external element to select a different order of selection. The different form factor of this device has the disadvantage of being sensitive to alignment and directional change, but the advantage is that the external cavity affords the opportunity to insert other optical elements for mode locking. These are useful to consider for ICLs to estimate the tuning range that could be achieved based on the material's gain bandwidth. Between 3 µm to 4 µm this design scheme has achieved 300 nm of tuning with ICLs [23]. This represents a good benchmark for the upper limit of what could be achieved with SVT ICLs.

2.5 Gas sensing using spectroscopic techniques

Sensing through optical absorption of a gas species is important for understanding and monitoring a variety of phenomena from industrial processes[103]. Optical absorption sensors offer fast response times and minimal drift[104]. Spectroscopy is the study of light-matter interaction and is a technique often employed to probe the optical absorption of gases. High-resolution measurements are often required to distinguish closely spaced spectral features and single-mode lasers that produce a single, narrow linewidth mode provide a higher spectral resolution in comparison to multi-mode lasers. Tunable single-mode lasers can be precisely tuned to a specific wavelength, allowing the isolation of individual spectral lines with one source. Meanwhile, multi-mode emission can lead to interference that complicates spectral analysis and gas identification.
Novel ICLs can easily be integrated in spectroscopic schemes as the tunable, single-mode source. They are both based on absorption spectroscopy, which is the application of Beer-Lambert's law[105]:

$$I = I_0 e^{-\alpha_g L_c} \tag{2.44}$$

where I is the intensity of light transmitted through the gas cell of length L_c, I_0 is the incident intensity, and α_g is the absorption coefficient of the sample. α_g is the product of the gas concentration and the specific absorptivity. Commonly used techniques include TLAS and QEPAS and will be described below.

2.5.1 Tunable laser absorption spectroscopy

TLAS is a powerful technique used for highly sensitive and selective measurements of trace gases. The interaction between a tunable laser source and a sample gas is used to measure the absorption of specific

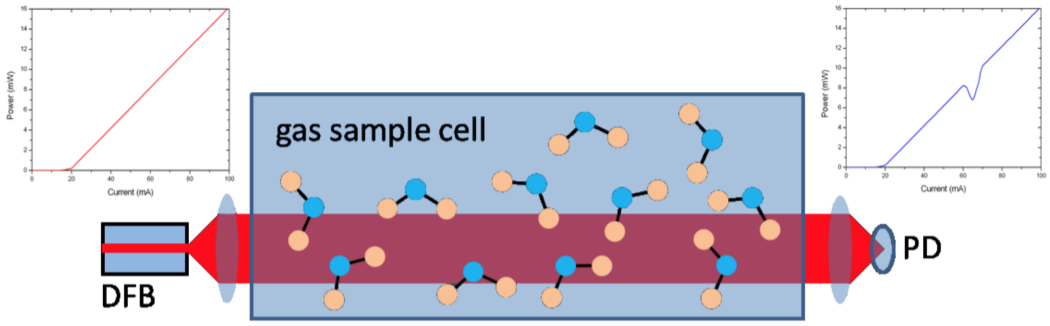

Figure 2.24: A scheme illustrating absorption spectroscopy through a gas cell [5].

wavelengths. The key component is the laser source which is directed through the sample gas that contains the molecule of interest, as depicted in Fig. 2.24. Typically the single-mode laser is a DFB and a photodiode (PD) measures the intensity of the laser light that has passed through the sample gas. Gas molecules selectively absorb light and the intensity of the transmitted light is reduced at that wavelength. The detector output is proportional to the absorption of the specific wavelength, and this signal is used to quantify the concentration of the target gas[106]. Sufficient laser power is required to obtain measurable absorption signals, especially for trace gas detection. The laser's output wavelength must be accurately calibrated to ensure the correct determination of gas concentrations. In some applications, rapid tuning of the laser wavelength may be necessary for real-time monitoring of dynamic processes.

2.5.2 Quartz-enhanced photoacoustic spectroscopy

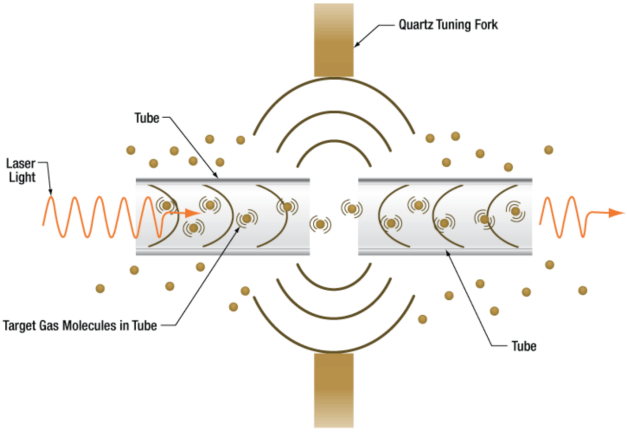

Figure 2.25: A scheme illustrating QEPAS absorption spectroscopy through a gas cell with a tuning fork [6].

QEPAS is a highly sensitive and selective spectroscopic technique used for the detection and quantification of trace gases. A modulated laser source is focused between the prongs of a tuning fork where the gas selectively absorbs light and emits sound waves due to the photoacoustic effect[107]. This is illustrated in Fig. 2.25.

The tuning fork acts as the sound detector and requires the laser to be modulated at its resonance fre-

quency, set by the specific geometry of the tuning fork. The laser beam acts as an acoustic source and induces vibrations of the fork due to the pressure waves generated by the gas. These vibrations are converted to an electrical signal, S, that is proportional to:

$$S \propto Q \cdot P \cdot \alpha_g \cdot \epsilon \tag{2.45}$$

where Q is the quality factor of the tuning fork, P is the power of the laser, and ϵ is the light-to-sound conversion efficiency. Thus, the performance of QEPAS-based sensors is directly affected by the laser power. The advantage of this technique is replacing a wavelength dependent PD with the tuning fork. This means laser sources with different emission wavelengths can be easily exchanged in this set-up.

Conclusion

This chapter presented an overview of semiconductor opto-electronics in order understand the challenges faced when designing single-mode laser sources the MIR. Better laser performance extends the range of applications these sources can be integrated with. Mid-infrared ICLs fabricated on GaSb are used for petrochemical sensing as they emit in the 3 µm to 5 µm spectral band which is of particular interest for the detection of gasses such as methane. Additionally, single-mode emission with a larger tuning range is ideal so the source is versatile for use in spectroscopic applications. There is a myriad of active research in the field of semiconductor laser engineering in order to improve the performance of these devices.

CHAPTER 3

Microfabrication of Fabry-Perot ICLs

Microfabrication refers to the collection of techniques that modify semiconductor materials through additive or subtractive processes and convert planar materials into complex structures with micrometer (or smaller) features[108]. Additive processes deposit thin layers of materials through epitaxy or vapor deposition while subtractive processes selectively remove, or etch, the material. The processes for the laser fabrication we will focus on in this chapter can be broadly divided into two categories: epitaxy and lithography. FP ICLs are constructed by modifying a substrate with planar layers of III-V-Sb materials epitaxially grown on it into a laser cavity through a sequence of photolithographic and etching processes. Only GaSb based ICLs that cover the 3 µm to 5 µm part of the MIR can offer CW emission above room temperature and be powered by a battery. Before single-mode emission can be pursued for gas sensing systems, foundational ICL technology must already be established. This was already developed via the growth and fabrication of FP ICLs. The design and fabrication process of creating low threshold FP ICLs at $\lambda \approx$3.3 µm to target methane absorption lines will serve as the foundation for the tunable single-mode ICLs to be developed[41].

Molecular beam epitaxy (MBE) is the deposition of vapour phase materials on a substrate in an ultra-high vacuum (UHV) environment, resulting in epitaxial films of high purity. MBE has been the favoured tool for producing III-V-Sb devices for multiple decades because of the versatility in layer composition and extreme control in layer thickness that can be achieved[109]. Photolithography is the process of printing a pattern onto a semiconductor substrate using light. Using multiple photolithography steps allows a complex device to be fabricated and underpins most of the fabrication steps that are undertaken to develop FP ICLs. These techniques will be introduced in this chapter in order to provide a complete overview of the procedure for fabricating FP ICLs: structural design, growth, device fabrication and characterization[110]. The ultimate metric for evaluating the various ICL growths was the CW PIV of the FP ICLs. Based on the central emission wavelength, changes were made to the active region structure during growth in order to better target 3.3 µm, and have material that was suitable for investigating waveguide designs for single-mode emission.

3.1 ICL Design for 3.3 µm emission



Figure 3.1: Schematic of a full ICL structure.

Modelling of the active region was carried out using nextnano software which calculates the band dispersion via the $k\dot{p}$ method to obtain the band structure such that the electron wave function obeys the time-independent Schrodinger equation in a periodic semiconductor crystal[111]. The foundation of ICL design is the structure developed by the Naval Research Laboratory (NRL) that first achieved room temperature CW operation[35]. From this design, changes were implemented based on recent advancements that improved overall performance or that focused on optimizing one aspect of performance, such as minimizing threshold power or maximizing output power, for example[7]. The complete structure of the ICLs designed for this project is illustrated in Fig. 3.1. The basic components of the ICL waveguide designed for this project include: an active region, symmetrical separate confinement layer (SCL)s, SL cladding layers, various transition SLs, a top contact layer, and a substrate. In general, a full picture of the heat, electrical, and optical properties must be considered in order to balance all of the trade offs that occur when designing each layer.

As is typical for other QW lasers, a separate confinement heterostructure is integrated with the active region for optical mode confinement. This structure involves two symmetric SCLs followed by asymmetric cladding layers that should minimize the internal loss and thus material gain required to reach transparency. Although the ICL active region is unique, the waveguide design follows similar principles as what is used for a diode laser, for example. The active core is surrounded by GaSb SCLs that are lightly n-doped. These layers prevent the optical mode from spreading out of the active region, whose average refractive index is similar to that of the top/bottom cladding, due to the higher index of refraction of GaSb (i.e. $n_{GaSb} > n_{cladd}, n_{AR}$).

The refractive index of the ICL was modelled by assuming a weighted average with respect to the

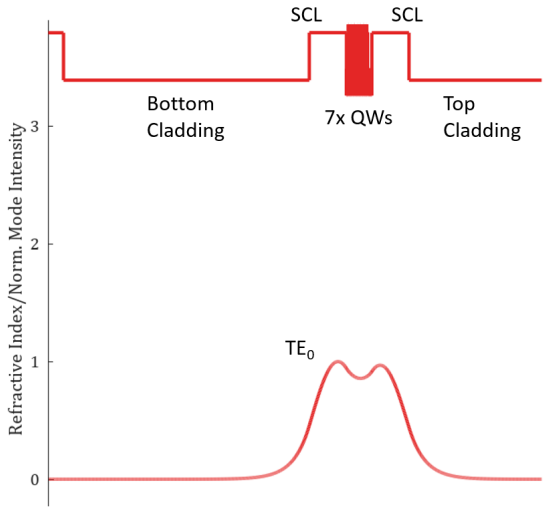

Figure 3.2: The refractive index of each layer in an ICL are plotted along with the mode intensity of the TE_0.

semiconductor compound thickness or composition would be representative of what the mode sees. For example, the ternary compound Ga_xInSb_{1-x} is present in the QWs of the active region the refractive index can be found from GaSb, n_{GaSb}, and InSb, n_{InSb}:

$$n_{GaInSb} = xn_{GaSb} + (1-x)n_{InSb} \tag{3.1}$$

Using $x = 0.65$, the refractive index was calculated at λ =3.3 µm to be $n_{GaInSb} = 3.7889$. This part of the QW is then fed into the calculation for n_{AR}, which is averaged according to the thickness of each material:

$$n_{AR} = r_{GaSb}n_{GaSb} + r_{InSb}n_{InSb} + r_{GaInSb}n_{GaInSb} + r_{AlSb}n_{AlSb} \tag{3.2}$$

where r_{GaSb} is the ratio of the thickness of the GaSb layer to the total thickness of the AR, so $r_{GaSb} + r_{InSb} + r_{GaInSb} + r_{AlSb} = 1$. For the entire ICL structure, n_g was calculated to be 3.8575.

The material model is based on values for compounds at room temperature, which while the operational temperature is set by the heat sink, the local active region temperature will be much higher. Additionally, for III-V-Sb materials different references for the refractive index are not in agreement[112, 113]. Modelling the material will be important for understanding relative changes in behaviour from the dispersion, but empirically determining n_g will be the most useful in improving the design.

The confinement factors of each layer should ensure that the material doesn't accumulate more loss than can be compensated for by the active region[114]. The SCLs must be thick enough to keep the TE_0 mode out of the cladding layers, but not so thick that it can support higher order modes. Fig. 3.2 shows the confinement of the TE_0 mode confined by the ICL described in Fig. 3.1. The optical mode profile was calculated using Lasim software which solves Helmholtz equations using finite element method[115]. The intensity distribution of the optical mode is calculated from the refractive index profile. This distribution represents a balance of increasing mode confinement to benefit from the active region gain, while also confining the mode to surrounding layers to minimize losses[116]. Γ for the active region is calculated to

be 20% and Γ in the SCLs is then 63%, while in the cladding layers it is 15%. The relative scaling of the different layer. A big uncertainty that remains is how much of the mode is optimal to be confined to the active region, since the internal loss of this layer is not known precisely.

An AlSb/InAs SL was chosen due to the lower series resistance and because of the lower optical losses with respect to the bulk quarternary AlGaAsSb. The trade-off being that the thermal conductivity is very poor in comparison to bulk material alternatives; $3\,\mathrm{W\,m^{-1}\,K^{-1}}$ in comparison to $7\,\mathrm{W\,m^{-1}\,K^{-1}}$ for AlGaAsSb due to the difference in lateral and longitudinal heat flow in this structure[117, 118]. There is a very high Al content in the cladding, around 85%, which makes the index of refraction lower than for the SL. The top and bottom cladding layers keep the mode away from the lossy metal contacts and to prevent mode leakage into the substrate[119].

The substrate used is *n*-type GaSb (Te doped) and the top contact is a highly doped InAs layer used to reduce series resistance. The doping levels of the top and bottom cladding are a gradient from high, near the contacts, to low, near the active region. The SL transition layers are more highly doped than the SCLs to reduce the parasitic voltage drops at the interface without increasing the optical losses near the mode. Increasing the doping levels of each layer represents a trade-off between lowering the series resistance and increasing the free carrier absorption losses.

One stage of the active region is designed according to the considerations discussed in Sec. 2.2.5. To choose the stage multiplicity, we have to decide on which metric is most important for the application - low threshold power or high output power. Empirically, it was shown that 5 stages result in devices with the lowest threshold powers, 7 stages offers more external different quantum efficiency[89]. The results of the cascade variation study are shown in Fig. 3.3, which was summarized from devices fabricated by NRL and the University of Wurzburg[7]. Fig. 3.3A shows a trend of decreasing threshold current densities for increasing stage number. If we compare with the threshold power density, we see that this

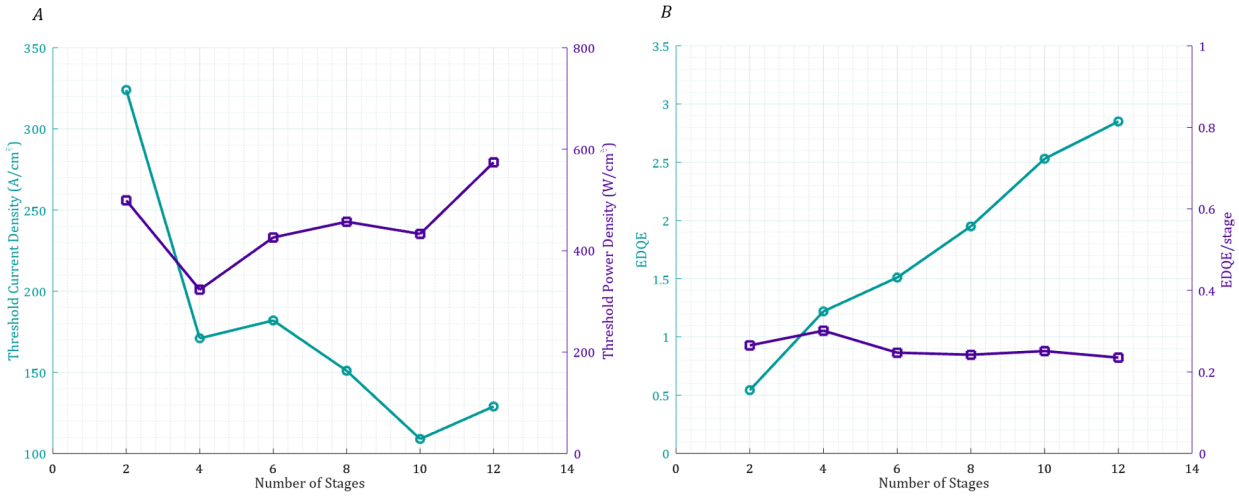

Figure 3.3: *A:* Threshold current and power densities are plotted with the number of stages for broad area ICLs (2 mmx150 µm. *B:* The total EDQE and EDQE per stage is plotted for the same broad area ICLs. Lasers are operated in pulsed mode and have $\lambda \approx 3.6$ µm. Both figures are adapted from [7].

reduction is associated with an increasing threshold voltage. For applications involving battery powered systems, this is an important result as threshold power densities below 500 W cm^{-2} can be reached for stage multiplicities between 4-10.
Fig. 3.3B shows that the external differential quantum efficiency (EDQE) scales with the stage number while the EDQE/stage is nearly constant. This result indicates the loss is independent of the stage number and so must be contributed by the different layers in the waveguide. If the surrounding SCLs and overlap is carefully optimized, a 7 stage device can be an effective trade-off between threshold power and output power[89]. Therefore, the SCLs designed for this project were thick, lightly n-doped ($5 \cdot 10^{16}$ cm^{-3}) GaSb in order to minimize the overall loss[120].
There are many parameters to explore since ICLs are made up of thousands of different layers. Design of an optimized ICL structure requires modelling to ensure the thicknesses appropriately align the band gaps of the different materials as well as empirical study to ensure performance improvements. The efficacy of these studies relies on material deposition at the molecular level for each layer, this can be achieved by epitaxially growing the layers with an MBE.

3.2 ICL epitaxy

State of the art ICLs require over 2000 epitaxial layers with accurate control of the each layer's thickness and composition[121]. High precision, crystalline semiconductor layers are grown using a technique known as MBE, which occurs in a UHV environment. The molecular beam part of the technique refers to the fact that the source material is heated in order to produce an evaporated beam of particles. Epitaxy is material deposition where crystalline layers are formed with a well-defined orientation with respect to a seed layer (the substrate or previous layer)[122].
In this section, three different techniques will be described involved in the growth of ICL structures: MBE, high resolution X-ray diffraction (HR-XRD), and photoluminescence (PL). HR-XRD allows characterization of periodic structure thicknesses, and PL allows characterization of QWs. Since the complete ICL structure is very complex, two different calibration structures are used to ensure the growth conditions for the cladding layer and active region are appropriate.

3.2.1 Growth and characterization techniques

MBE affords a high level of control over many properties of multiple epitaxial layers including thickness to the atomic level, doping profiles, interface sharpness, and composition variation[123]. A MBE reactor consists of 4 different vacuum chambers: the load lock, the UHV cluster, the outgassing, and the growth chambers. This configuration helps to ensure a very low vacuum ($\approx 10^{-10}$ torr) is achieved and maintained in the growth chamber. The load lock has exposure to atmosphere and allows samples to be taken in and out. The UHV cluster chamber has a automatic sample exchanger that allows samples to be moved in between chambers. The outgassing chamber has a heater to outgas the samples when they are first loaded. The sample holder in the growth chamber must have a heater and rotational mechanism to ensure homogeneity across the wafer(s). There is also a liquid nitrogen (LN_2) cryoshield that helps remove pollutants from the chamber.

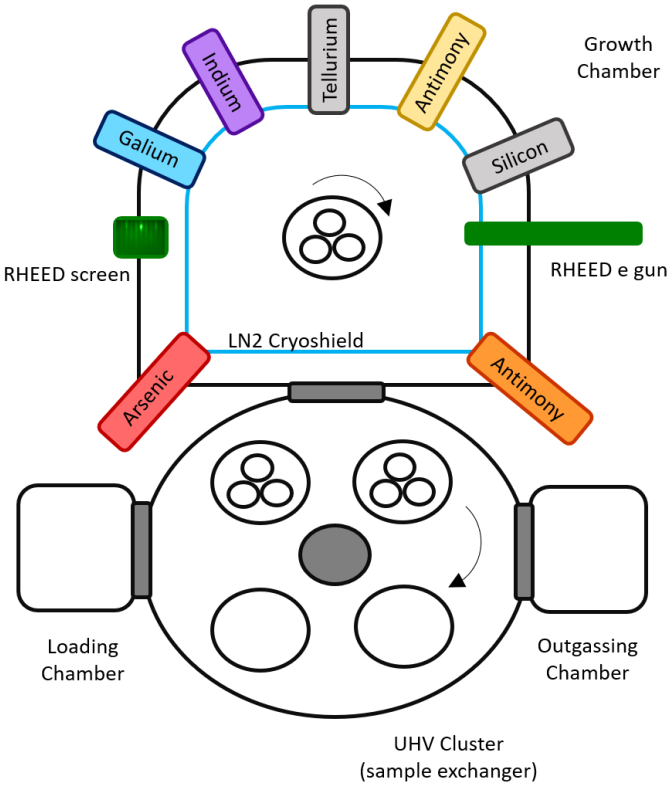

Figure 3.4: Sketch of the UHV chamber used to grow the full ICL structure

In order to grow III-V devices, the growth chamber must have the appropriate cells that can create a stable flux of the desired elements. A flux of column III elements can be generated using standard effusion cells[124]. Column V elements have a high vapour pressure and a low sublimation temperature so that tetramers are often formed. This requires the need of a sublimation and cracking section, such as for As and Sb, so the growth flux can be controlled via a valve. A typical MBE is sketched in Fig. 3.4.

There are two aspects that are important for MBE growth and this includes the surface preparation of the substrate and the real time control of the growth conditions through surface monitoring during deposition. Substrates are covered with an oxide that can be removed by simply heating the substrate in vacuum, leaving an atomically clean surface[123]. Starting from a clean surface is imperative to growing epitaxial layers. Surface monitoring, without interfering with the molecular beam, is the other important component to the real time control of the growth. The reflection high-energy electron diffraction (RHEED) technique utilizes a glancing angle electron beam to monitor the surface via a diffraction pattern[125]. The incident angle of the electrons is very shallow ($< 4^o$) so that only a few surface layers are penetrated which guarantees the surface is being probed. These diffraction patterns change based on the crystal orientation and the surface topography, so streaky diffraction patterns should be observed to indicate a clean, smooth surface[124, 126]. The crystal patterns observed are useful to determine the optimal growth conditions, including growth temperature and III/V gas flux ratios for example [127, 128]. The growth rate is determine using the RHEED intensity oscillation method from the period of the damped intensities oscillations from the diffraction pattern[126].

High purity growths can be achieved using an MBE because of the UHV environment and from the high degree of control over the growth rate from RHEED oscillations. The laser structures presented in this thesis were grown in a Riber 412 and C21E MBE reactor equipped with solid source effusion cells for Ga, Al, In, Si, and Te and valved cracker cells for As and Sb.
The crystalline quality and thickness of the layers involved in the ICL growth is studied via HR-XRD using PANalytical X'Pert3 MRD equipped with a PIXcel1D linear detector, an X-ray tube delivering CuKα1 radiation and a four-bounce asymmetric Ge (2 2 0) monochromator. Generally what is observed is the $\omega - 2\theta$ scan, where the incident angle of the x-rays with the sample is ω and the diffraction angle between the incident beam and detector is 2θ. Since ω and 2θ change in a coupled manner, the direction being measured does not change. Peak positions give the perpendicular lattice parameter of the layer so that the strain can be measured. The width of the peaks indicate the quality of the layers; a perfect crystal produces a very sharp peak[129]. The asymmetric orientation allows the measurement of the substrate Bragg peak and the growth Bragg peak which is important. When there is lattice mismatch between two layers, the growth has to be done carefully to create a pseudomorphic layer. This means the new layer will be strained in order to follow the lattice parameter of the previous layer. This strain is calculated from the XRD scan according to:

$$\epsilon = \frac{a_L - a_s}{a_s} \tag{3.3}$$

where a_L and a_s are the lattice parameters of the layer and the substrate, respectively. This can lead to compressive ($\epsilon < 0$) or tensile ($\epsilon > 0$) strain. The strain is calculated from the shift between the substrate peak and the layer peak angle in the XRD scans.
Atomic layer precision is then achieved by controlling the monolayer growth rate of each element. The next section will be more focused on material properties, rather than on laser operation, in the study of calibration structures for the active region and cladding layers. The growth parameters used to growth an ICL will be determined from these calibration growths.

3.2.2 Growth of type-II W-QWs and characterization

The initial phase of the fabrication process is centered around material growth, which forms the basis for the laser performance. Prior to commencing the epitaxial growth process for the entire structure, it is imperative to assess the growth conditions, with a particular focus on temperature since this parameter has a notable influence on the emission efficiency[2]. Consequently, four distinct W-QW structures were grown within the temperature range of 425 °C to 465 °C (as measured with an optical pyrometer) and were subsequently characterized by photoluminescence (PL).
The calibration structure is designed for emisison at 3.3 µm and is composed of five type-II-QWs: 2.5 nm AlSb/1.4 nm InAs/3.5 nm GaInSb/1.4 nm InAs/2.5 nm AlSb and separated with 20 nm thick GaSb. This MQW active region is placed between two GaSb and AlSb barriers. The purpose of the AlSb barriers is to prevent the dispersion of the carriers from escaping when the structure is pumped for PL. Fig. 3.5A depicts the band diagram for the structure and Fig. 3.5C shows the corresponding HR-XRD scan of the structure grown at 435 °C. The HR-XRD pattern exhibits a series of satellites peaks arising from the QW-barrier periodicity. The presence of well resolved Pendellösung fringes indicates a high crystalline

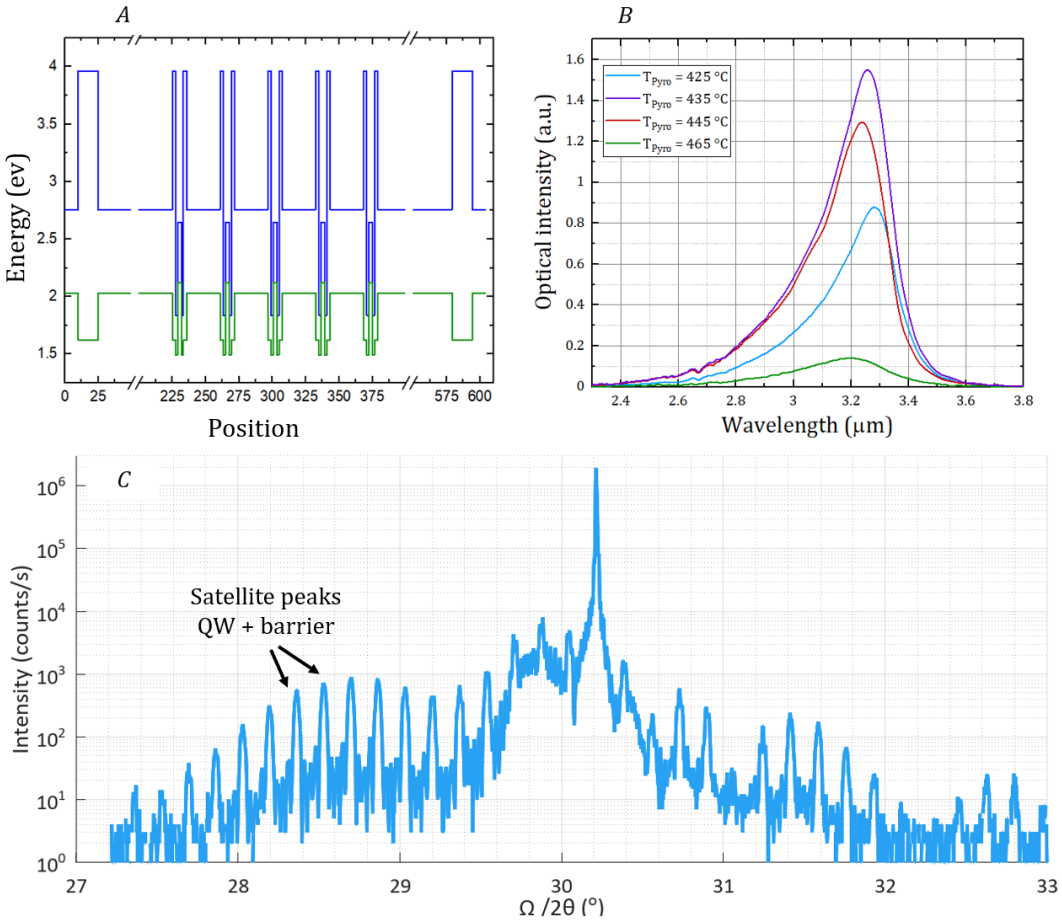

Figure 3.5: *A:* W-QW structure and characterization used to calibrate the growth parameters for the active region. *B:* PL curves from W-QW strucutres grown at four different growth temperatures. *C:* HR-XRD of the W-QW structure grown at 435 °C.

perfection. The thickness of the QW and barrier deduced from the angle separation between adjacent satellite peaks is 31.7 nm, in good agreement with the target thickness of 31.3 nm.

PL is the emission of light from a material that is caused by the absorption of light. This allows us to study the transition in the W-QWs that will suggest the emission wavelength of the final device and correct the QW thicknesses[130]. PL is conducted at room temperature using a 780 nm GaAs diode to optically pump the structure. The resulting spectra is measured using a Fourier transform Infrared (FTIR) spectrometer with a liquid nitrogen cooled InSb detector and is shown in Fig. 3.5B for four different growth temperatures. It is clear that a growth temperature of 435 °C yields the optimal PL performance. The deterioration of PL at lower growth temperatures indicates the formation of In clusters within the W-QW, while at higher temperatures, it is associated with atomic interdiffusion at the QW interfaces[2]. Therefore, the optimal conditions for the W-QW growth is 435 °C and will be the growth temperature for all the structures involved in this work.

3.2.3 Growth of AlSb/InAs SL cladding and characterization

The main concern for the growth of the SL cladding is the alternation of a tensile InAs (-0.62%) and a compressive AlSb (+0.65%) layer involving the exchange of both anions and cations at every interface (either InSb or AlAs like bonds). Thus, the AlSb/InAs SL has to be perfectly strain compensated to achieve the required thicknesses of the cladding layers and ensure a high crystalline quality of the ICL. The period of the SL is very short in comparison to the total thickness, around 4.7 nm, and so the pressures used to grow these layers needs to be stable so the thickness of the SL layers do not change during the growth of almost 1000 periods.

The calibration structure is composed of two 150 period SLs that have two different As valve positions for the growth of InAs. The residual As modifies the composition of the interface and therefore the strain of the SL. Fig. 3.6 shows the HR-XRD scan of this calibration growth; in general, the peaks are narrow and intense indicating high quality crystal growth.

As illustrated by the arrows in the figure, more As shifts the peak to higher angles (tensile strain) and more Sb shifts the peak to lower angles (compressive strain). The main feature in this scan is the doublets observed on the periodic peaks from the SL due to the two valve apertures. The order 0 of the two SLs are very close to the GaSb substrate peak and is estimated to be lattice matched to the substrate. From the spacing of these peaks the SL period was measured to be 4.63 nm, a value close to the thickness targeted. Between the cladding and SCLs are transition layers which are also SLs that are meant to smooth the transitions between layers. They can be grown using this calibration as well. Now that the growth parameters are fixed according to the calibration structures, a complete ICL structure can be realized.

3.2.4 Growth of a complete ICL structure

ICLs are typically grown on 2" (100) *n*-type GaSb substrates. Thermal de-oxidation under an Sb flux at 550 °C ensures a clean substrate[131]. The temperature is decreased to 500 °C to grow a 200 nm Te-doped

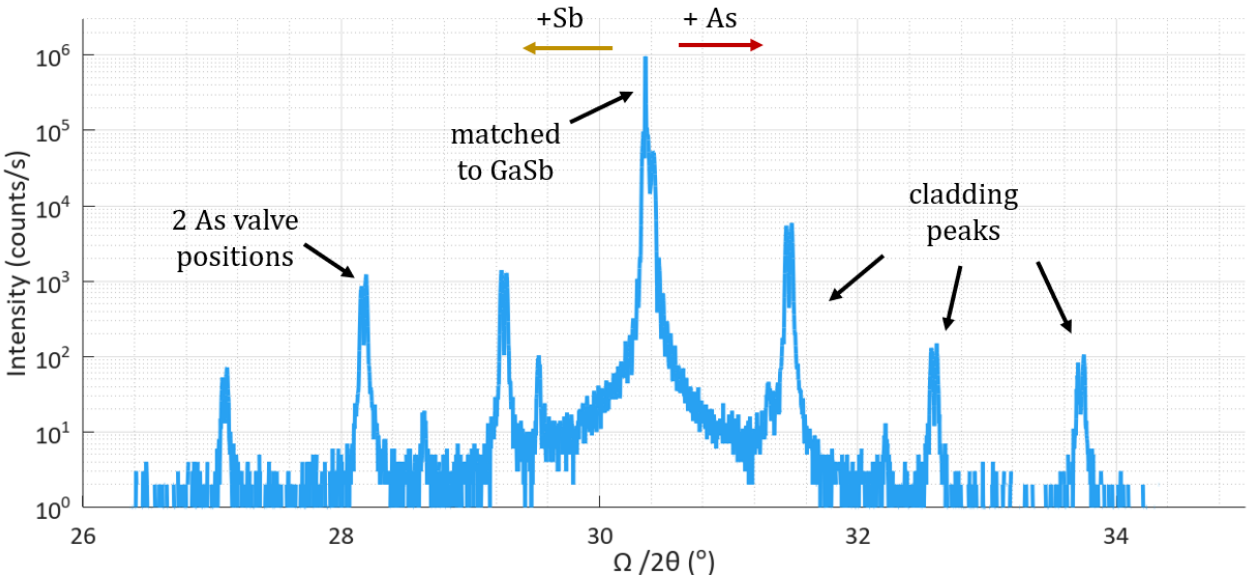

Figure 3.6: XRD characterization of the cladding growth parameters.

GaSb buffer layer so that the growth begins on a smooth surface[132]. The temperature is then further reduced to 435 °C to grow the subsequent layers. First, a transition layer offers a gradual change between the buffer layer's and cladding layer's band offsets via a 40 nm AlSb/InAs SL doped with Si at 10^{18} cm^3. Then, the3.2 µm thick bottom cladding AlSb/InAs SL with a gradient of decreasing Si doping levels is grown. Another SL transition layer is grown before the 450 nm lightly *n*-doped GaSb SCL. The growth of the active region is grown with 7 repetitions of the following sequence: 2 nm AlSb/ 1.4 nm InAs/ 3.5 nm $Ga_{0.65}In_{0.35}Sb$/ 1.3 nm InAs/ 1 nm AlSb/ 3 nm GaSb/ 1 nm AlSb/ 4.5 nm GaSb/ 2.2 nm AlSb/ 4.2 nm InAs/ 1.2 nm AlSb/ 3.2 nm InAs/ 1.2 nm AlSb/ 2.5 nm InAs/ 1.2 nm AlSb/ 2 nm InAs/ 1.2 nm AlSb/ 1.7 nm InAs/ 1.2 nm AlSb/ 1.5 nm InAs/ This corresponded to an emission wavelength of 3.4 µm. After the active region, a symmetric transition SL and 450 nm GaSb/ SCL are grown. A final transition SL leads to the 1.9 µm thick top cladding AlSb/InAs SL with a gradient of increasing Si doping is grown. This is capped with a 20 nm InAs contact layer, doped with $5{\cdot}10^{18}$ cm^{-3} Si.
The HR-XRD scan of a full ICL growth is presented in Fig. 3.7. The peaks are narrow and sharp indicating a very high quality of crystallinity. The shorter, tightly spaced peaks are related to the periodicity of the 7 stages in the active region, measured to have a thickness of 41 nm, while the taller, more widely spaced peaks represent the SL with a period of 4.62 nm. The broad peak on the right up the substrate peak is the InAs contact layer cap. The growth is perfectly lattice matched to the GaSb substrate with no strain.

A full ICL growth is around 8 µm thick and with strained layers. The growth rates will change with drifts in the pressure and temperature of the system, and this represents a challenge to maintain the 1 nm precision during growth times of over 20 h. Using the MBE technique, as opposed to other growth techniques used to fabricate other semiconductor lasers, makes the ICL design achievable. Further evaluation of the growth and design will be done via laser characterization.

3.3 Lithography for FP ICLs

Photolithography is the process of printing a pattern onto a semiconductor substrate using light. Using multiple photolithography steps allows a complex device to be fabricated and underpins most of the

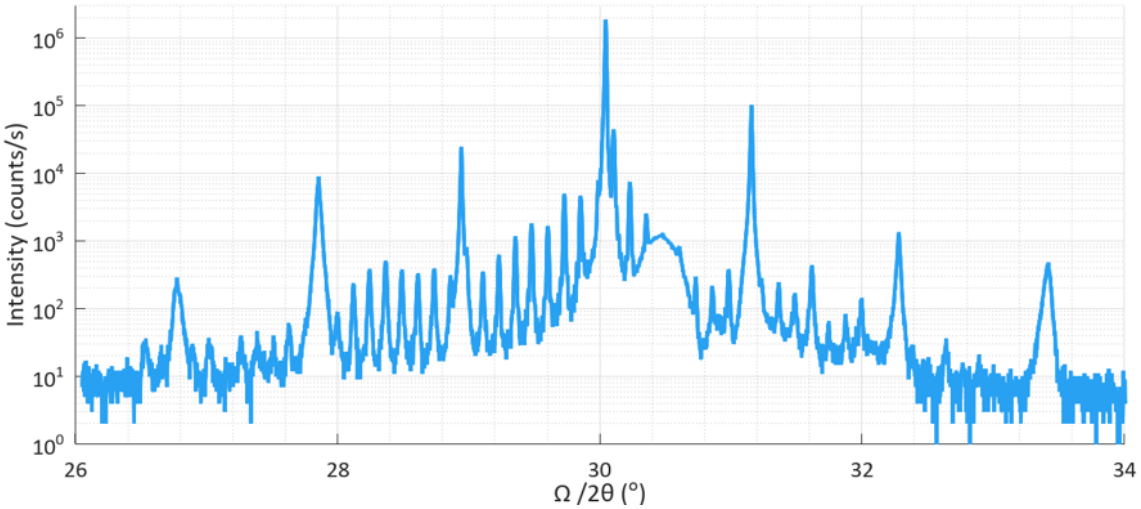

Figure 3.7: HR-XRD characterization of a full ICL growth.

fabrication steps that are undertaken to develop FP ICLs. There are 3 main steps involved in creating a feature: sample cleaning, photolithography, and pattern transfer. Different possibilities of these steps are illustrated in Fig. 3.8.

An overview of the techniques used in photolithographic processes will first be presented before describing the laser fabrication steps used to fabricate FP ICLs. The electro-optical characterization of the FP ICLs will be presented in the next section to evaluate the design of the active region and quality of the growth.

3.3.1 Fundamentals of photolithographic processes

After the growth of ICL, the sample is ready for processing. This begins with sample cleaning to ensures contamination from the surface is removed and the surface is prepared. This involves removing organic material, dehydrating the surface, and applying adhesion promoting layers. Organic material is removed using solvents such as acetone and isopropanol (IPA). Water is removed from the surface by heating the sample at 150 °C for 10 min. Adhesion promoters, such as hexamethyldisilazane (HMDS), are used to ensure the next layer deposited on the surface will not delaminate[133].

Photolithography

The next step is the realization of a pattern using photolithography. The steps involved in a photolithographic process include spincoating and soft baking a photoresist, exposure of the photoresist with a photolithography mask, and finally a hard bake (if necessary) and development of the photoresist.
Light sensitive polymers called photoresists are used and exposed to UV light through a mask that blocks or passes light through the chrome pattern printed on top of a glass slide. Similar to photographic film processing, the exposed substrate and photoresist is developed with chemicals and a positive or negative

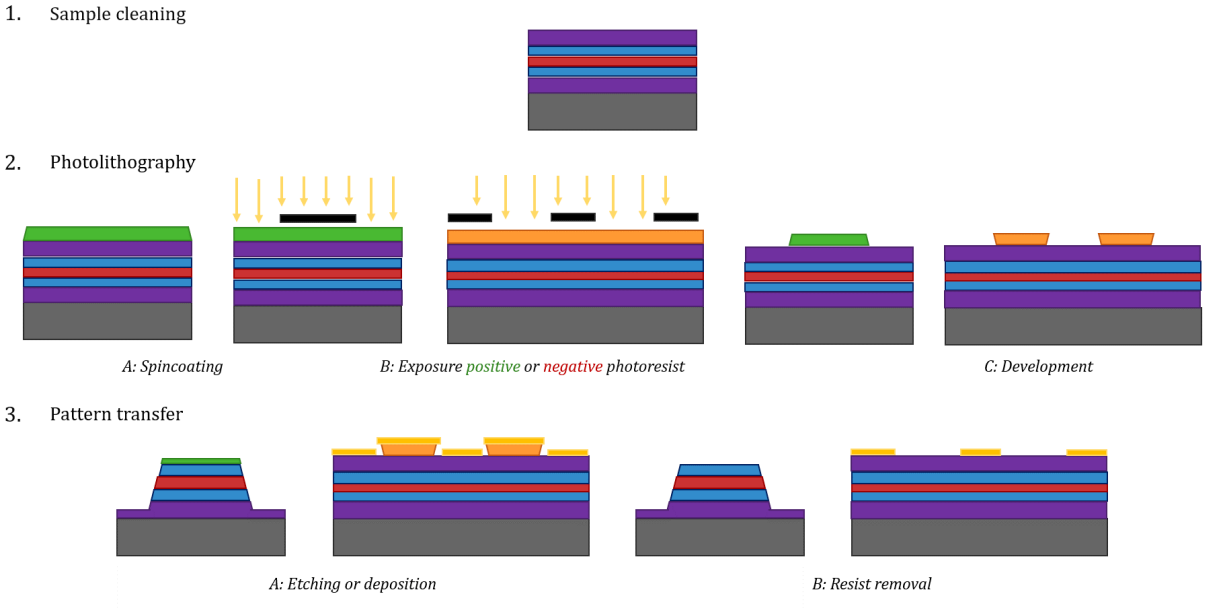

Figure 3.8: Steps involved in a photolithography process.

image of the pattern remains, depending on the type of photoresist used. Positive photoresists become more soluble when exposed to light so that areas exposed are removed at the development stage. The opposite is true for negative photoresists so that crosslinking happens when they are exposed to light and areas that were not exposed are removed during the development step. In general, positive photoresists are chosen when higher resolution is desired while negative photoresists are chosen when a higher aspect ratio is desired[134]. A positive photoresist was used in the FP ICL fabrication to define the mesa ridges, requiring a resolution of down to 5 µm, while a negative photoresist is used to aid in metallization due to the undercut profile. The sample coated in photoresist then undergoes a soft bake to remove excess solvent and stabilize the film.

Spincoating is the standard technique used to deposit a thin, uniform film in an easily controlled manner. The thickness, t, is controlled by the spin rate, ω, where $t \propto 1/\sqrt{\omega}$. The spin time helps to ensure the entire surface is coated and then solvent can evaporate away. The thickness is an important factor to control since it dictates the final resolution that can be achieved. If excess solvent remains, the film could delaminate the photoresist from the substrate during exposure and contaminate the mask.

A mask aligner was used to hold the photolithography masks, bring the substrate close (or in contact) to the mask and adjust its position, before exposing with UV light. Each photoresist requires a certain dose (intensity x exposure time) in order to make it soluble during development. The wavelength of light and the gap between the mask/substrate, g are important factors in determining the final resolution, R where $R \propto \sqrt{g + \frac{t}{2}}$ at some specific wavelength. The shorter the wavelength the higher, the resolution that can be achieved. Defects can come from overexposure, poor contact, or underexposure and can make it difficult to process small samples, as is done for the FP ICL fabrication.

Development can be done in a variety of ways, but commonly the substrate is fully immersed in a bath of the appropriate developer for a specified length of time. The pattern is observed for signs of underdevelopment or overdevelopment, depending on the resist profile desired.

Pattern transfer

After the development, the pattern is ready to be transferred to the material. Once the pattern is printed on the surface this is done via addition; by depositing other materials, or via subtraction; by etching away the epitaxial material.

There are two different physical vapor deposition (PVD) techniques used in FP ICL fabrication for adding metal contacts. They include e-beam assisted thermal evaporation and sputtering. These PVD techniques deposit a thin film of metal through a line-of-sight process and differ based on how the source material is evaporated. The thermal evaporation technique uses an e-beam to sublimate the material that needs to be deposited. The sample, placed above the source, is then coated in the vapor. Sputtering creates a plasma and then deposits the energized ions on the sample via RF fields. Thermal evaporation is favored for processes involving lift off while sputtering is favored when step coverage is important[135].

Selectively removing III-V-Sb material in the top layers of the ICL structure prove challenging due to the multilayer nature of the SL cladding. Dry etching is used because of the ability to control how anisotropic the etch is (in comparison to wet etching)[136]. Dry etching is carried out using an inductively couple plasma (ICP) reactive ion etching (RIE) system. A ICP source generates a plasma via RF coupling to

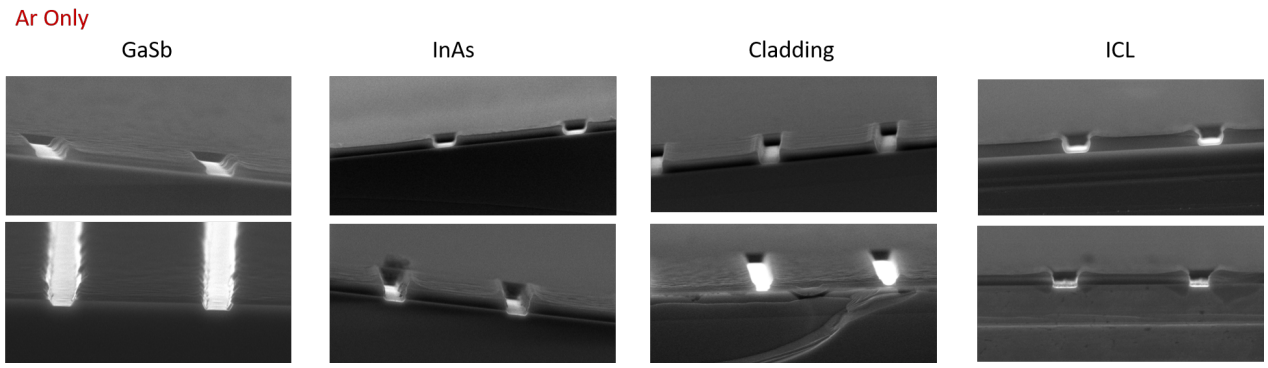

Figure 3.9: The top row shows Scanning electron microscope (SEM) images of the substrate with the mask before etching and the bottom row shows SEM images of the substrate after etching and mask removal. This allows a comparison of the etching profile achieved with Ar on different substrates.

the ionized gases in a vacuum chamber. These ions are accelerated to the sample via DC field, as in an RIE system. This allows ion energy and ion current to be decoupled and increase the degree of control over the etching process. Acceleration ions to the sample results in physical etching (via bombardement) while adding certain chemicals to the chamber can create radicals that react with the surface and result in chemical etching. Physical etching is more anisotropic while chemical etching is more isotropic[137]. Various combinations of $BCl_3/Cl_2/Ar$ are investigated to control the degree of anisotropy by changing the ratio of physical and chemical etching[138, 139]. Etching conditions are adjusted by changing the gas flow, pressure, RF power, plasma potential, or etch temperature, for example.

To understand the effect of the different species in the etching recipe on the constituent material of an ICL, individual substrates of GaSb, InAs, a failed AlSb/InAs SL growth (potentially poor surface quality), and a non-emitting ICL structure were prepared with a rectangular hole pattern. These samples were then etched with the individual gases: BCl_3, Cl_2, and Ar, at conditions similar to the ICL etching recipe[2]. The anticipated behaviour of the gases is that Ar represents the physical etching, Cl_2 represents the chemical etching, and BCl_3 represents a mix since there are Cl radicals but the B helps to remove the reactant products on the surface[137, 140]. The quality and profiles of the various dry etches should be compared since the samples were etched on different process runs. The etch duration was 5 min for the study.

Fig. 3.9 shows SEM images from a cross section of the features of the Ar only etching in the four different samples. The first observation is that the etch rate for all the substrates is extremely low - since the etch has had little to no impact on the surfaces. The second important observation is the degradation of the photoresist around the pattern. The decrease of the angle means that a less vertical shape will be transferred to the substrate.

Fig. 3.10 shows the cross section of the samples etched with BCl_3 only. The etching observed is pretty consistent across the various substrates with the sidewalls of the features having some roughness along the length, though it is small. The photoresist before etching has different angles but the shape after etching is always a flat bottomed V shape. Even for the ICL substrate, where the photoresist is very vertical before starting, there is quite an angle on the sidewalls and degradation of the photoresist is observed.

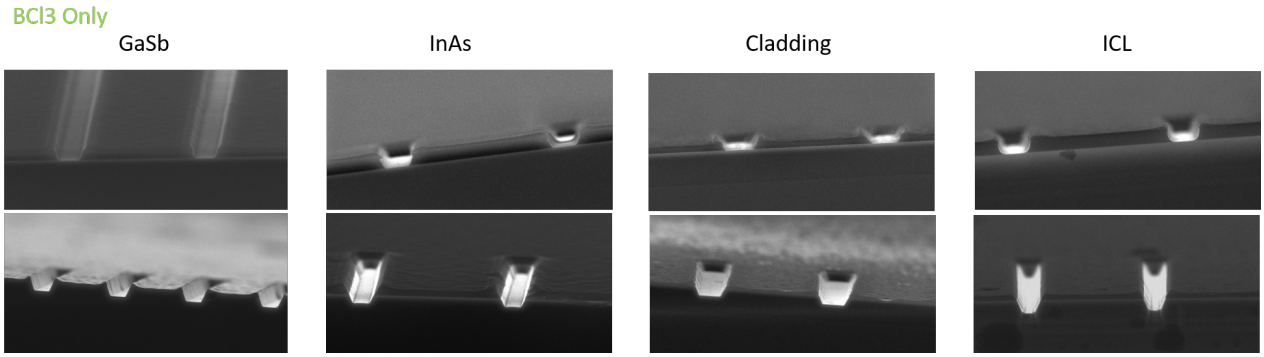

Figure 3.10: The top row shows SEM images of the substrate with the mask before etching and the bottom row shows SEM images of the substrate after etching and mask removal. This allows a comparison of the etching profile achieved with BCl_3 on different substrates.

Finally, Fig. 3.11 shows the cross section of the samples etched with Cl_2. Cl_2 etches the photoresist very quickly and laterally etches which results in the broad features, consistently for all the samples. The surface appears to be quite smooth, since the substrates did not have the extra debris removed, in comparison to the other gases. However, the angle of the slots is more exaggerated than with BCl_3 and they become very wide which is seen the most for InAs that has the lowest selectivity in comparison to the other substrates.

Based on the etching profiles observed of the individual gases, BCl_3 etching has the optimal balance between physical and chemical etching. In GaAs based etches, BCl_3 has also been observed to minimize the difference between GaAs and AlGaAs[140]. Of course, combining and changing the parameters can optimize other aspects of the etch such as uniformity and etch rates and may be required for small feature etching. When etching has to occur in small features, it is normal that the etch rate will change since there is a reduced ability to supply the etching gas and also to remove the reaction products. It has been shown that lowering the chamber pressure and adding Ar can reduce the effects of microloading and BCl_3/Ar etches have been shown to give smoother surfaces for ICLs [138, 140].

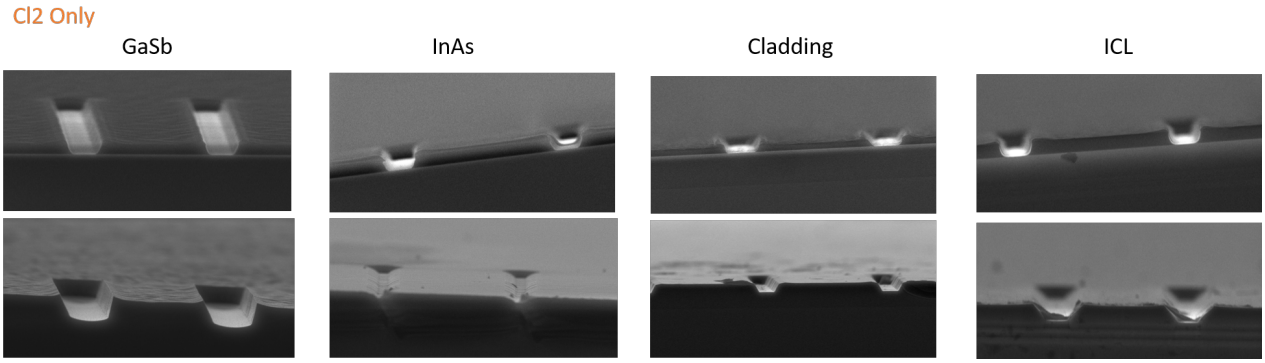

Figure 3.11: The top row shows SEM images of the substrate with the mask before etching and the bottom row shows SEM images of the substrate after etching and mask removal. This allows a comparison of the etching profile achieved with Cl_2 on different substrates.

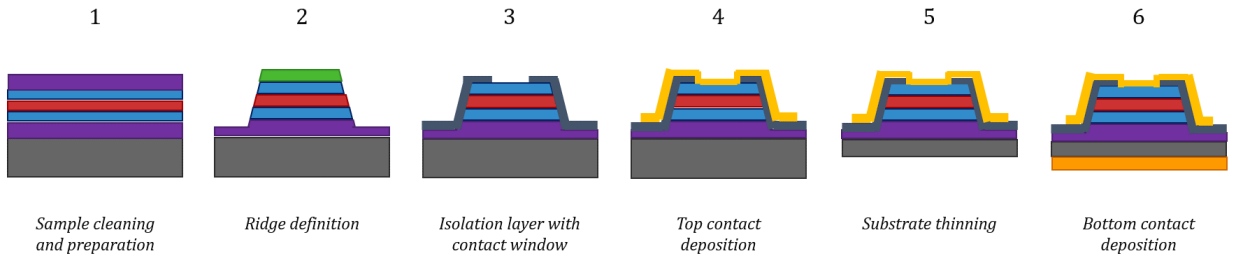

Figure 3.12: Photolithography process steps for fabricating FP ICLs.

3.3.2 FP ICL process

In order to create FP ICLs, the three main steps outlined in previous section are repeated multiple times to realize the device. The different steps involve an initial cleaning and surface preparation of the epitaxy, defining and etching the laser ridges (or mesa), depositing an electrical isolation layer and creating a contact opening, depositing the top metal contact, thinning the substrate, and depositing the bottom contact before annealing the sample. The device is then ready to have the lasers cleaved and mounted for measurement. An overview of these steps is shown below in Fig. 3.12.

Sample cleaning and preparation

The sample is cleaned by submerging it in a bath of acetone, IPA, and then water before being dried with N_2 gas. Following this, the surface is treated by exposing it to an O_2/Ar plasma for 5 min. These steps ensure all organic matter and debris is removed from the surface. The sample is then heated on a hot plate at ≈110 °C for 5 min in order to remove H_2O from the surface and ensure the photoresist will coat properly.

Ridge definition

The ridge definition begins with spincoating Microchemicals photoresist AZ1518 at 3000 rpm for 30 s, which results in approximately 2 µm of film thickness. The soft bake is at 110 °C for 1 min on a hot plate. The Karl Suss MA6 Mask Aligner was used to hold the $4x4$" masks, bring the ≈ $1x1$ cm sample close to the mask, and adjust its position, before exposing with UV light. The pattern is exposed using the mesa mask under soft contact for 25 s. The exposed photoresist is then developed in AZ726 for 32 s. The final pattern is shown in the SEM image of Fig. 3.13 where the ridge widths of 5 µm, 8 µm, 10 µm, and 100 µm can be seen from left to right in the image.

Finally, the mesa are dry etched until the top of the bottom cladding layer, giving a final height of ≈3 µm. The samples were loaded into an Oxford Plasmalab 100 ICP etcher and oil was used to ensure uniform substrate cooling. The dry etching recipe used is presented in Table 3.1[41].

The ICL samples are etched for ≈15 min depending on the thickness of the upper cladding and SCLs of the growth. An optical monitoring signal is used to determine which layer the etch reaches. Fig. 3.14 shows a typical signal of a mesa etch. Up to 300 s shows oscillations from the SL, while between 300 s to 400 s show an abrupt increase then four oscillations from the first SCL. The active region is marked by a decrease and two oscillations before an increase and four oscillations to the end of the second SCL. The

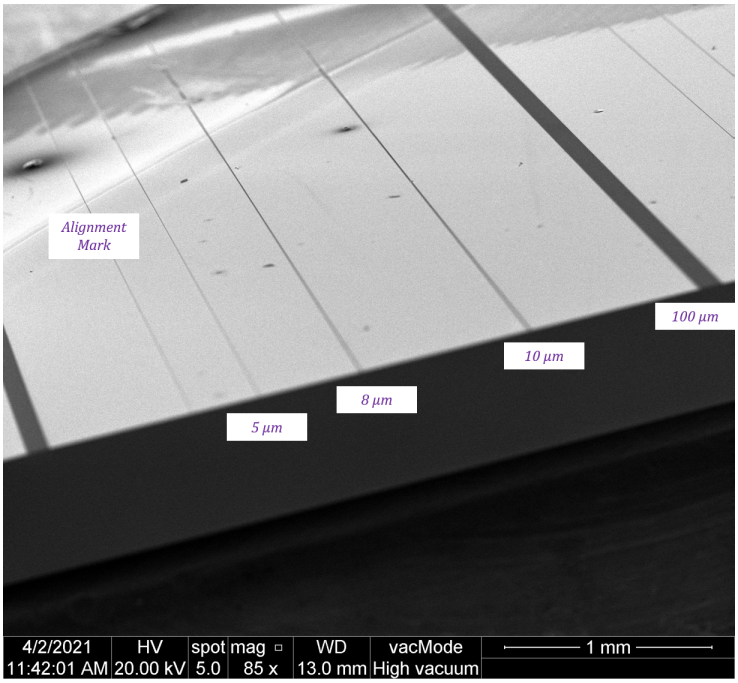

Figure 3.13: Exposed photoresist forming the etching mask for the laser ridges.

Parameter	Value	Unit
BCl3 Flow	4.0	sccm
Cl2 Flow	2.0	sccm
Ar Flow	6.5	sccm
Chamber Pressure	1.5	mTorr
RF Power	60	W
ICP Power	300	W
Table Temp	25	^{o}C

Table 3.1: Dry etching recipe parameters

etch is stopped after the drop in signal.

Isolation layer with contact window

The next photolithography is for the electrical isolation and contact window opening. Ideally, this occurs on the same day in order to protect the now exposed layers of the SL and active region; especially those that contain Al since they can form an oxide quickly[141].
The first step of this process is substrate cleaning since the etch mask must be removed. The sample is soaked in acetone immediately after removal from the ICP for upwards of 30 min if necessary, is rinsed in IPA and water before being dried with N_2 and put into a plasma of O_2 and Ar for 8 min to remove any remaining resist. Generally, this is sufficient to clean the surface again.
Before spincoating, the sample has a dehydration bake at 110 °C for 5 min. AZ1518 is deposited at 4000 rpm for 30 s before a soft bake at 110 °C for 1 min. The exposure opens contact windows on the top of the mesa ridges. The contact windows are openings in the photoresist and have at least 2 µm per side

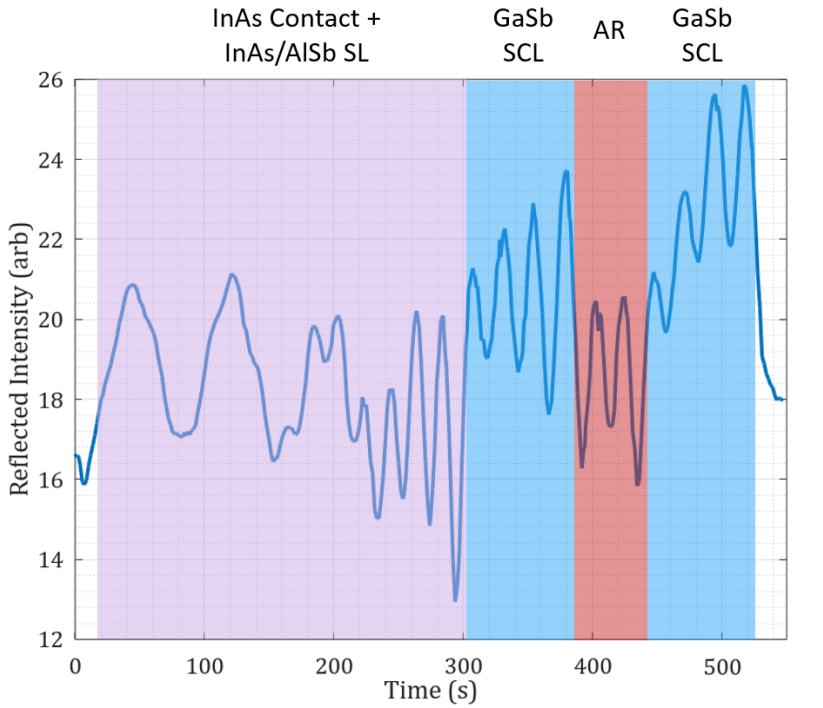

Figure 3.14: Optical monitoring signal used to observe the etch progression for the mesa.

to ensure covering of the ridge corners. This is depicted in Fig. 3.15 for a 5 µm ridge, which is on the left of an alignment marker.

After a soft contact exposure of 18 s, the film is developed in AZ726 for 25 s. Finally, the film is hard baked in an oven at 200 °C for 2 h.

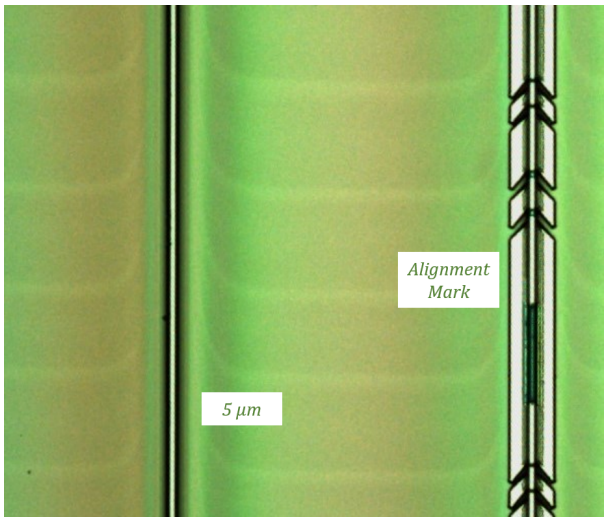

Figure 3.15: Exposed photoresist forming the contact windows on top of the laser ridges.

Top contact deposition

The top metal contact is deposited on the epi-side of the sample. A bilayer photolithography process is used in order to remove the metal to keep laser ridges electrically separate[2]. This is done via lift off and using the bilayer technique makes this process easier. The bilayer technique utilizes two layers: a photoactive resist is deposited on top of an optically transparent resist. The exposure and development steps are carried out so that a pronounced undercut forms, allowing the developer (or stripping solvent) to penetrate the features and remove the layers after metal deposition. Only the photoactive resist is affected by the exposure, so the development time must be tuned so that transparent resist is removed (the sacrificial layer) and the undercut forms in the photoresist.
The sacrificial layer is LOR5A, which is spun at 4000 rpm for 30 s and then soft baked at 180 °C for 2 min. A negative photoresist is used next for the ease of forming an undercut with the development time, so AZnLOF2020 is spun at 4000 rpm for 30 s and then soft baked at 110 °C for 1 min. This stack is exposed for 8 s so that an opening of 200 µm to 300 µm will be centered on the mesa. This ensures there will be sufficient space for probe contact during testing. For negative resists, there is a post exposure bake of 110 °C for 1 min to finish cross linking the polymers. Then the sample is developed for 105 s in AZ726 to give an undercut of around 5 µm. Metal is deposited with an e-beam assisted thermal evaporator and consists of 20 nm Ti and 400 nm of Au.
Lift off is done first in a bath of acetone to remove the photoresist. When the photoresist dissolves in the solvent, the metal attached is "lifted off" the substrate. The majority of the metal is removed during this step. To remove the LOR5A, and any remaining material, the device is placed in a bath of the developer. The top metal contact is now formed.

Substrate thinning

With the epitaxy protected by the top contact, the device can be mounted epi side down in protective wax. This allows the substrate to be thinned via polishing. Fine grit sand paper is rotated at 500 rpm and the substrate is removed until a thickness of 150 µm to 200 µm to ensure easy cleaving, minimal thermal resistance, and electrical conductivity.

Bottom contact deposition

The bottom metal contact is deposited on the substrate. The samples are mounted epi side down and a 5 nm layer of Pd followed by a 200 nm layer from an alloy of Au, Ge, and Ni is deposited.
The contact is annealed on a hot plate at 190 °C to ensure an ohmic contact forms[142]. A color change in the metal of the back contact observed under a microscope to ensure a sufficient temperature has been reached for the Au to diffuse through the substrate during the anneal.

Cleaving and mounting

The FP ICLs are cleaved to form cavity lengths between ≈1.5 mm to 2.5 mm. An example facet is shown in Fig. 3.16 for a 10 µm ridge. The two SCLs are visible surrounding the active region and defining the top and bottom cladding layers. Reflection from the Au top contact is also visble on top of the dark isolation

layer.
The devices can be mounted as bars or separated into individual devices as well as mounted either epi side up or down. They are solder to a copper block using In. Finally, they are ready for testing.

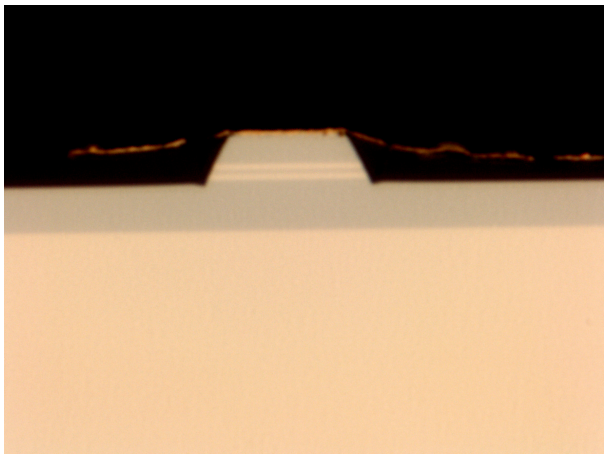

Figure 3.16: ICL facet after cleavage for a 10 µm ridge.

3.4 Electro-optical characterization of FP ICLs

The aim of the electro-optical characterization was to determine the bar level performance of the devices when mounted on a copper heat sink epi side up. The spectra were measured using an imaging spectrometer with slits and gratings. Thermal management could be improved by mounting the devices individually, epi side down to the heat sink and this would result in better performance such as higher P_{max} and lower I_{thr}. However, the main objective of fabricating FP ICLs is to characterize the material such that the material can be modelled for the multi-section tunable SVT ICL design. Independently pumping a multi-section device will require mounting devices epi side up so that probes can make contact with the correct section. As well, testing bars of devices will allow for higher volume testing and the ability to establish a reference standard for processing the ICL material.

3.4.1 Pulsed mode and CW performance

100 µm broad-area lasers are fabricated and first tested to characterize basic properties of the growth, such as J_{thr}, to ensure they are comparable to state-of-the-art ICLs. They are tested in pulsed mode with a low duty cycle in order to avoid heating affects from current injection. Typical settings for the pulsed measurements were a repetition rate of 10 kHz, with a 1 µs pulse, and theTEC set to around 20 °C. The output was measured with a LN_2 cooled InSb detector, which allows J_{thr} to be accurately.
The typical PIV characteristics for a 100 µmx2 mm laser is shown in Fig. 3.17. J_{thr} was measured to be 190 A cm^{-2} for emission around λ =3.4 µm at 20 °C. The corresponding threshold power density is around 650 W cm^{-2}). This is comparable to other 7 stage devices measured in the 3 µm to 4 µm region where the best performers easily have $J_{thr} < 200$ A cm^{-2}[7]. A summary of J_{thr} for the different growths studied can be found in App. 7. The inset of Fig. 3.17 shows the normalized spectra for narrow ridge device

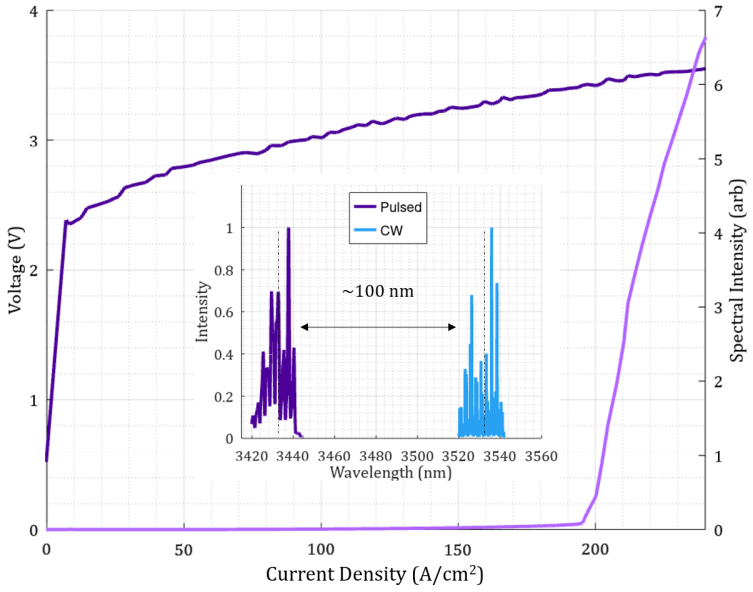

Figure 3.17: Characteristics of FP ICLs measured in pulsed mode and in CW. The main plot depicts the PIV performance in pulsed mode and the inset plot illustrates the spectra measured in pulsed mode and in CW.

(8 µmx2 mm). Due to device heating, the center of the emission envelope shifts by ≈100 nm.
Narrow ridge devices were then characterized to determine the PIV performance in CW mode with the output measured with a power meter equipped with an integrating sphere[143]. The output power reported here is the power/facet since the facets did not have any coatings applied. The narrow ridge devices would give a more accurate measurement of the emission wavelength in comparison to the PL measurements, as well as how it changes with temperature and current injection. T_0 was measured for the different growths to have an idea of how the material differed.
Narrow ridge ICLs mounted epi-side up will suffer from poor heat dissipation since the main mechanism for heat extraction is lateral heat flow to the top Au contact. The PI measurements for a 8 µmx1.6 mm device is shown in Fig. 3.18 in CW mode for several heatsink temperatures. The maximum operating temperature for this device was 33 °C. The threshold current at 20 °C is 56 mA and the maximum output power is 11 mW/facet.
T_0 is measured from temperature series measurements of I_{thr} and using Eqn. 2.17. This was done for devices with three different cavity lengths. Representative PIV characteristics for one of the devices is shown in Fig. 3.18, and T_0 =30 K for this growth. This is lower than the best performing devices, where T_0 is expected to be 45 K to 60 K, but these ICLs either use a thick layer of electroplated Au or where mounted epi-side down for thermal management[7]. This will affect the range of operating conditions that can be achieved, but with a low threshold current density the growth is of sufficient quality for investigating single-mode waveguide designs.

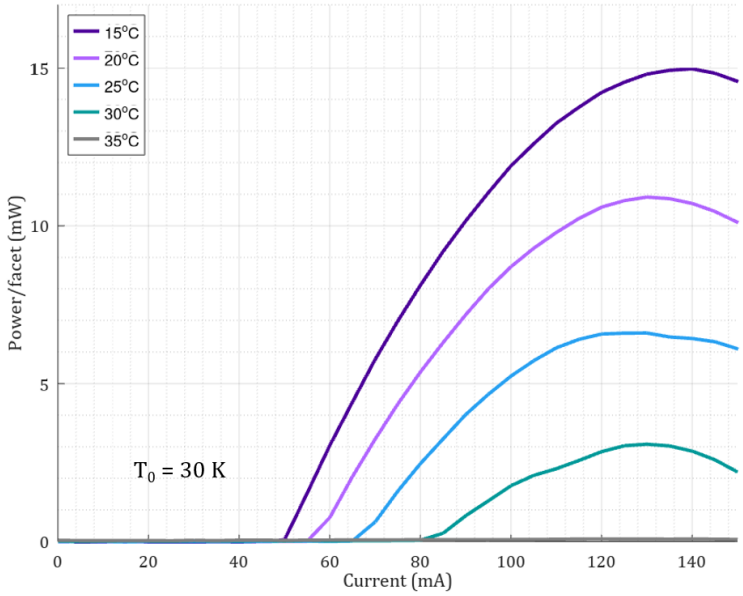

Figure 3.18: PI measurements of a 8 µmx1.6 mm device measured in CW at different heatsink temperatures.

3.4.2 Wavelength Tunability Measurements

The spectral measurements are key input parameters to the waveguide simulations. They will determine the variation of the wavelength emission for different electro-thermal conditions. Moreover, an estimation of the gain bandwidth can also be made for each growth based on the width of the spectral envelope for the emission. The techniques explored for single-mode emission rely on the ability to exploit differences in the refractive index of waveguide materials. This is done by measuring C_{FSR} and the amount the cavity modes shift as the operating conditions change. The spectra from the device presented in Fig. 3.18 is plotted in Fig. 3.19. At 20 °C and under a current of 100 mA (<I_{max}) the wavelength position of the peak with maximum intensity is 3496.6 nm, the FWHM of the emission envelope is 13 nm, and C_{FSR} =0.78 nm. The spectrum is also measured when the temperature is increased to 22 °C and a current near I_{max} of 130 mA. The wavelength position of the peak with maximum intensity is 3508.9 nm but the profile now has three bundles of modes. Likely, the gain and loss of the device is not uniform across the wavelengths and the lower wavelength modes are able to bleed through when pumped well above threshold. Therefore, we will measure and consider wavelength tuning below I_{max} to avoid regions where other modes can be pumped in a non-trivial way[89, 144].

For a fixed cavity length, changes in C_{FSR} is due to changes in n_{eff}. The wavelength tunability was determined by changing the current and temperature of the device independently. In order to track a specific cavity mode, the current (temperature) had to be increased by a small amount as plotted below in Fig. 3.20. Two different ICLs from different growths are presented. In Fig. 3.20A, the temperature of the heat sink is held fixed at 20 °C while the current is incremented by 2 mA starting at 123 mA. The central wavelength of emission for this device is 3458 nm at the lower current values and the electrical wavelength tuning was 0.07 nm/mA.In Fig. 3.20B, the current is fixed at 114 mA while the temperature is incremented by 0.5 °C starting at 20 °C. The central wavelength of emission for this device is 3532 nm

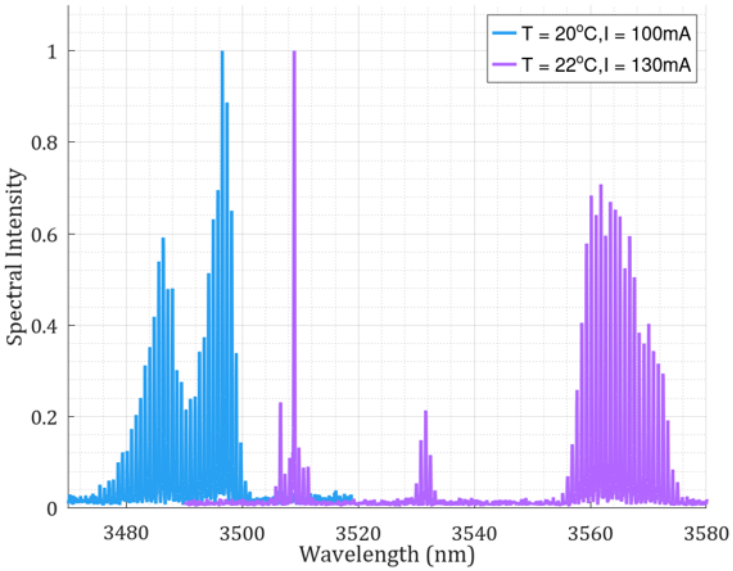

Figure 3.19: CW spectra of a 8 µmx1.6 mm ICL.

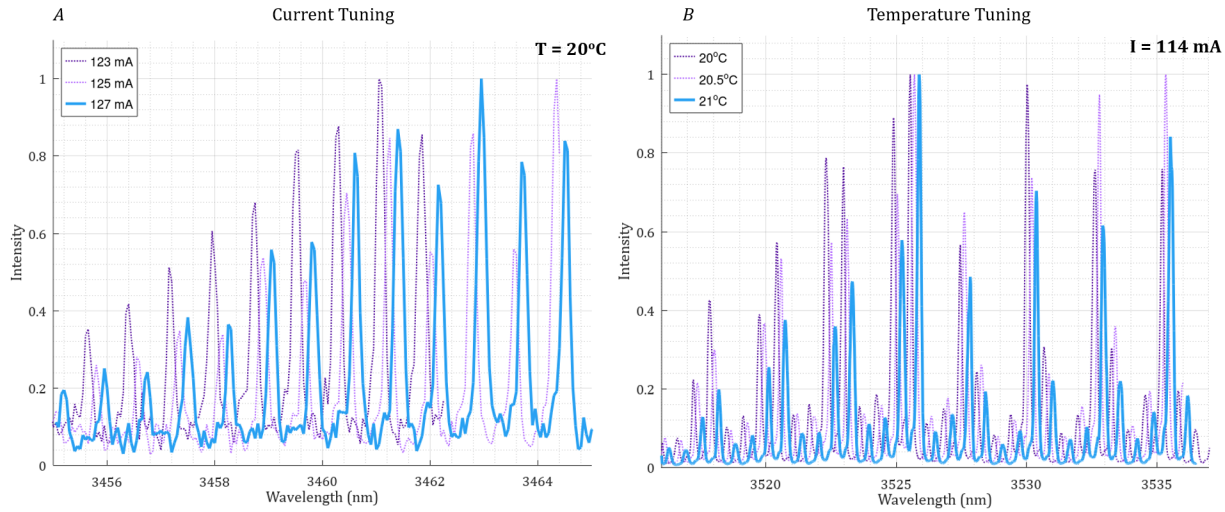

Figure 3.20: Two different FP ICLs are presented that were used to investigate the tuning properties of the material. *A:* Selected CW spectra of FP ICL for the current tuning with the heat sink set to T =20 °C. *B:* Spectra for the temperature tuning with the current set to I =114 mA.

at the lower temperature and the thermal wavelength tuning was 0.34 nm/^{o}C. This larger value makes sense since the ICL active region is more sensitive to temperature variation.

An estimate for $\Delta\lambda_{shift}$ can be made for the available current range of ≈70 mA between $[I_{thr}, I_{max}]$ and could be up to 10.3 nm from Eqn. 2.39. It is not useful using the available temperature range, although the sensitivity is higher, because different sections of the tunable device won't be thermally isolated.

This data is important to simulating the correct parameters corresponding to the target wavelength and to estimating the amount of tuning possible from current injection and temperature changes. Current injection causes a change in the charge density of the material while heating the material also shifts the

wavelength. Potential changes in the sign of the tuning direction can be anticipated due to the change of increasing or decreasing refractive index over the wavelength range.

Conclusion

This chapter presented an overview of the steps involved in the microfabrication of FP ICLs. Once the ICL active region and waveguide are simulated for a specific emission wavelength, the structure is grown using a MBE. Calibration structures are used to ensure high crystalline quality of the epitaxy.
From there, the wafer is processed using multiple photolithography processes to form laser ridges. The FP cavities are then defined by cleaving facets before they are soldered on heat sinks. The electro-optical characteristics were measured to evaluate the quality of growth and processing, ensuring low power consumption but high output power, and the correct emission wavelength.
Based on the growths and characterization of the FP ICL devices processed from this material, a good foundation has been laid that will allow the new single-mode waveguide designs to be explored.

CHAPTER 4

First development of single-mode slotted ICLs

The first slotted ICLs involve the development of both simulation and microfabrication techniques for a waveguide with a single section of slots along a FP cavity. Modelling of the waveguide is done passively in order to simplify the computation and accuracy of the material modelling required to target a specific wavelength of an ICL growth. The placement and spacing of the slots is the most important parameter in selecting the wavelength, however the quality of the fabrication of the slots will also affect the performance of the device. Since the slots are microscale features they may induce losses that could result in local heating effects that shifts the gain, reducing the output power and SMSR. The trade-off is that reducing the losses from the slots results in less interaction with the cavity modes and ultimately reduces the final SMSR achieved.
The main goal of this single-mode laser is to provide an idea of how the device will operate far from threshold based on the passive design. The main characteristic of interest is the measurement of the wavelength tunability and the maximum $\Delta\lambda$ from changes in current injection and heat sink temperature.

4.1 Modelling slotted waveguides

Realizing single-mode slotted lasers requires the simulation of different waveguide geometries that can select the correct wavelength and have features that are realistic to fabricate using photolithography. The main objective of the simulations for a slotted waveguide is to determine the spacing of the reflectivity peaks, S_{FSR}, and ensure it matches up with the gain bandwidth of the material. The guiding concepts to optimizing the slots determining which parameters maximize the reflectivity and minimize the width of the peaks. This will result in the most selective optical feedback from the waveguide.
Simulations for potential waveguide designs were carried out using a mode solving software called FIMMWAVE by Photon Design with the FIMMPROP module that enabled the simulation of optical mode propagation[145]. FIMMWAVE uses finite element and difference methods (FEM and FDM) to solve for

the eigenmodes of Maxwell's equation:

$$\Phi(x,y,z) = \psi_m(x,y)e^{i\beta z} \tag{4.1}$$

where we have assumed that the refractive index is independent of the propagation direction, z, and β is the propagation constant of mode m. It is related to n_{eff} by the wave vector k_0 via the relation: $n_{eff} = \beta/k_0$. Propagation is simulated using the eigenmode expansion method where solutions of Maxwell's equations are written as a superposition of forward and backward propagating modes:

$$\Psi^m = \sum_{i=1}^{N}(a_i^m \Psi_i^m(x,y)e^{i\beta_i^m z} + b_i^m \Psi_i^m(x,y)e^{-i\beta_i^m z}) \tag{4.2}$$

Only transverse electric (TE) modes are considered due to the selection rules in the ICL active region. The QWs are compressively strained, which increases the heavy-hole VB so that emission is predominantly between the CB and the heavy-hole band and the TE mode is favored[62, 146]. The device can be divided into segments with the same refractive index and then expressed as a scattering matrix:

$$\begin{pmatrix} a^- \\ b^+ \end{pmatrix} = S_J \begin{pmatrix} a^+ \\ b^- \end{pmatrix} \tag{4.3}$$

where a and b are vectors of the mode amplitudes for the forward and backward propagating components on either side of the interface between two sections of the device. In order to save on computational time, one mode is studied and so the absolute value of the modulus squared values for the reflection and transmission coefficients is not physically accurate since they come from an incomplete basis set[147].

4.1.1 Design concepts for ICL slotted waveguides

The trade off faced in the design is to add slots that maximize the optical feedback but also minimize the total device length in order to keep the threshold low. The parameters that can be changed to address this goal were already introduced in Chapt. 2.3.2. To repeat them for easy reference here, they include the slot spacing (d), slot width (d_s), etch depth (t_E), number of slots (N) and device length. An illustration of the structure with these parameters labelled and the refractive index profile is shown in Fig. 4.1.

Fig. 4.1A shows the refractive index of each layer and highlights where the TE_0 mode exists. When slots are introduced, as shown in the ICL of Fig. 4.1B, the upper cladding refractive index is perturbed by air ($n \simeq 1$) and this provides the reflective surfaces resulting in an index coupled device. The approach to modelling the ICL material that allows n_{eff} and n_g to be calculated was discussed in detail in Sec. 3.1. Fig. 4.1C illustrates the important parameters for the simulation that ensure single-mode operation from the geometry of the slots placed in the waveguide. The equations are meant to provide an intuitive picture of the importance of the effective refractive index on meeting the criteria for constructive (even n, as for d) vs destructive interference (odd m, as for d_s)[85].

In the following discussion the main effects of the individual parameters will be discussed as if they would be independently changed though it is important to keep in mind that the overall picture is important for a robust design. The behaviour of these parameters is studied with a laser that has symmetric cladding,

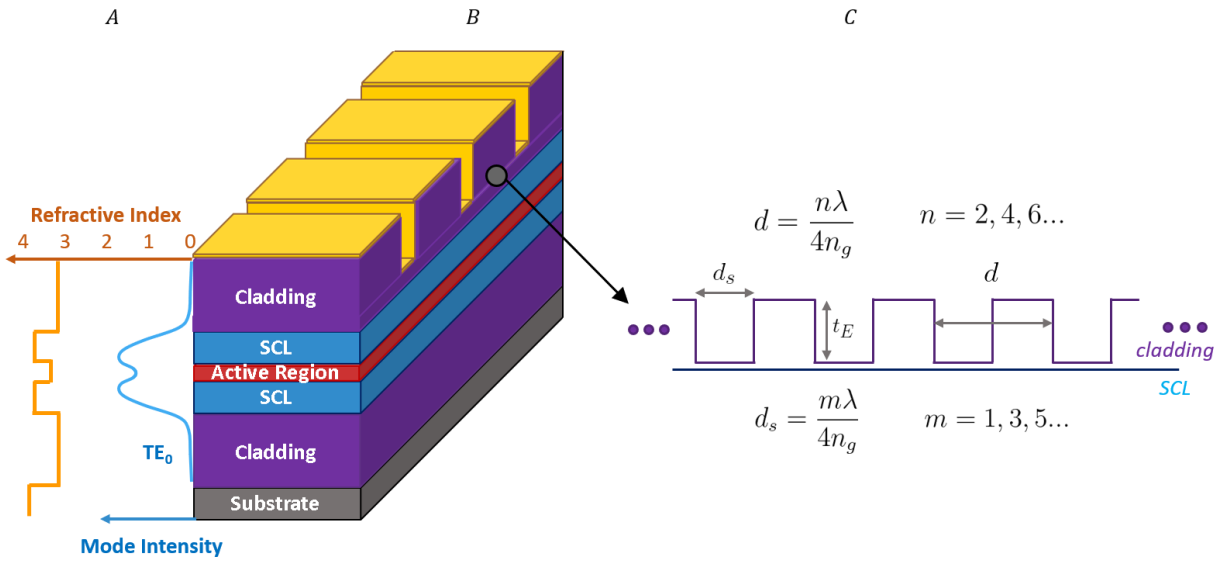

Figure 4.1: *A:* The refractive index and mode intensity is plotted for each layer in an ICL. *B:* The cross section of a typical ICL is shown with the slotted waveguide along the length of the cavity. *C:* The simulation parameters of the slotted waveguide are labelled on the features in the waveguide, highlighting the constraints placed on their size.

without the material dispersion, and without gain to have a simple idea of how they elicit a response in the reflectivity spectra. The top and bottom cladding thickness was 2800 nm, the SCL thickness was 500 nm and the active region thickness was 300 nm.

d is used to ensure the desired lasing wavelength is selected and with a S_{FSR} will result in single-mode emission. As expected based on the conversion between real space and frequency space, the larger d is the narrower S_{FSR} is. To ensure single-mode emission the guiding principle is to make S_{FSR} larger than the expected gain bandwidth from the ICL active regions which could be as large as 300 nm[23]. However, the measured spectral envelope of emission of FP ICLs was much narrower than this, even accounting for the shift in wavelength at different levels of pumping. So, d was chosen such that S_{FSR} >100 nm, as seen in Fig. 4.2A. When S_{FSR}<100 nm, multiple reflectivity peaks can overlap with the cavity modes and leads to multi-mode emission. According to simulations, small periods of around d<20 µm is required for a S_{FSR} that satisfies this condition.

d_s can also be responsible for changing the S_{FSR} if the edge to edge distance between slots is fixed. Though its main effect is on the strength of reflectivity from the waveguide. Both of these effects are illustrated in Fig. 4.2B. The limit of UV photolithography at λ=365 nm is around 1 µm, depending on the exact process and how well the resist thickness is optimized. Having a range of d_s to study around this value will allow some flexibility during fabrication.

t_E changes R and the FWHM of the S_{FSR}. Etching affects these parameters because it controls the degree to which the interface will interact with the tail of the propagating mode. Therefore, R is expected to have an exponential behaviour with respect to t_E. Indeed, this is seen in Fig. 4.3A, where t_E is varied up to the SCL. The deeper slots have broader reflection peaks, with the FWHM increasing to 0.9 nm at the cladding-SCL interface as plotted in Fig. 4.3B. The reflectivity peaks do not significantly start to appear until 2.2 µm, or

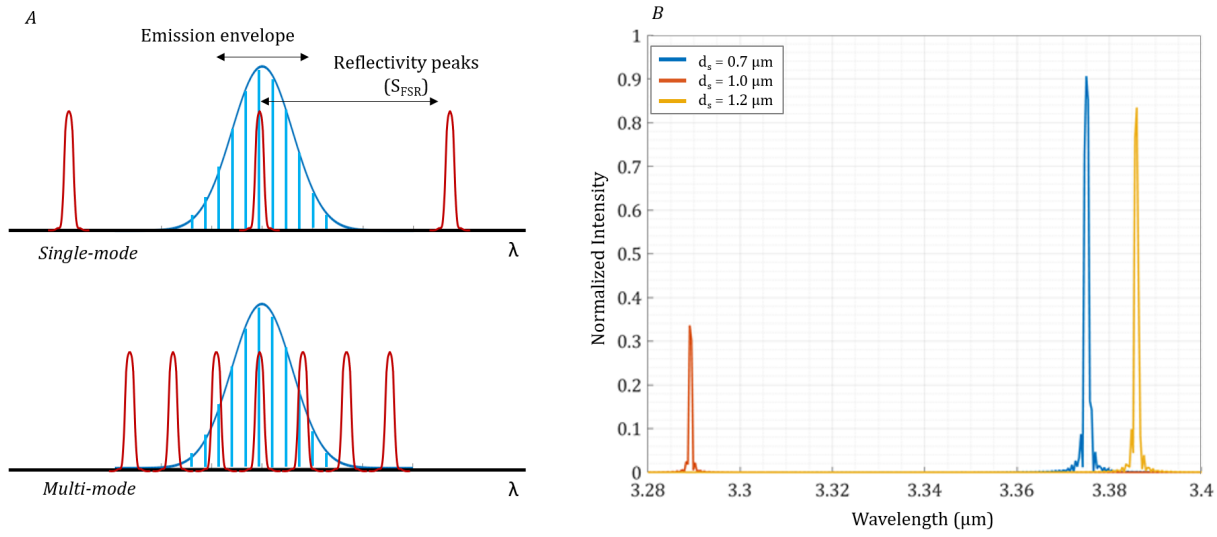

Figure 4.2: *A:* Schematic illustrating how single-mode vs multi-mode emission can be realized with respect to the width of emission and S_{FSR}. *B:* The reflectivity spectra from different slot widths appropriate for fabrication with photolithography.

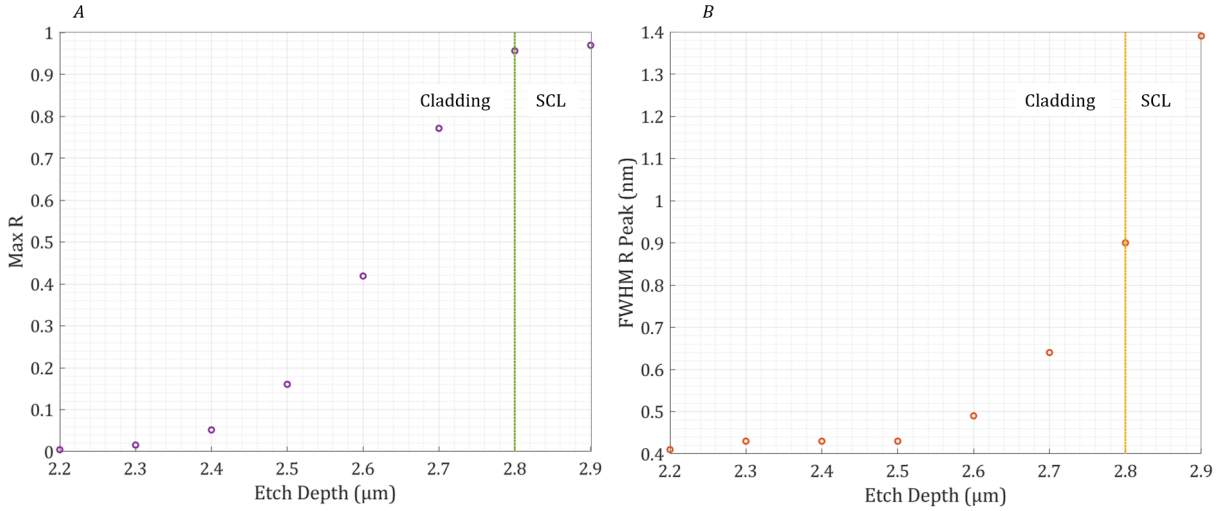

Figure 4.3: *A:* The simulated R is shown with respect to t_E for $\lambda \approx 3.3\,\mu$m. *B:* The FWHM of R is plotted as a function of t_E.

about 80% of the way through the top cladding until it saturates near its maximum at the cladding-SCL interface, indicating that fairly deep slots may need to be fabricated.

In order to have an overall interference effect, the number of reflections at the slot-air interfaces have to accumulate over the length of the device. This happens when we increase N. For deep slots, with $t_E = 2.7\,\mu$m, the reflectivity increases monotonically. Based on the period of 6.5 μm, the device length for $N = 150$ is 0.98 mm. In this case, as N increases and R increases, the FWHM decreases. This is shown in Fig. 4.4A and Fig. 4.4B for R and the FWHM, respectively. As N increases, the device length increases as

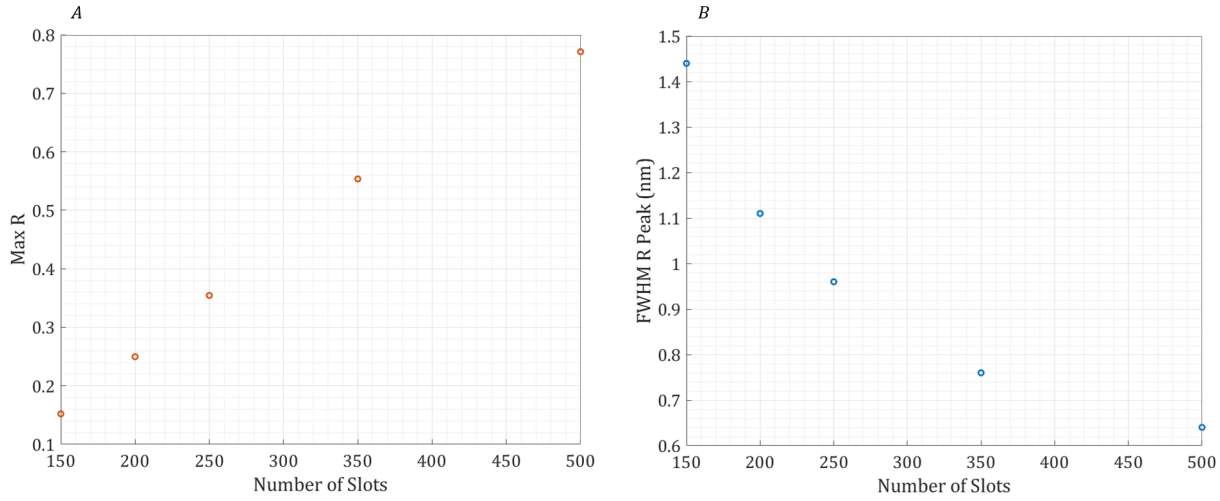

Figure 4.4: *A:* The simulated response for R is plotted as N is varied. *B:* The change in the FWHM of R is plotted as a function of N at $\lambda \approx 3.3\,\mu m$.

well which will affect C_{FSR} according to Eqn. 2.8. The maximum FWHM allowed for single-mode emission can be estimated from C_{FSR} at a given device length, since the longitudinal modes are generated from the facet reflections. A practical challenge of using cleaved facets to define the cavity will be the precision for the total length of the device. In general, the final cleavage position occurs within $\pm 50\,\mu m$ of the scribe position. This uncertainty then translates to an uncertainty in the final mode spacing of the device. The consequence of these considerations is explored in Fig. 4.5A using $n_{eff} = 3.8575$ and $\lambda = 3.3\,\mu m$. As expected, shorter lasers will have a larger shift in C_{FSR} from cleave discrepancies; however, longer lasers will require a much narrower FWHM from the slotted waveguide in order to be single-mode. The change from single-mode to multi-mode emission from a change in C_{FSR} is illustrated in Fig. 4.5B. If more than one cavity mode is within the reflection band from the slots, the laser will no longer be single-mode. In general, single-mode emission is expected if the following condition is met:

$$C_{FSR} > \frac{1}{2} FWHM \tag{4.4}$$

The effect of wavelength tuning needs to be considered as well to determine an appropriate FWHM. Wavelength tuning refers to the controlled shift of the cavity mode by changing the refractive index. This can be achieved through the current injection or temperature changes, since this will alter the optical path length. The differential change of the refractive index induces a change of the gain modulation envelope with respect to the cavity modes. In other words, wavelength tuning is accomplished by shifting the mode of interest together with the gain envelop and reflectivity peak from the slotted waveguide. Continuous tuning is difficult to achieve since these effects can occur at different rates. This will be explored empirically for the devices.

The simulations presented in this section illustrate how the relevant parameters, R, FWHM, and S_{FSR}, change as the geometry of the slots are altered. A priori, it is unknown what value of R is sufficient for interaction with the cavity lasing modes. This is because a full laser simulation is difficult to achieve due

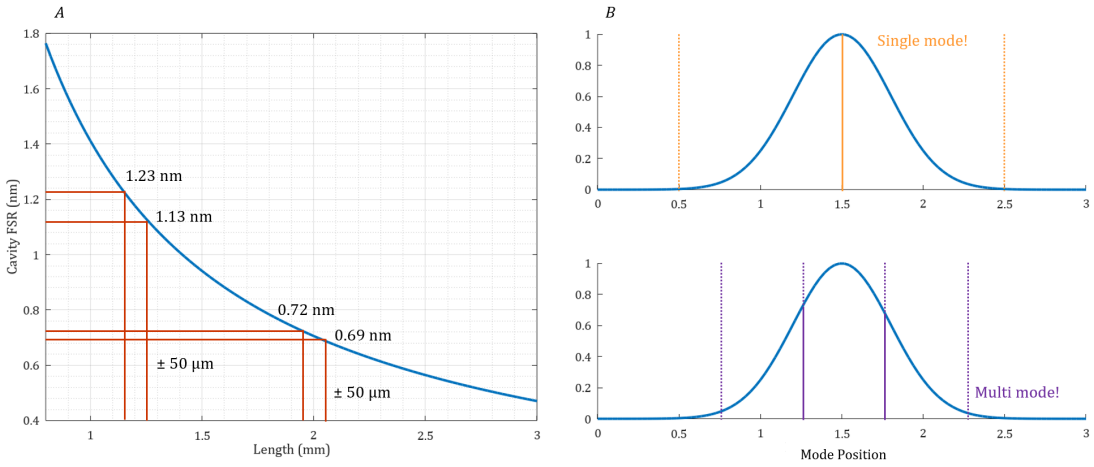

Figure 4.5: *A:* A plot of C_{FSR} as a function of the cavity length.*B:* An illustration representing multi-mode vs single-mode emission as C_{FSR} changes.

to the unstudied response of the gain/loss in the active region to far from threshold pumping. In context of a laser with gain and loss, the constructive vs destructive interference from the slot placement modifies the threshold gain values needed to support each cavity mode. The amount of reflectivity that is required for single-mode emission has to compete with the gains and losses present in ICL and the desired output power desired. The interference can be likened to extra gain that is added to the desired modes, allowing them to overcome the losses more quickly and subsequently lase before others within the gain bandwidth. We choose to keep the simulation passive and make an empirical link to this after in order to optimize the design on performance. The important take away from this example is that by altering the geometry of the slots – even just with one parameter such as the slot spacing – there is a lot of control over the emission mode profile.

4.1.2 Slotted waveguide mask design for multiple wavelengths

The main goal of the single-mode slotted ICL was to chose a design that maximizes the SMSR. The concepts discussed in the previous section will come together for the design of a photolithography mask that can target multiple wavelengths. This was done so that the mask could be re-used for growths with different central emission wavelengths because they can take a long time to print and are expensive. For this thesis, I had five growths to work with. The FP ICLs fabricated included wavelengths of 3.34 µm, 3.39 µm, 3.46 µm, 3.53 µm, and 3.62 µm, representing a span of 280 nm to cover with just one mask.
Simulations were conducted on a laser that had material dispersion effects added and the structure described in Fig.3.1. The choice of d and d_s was made with respect to the emission of the FP ICLs. The comparison of the different waveguide configurations simulated with respect to the emission spectra is summarized in Fig. 4.6. d was chosen such that two reflectivity peaks overlapped with the spectra of two of the growths to make efficient use of the photolithography mask space. This automatically ensured S_{FSR} was wide enough to be single-mode. The spectra is expected to be red shifted when operated in CW mode, which is why some of the peaks from the slots are offset. The slot spacing was d =6.68 µm and d =13.1 µm. Some variation was put on the slot width to allow some flexibility during processing,

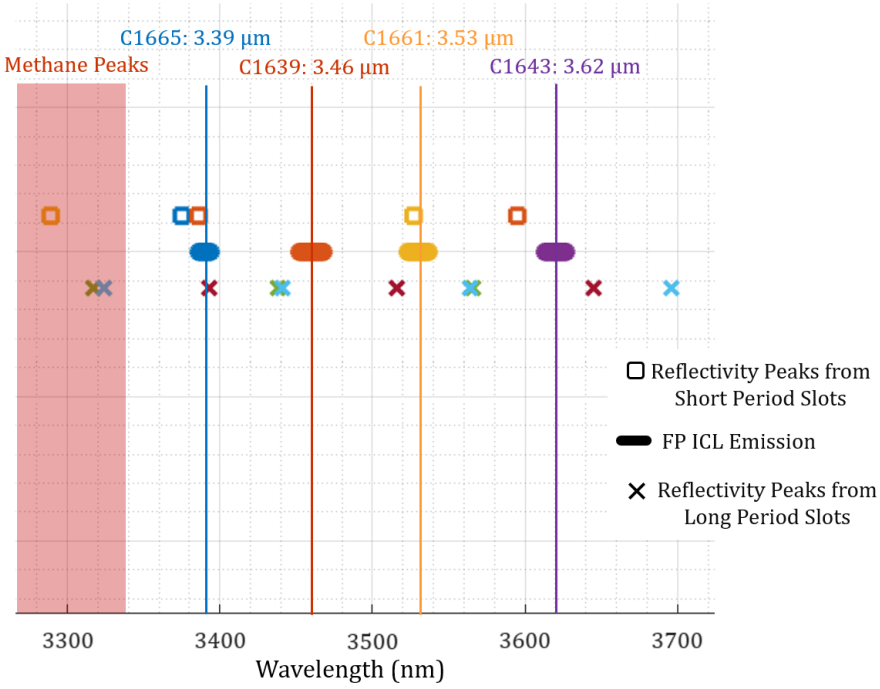

Figure 4.6: The reflectivity peaks for the short period slots, d =6.68 µm, and the long period slots, d =13.1 µm, are plotted the pulsed emission from FP ICLs fabricated on four of the growths. The different colours represent the different slot width combinations possible.

so d_s =0.7 µm, 1.0 µm and 1.2 µm was used. In total this gives 6 different simulation configurations that were distributed on the masks.

Slotted lasers normally have a small number of slots and are operated as a two section device with a separate gain section and slot waveguide[148]. In this design a single section is used and slots are placed along the total length of the laser for more flexibility during fabrication. This allows for the study of C_{FSR} with respect to the FWHM from the waveguide. The consequence of this choice is that d and N will determine the length of the laser. Based on the FP ICLs fabricated for multi-mode emission, the typical length of the low threshold current devices are between 1 mm to 2 mm, which will also guide the choice for d and N.

Fig. 4.7A shows the change in R and the FWHM from a waveguide design with d =6.68 µm, d_s =1.2 µm, t_E =1.2 µm as N is changed. The simulated FWHM is compared to the calculated C_{FSR}, using $n_g = 3.8575$ obtained from FIMMWAVE. When the FWHM is smaller than C_{FSR}, the overlap of these peaks can be optimized via current and temperature operating conditions. When the FWHM is larger, multi-mode emission will occur since multiple cavity modes are contained in the reflectivity peak. These simulations suggest it would better to cleave shorter lasers, below ≈2 mm.

Independently of N, R and the FWHM can be further tuned by changing t_E, as shown in Fig. 4.7B with $N = 298$. There is an exponential dependence on t_E, as expected, and the corresponding FWHM is plotted up to just before the SCL (to preserve mode confinement). It is important to keep in mind that more R is not necessarily better - cavity facets have ≈30% R and can support lasing while still extracting laser output. As well, the deeper slots have a broader FWHM so keeping t_E <1.5 µm would then be a good

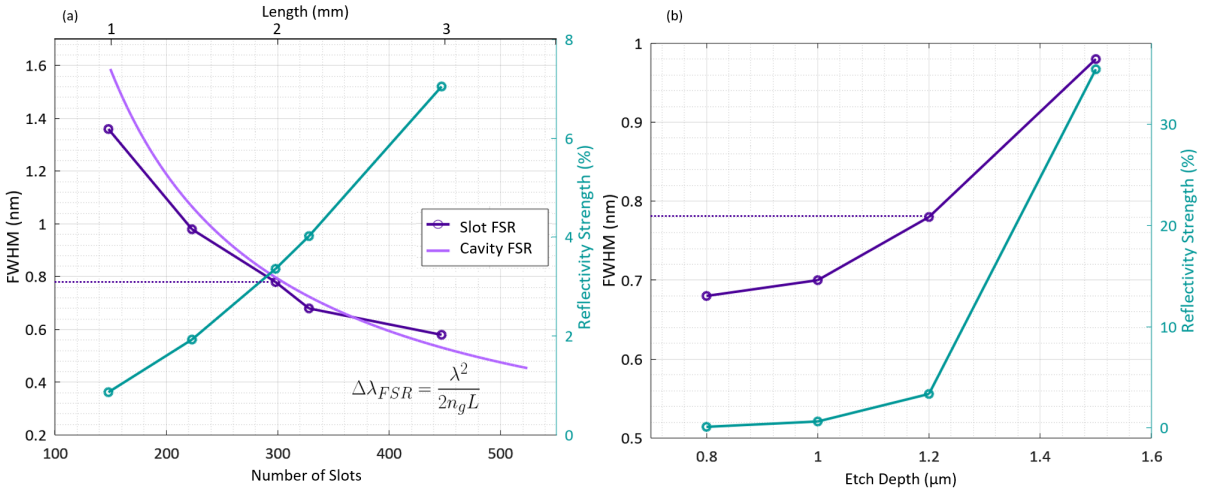

Figure 4.7: A: The dependence of the reflectivity strength (R) and the reflectivty peak FWHM is shown with respect to the number of slots. The cavity mode spacing, C_{FSR} is also plotted with the simulated FWHM while changing the total length (equivalently, N). B: The dependence of R and the FWHM are shown with respect to t_E.

starting point.

The two different d simulated are shown in Fig. 4.8 along with the emission spectra from a FP ICL measured at T =20 °C in CW mode with two different currents, I =100 mA and 130 mA, to verify the feasibility of single-mode emission at ≈3.5 µm. The corresponding two S_{FSR} simulated are 132 nm and 236 nm from d =13.1 µm and 6.68 µm, respectively.

The parameters discussed are closely linked and there are a few trade offs. The ultimate number of slots needed for interaction with the cavity modes is more or less controlled by the contrast of the index of refraction of the cladding layer and the slot (how much the air can introduce a contrast, controlled by t_E) and is determined by the material system and model. The smaller the contrast the more slots that will be needed in order to have an appropriate response. The more slots needed, the longer this laser will need to be which in turn makes C_{FSR} more dense. In the context of a pumped laser, an increase in length increases the amount of gain offered by the material, but more slots increase the total losses as well. So, the value of R that is needed must be strong enough to suppress other modes but not introduce too many losses to the one desired mode. An important outcome of this work will be creating an experimental link to the simulated value of R, as will be discussed in the following sections.

4.2 Slotted laser process development

The main objective of this work is to offer a less complex alternative to single-mode waveguide fabrication which is typically done either with re-growth steps or e-beam lithography. Therefore the fabrication of the slotted ICLs was done entirely with UV lithography and dry etching, as previously mentioned. Slots will be added as an initial step to the FP ICL process described in Sec. 3.3.2.

The easily achieveable resolution limit of UV photolithography is around 1 µm and depends on the photoresist, thickness, wavelength, quality of surface, and specific lab equipment. The smaller slot widths

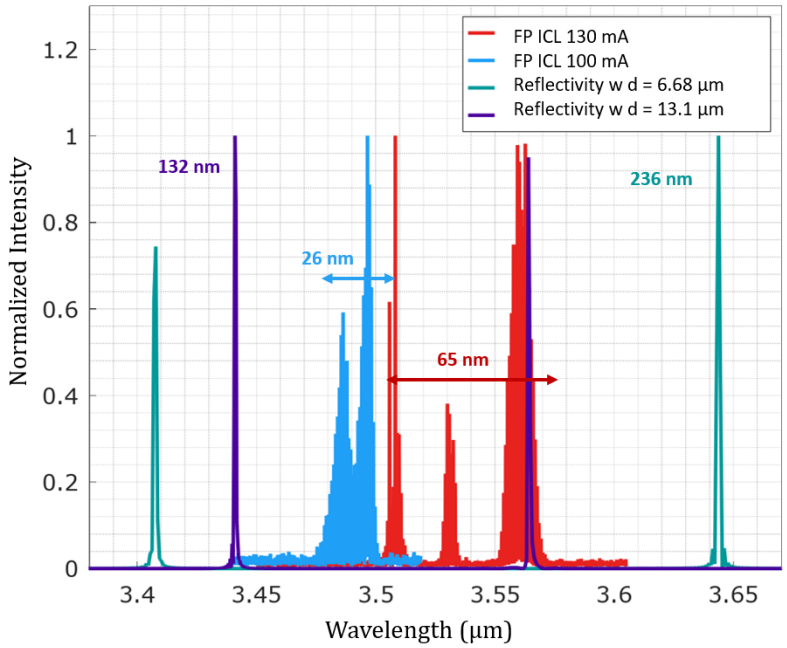

Figure 4.8: Simulations of slot patterns with d =13.1 µm and 6.68 µm are shown for a FP laser measured at T =20 °C in CW mode with injected current I =100 mA and 130 mA.

could pose a problem during the dry etching step due to the decreasing aspect ratio (depth/width), which at approximately 2 µm/1 µm is not without challenges[139, 149]. Easier to fabricate slots of 1.2 µm were targeted for the initial process development.

The overview of the processing steps to fabricate the slotted ICLs is shown in Fig. 4.9. The fabrication begins with the definition of the slots first in order to maximize the resolution from a uniform surface with the remaining steps following FP ICL steps with some optimization changes from the original procedure. The steps to creating the slots include surface treatment to ensure photo resist adhesion, the deposition of a dielectric hard mask, the photolithography to define the slot pattern, the dry etching to transfer the pattern to the sample, and mask removal and cleaning. The focus of the development was to optimize the dry etching recipe to address the challenge of creating a high aspect ratio feature and to create more vertical sidewalls. Initially, new recipes were optimized on GaSb samples before testing on ICL samples in order to save material.

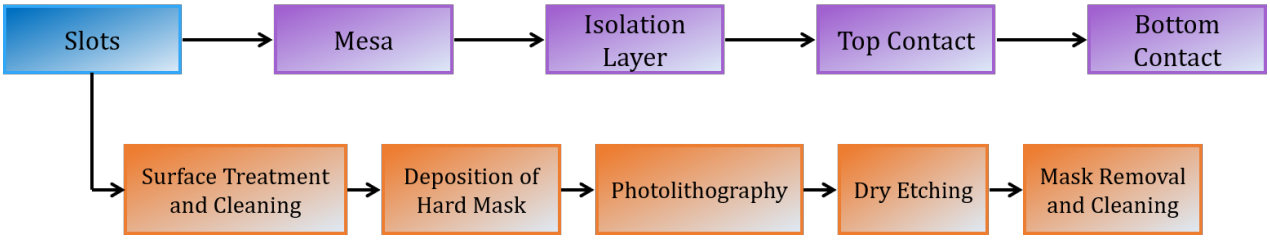

Figure 4.9: A general overview of the steps involved in the technological process fabricating a slotted ICL. The box for defining the slots is blue, highlighting that it is the new addition to the FP ICL fabrication. The main steps that are required to define the slots are expanded in orange boxes.

4.2.1 Photolithography development on GaSb

The first process developed for the definition of the slots explored different strategies to ensure small slots could be defined and etched with vertical sidewalls. The process for FP ICLs lead to mesa with angled sidewalls (see Sec. 3.3.2 and [2]) and we hypothesized there were two reasons for this: a non-optimized photolithography step and a non-optimal dry etching recipe. Dry etching involves the transfer of the mask pattern to the substrate material, which means that the shape of the mask is important to the final shape of the feature. If the walls of the resist degrade, the angled shape and/or roughness can also be transferred to the material. For this reason, and with the idea that a thick mask would be needed to etch deep slots, the use of a negative photoresist was initially explored.
A pattern is imparted to a negative photoresist in the areas exposed to light because cross linking in the polymers begins[150]. A post exposure bake finishes this reaction and the development step removes the areas that were not cross linked. In general, negative photoresists are very resistant to dry etching and $SU-8$, specifically, is well known in the microfluidics community to have very vertical sidewalls[151, 152]. A process utilizing $SU-8$ was developed on GaSb wafer test samples but the steps were time consuming in order to gently evaporate the excess solvent and to remove the edge bead from spincoating. This lead to extremely inconsistent fabrication results, though some samples had very vertical etch profiles. The process using $SU-8$ is described in App. 7. An alternative was subsequently explored using a dielectric hard mask which is resistant to erosion during dry etching and should then lead to vertical sidewalls. Material that is considered "hard" means that it has a slow etch rate in comparison to the material you would like to pattern in a certain gas mixture (high selectivity). Using a dielectric material means that a thinner mask layer can be used with respect to hardened photoresist, leading to improved the resolution and wall angle of the etched pattern.
One of the other benefits of using a hard mask is that the shape of the photoresist defining the features is less important and since it is not used to protect some regions of the sample any more, a very thin layer can be used to define the pattern which increases the achievable resolution again[135]. In order to maximize the resolution, a positive photoresist can be used which has the added benefit of simple edge bead removal via a flood exposure. There is also no post exposure bake, which helps simplify the optimization process. In order to take advantage of these benefits, a new fabrication procedure using a thin, positive photoresist was developed. The hard mask was Si_3N_4 deposited on the sample via plasma enhanced chemical vapour deposition (PECVD).
In Fig. 4.10 the use of AZ1505 and AZ1518, panel A and B, respectively is compared. Spincoating at 3000 rpm gives a resist thickness of 500 nm for AZ1505 and 1800 nm for AZ1518. In Fig. 4.10A, the edge bead was removed by carefully taping the edges of the sample to a Silicon carrier wafer and spincoating the resist on the sample. The tape gives a path for the resist to flow to the carrier wafer and prevent build up at the edge from the surface tension[153]. In Fig. 4.10B, the edge bead was removed by covering the middle area with a piece of Si cleaved to approximately the sample shape and then flood exposed to make the edge bead soluble in developer. This method is simple to execute, but difficult because of the small and arbitrary sample sizes studied. This point also attributes to the non-uniform resist deposition which leads to areas underdeveloped on the sample, as is shown in Fig. 4.10B. To impart the 1.2 µm slot pattern the thinner photoresist AZ1505 was chosen.

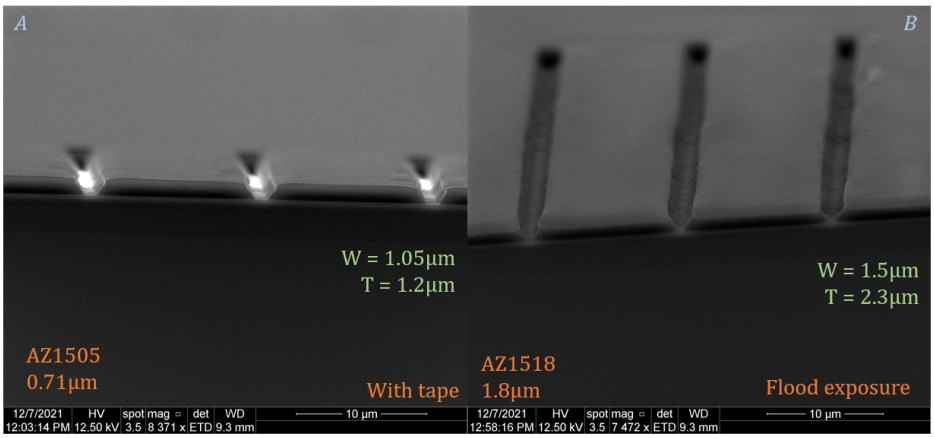

Figure 4.10: Deposition of two potential photoresists that could be used to transfer the slot pattern to the hard mask. *A:* AZ1505 and *B:* AZ1518.

Initial etching tests done on GaSb substrates using SU − 8 were a bit larger than desired at 2 µm but had very vertical sidewalls. A similar optimization strategy using the hard mask did not yield vertical sidewalls on the ICL material, though the features were smaller. A comparison of the etching is shown in Fig. 4.11 where A shows the mask profile before etching, B shows the etching on a GaSb substrate, and C shows the same dry etching recipe for ICL material. In Fig. 4.11A, sidewalls have an angle between 91°-96° and d_s ≈2 µm. Comparing Fig. 4.11B and C, a very angled profile is observed on the ICL material in comparison to the GaSb etch. For the ICL material d_s ≈1.2 µm at the top of the slot.

This could be due to an erosion of the hard mask profile or it could be a consequence of different etching conditions due to the smaller features. Perhaps below about 2 µm the local etching properties change and the result is much different than for larger structures. For example, chemical etching often requires some physical etching in order to remove the involatile species and this may happen more inefficiently. Alternatively, chemical etching could happen more inefficiently because of the decreased surface area and physical etching dominants. Both situations require a different gas compositions and should be investigated on the real material with the smallest structures. However this study demonstrates that the

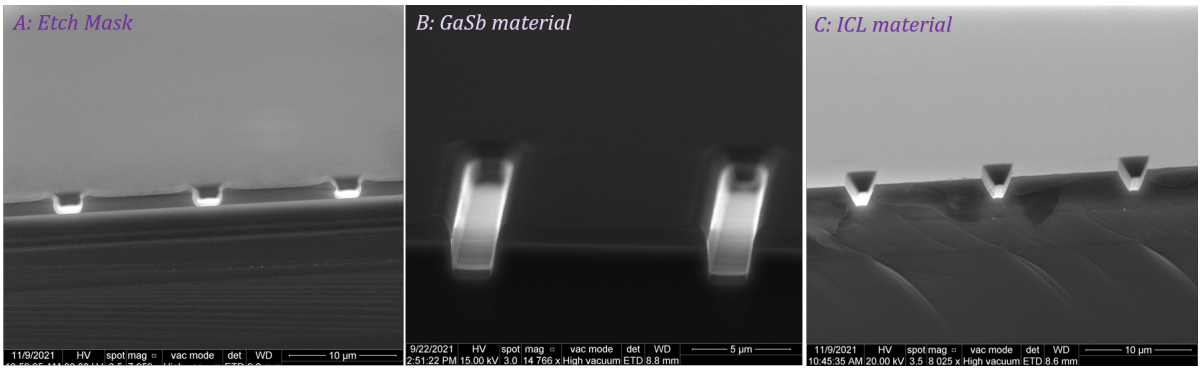

Figure 4.11: Comparison of dry etching in ICL material and in GaSb. *A:* Shows the vertical photoresist mask from SU8 photolithography. *B:* Shows the dry etching process in GaSb material with the etching mask still on.*C:* Depicts the dry etching process in ICL material, with the etching mask removed.

choice of mask is not the limiting factor in etching vertical sidewalls and it has to do with the SL cladding material. We conclude that photolithography optimization can be done using GaSb substrates while the etching optimization must be done on ICL material.

4.2.2 Dry etching optimization on ICL material

In order to improve the uniformity of the photoresist for a dry etching study, a large sample of ICL material was used to expose the pattern and was then cleaved into smaller pieces. Table 4.1 details the different recipes that were used to try and improve the angle of the sidewalls. The first four recipes follow the mesa dry etching recipe for the FP ICLs, while the last three return to the simple recipes explored in Sec. 3.3.1. The following recipe changes were made:

- Recipe 1 is the FP mesa etching recipe and served as the reference to the other parameter changes.
- Recipe 2 shows a change in the flow rate of the gases; trying to decrease the amount of physical etching.
- Recipe 3 increases the substrate temperature by 10 °C to improve etch product volatility.
- Recipe 4 doubles the ICP power to increase the etch rate.
- Recipe 5 uses only BCl_3 and an increased RF power to improve the angle of the walls.
- Recipe 6 uses only BCl_3 again but an increased RF power and chamber pressure with the expectation the walls would be more angled. This was done to show a contrasting effect to understand the behaviour.
- Recipe 7 uses a BCl_3 : Ar mixture with a flow rate of 4 : 2 and an increased RF power.

The first 4 recipes were tested on the same sample while the last 3 recipes were tested on a different sample.
The results from these recipe changes can be seen by viewing the cross section of the slots in Fig. 4.12.

Recipe	Gases	Flow Rate	Pressure	RF	ICP	Temp	Etch Rate	Angle
1	BCl_3:Cl_2:Ar	4:2:6.5	1.5	60 W	300 W	25 °C	280	113°
2	BCl_3:Cl_2:Ar	6.5:2:3	1.5	60 W	300 W	25 °C	290	111°
3	BCl_3:Cl_2:Ar	4:2:6.5	1.5	60 W	300 W	35 °C	280	114°
4	BCl_3:Cl_2:Ar	4:2:6.5	1.5	60 W	600 W	25 °C	440	113°
5	BCl_3	4	1.5	75 W	300 W	25 °C	250	115°
6	BCl_3	4	3.0	75 W	300 W	25 °C	220	119°
7	BCl_3:Ar	4:2	1.5	75 W	300 W	25 °C	270	116°

Table 4.1: Dry etching recipes that were explored to optimize the etch profile of the slots. The flow rates are given in sccm, the pressure is in mTorr, and the etch rate is in nm/min.

Fig. 4.12A shows the typical profile of the photoresist before opening the Si_3N_4 hard mask, the angles measured were between $100 - 115^o$. Fig. 4.12*B-E* correspond to the results from recipes $1 - 4$. The hard mask was left on in these images to have an idea of the mask profile after etching. The measured sidewall

angles listed in Table 4.1 indicate that changing these parameters did not lead to any appreciable changes in the etching profile. Perhaps this means that the variables were not changed enough or perhaps this means that the wrong variables were changed. The slots were etched into the substrate with around 110°regardless of the etching recipe used. The only big change observed was due to the increased ICP power, though this didn't improve the etch profile. The bottom of the slot also had a curved profile for these recipes which could induce more losses or reduce their effectiveness. Fig. 4.12*F-H* show the results from recipes $5-7$. Between these tests, recipes 5 and 7 have slightly more vertical walls, though a large difference is not observed. The sidewalls were smoother for these recipes that didn't include Cl_2. Indeed, the higher chamber pressure increased the sidewall angle and perhaps adding Ar erodes the photoresist more quickly leading to a larger angle. A similar recipe 7 would be implemented in the first laser fabrication because of the smoothness and higher selectivity due to the higher material etch rate, but with a reduced chamber pressure based on the results from recipe 6.

The ICL material did not respond to the dry etching parameter changes in the same way as GaSb, likely because the different constituent compounds in the SL (AlSb and InAs) form different etch products and/or have very different physical properties. However, using the same etching recipe with hard mask has been proven to give vertical sidewalls in larger features in the high Al content bulk AlGaAsSb cladding[40]. We hypothesize this is because the decreased selectivity in the small slots results in more difficulty removing the etch products. Angled sidewalls will reduce the reflectivity strength of the slot pattern, but as long as the period is correct it is suspected the waveguide should still suppress the unwanted cavity modes.

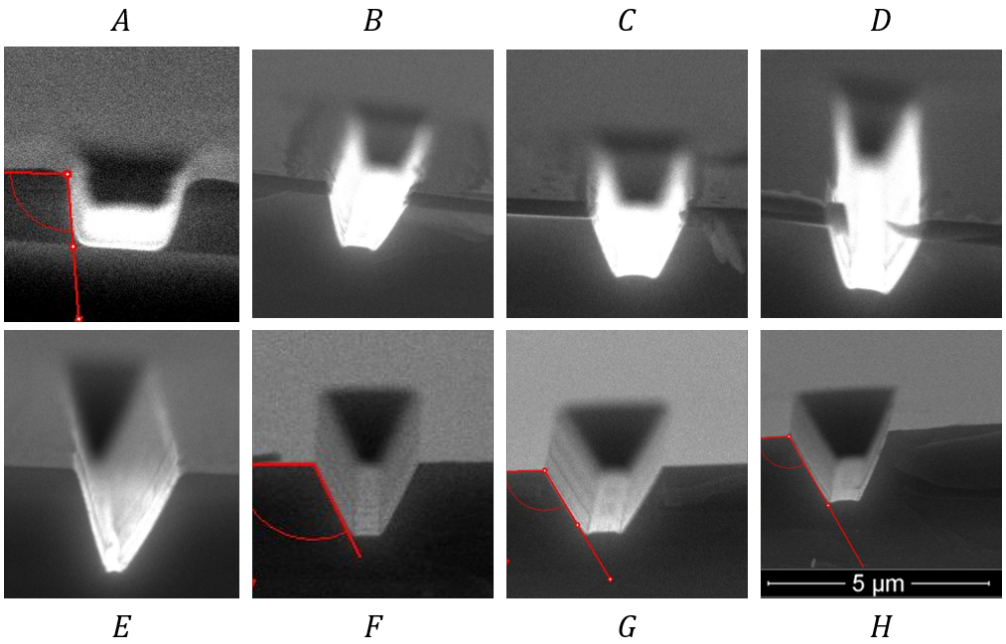

Figure 4.12: Altering parameters of the FP ICL dry etching recipe. *A:* Etch mask *B:* Recipe 1 (FP ICL) with hard mask *C:* Recipe 2 *D:* Recipe 3 *E:* Recipe 4 *F:* Recipe 5 *G:* Recipe 6 *H:* Recipe 7

4.2.3 Slotted ICL fabrication

After the optimization of the photolithography on GaSb and the dry etching recipe study on ICL material, the process was realized on C1661, with emission at 3.5 µm. Devices were fabricated by defining the slots first and then following the FP ICL fabrication steps.

Cleaning and hard mask deposition

The sample is cleaned in a bath of acetone, IPA, and then water before being dried with N_2 gas. The surface is treated by exposing it to an O_2/Ar plasma for 5 min before a Si_3N_4 hard mask is deposited on the ICL sample using PECVD. The target mask thickness is 550 nm for etch depths of 0.9 µm.

Photolithography

After hard mask deposition, AZ 1505 is spun onto the surface at 2000 rpm to achieve a thickness around 1.5 µm. The edge bead is removed by taping the sample to a carrier wafer before spin coating to allow the resist to flow down the tape[153]. The soft bake is carried out before the tape is removed for 45 s at 100 °C. The tape is removed and the sample is left to rest for 5 min. The pattern is exposed to the resist in vacuum contact for 19 s before development in AZ726 for 20 s. Finally, the resist is hard baked for 50 s at 115 °C. The cross section of the slots in the resist is shown in Fig. 4.13A. The target slot width was 1.2 µm and the resolution achieved was typically 1.1 µm to 1.3 µm.

Dry etching

The hard mask is opened using a fluorine-based dry etch optically monitoring the Si_3N_4 thickness where the edge bead was removed. The slot pattern is transferred to the ICL sample using the $BCl_3 - Ar$ dry etch recipe detailed in Table 4.2. The etch depth cannot be precisely controlled due to small size of the slots, so we can only ensure the etch is in an appropriate range indirectly by controlling the etch time ($\approx$1 µm). The cross section of the etched slots is shown in Fig. 4.13B. The sidewall angle was $\approx 110^o$ and the bottom of the slots had widths between 0.9 µm to 1.2 µm while the top of the slots had widths 1.5 µm to 2.0 µm when the target slot width was 1.2 µm. Etch depths between 0.7 µm to 1.9 µm was obtained for etch times between 4 min to 7 min, as can be seen in Fig. 4.13C. These values are measured from the cross section of slots in a nearby 100 µm ridge.

Parameter	Slot recipe
Gas Composition	BCl_3:Ar
Flow Rate	4:2 sccm
Process Pressure	0.8 mTorr
RF Power	75 W
ICP Power	300 W
Bias	254 V
Table Temp	25 °C
Typ. Etch Rate	250 nm/min

Table 4.2: Final dry etching recipes used in the slotted ICL fabrication.

Mask removal and cleaning

The residual photoresist is removed by submerging the sample in a bath of acetone, IPA, and then water before being dried with N_2 gas. The hard mask is completely removed using the same fluorine-based dry etch. The surface is prepared for the mesa photolithography using an acid dip of 35 s in diluted HCl.

Fabrication continues following the procedure for FP ICLs. This starts with the definition of the mesa: narrow ridges of 8 µm, 10 µm, and 12 µm to sudy CW operation. The mesa with respect to the slots is shown in Fig. 4.13C after dry etching the mesa. Fig. 4.13*D* shows the cross section of the mesa after top contact deposition, where angled sidewalls are still observed. Fig. 4.13*E* and *F* show the slots after top contact deposition. Resist remains in the slots after the exposure during the isolation layer photolithography, preventing Au from being deposited to the bottom. Following the normal substrate thinning, lasers of lengths between 1 mm to 2 mm are defined by cleaving facets. These are then mounted epi-side up to a copper heatsink.

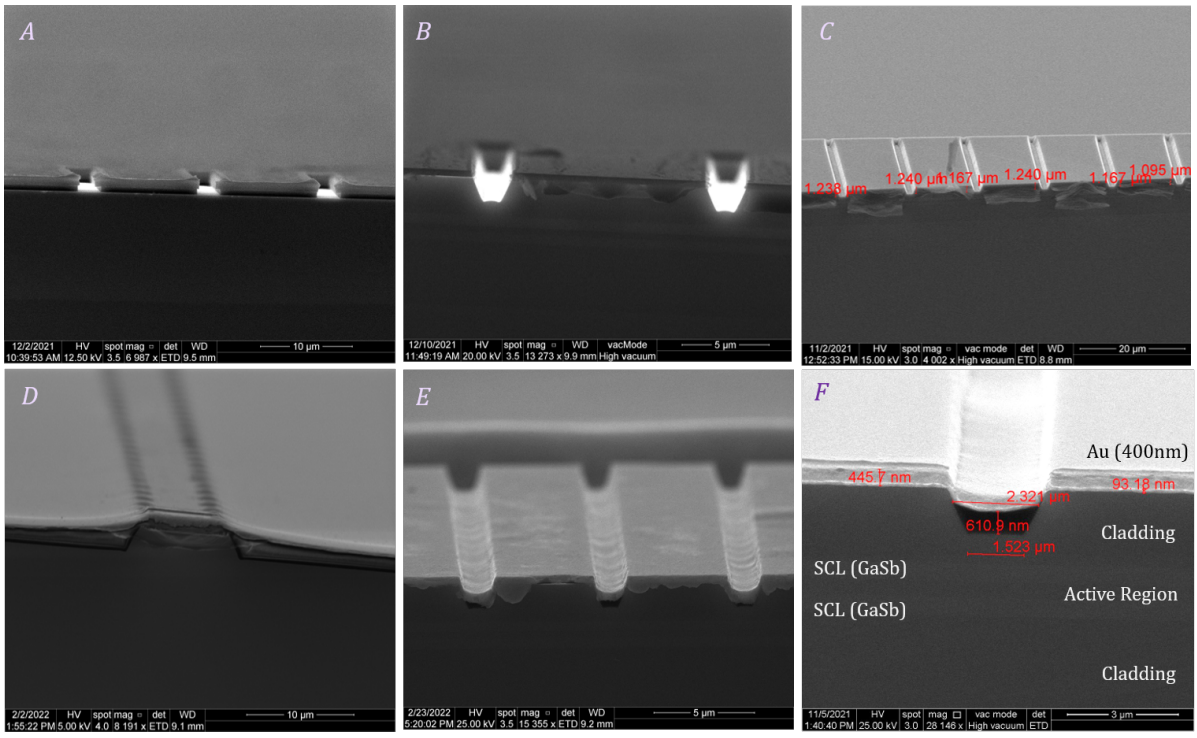

Figure 4.13: Slots and mesa profiles at various stages of the process. *A:* Shows the slot openings in the etch mask. *B:* Shows the slots after etching the cladding layer, with the hard mask still on the sample. *C:* Shows a cross section of the slots in the ridge before metallization. *D:* Shows the cross section of the mesa after metallization. *E:* Shows the slots after metallization. *F:* Shows a close up of the slot after the process is complete.

4.3 Slotted ICL Performance

The electro-optic characterization of the slotted ICLs at bar level was measured using the same set up as for the FP ICLs. A series of operating conditions were studied in order to understand the range of

single-mode operation. Current was injected through the top contacts of the lasers and the output from one of the facets is monitored by a power meter or directed into a spectrometer. All of the slotted ICL facets were left uncoated, so the power reported is the power/facet.
The first slotted ICLs were fabricated on C1661 whose emission was centered at 3.53 µm and the results presented below are for slots with d =6.68 µm and d_s =1.2 µm. One fabrication run of the d =13.1 µm was attempted for t_E =1.2 µm but the emission was all multi-mode, as could be expected from Fig. 4.6. Therefore, only d =6.68 µm was explored to investigate the performance.
For each process run, hundreds of lasers are fabricated from each sample and many of these are then tested. Each process run will have some variation due to inconsistencies between separate fabrication processes which can make it difficult to find trends in the behaviour as many statistics are needed to account for the large variance. Results from selected lasers are presented that summarize the performance.

4.3.1 Comparison to FP ICL Performance

The PIV curves of a FP ICL and slotted ICL are compared in Fig. 4.14 for lasers with ridge widths of 8 µm and lengths of 1.6 mm and 1.8 mm for the FP ICL and the slotted ICL, respectively, at 20 °C[154] with t_E =1.0 µm. As expected I_{thr} increases from 55 mA for the FP ICLs to 80 mA for the slotted ICLs. I_{max}, P_{max} occurs at 130 mA, 11 mW for the FP ICLs and 160 mA, 5 mW for the slotted ICLs. The V_{OC} of the FP ICL and the slotted ICL were 3.6 V and 3.1 V, respectively. The R_s of the FP ICL is 11.5 Ω and only 8.3 Ω for the slotted ICLs. These are typical values for devices with good performance and the difference is probably due to process variation or a slight difference in the thermal management of between the different devices. The overall performance illustrated by the PIV curves ensures the fabrication process for both devices was successful.

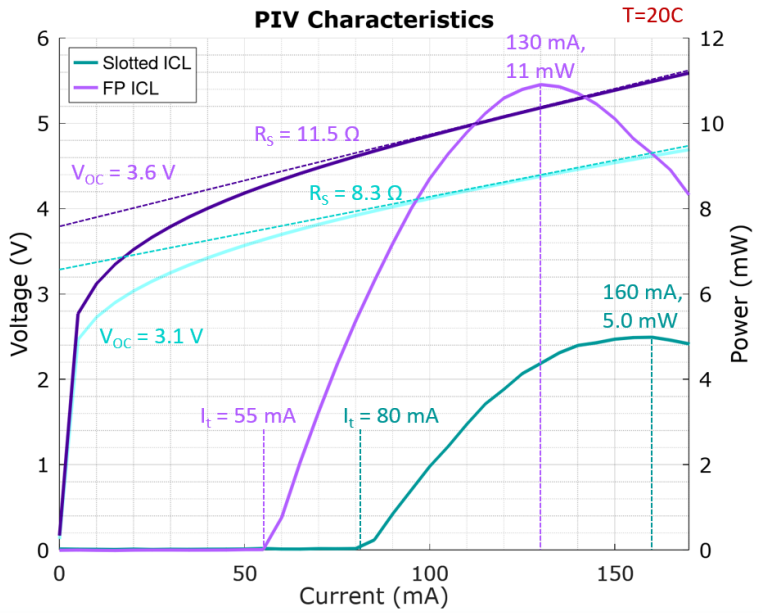

Figure 4.14: PIV curves of a FP ICL and slotted ICL are shown at 20 °C in CW operation for lasers with a 8 µm wide mesa. The FP ICL has a length of 1.6 mm while the slotted ICL has a length of 1.8 mm. The slots were etched with t_E =1.0 µm.

The important figure of merit to confirm the successful design of the slotted ICL waveguide is the SMSR. Fig 4.15A confirms the stable single-mode operation of the slotted ICL in comparison to the FP ICL at their respective I_{max} 130 mA and 160 mA at 27 °C. Even partial success of the design is confirmed at other operating conditions, such as those shown in Fig. 4.15B, where the FP ICL spectra is narrowed down to only 5 modes at 21 °C. The PI curves are quite different between the FP ICL and the slotted ICLs which makes difficult to compare identical operating conditions for the spectra. For example, I_{max} of the slotted ICLs is well past the rollover point of FP ICLs and operating the laser past this point can lead to non-trivial pumping of modes, as previously observed in Sec.3.4.2. This can explain the difference in central wavelengths, since different operating conditions can cause a different local temperature of the active region and alter the index of refraction. Comparing the lasers at the same relative position with respect to the rollover point and threshold current is the best we can do.

The other factor to consider is the shape of the gain curve since it is not flat and can change shape as the injected current changes. Perhaps the overlap of the reflectivity peak with the absolute minimum of the loss curve is not perfect and when it overlaps with a nearby local minima, we can have single-mode emission but also enough gain that the FP modes are above threshold. Potentially the increased heating of the active region helps to suppress the modes near the reflectivity peak or the cavity mode becomes more aligned with the reflectivity peaks of the slots leading to single-mode emission, supported by the increasing SMSR of some devices. The 8 µm ridge width may also be wide enough to support higher order transverse modes at this wavelength, but a method for measuring the far field beam spot was not available. The spectral envelope of emission is significantly narrowed for the slotted ICL indicating some coupling of the slots to the active region even though the suppression isn't optimal.

4.3.2 Dependence on etch depth

For the different etch depths investigated over four process runs, single-mode emission was measured under all expected the deepest slots. The slot depth was indirectly inferred by measuring the slot depth

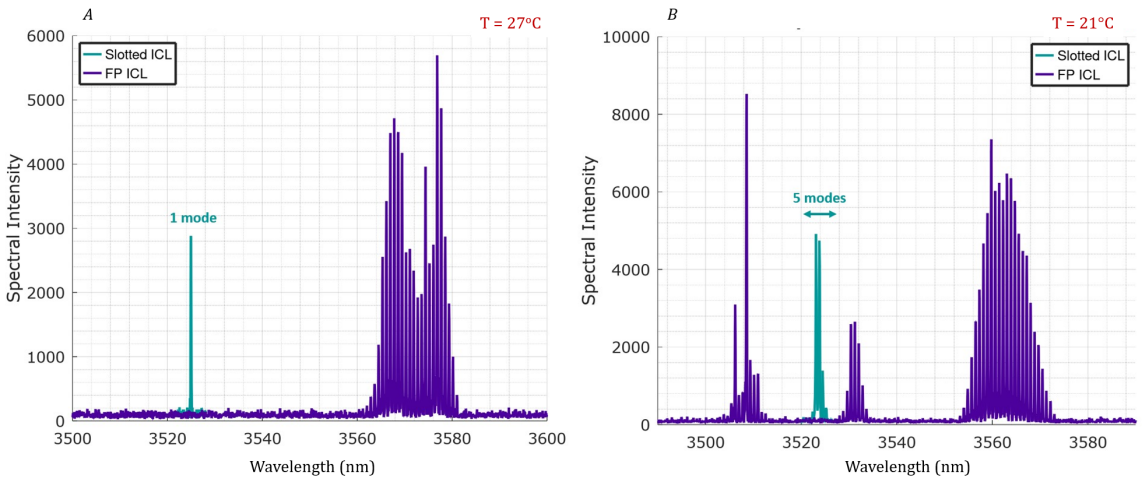

Figure 4.15: Comparison of the spectra between the FP and slotted ICL in CW at their I_{max} currents and heatsink temperatures of *A:* 27 °C and *B:* 21 °C.

from a cleaved 100 µm ridge near the sample edge. Etch depths of 0.8 µm, 1.0 µm, 1.2 µm, and 1.9 µm were fabricated to study the influence of the slot interaction on the modes from the FP cavity. The slotted ICL with t_E =0.8 µm is 1.8 mm long and the spectrum is taken at 21 °C and 145 mA. The slotted ICL with t_E =1.2 µm is 1.6 mm long and the spectrum is taken at 23 °C and 145 mA. The slotted ICL with t_E =1.0 µm is 1.8 mm long and the spectrum is taken at 30 °C and 180 mA. The slotted ICL with the deepest slots of 1.9 µm did not lase, but had IV curves indicating high processing quality, similar to the other slotted ICL fabrications.

We posit that this means that the losses from etching entirely through the upper cladding were too great to be compensated for with the gain of the active region. The spectra from the operating points resulting in the best SMSR are presented in Fig. 4.16. The shift in spectral lines are likely due to the different operating temperatures and injected currents, as well as variations from different process runs, though the threshold currents and output power for all of these lasers were comparable.

4.3.3 Wavelength tunability

The PI measurements for a 8 µmx1.8 mm slotted ICL is shown in Fig. 4.17 in CW mode for several heatsink temperatures. The maximum operating temperature for this device was 23 °C. The threshold current at 20 °C is 88 mA and the maximum output power is 2.2 mW/facet. The IV curves are shown in the inset figure and do not vary appreciably. The V_{OC} was 3.3 V and R_s was 8.5 Ω.

T_0 is measured from temperature series measurements of I_{thr} using Eqn. 2.17 to be 23 K for this growth. This is lower than what was measured for the FP ICLs and is reflected in the reduced range of operating temperatures. We expect that the reason for this is extra heating induced by the losses from the slots and a non-optimal process resulting in poor thermal management. However, the growth and process were of

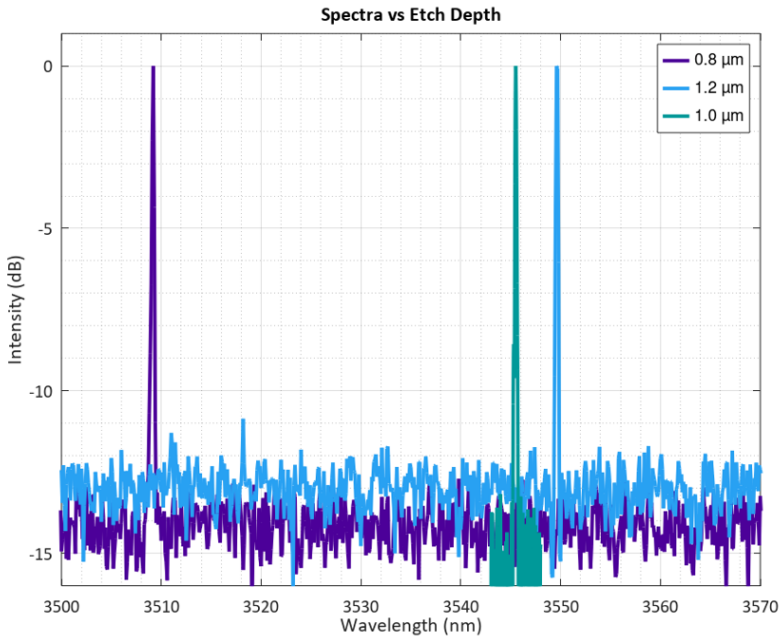

Figure 4.16: The spectra for slotted ICLs with different etch depths are presented at conditions were single-mode emission was observed.

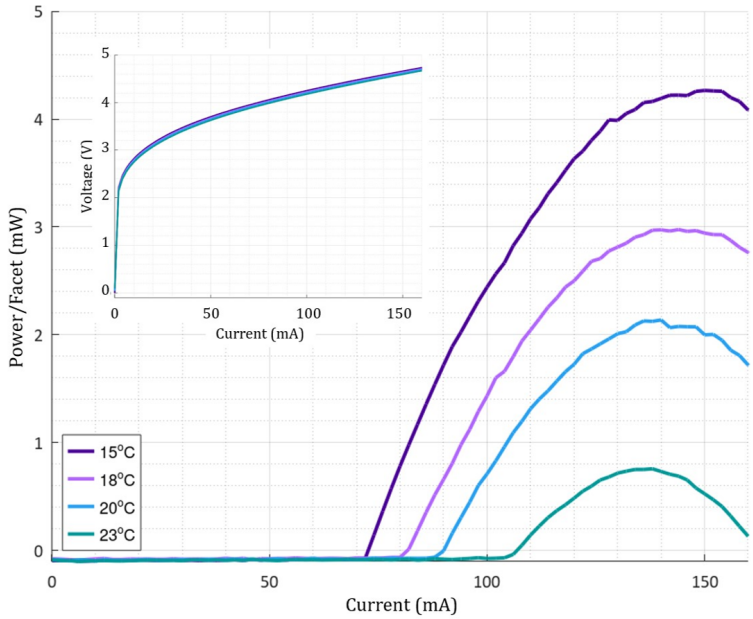

Figure 4.17: The temperature dependence of the PI curves a slotted ICL are shown in CW operation for lasers with a 8 µm wide mesa and a length of 1.8 mm with the IV curves shown in the inset figure. The slots have t_E =1.0 µm.

sufficient quality to observe lasing and to investigate the electrical and thermal tuning properties.

Over the range operating conditions investigated, what was typically observed is presented in Fig.4.18. Some regions of operation lead to multi-mode emission that would transition to regions of single-mode emission, likely as alignment of the slot FSR to the FP modes was optimized. This can be seen in Fig.4.18A at 20 °C as the current is adjusted around I_{max}. Below I_{max} at 118 mA multi-mode emission is observed, though some suppression occurs from what is expected from a FP ICL. At I_{max} (140 mA) the emission

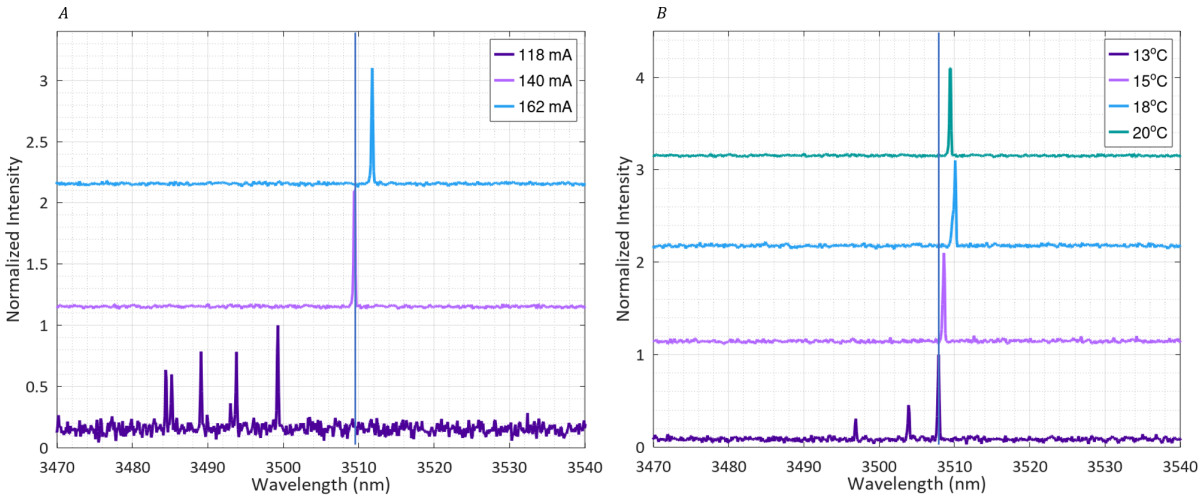

Figure 4.18: The emission of a slotted ICL with t_E =0.8 µm over a series of different operating conditions.*A:* The temperature is fixed at 20 °C and I is varied from below I_{max} to I_{max} and above I_{max}. *B:* The current is fixed at I_{max} for the temperatures between 13 °C to 20 °C.

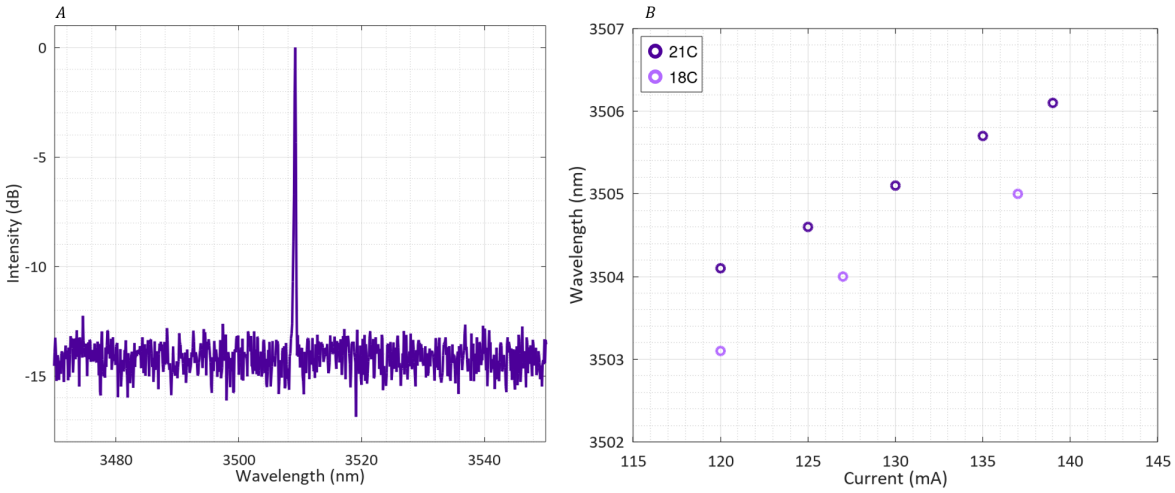

Figure 4.19: *A:* The spectra for the slotted ICL at 20 °C and $I = I_{max}$ is plotted. *B:* The wavelength tuning for $I_{Th} < I < I_{max}$ at two different temperatures is plotted for when single-mode emission was achieved.

becomes single-mode and remains that way past the rollover point to 162 mA. In Fig.4.18B the temperature is adjust with the current set to I_{max}. Multi-mode emission is observed at 13 °C and is single-mode for 15 °C and 20 °C. At 18 °C emission peak broadens and it likely that this is due to a second peak appearing under the slot reflectivity peak that was not resolved by the spectrometer. The second peak could appear if the slot reflectivity peak has a FWHM$\approx C_{FSR}$. This would explain the wavelength shift of 18 °C past the emission at 20 °C.

The slotted ICL with the widest range of singe mode operation had t_E =0.8 µm. The best SMSR was achieved was 13 dB at 20 °C near I_{max} for this device (at 145 mA), as shown in Fig. 4.19A. The electrical tuning is presented in Fig. 4.19B over the range where stable single-mode emission and predictable tuning could be expected for $I_T < I < I_{max,Slot}$. At 21 °C and 18 °C wavelength tunability of $\approx$0.1 nm mA^{-1} was measured, with the SMSR improving from $\approx$8 dB at 120 mA to $\approx$12 dB at 139 mA[154].

The SMSR of this slotted ICL is lower than what is reported from commercially availabe DFB ICLs. However, these measurements were conducted using an imaging spectrometer with slits and gratings, which lead to a high noise floor due to scattering and a decreased single due to beam divergence and input coupling issues. This leads to a reduction in the dynamic range in comparison to an optical spectrum analyzer that includes narrow optical filters to improve the dynamic range as is typically used. Consequently, this means our measurements represent a minimum SMSR of the device.

Conclusion

This chapter presented the design, fabrication, and testing of the first slotted ICLs created using GaSb materials. Simulations of the waveguide were conducted to determine the best geometry of the slots that were subsequently patterned on ICL mesa ridges using standard UV photolithography and dry etching. The material model used for FIMMWAVE simulations has been verified to yield a functional waveguide design. Because the devices fabricated were indeed single-mode, an empirical link to a gain margin given

by $R < 1\%$ was established for the passive simulations. Single-mode emission was demonstrated for a 1.8 mm long and 8 µm wide laser in CW mode around 20 °C with a wavelength tunability of $0.1\,\mathrm{nm\,mA^{-1}}$, a threshold current of 88 mA and a maximal output power of 2 mW per facet. The $\Delta\lambda$ achieved was a continuous 2 nm shift of a single-mode at 18 °C and 21 °C. Even when multi-mode emission was measured, some distributed feedback reduced the number of modes lasing with respect to a FP ICL. The performance validates the integration of a slotted waveguide with ICL architecture emitting at λ =3.5 µm.

CHAPTER 5

Improvement of slotted ICL fabrication and performance

The performance of the first slotted ICLs was an important starting point for optimization indicating which design assumptions were confirmed and which should be explored further. The threshold current, the maximum operating temperature, and the output power could all afford to be improved, pointing towards the need for loss reduction and better thermal management from the fabrication. The length of the devices were shortened from 2 mm to 1.8 mm to achieve single-mode emission, so shorter devices will be pursued in the next iterations. As well, a starting etch depth was established and will target $R < 1\%$ given the number of slots expected from the device length.
Improving the slotted waveguide process will occur on different growths and will test the larger slot period on the masks at 3.3 µm and 3.4 µm. This will further verify the efficacy of the design. The process optimization occurred in two different clean rooms from the first development of the slotted ICLs. The second iteration of slotted ICLs were developed at the company nanoplus, making use of their expertise in DFB ICL fabrication[5]. The third iteration of slotted ICLs was developed at the Tyndall National Institute, making use of their expertise in slotted waveguides[155].
The main goal of the next process developments was to improve the power output, SMSR, and tuning range. The photolithography and dry etching steps of the microfabrication were adjusted in order to realize more ideal slots in order to contribute less losses to operation. This involved decreasing the slot width and making the slots with vertical sidewalls. To extend the range of conditions that yield single-mode emission, the FWHM is narrowed with shallower slots. The FWHM should be <1.5 nm and the etch depth can be decreased from t_E =1 µm.

5.1 Second iteration of slotted ICLs

The second slotted ICLs were developed on C1665 with emission around 3.4 µm. In order to realize single-mode emission, the long period slots with d =13.1 µm were implemented. Despite the dry etching challenges encountered during process 1, commercially available ICLs are etched with vertical

sidewalls[19, 81]. With a similar dry etching recipe for the second process development, similar results are expected. The details of the recipe and the layer thicknesses are not disclosed since they are confidential to nanoplus. The main objectives of the changes made to the design and process were to increase the SMSR and output power of the laser. The effects of making small adjustments to the slot period and improving the profile of the slots were studied to address these objectives.

5.1.1 Slot process optimization

This section will outline the differences from process 1 described in Sec.4.2.3 that will be implemented based on the slotted ICL performance and the DFB expertise of nanoplus. This includes modifications to the mask design and improvements in the slot photolithography.

Mask Design

The design changes to the mask layout include:

- Mesa widths decreased to between 1.3λ and 2λ: 5 µm, 5.8 µm, 6.6 µm[88]
- The slot period was iterated across the mask: d =13.1 µm was varied between 12.8 µm to 13.3 µm in increments of 0.1 µm
- The targeted slot width was decreased to d_s =1.0 µm
- Testing sections for monitoring the dry etching quality were added
- The slot width lengths were increased to be larger than the mesa widths
- Narrow ridge FP ICLs were added for reference

The mesa widths were decreased to ensure transverse single-mode emission, however some widths of 8 µm, 10 µm, and 100 µm were kept for comparison to the first slotted ICLs. The iterations of the slot period were implemented to increase the likelihood of optimal overlap of S_{FSR} with the gain bandwidth of the growth. The slot width could be decreased using standard UV photolithography by using a smaller target; d_s =0.7 µm was used to obtain 1.0 µm. The dry etching test sections for the slots and mesa were added to allow the sample to remain in tact, as opposed to cleaving ridges and risking damaging the sample. Making the slots longer than the mesa is a design consideration commonly implemented to reduce the need for precise alignment between photolithography steps.

Photolithography

Each of the photolithography steps were accomplished using contactless photolithography. This technique uses a laser and spatial light modulator to raster scan the pattern onto the photoresist[156]. The advantage of using this technique was increased flexibility in testing different slotted waveguide designs; designs could be altered for each process run. As well, the edge bead was no longer an important factor in the final resolution that was achieved. The disadvantage was that the automatic alignment is not as accurate as manual alignment and this error propagates to subsequent layers. A high resolution photoresist was used for the slot process and a more dry etch resistant photoresist was used for the mesa process.

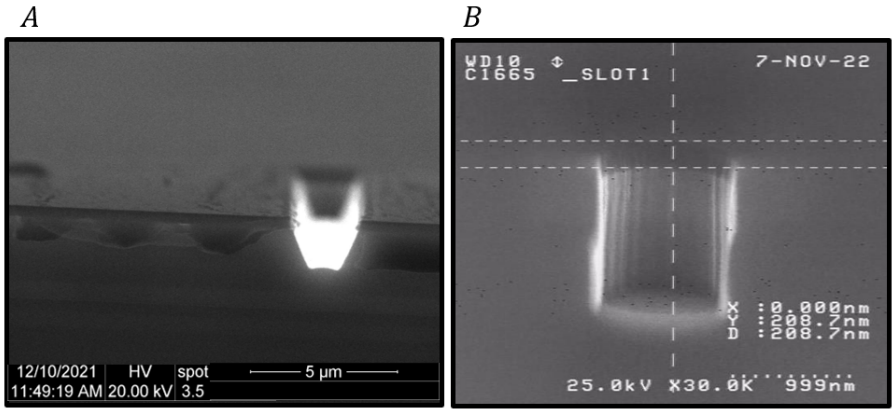

Figure 5.1: SEM images comparing slot etching on ICL samples. *A:* Slot recipe 1, taken from a cross section of a cleaved 100 µm ridge. *B:* N+ recipe, taken from a slot test section.

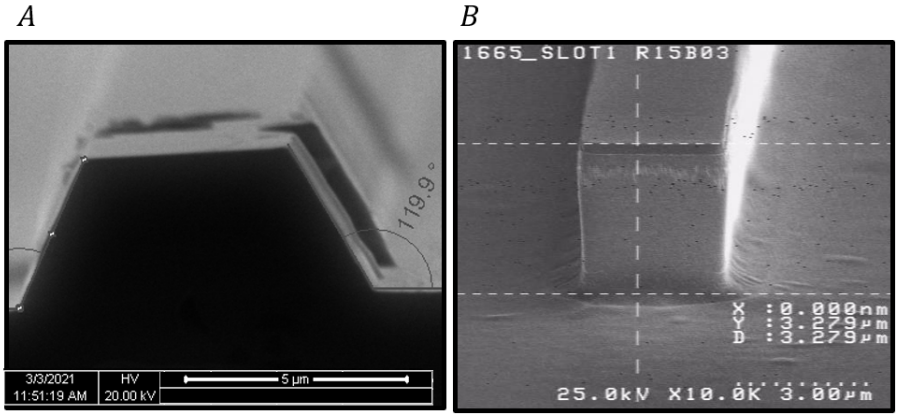

Figure 5.2: SEM images comparing mesa etching on ICL samples. *A:* Slot recipe 1, taken from a cross section of a 8 µm ridge. *B:* N+ recipe, taken from a mesa test ridge.

5.1.2 Initial dry etching process

The recipe used to etch the mesa for DFB lasers was implemented for slot etching and mesa etching for an initial starting point for further optimization. This is a high temperature Cl_2/Ar recipe, referred to as the N+ recipe, and is compared to the process 1 recipes, referred to as slot and mesa recipe 1.
The slot dry etching is presented in Fig. 5.1, with slot recipe 1 shown in Fig. 5.1A and the N+ recipe shown in Fig. 5.1B. Both images have the hard mask still on the sample. The slot walls are completely vertical using the N+ recipe. The walls appear to be rougher than what is generally observed from slot recipe 1. Additionally, there is a jump near the middle of the N+ slot, but this happens because of the stepper motor.
The mesa dry etching is presented in Fig. 5.2, with mesa recipe 1 shown in Fig. 5.2A and the N+ recipe shown in Fig. 5.2B. The mesa are trapezoidal and some ripples are observed along the ridge using mesa recipe 1, with some defects near the cross section from cleaving, while they are vertical and smooth, except near the top of the ridge, using the N+ recipe.

From these initial results, we can conclude that the key parameter in obtaining a vertical etch profile is the etch temperature. This is because a higher temperature increases the rate of surface reactions and the volatility of InClx etch products, which are difficult to remove[157].
Although the etch profile was improved, a defect was observed at the slot-mesa ridge boundary that we refer to as "wings", shown in Fig. 5.3. This was an unforeseen consequence of making the length of the slots larger than the mesa width. Fig. 5.3A shows the slot-mesa boundary from the process 1 when there was slight misalignment of the mesa mask and the slots protruded from the mesa, but no wings were observed. Fig. 5.3B shows the slot-mesa boundary from the new process where wings are observed that are over 2 µm high. These wings could cause shorts, since it may be difficult to ensure they are completely covered by the isolation layer and they have a direct connection to the active region. Methods for avoiding or minimizing these features will be discussed in the following section.

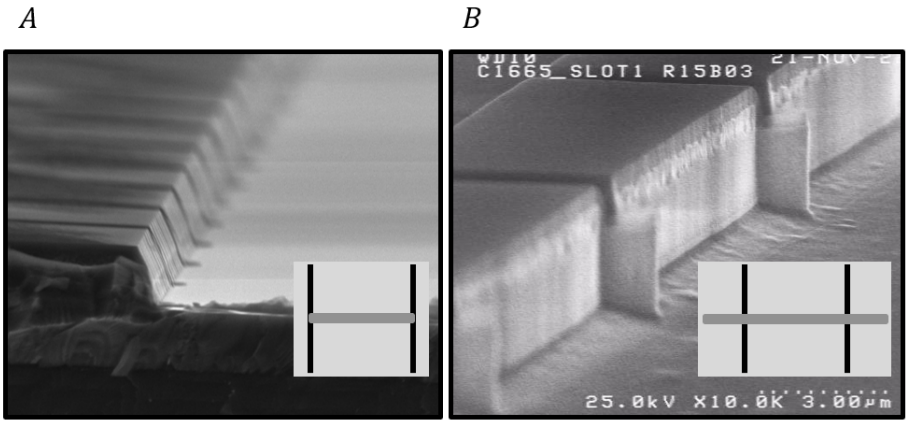

Figure 5.3: SEM images comparing slot-mesa layouts. *A:* Slot lengths are the same size as the mesa width. *B:* Slot lengths are larger than the mesa widths.

5.1.3 Dry etching optimization for wing reduction

To understand the formation of the defects, the dry etching recipe was altered in an attempt to remove or reduce the wings. We hypothesized that the wings formed due to plasma charging at the boundaries, or similar corner effects that affect local etching conditions.
This study was carried out on test material from nanoplus, which was an ICL growth that did not lase. One 11 mmx10 mm sample was prepared to the step before mesa dry etching. It was subsequently cleaved into four pieces so that four variations of the N+ recipe could be investigated from the same starting conditions. The parameters varied included: the pressure, the Cl_2 flow rate, and the Ar flow rate. Increasing/decreasing the chamber pressure was meant to increase/decrease the proportion of chemical etching, respectively. Increasing the flow rate of Ar was meant to increase the amount of physical etching. Increasing the flow rate of Cl_2 was a different method to increase the amount of chemical etching. The different recipe variations are summarized in Table 5.1. We anticipated that the changes that increased the amount of chemical etching would have the best results, with the increased chamber pressure being the easiest way since the quality of the dry etch is quite sensitive to the flow rate of Cl_2[158, 159].

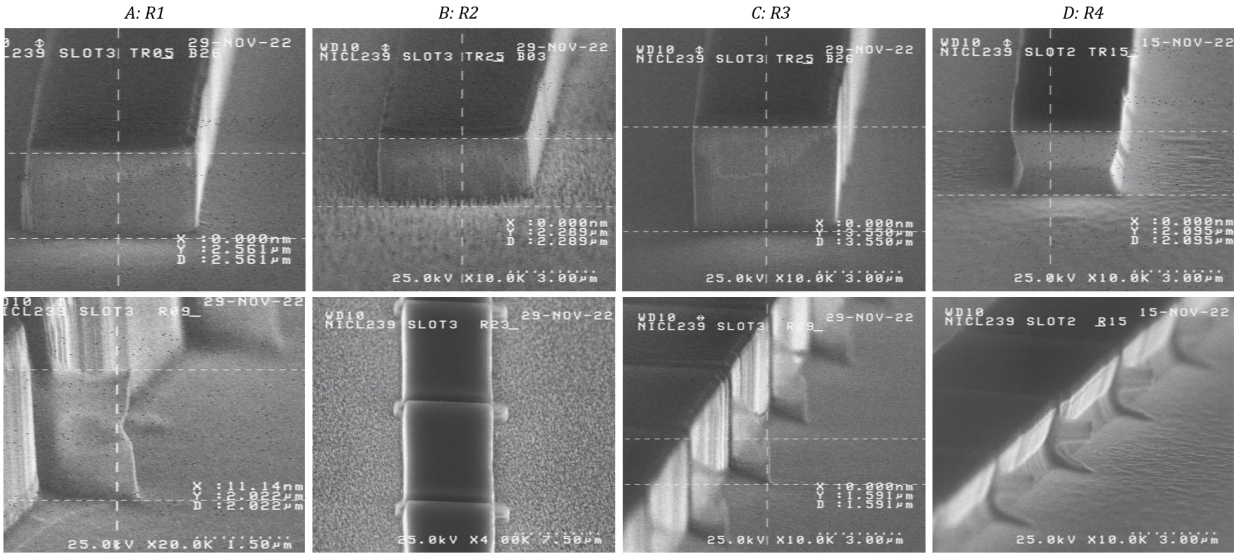

Figure 5.4: SEM images from the mesa cross section and slots > mesa width profiles are shown, from top to bottom. *A:* Effects of recipe 2, decreasing the pressure, are depicted. *B:* Effects of recipe 3, increasing the Cl_2 flow rate, are depicted. *C:* Effects of recipe 4, increasing the pressure, are depicted.

The result of the dry etching variation study is presented in Fig. 5.4 with the top row showing the cross section of the mesa ridge and the bottom row showing a view of the resulting wings. For reference, in the N+ recipe the mesa height was 3.1 µm and the wing height was 2.7 µm. Fig. 5.4A depicts the results from increasing the Ar flow rate. The mesa height was 2.6 µm and the height of the wings was 2.0 µm. The relative height of the wing with respect to the mesa did not decrease with the lower etch rate. Qualitatively, the wings appear to be less solid. Fig. 5.4B depicts the etch quality when the chamber pressure is lowered. The mesa height was 2.3 µm and the height of the wings was approximately 1.4 µm. The biggest change for this etch is the formation of "grass" (the needle like structures) on the surface, likely due to micromasking at the lower pressure[160]. The formation of grass is problematic for the metallization deposition, as it may not be covered completely. Fig. 5.4C shows the etch change from increasing the flow rate of Cl_2. The mesa height was 3.6 µm and the height of the wings was approximately 1.6 µm. Wings are still observed though they appear to be less stable/more transparent while the sidewall angle of the mesa remains unchanged. Likely this effect occurs because of an increased lateral etch due to the isotropic nature of chemical etching[137]. Fig. 5.4*D* shows the etch change when the chamber pressure is increased. The mesa height was 2.1 µm and the maximum height of the wings was 2.0 µm. The amount of chemical etching increases a lot, which is evident from the undercut in the mesa sidewalls. This amount

Recipe	Cl_2 flow rate	Ar flow rate	Chamber pressure	Etch time
R1	same	increase	same	30 min
R2	same	same	decrease	30 min
R3	increase	same	same	30 min
R4	same	same	increase	30 min

Table 5.1: The dry etching recipes studied to minimize wing formation.

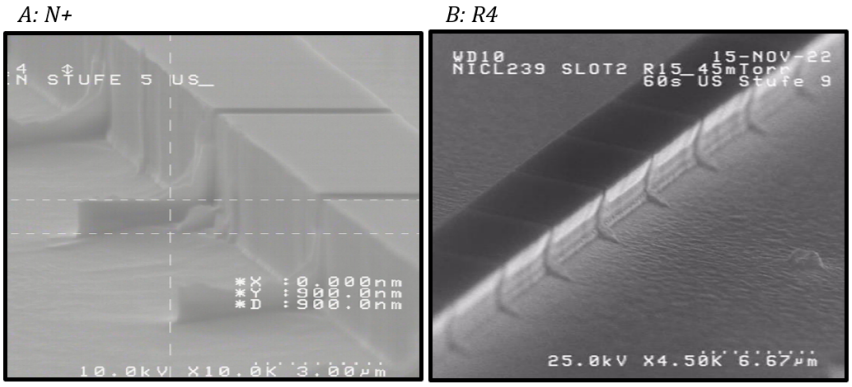

Figure 5.5: SEM images comparing the wings after ultrasonication. *A:* Sample etched with N+ recipe. *B:* Sample etched with R4.

of undercut is too severe for the ICLs, but a great deal of lateral etching is seen in the wings.
These dry etching recipe variations did not manage to eliminate the wings. In an effort to reduce the wings, the samples were sonicated to try and them break off, as shown in Fig. 5.5. Fig. 5.5A shows the sample etched with the N+ recipe after being sonicated. The wings shrank to 900 nm. Fig. 5.5B shows the sample etched with the increased chamber pressure after being sonicated and the top portion of the wing was completely removed.

The increased chamber pressure undercuts the mesa too much for laser ridges. However, increasing the chamber pressure resulted in wings that could be easily broken with sonication after. Therefore, during the C1665 etch a smaller increase in chamber pressure was used; a 25% increase instead of a 50% increase, and the sample was sonicated after. Any residual material could be sufficiently coated during deposition of the isolation layer.

5.1.4 Second slotted ICL fabrication

Upon conclusion of the previous studies the necessary adjustments were made to the process and the second iteration of slotted ICLs were fabricated on C1665. For this fabrication run, slot widths of 1.0 µm were targeted with a nominal slot spacing of13.1 µm and etch depth of 1.0 µm. An overview of the development for process 2 is illustrated in Fig. 5.6. Process 2 is similar to process 1 (purple boxes) with the addition of Au electroplating and AR/HR facet coating steps (blue boxes). The adjustments made to the steps are highlighted in the orange boxes and will be detailed below.

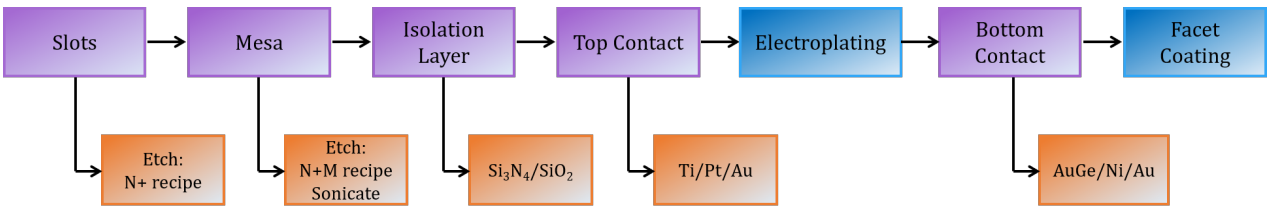

Figure 5.6: Summary of process 2 for the second iteration of slotted ICLs.

Slot definition

A Si_3N_4 hard mask is deposited on the ICL sample using PECVD. The target mask thickness is set for etch depths of 1 µm. Contactless photolithography is performed to define the slot pattern with slot widths of 700 nm in the mask (for 1 µm etched slots). The hard mask is then opened using a F-dry etch. Fig. 5.7A shows an SEM of the slots at this stage with the targeted width of 1.0 µm. The slot pattern is transferred to the ICL sample using N+ recipe with increased chamber pressured. The targeted etch depth was reached with a measured etch depth of 0.98 µm and the sidewalls are vertical, as seen in Fig. 5.7B. The residual Si_3N_4 hard mask is removed via F-dry etching.

Ridge defintion

A thicker Si_3N_4 hard mask is deposited for mesa etching. Mesa ridges, including widths of 5 µm, 5.8 µm, 6.6 µm, 8 µm, 10 µm, and 100 µm are defined with photolithography. The mask is opened using a F-dry etch. Fig. 5.7C shows mesa with a targeted width of 5 µm measured to be 4.8 µm. The mesa are then etched until the start of the second SCL using the N+ recipe with increased chamber pressure. Wings with heights around 2.8 µm formed before sonication broke them down to around 0.9 µm. This process can be compared between Fig. 5.7*D* and Fig. 5.7*E*. The mesa profile is still vertical and smooth. The residual Si_3N_4 hard mask is removed via F-dry etching.

Isolation layer with contact window

The isolation layer was changed from hardened photoresist to a dielectric bilayer of Si_3N_4 and SiO_2. The purpose of this was twofold: for narrower mesa the photoresists will flow into the contact window openings when they are heated and because wire bonding is not possible with hardened photoresist. The top contact metal is pulled off during the wire bonding process and this affects the ability to package working devices.
The Si_3N_4/SiO_2 bilayer is then sputtered on the sample. Photolithography is used to pattern openings on top of the mesa ridges, where the contact window openings are set to be at least 30% of the ridge width (1.5 µm openings for the 5 µm ridges). The contact windows are opened using a F-dry etch.

Top contact and electroplating

A single layer of a thick, negative photoresist is used for lift-off after the top contact is deposited. Photolithogrpahy is used to define patterns of contact pads on top of and beside the ridges. The top contact was modified to the deposition of Ti/Pt/Au. A thin layer of Pt helps improve the conductance of the contact[142]. Thin layers of Ti/Pt and a thicker layer of Au are thermally evaporated on the sample to form the top contact layer. Lift-off in a solvent removes the resist and unwanted metal. Photolithography is used to define the electroplating contact layer. 11 µm of Au is then electroplated on the top contact pads. This improves the heat dissipation and helps to increase the maximum operating temperature, which is extremely beneficial in epi-up mounted devices[161]. A cross section of the ridge after electroplating is shown in Fig. 5.7*F*, though there is some damage to the sample from the cleaving.

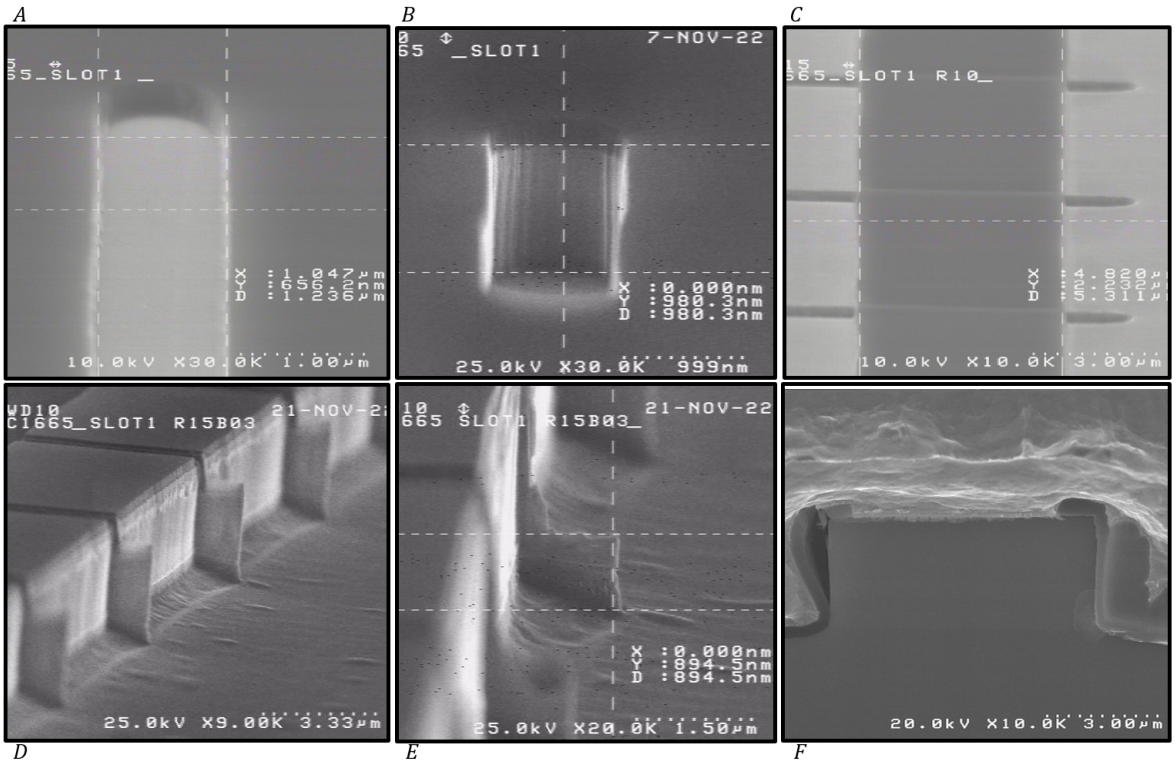

Figure 5.7: SEM images highlighting key features of the process. *A:* Hard mask opening after slot photolithography. *B:* Slot dry etch with hard mask on sample. *C:* Hard mask openings after mesa photolithography. *D:* Mesa dry etch, with wings before sonication. *E:* Wings after sonication. *F:* Cross section of the final device after electroplating.

Bottom contact deposition

The substrate is thinned to <200 µm before the bottom contact is sputtered on. Thin layers of AuGe and Ni are deposited followed by a thicker layer of Au to form the bottom contact. The sample is then annealed in a rapid thermal annealing (RTA) oven under N_2 to ensure an ohmic contact [142].

Cleaving and facet coating

Lengths of 900 µm, 1200 µm, 1500 µm, and 1800 µm are cleaved into bars before their PIV characteristics are measured to ensure no fabrication defects. This is a check before the anti-reflective (AR) and high reflective (HR) coatings are deposited on the facets using ion beam deposition. These coatings enhance the cavity feedback gain and increases the output power from one facet. The AR coating is a thin layer of Al_2O_3 while the HR coating is a metal based mirror. They are then ready for more extensive testing before selecting the best performers for mounting.

5.1.5 Performance of second iteration slotted ICLs

The PIV characteristics of the slotted ICLs were measured with the laser bars placed on the TEC. The measurements discussed here were before the facet coating step.

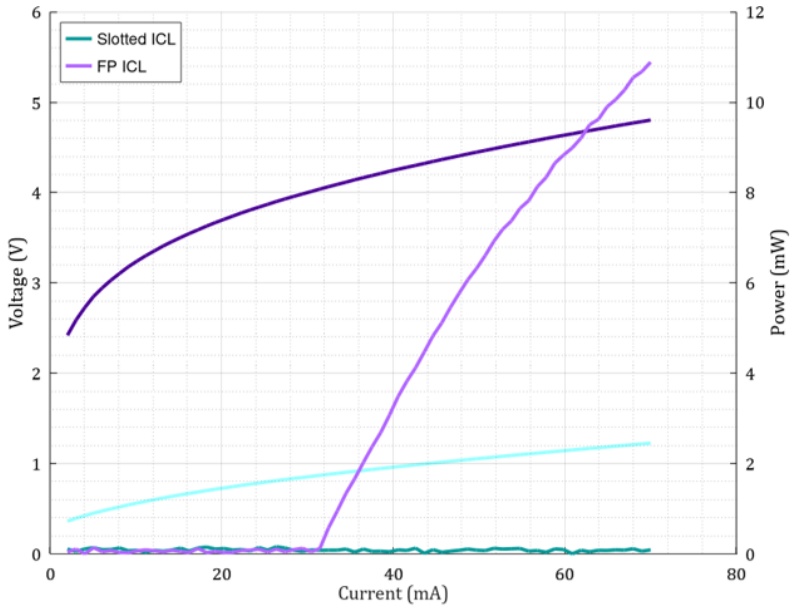

Figure 5.8: PIV characteristics of a slotted ICL and reference FP ICL for L =1200 µm, w =6.6 µm at 10 °C.

The slotted ICLs did not lase but the reference FP ICLs lased, as shown in Fig. 5.8. The purple lines show the PIV performance at 10 °C of a FP ICL with width 6.6 µm and length 1200 µm and the blue lines show the performance from a nearby slotted ICL. The FP ICL reference exhibits typical behaviour; I_{thr} is 31 mA, V_{OC} is 3.5 V and R_s is 7.6 Ω. Meanwhile, the low voltage from the IV curve of the slotted ICL indicate an electrical short. We posit these shorts originate from the wing features and that they were not fully covered by the isolation layer. The total thickness of the passivation layer is between 300 µm to 400 µm whereas the wing height was between 800 nm to 900 nm after sonication was used to break down the wings. Another source of error for the shorts could be from misalignment of the contact window opening with the mesa on the narrow ridges, since the exposed corners of the mesa can lead to shorts and poor current injection due to the current spreading that happens in the SL cladding layer. However, this is less likely since the FP references worked. We did not suspect that the slots were etched too deeply (t_E =1000 nm) since this depth is in alignment with the working devices from process 1.
From these results we can conclude that another slot length-mesa width configuration is needed to avoid wings. In future processes, the slot length will be made to be narrower than the mesa width to allow for alignment. A study was conducted regarding the slot length and is described in App. 7. This will eliminate the need for dry etching optimization to remove the wings or altering the process to do the slot-mesa etch in one step[162]. There may be an analogous defect inside the slots, but this could be an advantage for wider ridges. Defects inside the slot may induce losses to the higher order modes; working as to an "inverted" corrugated ICLs[163].

5.2 Third iteration of slotted ICLs

The third slotted ICLs were fabricated on E802A with emission around 3.3 µm. Wing formation would no longer be an issue because of the return to contact photolithography and the original set of masks.

The long period slots with d =13.1 µm would be used to achieve single-mode emission. GaSb lasers had not been processed in Tyndall before, but GaAs and InP slotted waveguide lasers routinely are, so this expertise would be used to further develop the process[101, 148, 162]. The main objectives of the fabrication changes remained the same: increase the SMSR and output power of the slotted ICLs. The effects of the improved slot profile would be studied to address these objectives.

5.2.1 Photolithography changes

This section will outline some differences in the photolithography for creating the slot and mesa dry etching masks from process 1 and 2 that will be implemented based on the results from these processes. For process 3, new photolithography masks were not printed which means the design could not be modified. The same technique for improving the resolution, as in process 2, was utilized but with 1.0 µm slots widths since the 0.7 µm slot openings were not printed correctly. Returning to the original masks also meant a return to the broader mesa widths of 8 µm, 10 µm, 12 µm, 20 µm, and 100 µm and again, higher order transverse modes may be observed.

Each of the photolithography steps were accomplished using contact photolithography and SUSS MicroTec MA6 NFH or MA8 MA/BA Gen4 mask aligners. An adhesion promoter, HMDS (hexamethyldisilazane), was coated on cleaned substrates before using a new positive photoresist, S1813 from microposit, according to standard procedure [133, 164]. Photolithography optimization was conducted on GaSb substrates to ensure the photoresist thickness, exposure dose, and development was appropriate for the targeted slot and mesa sizes.

Edge bead removal was paramount in decreasing the minimum slot width that could be exposed, so different techniques were explored. The sample sizes were standardized to 11 mm x 10 mm rectangles and were diced along the crystal planes. This improved the repeatability of spincoating and allowed flood exposures to be conveniently used for edge bead removal, since one blank could be diced and repeatedly used. Other methods were explored, but they were inconvenient or caused scumming of the resist.

5.2.2 Initial dry etching process

Dry etching optimization was conducted on an ICL structure, similar to that described in Fig. 3.1. Two key parameters of the dry etching recipe were varied: the etching temperature and the gas composition. The reason to avoid a high table temperature is because, without a dedicated Sb-etcher, it can take over 12 h to process one sample and return the system to room temperature. It would also verify the hypothesis that the high temperature was the key parameter in achieving vertical sidewalls. The gas composition was varied to compare changes achieved in the etching profile.

The initial etching study involved the recipes presented in Table 5.2. The sample was etched either to the bottom cladding layer or for a maximum of 15 min using a 600 nm thick Si_3N_4 hard mask. The UMV2 recipe is a modified version of mesa recipe 1. The GATYN recipe is inspired by a GaAs facet etching recipe, previously used in Tyndall. These two room temperature etches are studied at low chamber pressures. In UMV2, the RF/ICP power ratio was adjusted to try to improve the angle of the etching profile. The selectivity, S, measured was 4 for an etch rate of 120 nm/min. In GATYN, N_2 is added to induce sidewall protection through passivation and increase the smoothness of the process[165]. The etch

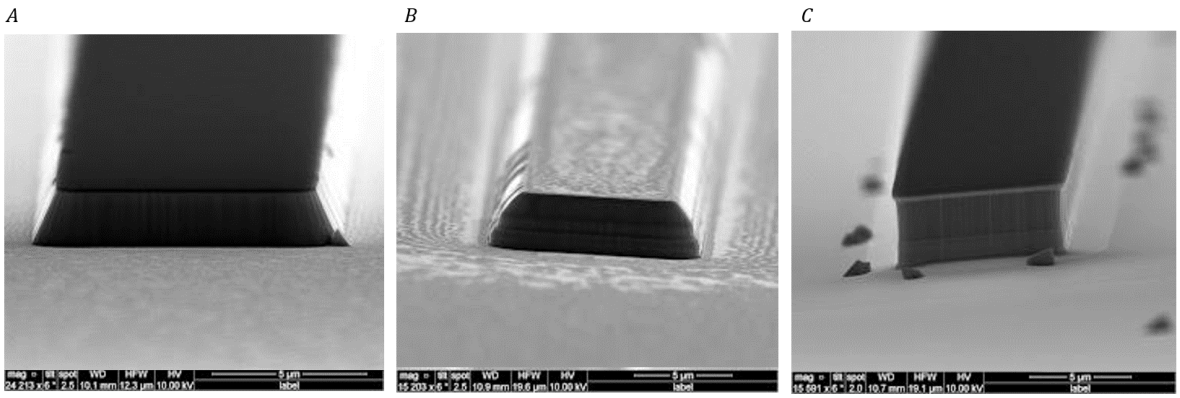

Figure 5.9: SEM images from the dry etching tests showing the profile on ICL material after being etched with *A:* UMV2 *B:* HTTYN and *C:* GATYN.

Recipe	Gases	Flow rate	Pressure	RF	ICP	Temp	Etch rate	S
UMV2	BCl_3:Cl_2:Ar	10:5:16.3	1.5	100 W	150 W	20°C	120	4
GATYN	BCl_3:Cl_2:Ar:N_2	10:5:10:4	2.5	100 W	600 W	20°C	NA	NA
HTTYN	Cl_2:Ar	2.5:25	20	75 W	600 W	220°C	360	8

Table 5.2: Dry etching parameter comparison for the recipes used to explore different gas compositions, etch temperatures, and pressures. The flow rates are given in sccm, the pressure is in mTorr, and the etch rate is in nm/min.

rate and S could not be reported for the sample because the etch rate was so high the etching mask was completely consumed. The HTTYN recipe is a high temperature etching recipe developed to replicate the results from process 2. It involves a simpler gas composition of only Cl_2:Ar at a high chamber pressure in comparison to the other two recipes. S of 8 was measured for an etch rate of 360 nm/min.

Fig. 5.9 shows the resulting profiles from the initial dry etch process. The UMV2 recipe is shown in Fig. 5.9A and a trapezoidal profile is observed. The etch rate too slow and was terminated in the upper cladding after 15 min. The GATYN recipe is shown in Fig. 5.9B where a bumpy trapezoidal profile is observed. The sidewalls were smooth but a different etching angle is observed in each layer; i.e. in the cladding, SCL, and active region. The hard mask was entirely etched away as can be seen on the top of the sample. The HTTYN recipe is shown in Fig. 5.9C and the etch profile is the most vertical of the three recipes, though a slight undercut is observed.

The best etching profile results from the HTTYN recipe and will be studied further to see if the undercut can be removed and the roughness of the sidewalls reduced.

5.2.3 High temperature etching gas study

The following variations of the HTTYN recipe changes were studied:

- V1 is a decrease in chamber pressure.
- V2 is a further decrease in chamber pressure and an increase in the RF power.
- V3 switches to a BCl_3/Ar recipe, with an increase in the Ar flow rate and the RF power.

- V4 incorporates Cl_2 into the BCl_3/Ar mix and increases the ICP power.
- V5 is V4 with increased ICP and RF power.

The first two variations were made with a Cl_2/Ar mixture while the remaining three variations studied the incorporation of BCl_3. The details of the recipes are summarized in Table 5.3, with HTTYN included for reference. HTTYN, V1, and V2 were etched to the bottom cladding layer and V3-V5 were stopped after 15 min.

Fig. 5.10 shows mesa sidewalls from the variations in the high temperature etch recipe. Fig. 5.10A shows the profile of the mesa from the reference sample etched using the HTTYN recipe. The sidewalls are quite rough on this sample, with more roughness near the top of the ridge (near the mask). This suggests that the mask needs to be thinner and perhaps have the opening angle improved. However, this was not observed before in Fig. 5.9 with the same etching mask, so this could be a defect specific to this process run. There is also a shallow trench observed near beside the mesa, though the sidewall is vertical. This could be caused by ions reflected from an angled hard mask and too much physical etching[166]. Fig. 5.10B shows the profile of the mesa etched with V1 where the chamber pressure was decreased. The roughness near the top of the ridge remains but the etch becomes more smooth. There is a bit of roughness observed near the mesa on this sample, but no trenching, and the etch profile is vertical. This could be the result of defects from mask cleanliness during the photolithography step. This etch is improved with respect to the reference. Fig. 5.10C shows the profile of the mesa etched with V2 where the chamber pressure was decreased again and the RF power was increased. The etch is smooth over the entire height of the ridge at this location, though some areas along the mesa had rough patches. There is no roughness observed near the top of the ridges, but there is more roughness observed beside the mesa, and the sidewall is vertical.

Fig. 5.10*D* shows the profile of the etch from V3; the first recipe incorporating BCl_3. The etch through the cladding is extremely rough and the circular holes in the sidewall indicate too much chemical etching. The sidewall angle remains vertical. Fig. 5.10*E* shows the profile of the etch from V4, with the addition of Cl_2 and increase of ICP power. The etch in the cladding is rougher and with more lateral etching a pronounced undercut is observed. Fig. 5.10*F* shows the profile of the etch from V5, where the RF power is increased with respect to V4. It appears the etch was terminated in the active region because the cascades are visible beside the mesa. Lateral etching is increased and the roughness is worse than in V4 and V5.

In order to successfully incorporate BCl_3 into the high temperature recipe, a larger study needs to be conducted since 10 sccm appears to be too high. The best etching recipe variations in this study were

Recipe	BCl_3	Cl_2	Ar	Pressure	RF	ICP	Etch rate	S	Quality
HTTYN	0	2.5	25	20	75 W	600 W	530	4.1	Rough
V1	0	2.5	25	15	75 W	600 W	600	5.2	Smooth
V2	0	2.5	25	5	100 W	600 W	530	4.4	Smooth
V3	10	0	50	20	100 W	600 W	210	3.3	Rough
V4	10	1	50	20	75 W	700 W	220	3.7	Rough, undercut
V5	10	1	50	20	100 W	700 W	170	2.8	Rough, undercut

Table 5.3: Dry etching recipes that were explored to optimize the etch profile of the mesa at 220 °C. The flow rates are given in sccm, the pressure is in mTorr, and the etch rate is in nm/min.

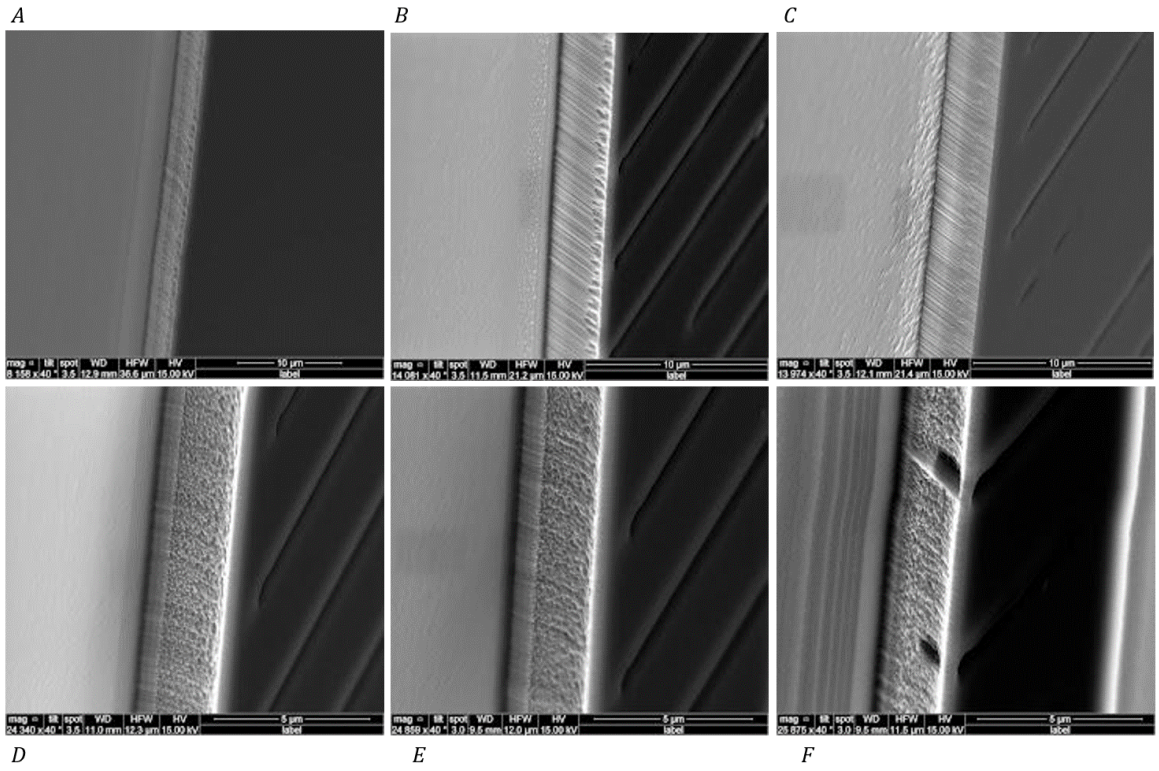

Figure 5.10: Dry etching recipe variations on ICL samples, with the hard mask left on. *A:* Reference sample using HTTYN. *B:* Etch using V1. *C:* Etch using V2. *D:* Etch using V3. *E:* Etch using V4. *F:* Etch using V5.

from V1 and V2. Qualitatively, it seems that V1 provided a smoother etch because the area near the ridges has no roughness. This recipe will be used to etch the slot and mesa in process 3.

5.2.4 Third slotted ICL fabrication

From the results of the previous etching studies, the necessary modifications were made to the process and the third iteration of slotted ICLs were fabricated on E802A. For this fabrication run, slot widths of 1.0 µm were targeted with the 13.1 µm slot spacing. A study consisting of three different etch depths was conducted, including 1.0 µm, 1.35 µm, and 1.7 µm, named LP1, LP3, and LP2, respectively. An overview of process 3 is illustrated in Fig. 5.11, which is similar to process 1 with the adjustments highlighted in orange and detailed below.

Slot definition

A Si_3N_4 hard mask is deposited on the ICL sample using PECVD, with a target mask thickness of 300 nm for etch depths of ≈1 µm. Contact photolithography is performed to define the slot pattern with d_s =1 µm in the mask. The hard mask is then opened using a F-based recipe composed of $SF_6/C_4F_8/H_2$/He that developed to etch SiO_2/Si_3N_4 stacks with an etch rate of $Si_3N_4 \approx 300$ nm/min. Following this etch, the

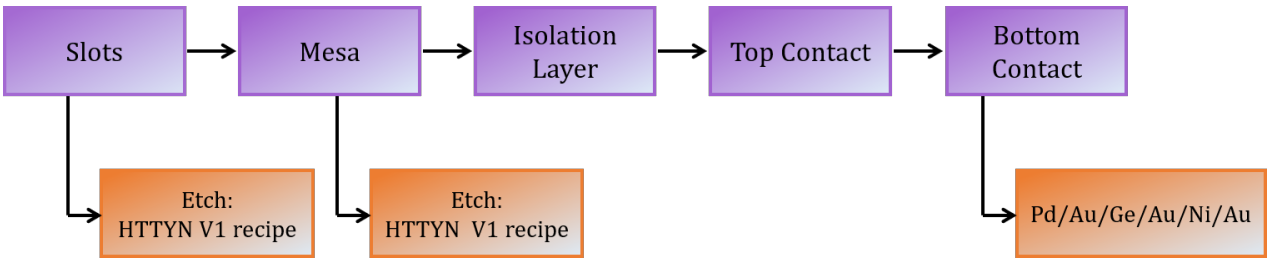

Figure 5.11: Summary of process 3 for the third iteration of slotted ICLs.

slot pattern is transferred to the sample using the HTTYN V1 recipe described in Table 5.3. The etch depths are controlled with the etch time. LP1 was etched for 102 s, L2 was etched for 174 s, and LP3 was etched for 138 s.

Fig. 5.12A shows an SEM of the slots after the hard mask opening and Fig. 5.12B shows an SEM of the slots after being etched into the upper cladding. In Fig. 5.12A, there is etching of the InAs top contact layer, visible from the etch below the dark Si_3N_4 layer. The sidewalls look rough at this interface which is attributed to an overetch of the hard mask and ripples in the photoresist. The slot widths are larger than the target at 1.1 µm to 1.2 µm, but are within an acceptable range. In Fig. 5.12B, the sidewalls are vertical but there appears to be roughness at the bottom of the slot, likely from the hard mask. The residual Si_3N_4 hard mask is removed via the same F-dry etching.

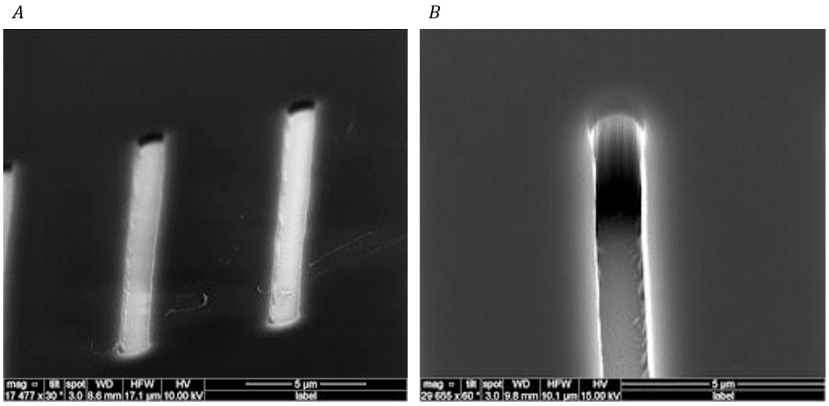

Figure 5.12: SEM images looking at the quality of the slot definition during the fabrication. *A:* Slot pattern etched into the Si_3N_4 layer. *B:* Slots etched into the cladding layer with vertical sidewalls.

Ridge definition

A 600 nm thick Si_3N_4 mask is deposited before photolithography is performed to define mesa ridges with widths of 8 µm, 10 µm, 12 µm, 20 µm, and 100 µm. The mask is opened using the F-dry etch described above. The mesa are then etched until the start bottom cladding using the HYTTYN V1 recipe detailed in Table 5.3, observing the oscillation monitoring signal. The remaining hard mask is removed from the top of the ridges using the F-dry etch.

Fig. 5.13 presents SEM images illustrating the etch quality of the third process. The vertical etch profile is observed from an alignment marker in Fig. 5.13A. Fig. 5.13B shows a 10 µm mesa, with a ridge height of approximately 3 µm, and three slots. Fig. 5.13C shows a close up of a slot protruding from the ridge due to misalignment. From Fig. 5.13B and C, in reference to Fig. 5.12B, it is evident that the etching mask was not effectively removed from the slots. We do not believe it is critical to remove all of the dielectric from the slots until after the contact window opening in the isolation layer. The measured top of the slot width is close to the targeted with at 1.1 µm, while the bottom of the slots is measured to be 400 nm and an angled sidewall is apparent. The mesa profile is vertical and smooth in some places along the ridge but rougher, with signs of more chemical etching than for the other samples, comparing Fig. 5.13A, B, and C.

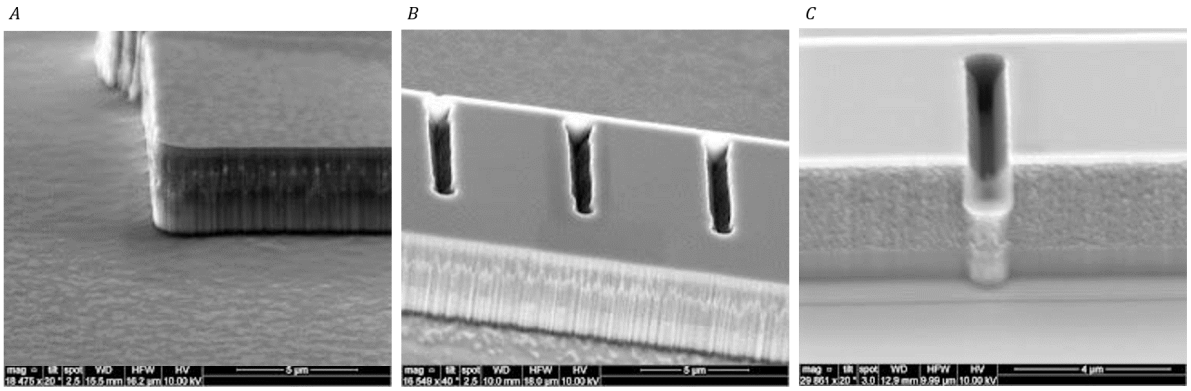

Figure 5.13: SEM images illustrating the etching profile during the fabrication. *A:* Vertical profile of the mesa etch from an alignment marker. *B:* Slot and mesa etching from a 10 µm mesa after Si_3N_4 mask removal. *C:* Slot after the mesa etch and removal of the Si_3N_4 mask.

Isolation layer with contact window

Using PECVD 20 nm of Si_3N_4 was deposited followed by 250 nm of SiO_2 on the samples. This must be done on the same day as the mesa etch to prevent an oxide layer from forming, especially from the exposed Al layers[141]. Photolithography is used to pattern openings on top of the mesa ridges.
The hard mask is then opened using two variants of the F-based recipe described before. The first variant is $SF_6/C_4F_8/He$ at a lower etch temperature to achieve fast, high aspect ratio etching of SiO_2 and Si_3N_4 with an etch rate of ≈ 300 nm/min. It removes the dielectric from the top of the mesa.
The second variant is then just C_4F_8/He and the etch rate of decreases to ≈ 80 nm/min. It is used to remove the dielectric from inside the slots. Optical monitoring can not be used at this step because of the small openings of the slots, but the alignment markers are monitored for reference and the etch is stopped when the material is removed from these features.
This dry etching recipe combination managed to etch an estimated 60% of the SiO_2/Si_3N_4 from inside the slots, as is shown in the top row of Fig. 5.14. The etching profile is not uniform across the samples or along the ridges. For example, sometimes a more vertical center is etched from the slot, as is seen in Fig. 5.14B for sample LP2. Therefore the high aspect ratio alterations to the F-dry etch were not sufficient to address the $\approx$1 µm slot widths. In comparison to process 1 shown in Fig. 4.13*F*, this is still an improvement. A

more systematic study of the F-dry etch recipe is required to optimize this step.

Top contact

Photolithography defines the contact strips on top and beside the mesa ridges. The single layer lift-off technique is used with a thick photoresist which was developed for a pronounced undercut. Thermal evaporation is used to deposit 20 nm/30 nm/250 nm of Ti/Pt/Au. The newly vertical mesa sidewalls are coated with the samples rotating to increase the line of sight to these areas. This should prevent open circuits due to a disconnect between the top of the ridges and contact pads. Lift off is done in a resist stripper to remove the resist and unwanted metal.

Bottom contact deposition

The substrate is thinned to >200 µm using chemical etching in a bath of Br diluted with methanol such that the etch rate is ≈ 40 μm/min. The bottom contact is formed from the thermal evaporation of 5 nm/14 nm/14 nm/14 nm/11 nm/150 nm of Pd/Au/Ge/Au/Ni/Au. These are the same materials as used in process 1, but with a different deposition technique that results in more control over the contact composition. The contacts are annealed at 225 °C on a hot plate for around 2 min or until the colour change from Au diffusion is observed.

Cleaving and mounting

Laser bars with lengths of 1.6 mm are cleaved and mounted epi-side up to copper heat sinks for initial PIV characterization.

The cross sections of the LP samples from process 3 are presented in Fig. 5.14. The top row shows a cross section of the slots taken from a cleaved 100 µm ridge on each sample, recall the target slot width was 1 µm. The bottom row of Fig. 5.14 shows a cross section of the mesa from a ridge on each sample. Fig. 5.14A shows a slot from LP1, where the measured slot width was 0.86 µm. The target slot depth was 1 µm and the measured slot depth was 0.8 µm. There is a slight undercut observed and the side wall angle 88°. Fig. 5.14B shows a slot from LP2, where the measured slot width was 0.74 µm. The target slot depth was 1.7 µm and the measured slot depth was 1.1 µm. There is a slight undercut observed and the side wall angle 89°. Fig. 5.14C shows a slot from LP3, where the measured slot width was 0.79 µm. The target slot depth was 1.4 µm and the measured slot depth was 1.0 µm. There is a slight undercut observed and the side wall angle 88°. Over the three LP samples, the slots are 20% smaller than the target slot width. This means sub-micrometer resolution was achieved with this process, but that the slots were under-etched with respect to the hard mask opening potentially due to plasma charging of the slots. There is a small undercut observed near the top of the top of the slot, but vertical sidewalls towards the bottom.
In Fig. 5.14*D* on LP1, the targeted mesa width was 8 µm and the measured mesa width at the bottom of the etch was 7.8 µm. The measured contact window was 4.8 µm. The profile is quite vertical and smooth near the bottom, but lateral etching is observed near the top of the ridge. In Fig. 5.14*E* on LP2, the targeted mesa width was 20 µm and the measured mesa width at the bottom of the etch was 20.1 µm.

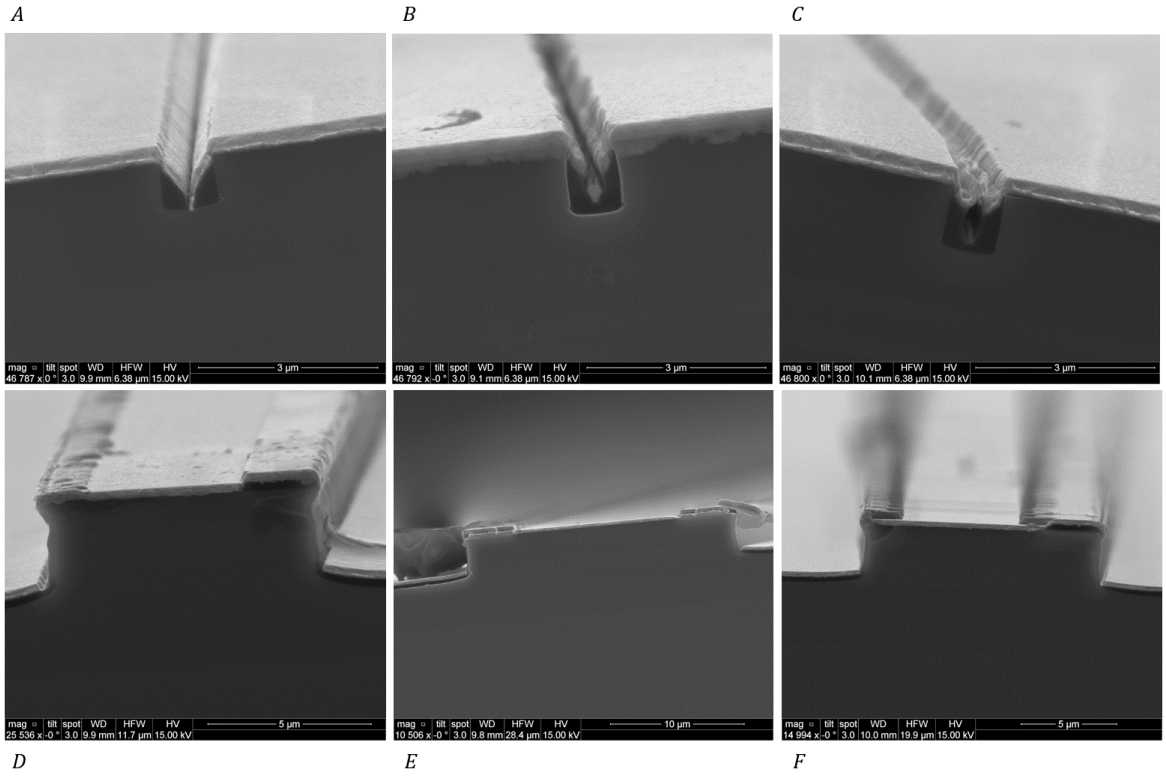

Figure 5.14: SEM images of slotted ICLs from process 3. *A:* Cross section of a LP1 slot. Inset is a zoomed out view of the slot spacing from a cleaved 100 µm ridge. *B:* Cross section of a LP2 slot. *C:* Cross section of a LP3 slot. Cross sections are shown for *D:* LP1 mesa width 8 µm, *E:* LP2 mesa width 20 µm, and *F:* LP3 mesa width 12 µm.

The measured contact window was 12.3 µm. Vertical sidewalls with a slight undercut is observed. In Fig. 5.14*F* on LP3, the targeted mesa width was 12 µm and the measured mesa width at the bottom of the etch was 12.1 µm. The measured contact window was 6.1 µm. The mesa sidewalls are quite vertical, but some lateral etching occurs near the top of the ridge.

Fig. 5.15 summarizes the fabrication of the slotted waveguide on the LP samples. Fig. 5.15B shows a zoomed out view of the cleaved 100 µm ridges in order to observe the quality of the sample and measure the slot spacing. Fig. 5.15A plots the expected values with the measured values for: *i* the slot width d_s, *ii* the etch depth t_E, and *iii* the number of slots N. The values from Fig. 5.15*A(i),(ii)* are from measurements of SEM images of the slots, as described above. The values from Fig. 5.15*A(iii)* are derived according to the slot period and the calculated number of slots in a 1.8 mm device. The targeted slot period was 13.1 µm, so the targeted N is 140. Fig. 5.15B depicts the measured slot periods on the LP samples. The measured slot period for both LP1 and LP3 was 13.0 µm, therefore $N = 138$. Meanwhile, the exposure on LP2 suffered from mask contamination and resulted in defects. The slots did not uniformly develop along the ridge and, as a result, many were missing. The SEM image in Fig. 5.15B for LP2 shows a length of ridge where six slots should be observed, but two are missing resulting in a superposition of two periods. The average measured slot period was 39.1 µm, leading to $N = 50$. Where the slots were properly formed, the measured slot spacing was 13.1 µm. This should maintain the proper wavelength selection, though

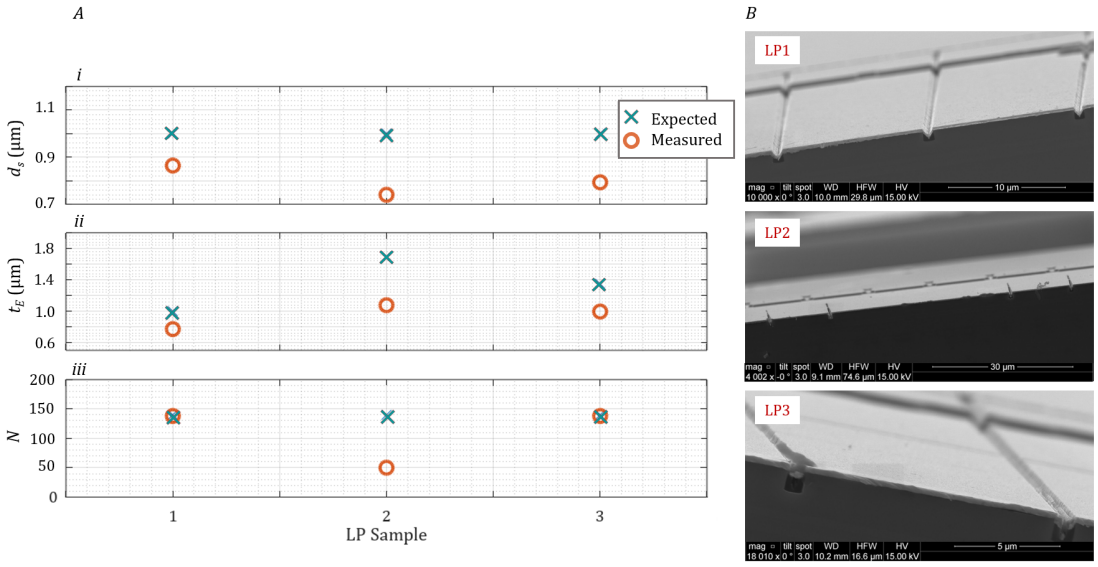

Figure 5.15: Evaluation of the fabricated slotted waveguide parameters. *A:* The expected vs measured dimensions are summarized from the LP samples. Plot *(i)* shows d_s, plot *(ii)* shows t_E, and plot *(iii)* shows N for a device with length 1.8 mm. *B:* SEM images from a zoomed out view of the slot spacing from a cleaved 100 µm ridge on the LP samples.

the reflectivity strength will be affected due to the missing slots.

5.2.5 Performance of third iteration slotted ICLs

The PIV characteristics of the slotted ICLs were measured using the same set up that was used for the first slotted ICLs. A series of operating conditions were studied in order to understand the range of single-mode operation.

PIV characteristics

The performance of the slotted ICLs from the LP study mounted epi-side up are presented in Fig. 5.16 for ridge widths of 8 µm and lengths of 1.6 mm. Fig. 5.16A depicts the PIV performance of LP1, LP2, and LP3 at 15 °C in CW mode. Note, the noise on the IV curves from LP2 and LP3 was due to poor contact of the probe tip with the device and not due to a processing defect. Only LP1 and LP2 devices lased. No fabrication defects are suggested by the IV curve for LP3, since it is consistent with a working ICL.
For LP1, I_{thr} was measured to be 62.6 mA, V_{OC} was 3.4 V, P_{max} was 8 mW at an I_{max} of 124 mA, and R_s was 9.9 Ω. For LP2 I_{thr} was measured to be 41.5 mA, V_{OC} was 3.8 V, P_{max} was 12 mW at an I_{max} of 107 mA, and R_s was 12 Ω. Less leakage current in this process is observed in comparison what is observed from process 1. Fig. 5.16B depicts the temperature dependence of the PI curves from LP1. T_0 is estimated from the corresponding series of I_{thr} to be 40 K.
Since LP3 did not lase, we can conclude that the losses from the slots and resultant heating was too high. This can be used to set a new boundary on the combination of slot width and etch depth in the waveguide geometry for future simulations. It also suggests the need to explore better thermal management options in the fabrication, since a thinner top contact in comparison to process 1 was used. LP3 had the narrow

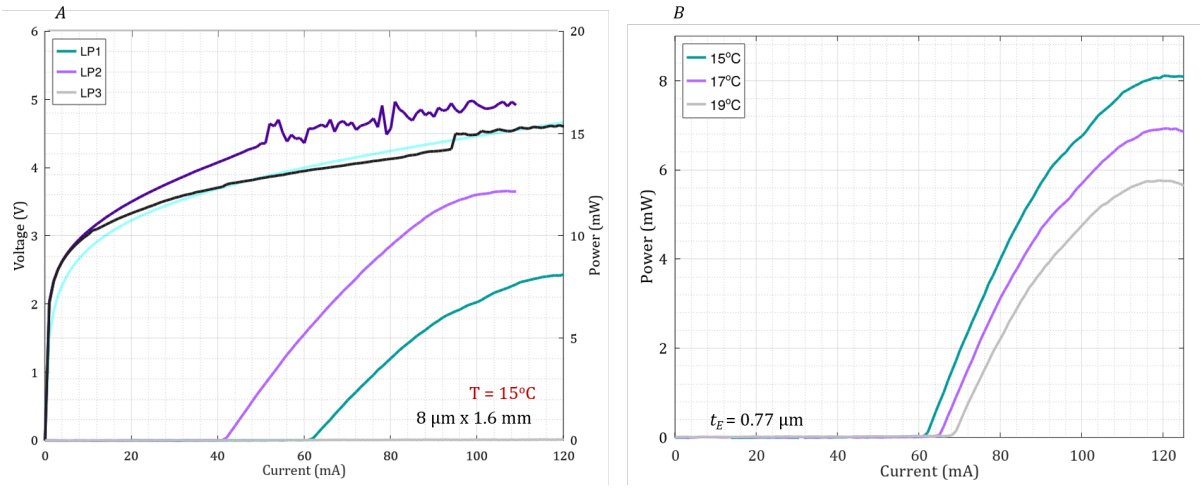

Figure 5.16: *A:* PIV characteristics from the LP samples mounted epi-up in CW mode are shown at 15 °C for devices with a ridge width of 8 µm and length of 1.6 mm. *B:* The temperature dependence of the PI curves from LP1 are shown.

and relatively deep slots which, in combination with heating issues, could explain why it did not lase. In general, the PIV characteristics of the other LP devices demonstrate an overall improved process for creating slotted ICLs.

Wavelength tunability

The goal of the improving the fabrication was to improve the SMSR and the single-mode output power, leading to a wider tuning range. A wide range of operating conditions were explored in the hopes of measuring single-mode emission.

For LP1 the highest SMSR recorded was 19.5 dB, with λ =3369 nm at 23 °C and 85 mA for a device 8 µmx1.6 mm, as illustrated in Fig. 5.17A. The electrical tuning measured was 0.12 nm mA^{-1} and the thermal tuning measured was 0.3 nm °C^{-1} from the single-mode spectra. At 25 °C between 87.5 mA and 95 mA, the range of single-mode emission was from 3369 nm to 3377 nm, however the electrical tuning was not continuous as a mode hop was observed.

For LP2 the highest SMSR recorded was 20.7 dB, with λ =3392 nm at 25 °C and 70 mA for a device 8 µmx1.6 mm, as shown in Fig. 5.17B. The SMSR drops sharply after this point, so no tuning is reported. However, because there is an oscillation between mutli-mode and single-mode emission as the current is increased, C_{FSR} can be measured and an estimate of the width of the S_{FSR} can be inferred. At 25 °C when the current is increased to 75 mA C_{FSR}=0.92 nm, which should be >FWHM/2. We assume we are close to not meeting this criteria, since the tuning changed the emission from single-mode to dual-mode, and this leads to an estimate of FWHM around 1.8 nm.

From the design and simulations, shorter lasers should fulfill this criteria more readily and thus be more single-mode over a larger current range. Therefore, another 8 µm laser was cleaved from LP2 for a cavity length of 1.2 mm and mounted epi-up on a copper heat sink. At 17 °C, I_{thr} was measured to be 54.2 mA, using an uncalibrated InSb detector. The spectra recorded with an FTIR are shown in Fig. 5.18, summarizing the wavelength tunability of this device at 17 °C. Fig. 5.18A highlights selected spectra

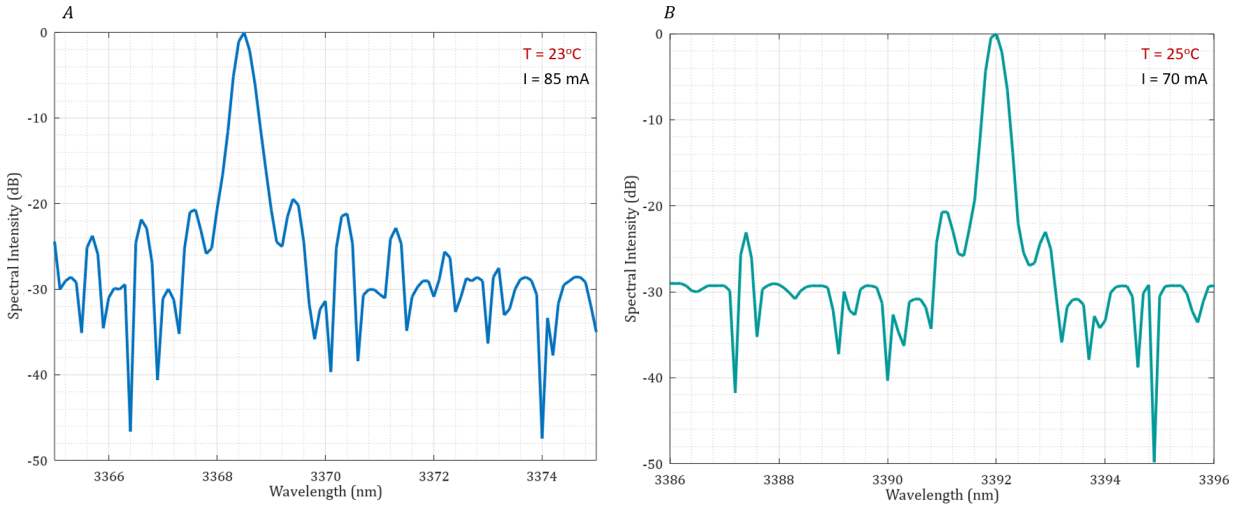

Figure 5.17: The spectra for the highest SMSR from LP1 and LP2 mounted in the epi-up configuration with dimensions 8 µmx1.6 mm operated in CW mode. *A:* LP1 is shown at 23 °C and 85 mA. *B:* LP2 is shown at 25 °C at 70 mA.

over the tuning range from 89 mA to 103 mA. The highest SMSR recorded was 22.3 dB, with λ =3428 nm at 90 mA. Fig. 5.18B summarizes the wavelength tunability of this device. Fig. 5.18*B(i)* illustrates the continuous wavelength tuning, with single-mode emission between 3427 nm to 3430 nm for currents 89 mA to 103 mA. Fig. 5.18*B(ii)* plots the SMSR over the range. The average SMSR over this range is 18.4 dB. Fig. 5.18*B(iii)* plots in the instantaneous electrical tuning rate measured. The average tuning rate was 0.2 nm mA^{-1}. At 93 mA there is a change in the tuning rate and a drop in the SMSR. This could be due to a change in cavity mode overlap with the reflectivity peak from the slotted waveguide.

From the result with LP2, we can conclude that the process modifications optimized the performance of the slotted ICLs. Another factor that could attribute to the improved wavelength tunability with respect to process 1 is the change in d and a more optimal overlap with the emission bandwidth of the growth. The max SMSR improved from 13 dB to 22.3 dB. The single-mode emission wavelength range, for one temperature, increased from 2 nm to 3 nm. From all the devices tested, single-mode emission was observed at lengths of 1.2 mm, 1.6 mm, and 1.8 mm indicating a more robust device design and fabrication.

Unfortunately, the fabrication of the LP samples did not result in slots that had a consistent slot width and period. Along with the three etch depths achieved in the LP study, three slot widths were realized with measurements of 0.86 µm, 0.74 µm, and 0.79 µm for LP1, LP2, and LP3 devices, respectively. This prevents trends with respect to etch depth from the electro-optical performance to be observed as intended at the beginning of the fabrication study. Nevertheless, there are a few trends observed that could be useful in future slotted waveguide designs and warrant further investigation.

A summary of key metrics from the epi-up spectral emission properties are compared alongside slot dimensions realized in process 3 in Table 5.4. When the length is decreased between the two LP2 lasers, the SMSR increases, as expected. The decreased length (increased C_{FSR}) also results in a larger response to electrical tuning and a larger range of continuous single-mode emission. When t_E increases and d_s

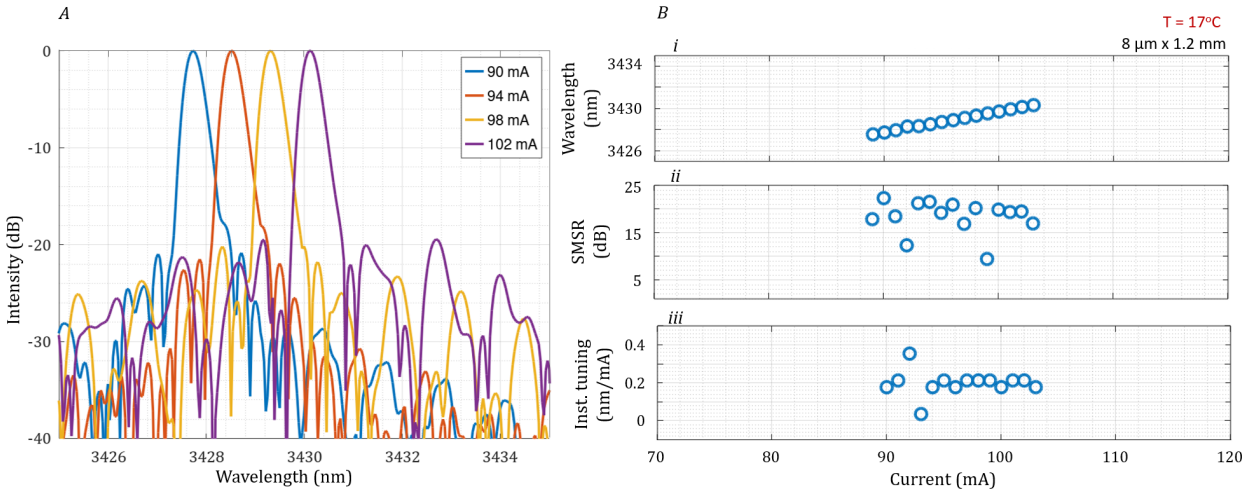

Figure 5.18: Summary of the emission measured from the LP2 laser mounted in the epi-up configuration with dimensions 8 µmx1.2 mm operating in CW at 17 °C. *A:* Selected spectra over the current tuning range between 89 mA to 103 mA. *B:* Summary of the electrical tuning achieved including *(i)* the wavelength of single-mode emission, *(ii)* the SMSR, and *(iii)* the instantaneous tuning.

Sample	d_s (μm)	t_E (μm)	L (mm)	N	d (μm)	λ (μm)	SMSR	Tuning	CSMR
LP1	0.86	0.8	1.6	123	13.0	3.37	19.5	0.13	0.6
LP2	0.74	1.1	1.6	45	13.1/39.1	3.39	20.7	0.12	0.6
LP2	0.74	1.1	1.2	34	13.1/39.1	3.43	22.3	0.20	2.7

Table 5.4: Summary of epi-up single-mode behaviour for 8 µm wide devices with respect to slot dimensions in the LP study. The SMSR is the max value measured and given in dB, the tuning refers to the electrical tuning in nm/mA, and the CSMR is the continuous single-mode wavelength range in nm.

decreases between LP1 and LP2, an increase in the SMSR is also observed. LP1 should have a narrower FWHM, due to a higher N, but this seems to be compensated for by the larger t_E for LP2, which results in a higher suppression strength of the S_{FSR}. The other factor could be a change in suppression strength from the change in d_s. Since d_s needs to be an integer multiple of $\lambda_n/4 \approx 0.22$ ($n_g = 3.8575$ from simulation at 3.39 µm), the change of 0.12 µm from LP1 to LP2 could have improved the SMSR by moving the S_{FSR} peak closer to an optimal width for maximum interference.

Additionally, there is a difference in d between these two devices. Due to defects during the fabrication of LP2, roughly two slots out of every four were missing. This means there were two periods superimposed on the waveguide; d_1 =13.1 µm and d_2 =39.1 µm. Single-mode emission is still expected since $3d_1 \approx$39.3 µm, but the S_{FSR} from d_2 would be smaller. Two superimposed S_{FSR} can enhance the suppression capabilities of the waveguide[85]. This effect makes it difficult to understand the trend between the samples, since the design is effectively different.

Conclusion

This chapter explored how the quality of the fabrication of the slotted waveguide affected the ability to achieve single-mode emission. Two different fabrication runs of slotted ICLs were conducted: the first, process 2, tested design modifications and the second, process 3, tested the improved slot fabrication. In process 2, electrical shorts from a design change to the slots prevented lasing. In process 3, decreasing the device length to 1.2 mm improved the SMSR and increased the range of operating conditions for single-mode emission. The best performer came from the third iteration of slotted ICLs with single-mode emission for a 8 µmx1.2 mm laser in CW mode at 17 °C. A wavelength tunability of 0.2 nm mA^{-1}, a threshold current of 54.2 mA and an output power of >1 mW per facet was measured. The wavelength range was 3 nm, with a max SMSR of 22.3 dB at 3.43 µm. From the interplay between single-mode and multi-mode emission, C_{FSR} was used to estimate the FWHM of S_{FSR}. A waveguide with $N = 45$ and t_E =1.1 µm resulted in a FWHM close to 1.8 nm. This means the goal of increasing the SMSR and tuning range was met.

After three slotted ICL fabrication runs, two different slotted waveguide geometries have been tested and successfully yield single-mode slotted ICLs at wavelengths of 3.4 µm and 3.5 µm. This verifies the mask design was successful addressing multiple growths. Improving the process to increase the efficiency will be important to the development of a Vernier tuned device since two slotted waveguides will be required to operate in tandem.

CHAPTER 6

Towards Widely Tunable ICLs

Widely tunable ICLs are useful because they can be used to detect multiple gas species and replace multiple sources, leading to cost-effective sensors[19, 167]. The ultimate goal of this thesis was to design a single-mode ICL with an extended tuning range. The previous slotted ICLs that have been fabricated formed the foundation for the multi-section device that would exploit the Vernier tuning concept to achieve broadband tuning. These single section slotted ICLs addressed many of the processing obstacles and allowed design and conceptual challenges to be focused on.
Moving from slotted ICLs to Vernier tuned devices requires a concept shift. Single-mode emission comes from the mutual overlap of two reflectivity peaks from the different slotted waveguides with a cavity mode defined by the effective cavity length, rather than the facet-facet distance. Their overlap must be precise enough and the peaks must be narrow enough to support only one cavity mode. If we consider just one slotted waveguide, there will be many positions where the reflectivity peaks overlap with the cavity mode but the supported modes will be spaced by S_{FSR} rather than C_{FSR}.
The extended tuning range occurs from the ability to overlap *different* reflectivity peaks of the two slotted waveguides via current injection. This allows many wavelengths to be covered within the gain bandwidth of the active region. Implementing Vernier tuning results in new processing and design challenge: facet reflections need to be suppressed, the total laser length is increased, and electrical isolation between two sections must be achieved for independent pumping. The challenges in moving from the single section devices towards the complex multi-section design will be described in the following sections. Simulations and design concepts will be presented followed by the process developed for SVT ICLs and their performance. The SVT ICLs were fabricated at nanoplus and subsequently characterised in Tyndall.

6.1 Modelling slotted waveguides for Vernier tuning

The SVT ICLs were designed for C1643 whose emission wavelength was around 3.6 µm. This growth was chosen because the output power was higher with respect to the other structures available; the

average output power in CW mode from FP ICLs was 10 mW in comparison to around 5.5 mW from other ICL structures (see App. 7). The high output power could compensate for an initial design that wasn't optimized.

6.1.1 Design objectives for Vernier tuning

The key differences from the slotted ICLs that would need to be addressed by the SVT ICL design include:

- d was increased to have a smaller S_{FSR} that was no longer larger than the gain bandwidth of the active region
- N was decoupled from the length for independent control of this parameter
- due to the number of sections and desired emission wavelength, these devices were much longer than the typical 1 mm to 2 mm previously fabricated
- structures needed to be implemented in the waveguide that could achieve electrical isolation without affecting the optical output
- a larger slot width was implemented and d_s =1.25 µm was fixed to simplify the fabrication and minimize simulation parameters

Two slotted waveguides were designed to overlap at 3.6 µm with similar S_{FSR} set by d. d was chosen so that S_{FSR} was within maximum wavelength shift of 5 nm to 10 nm from electrical tuning (set by material). This range is in agreement with the predicted 6 nm to 7 nm expected from wavelength tunability measurements of the FP and slotted ICLs fabricated, described in Sec. 3.4.2. If a smaller maximum wavelength shift than the target is realized, the continuity of the tuning will be affected and there will be some wavelengths within the tuning range that are not accessible. InP slotted waveguide lasers can achieve 5 nm but not 10 nm, so this was a good starting point for the design on ICLs[101, 168].
There is a trade off between a having a wide, continuous tuning range and having a high SMSR in Vernier tuned lasers. The tuning range is given by Eqn.2.40, and is inversely proportional to the difference between the S_{FSR} of the two slotted sections; the closer they are, the larger the tuning range is. However, this eventually leads to partial overlap of the reflectivity peaks from the waveguides and will therefore decrease the SMSR achieved. A decreased SMSR happens either because multiple cavity modes are supported by the partial overlap or because multiple reflectivity peaks from the slots overlap (Eqn.2.41). The smallest ΔS_{FSR} that can be employed but still achieve single-mode emission ultimately depends on the FWHM that is achieved in the reflectivity peaks from the slots. We decided ΔS_{FSR} =1 nm was a benchmark the design to achieve single-mode emission with quasi-continuous tuning; above this the SMSR can improve but at the cost of the continuity of wavelength tuning [148, 168].
The large gain bandwidth of the ICLs poses a challenge to the maximum tuning range achievable because the overlap of the reflectivity peaks from the slotted waveguides is periodic. The larger the gain bandwidth of the material, the larger the difference in S_{FSR} must be to avoid the periodic overlap within the gain bandwidth. This reduces the tuning range achievable. The envelope of spectral emission is narrower with respect to the actual gain bandwidth, so this would be investigated empirically.

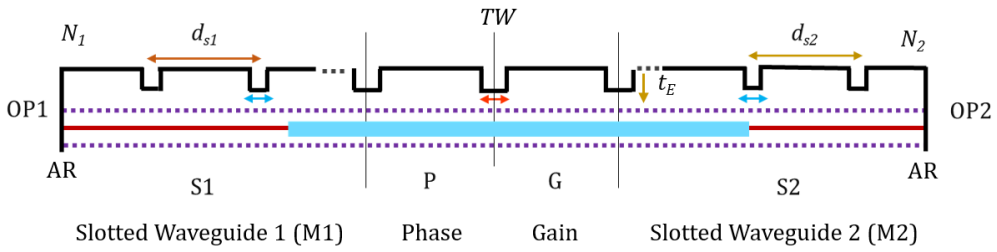

Figure 6.1: A schematic illustrating the general design for the slotted Vernier tuned ICL. Two slotted sections are separated by a phase and gain section with isolation trenches. The total device length is defined by cleaved facets with AR coatings.

Another potential section that could be added to the ends of the device is an SOA.These are integrated in InP SVT lasers, and additionally have AR coatings to further reduce the facet reflections[87] (see Sec. 2.4). They are typically curved to meet the facet at an angle of 6° to 7°. This design minimizes the facet reflections and is important because the reflection strength is quite strong at 30% (Sec. 2.1.3). Facets are not needed since the slots are deep enough to provide sufficient reflection for feedback. SOAs would achieve two things: it would prevent facet reflections and would be a boost to the power. The InP SVT lasers are not etched through the active region and it was unclear if the same form factor could be directly transferred to ICLs that have mesa etched through the active region for mode confinement and current spreading. We thought that it would be better to reduce the complexity (and length) of the first SVT ICL process and opted for AR facet coatings only.
While the purpose of fabricating a SVT ICL is to extend the tuning range, *maximizing* the tuning range was not the priority for the first design. The tuning range would target the upper limit of what is achieved by DFB lasers (around 20 nm[92]) and prioritize a high SMSR in order to better characterize the behaviour. The consequence of this objective for the design and process will be described in the following sections.

6.1.2 Slotted waveguide simulations for Vernier tuned ICLs

As for the slotted ICLs, simulations were conducted using FIMMWAVE and represent a passive system. They do not account for material losses/gain of an active laser system so these parameters need to be characterized empirically. With these new considerations the same simulations that were performed for the slotted ICLs were carried out to shape a device like that illustrated in Fig. 6.1, previously described in Sec. 2.3.3.

The main parameters that were adjusted to meet the design targets were d and N. Fig. 6.2A illustrates the different S_{FSR} that is realized with d between 10 µm to 200 µm, t_E =1.8 µm, and $N = 7$. The width of the emission envelop is plotted for reference to the slotted ICL waveguide simulations; $d \approx$10 µm for S_{FSR}>100 nm. In contrast, the maximum S_{FSR} for the SVT ICLs is 10 nm which leads to large slot periods with d>145 nm. With multiple slots needed, larger d leads to a longer total device length. Fig. 6.2B depicts the mean reflectivity strength from two reflectivity peaks around 3580 nm for N between 5 and 10. Following the correlation between the simulation and performance of the first slotted ICLs, the simulation design target was a reflectivity strength of 0.1%. The target reflectivity strength could be met with less

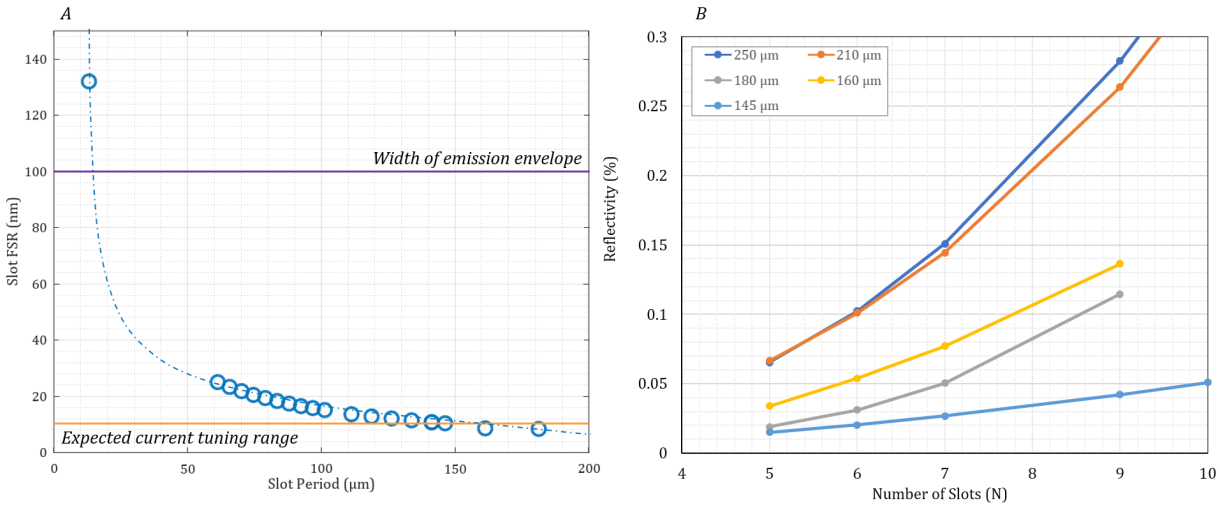

Figure 6.2: *A:* The slot reflectivity peak spacing is shown for different simulated slot periods for t_E =1.8 µm and $N = 7$. *B:* The mean reflectivity strength of different slot periods was simulated with respect to the number of slots with t_E =1.8 µm.

than 10 slots, which is important for minimizing the device length.

Fig. 6.3 illustrates three different slot periods with suitable S_{FSR} for the expected current tuning range achievable. The simulated values of S_{FSR} was 8.7 nm, 6.4 nm, and 5.3 nm, for the slot periods M1 with d =181 µm, M2 with d =251 µm, and M3 with d =294 µm, respectively. Fig. 6.3A depicts the ideal situation with overlap of M1 and M3 at 3575 nm and no other peaks. ΔS_{FSR} for this combination was 2.3 nm and predicted a tuning range of T =24 nm. Fig. 6.3B depicts the less ideal situation when there is partial overlap between M2 and M3 at 3576 nm and 3581 nm. M2 and M3 have more similar S_{FSR} and electrical tuning needs to be used to ensure single-mode emission. ΔS_{FSR} for this combination was 1.1 nm and predicted T of 31 nm.

The FWHM of the design is the other important parameter for single-mode emission and is controlled

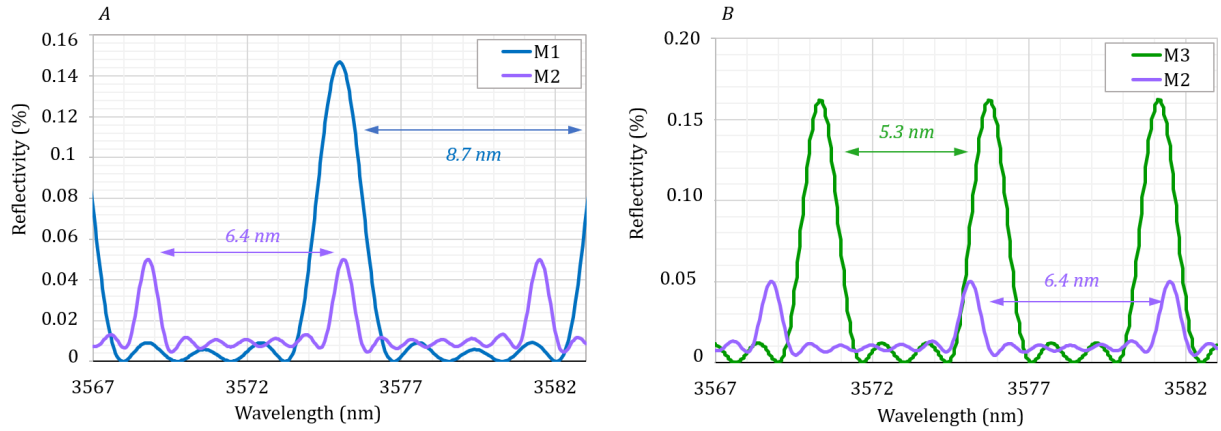

Figure 6.3: Simulations depicting different slotted waveguide configurations. *A:* Resulting S_{FSR} combinations for M1 with d =181 µm and M2 with d =251 µm. *B:* Resulting S_{FSR} combinations for M2 and M3 with d =294 µm.

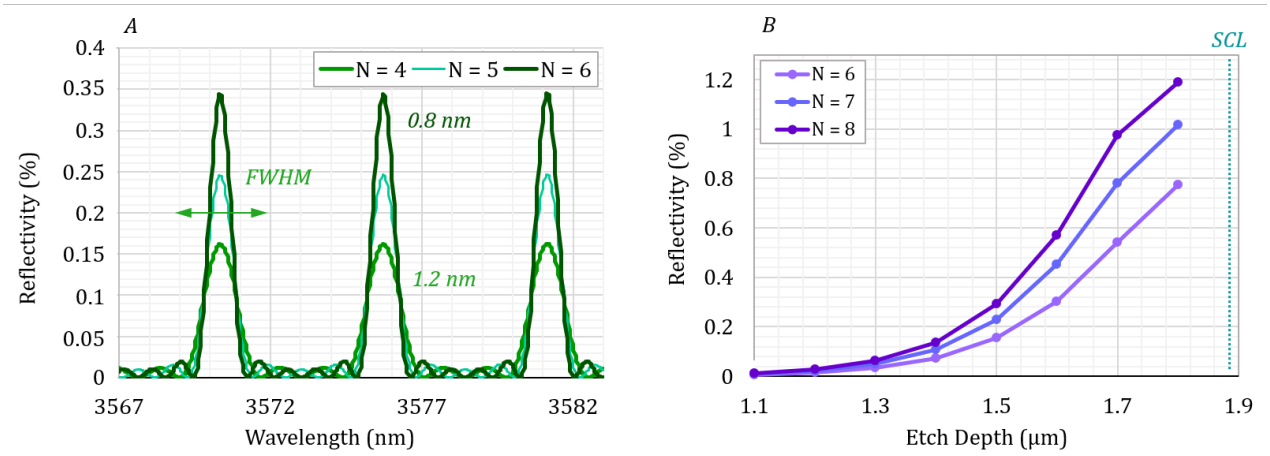

Figure 6.4: *A:* The simulated S_{FSR} used to calculate the FWHM as N is changed for t_E =1.5 µm and d =294 µm. *B:* The reflectivity strength as a function of t_E, until ≈100 nm before the SCL, as N is increased for d =181 µm.

by N and t_E. Fig. 6.4 presents the simulations results after changing t_E and N to see if limiting the section length could still meet the target R value and what the corresponding FWHM would be. Fig. 6.4A illustrates the FWHM changing for d =294 µm with N between 4 and 6. As N increases from 4 to 6 the FWHM decreases from 1.2 µm to 0.8 µm and R increases from approximately 0.1% to 0.3%. Fig. 6.4B illustrates the effect of t_E on R for d =181 µm with N between 6 and 8. Changing the etch depth by 200 nm, a typical spread from process fluctuations modifies the reflective strength from 0.2% to 0.6%.

This covers the simulation results of the slotted waveguides around their anticipated values. The results of the simulations indicate a very large slot separation is needed for the MIR and increasing the number of slots to decrease the FWHM will result in long devices. This challenge is not experienced to the same degree for InP based Vernier tuned lasers which is a consequence of increasing the emission wavelength to the MIR; for the same order of grating, longer periods are required at longer wavelengths.

There are a large number of parameters to explore in the SVT design because there are 4 sections. The final choice of the slotted waveguide geometry will depend on the remaining considerations for gain and phase sections. Shorter gain section lengths need to be integrated into the device which will affect the C_{FSR} and output power. These section lengths will be finalized after considering the practical challenge of designing the photolithography mask that will allow the systematic study of these effects of these design choices on the laser performance.

6.2 SVT ICL Mask Design

Due to the complexity of the devices, there were many practical considerations that needed to be accounted for in the mask design. The devices were long, needed to be repeated to account for variations in the sample center vs edge, need to fit on a sample size of 11 mmx10 mm, and also had to be organized in a way that was practical to cleave. The cleave position had a tolerance of approximately 50 µm, so the starting position of the slots with respect to the anticipated facet position was varied in the hopes that the cleave position would be suitable on some of the devices. In order to coat the facets, at least 8 devices

along the cleave would need to have the same length to be mounted into the holders.
An unknown parameter was the minimum number of slots required to interact with the cavity modes. The reflectivity strength required was empirically bench marked, but an empirical FWHM was not measured yet. Adding more slots is a convenient way to decrease the FWHM and suppress more cavity modes. However, this can also be done by increasing the etch depth (until the SCL). This caused a large variation in the total device lengths, so there were limitations on the freedom of varying the gain length. The extent that the number of slots and etch depth can be manipulated will then be limited by losses accrued that could prevent the material from meeting threshold conditions, Eqn. 2.21. This will need to be investigated empirically. As the length increases, the losses will also accumulate and the same problem will be encountered. Additionally, long lasers begin to become impractical to handle and mount as they can break easily, so a design constraint placed on the devices was that the total length should be less than 1 cm. The phase section was paired with the slotted section that had the shortest period to help minimize the length of the devices.
Four laser lengths were chosen to investigate the effects of different parameters on the emission from the slot period combinations designated B; $M1$ =251 µm and $M2$ =294 µm. This included 3381 µm, 3661 µm, 4878 µm, and 5251 µm. Table 6.1 summarizes the parameter variations in the B series, where $M1$ is the position of the slotted waveguide beside the phase section and $M2$ is the position of the slotted waveguide beside the gain section. The B devices targeted a tuning range much larger than what could be achieved with DFBs at 38 nm and included iterations that investigated the effect of the number of slots on meeting the single-mode criteria. From the simulated FWHM of these device done at an etch depth of 1.5 µm, single-mode criteria was not met according to Eqn. 2.41. However, the final FWHM of the reflectivity peaks would be greatly dependent on the quality of the process, as well as the final etch depth, and we wanted to measure this consequence. The variations of B had gain lengths that corresponded to the typical working devices around 2 mm, which was good for output power but lead to a calculated C_{FSR} that were too dense for single-mode emission. It was not clear if the effective cavity length will be accurately defined by Eqn. 2.42, since the gain compensation factor for ICLs is unknown [87]. This means the C_{FSR} calculation is just an estimate. The S_{FSR} for these devices were on the smaller end of the targeted range and the total physical length of the B devices were around 5 mm. With respect to other design iterations, this represents a modest increase in device length that we hope will not prevent lasing.
Table 6.2 includes the device parameters resulting from the slot period combinations designated C with $M1$ =251 µm and $M2$ =294 µm. The C devices were designed to achieve a similar tuning range to DFBs, with a tuning range of 22 nm. Quasi-continuous tuning was challenged in these devices by selecting a higher S_{FSR} of 8.8 nm. From the simulated FWHM of these devices, done at an etch depth of 1.4 µm, and calculated C_{FSR} single-mode criteria was met according to Eqn. 2.41. With the large value of ΔS_{FSR} between the two slotted sections, the C designs should have the highest SMSR. The C devices are shorter than the B devices and have a total length that is closer to the typical FP ICL length. However, the gain lengths are much shorter so meeting criteria for threshold may be the challenge for these devices.
The focus of the two different designs, B and C, was to test different ΔS_{FSR} while still targeting the emission wavelength of C1643. The second goal was to investigate the effect of different gain section lengths and the number of slots. At a high level, these designs represent probing two different modes of

Parameters	B3	B4	B5	B6
M1 Period (μm)	251	251	251	251
Phase Length (μm)	499	499	499	499
M2 Period (μm)	294	294	294	294
M1 FSR (nm)	6.3	6.3	6.3	6.3
M2 FSR (nm)	5.4	5.4	5.4	5.4
ΔFSR (nm)	0.9	0.9	0.9	0.9
Tuning Range (nm)	38	38	38	38
M1 N	5	6	6	7
M2 N	4	5	6	6
M1 Length (μm)	1253	1504	1504	1754
M2 Length (μm)	1177	1471	1765	1765
M1+M2 Length (μm)	2430	2975	3269	3520
M1 L_{eff} (μm)	501	627	627	752
M2 L_{eff} (μm)	441	588	736	736
M1+M2 L_{eff} (μm)	943	1215	1362	1487
M1 HWHM (nm)	0.5	0.47	0.47	0.395
M2 HWHM (nm)	0.60	0.50	0.4	0.4
Half ΔFSR (nm)	0.45	0.45	0.45	0.45
Desired Device Length (μm)	4878	5251	4878	5251
Res. Gain Length (μm)	1949	1777	1110	1233
New Cavity FSR (nm)	0.50	0.48	0.57	0.52
Single-mode criteria?	N/N	N/N	N/N	N/N

Table 6.1: Design iterations implemented for the slot period combination designated B in order to meet the organization constraints and consequences of the adjustments.

operation: short devices with a small tuning range and long devices with a large tuning range. Other designs, designated A and D, were simulated and considered, but could not be included in the mask design. They are included in App. 7.

The arrangement of these SVT designs on the mask are shown in the layout depicted in Fig. 6.5. The slot and mesa layers are included with the cleave order highlighted and numbered in red. This also separates the different design regions, highlighted with purple boxes. The C devices are in the first 8 rows (of 32) lasers but share the total length. The B devices are at the beginning of the remaining rows. The ends of the rows include test sections that will help diagnose any issues with the fabrication or performance encountered.

At the top right of the sample is the electrical isolation test section. Trenches with widths of 10 µm, 15 µm, 20 µm, 30 µm, and 50 µm were etched into 8 µm mesa. We refer to the features as trenches to distinguish the difference in their function from slots. Slots provide reflection to the optical modes while trenches provide electrical isolation between sections to allow independent operation. It was anticipated that the

Parameters	C7	C8	C9	C10
M1 Period (μm)	181	181	181	181
Phase Length (μm)	360	360	360	360
M2 Period (μm)	251	251	251	251
M1 FSR (nm)	8.8	8.8	8.8	8.8
M2 FSR (nm)	6.3	6.3	6.3	6.3
ΔFSR (nm)	2.5	2.5	2.5	2.5
Tuning Range (nm)	22	22	22	22
M1 N	5	6	5	6
M2 N	7	7	7	7
M1 Length (μm)	906	1088	906	1088
M2 Length (μm)	1754	1754	1754	1754
M1+M2 Length (μm)	2611	2842	2661	2842
M1 L_{eff} (μm)	363	453	363	453
M2 L_{eff} (μm)	752	752	752	752
M1+M2 L_{eff} (μm)	1114	1205	1114	1205
M1 HWHM (nm)	0.635	0.635	0.635	0.635
M2 HWHM (nm)	0.405	0.405	0.405	0.405
Half ΔFSR (nm)	1.25	1.25	1.25	1.25
Desired Device Length (μm)	3381	3381	3661	3661
Res. Gain Length (μm)	360	179	640	459
New Cavity FSR (nm)	0.92	0.97	0.80	0.83
Single-mode criteria?	Y/Y	Y/Y	Y/Y	Y/Y

Table 6.2: Design iterations implemented for the mirror combination designated C in order to meet the organization constraints and consequences of the adjustments.

SL cladding may be a difficult material to achieve electrical isolation in because of the current spreading. The isolation test section allowed the resistance between the sections to be measured to see how it scaled with trench volume. The minimum target for electrical isolation was $\approx$1 kΩ. In the SVT devices, one trench width was chosen a priori to simplify the design; a trench width of 15 µm was selected.

Below this, next to the B3 and B5 devices, is the FP ICL test section. This section had two purposes: checking the quality of the fabrication run between the different samples and having material to cleave into different lengths to investigate the cavity spacing. This could be used to infer the effective cavity length based on the mode spacing observed in the SVT ICLs.

With the remaining space on the sample, two-section slotted ICLs were added. There was enough space for two permutations of each slot period and slot number. The gain section's length was determined by the remaining space to the edge of the sample. These lasers would have multiple slot reflectivity peaks within the gain bandwidth of the ICL, but they should be single-mode within that peak. The means the measured mode spacing in the spectra should match the simulated S_{FSR}. This section allowed the

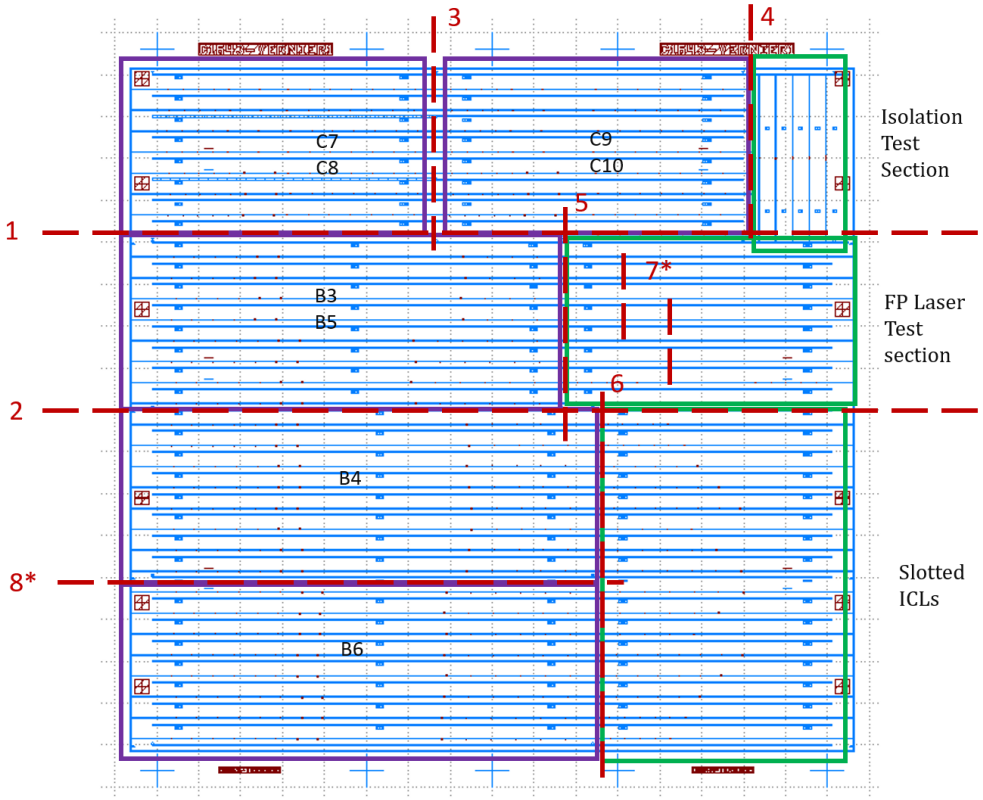

Figure 6.5: The SVT photolithography mask layout with the mesa ridges. The purple boxes represent the groupings of the different designs. The different iterations are labelled as well. The red lines and numbers represent the cleave lines and the order. The green boxes represent the devices that are not SVT; the isolation slot test section, the FP laser test section, and the two section slotted ICLs.

different slot patterns and tuning capabilities to be tested independently. Based on the slot number from each pattern and etch depth on the sample, the relationship between the FWHM of the reflectivity peaks and cavity FSR on the SMSR of these designs could also be investigated.

6.3 Multi-section Laser Fabrication

The first fabrication run for the SVT ICLs followed the same fabrication steps as process 2 for slotted ICLs, Sec. 5.1, with a few modifications. An overview of the SVT ICL process is illustrated in Fig. 6.6. Process 2 steps are represented in purple boxes with an additional step for the isolation trench openings highlighted in blue. For this fabrication run, slot widths of 1.25 µm and ridge widths of 8 µm implemented with targeted etch depths of 1.4 µm, 1.6 µm, and 1.8 µm for samples SVT1, SVT2, and SVT3. The mesa were all 8 µm wide even though this was a bit larger than the 2λ =7.2 µm limit predicted for transverse single-mode emission. In order to avoid the wings that resulted from the mesa etching, the slots were made narrower and a slot length of 5 µm was used.

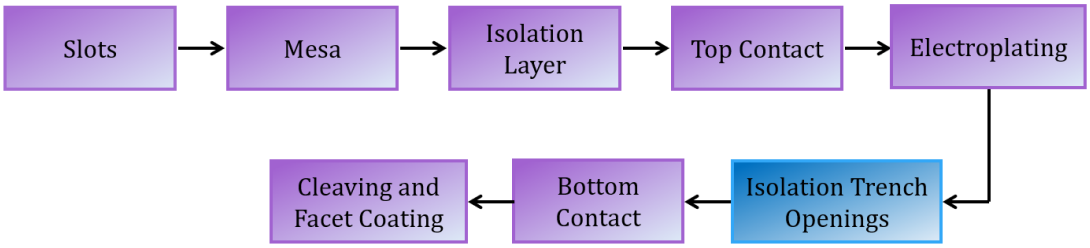

Figure 6.6: Overview of the SVT ICL process.

Isolation trenches

The isolation trenches on the sample were made to be the same length as the mesa. This choice was made to ensure electrical isolation and no wing formation at the mesa boundary during dry etching. They could not be covered by top contact of Ti/Pt/Au or by the electroplated Au in order to ensure isolation. The FP ICL test section was also not electroplated so that there could be flexibility in cleaving the lengths after fabrication and testing, described previously. The entire isolation trench test section was also not electroplated for convenience.

In order to be able to electroplate a section, a current needs to be able to flow there. This meant that the top contact layer needed to be connected between the sections of the SVT ICLs during the electroplating step. These connections needed to be broken after to remove the electrical connection between the sections so the lasers could be independently pumped. These connections were broken via ion bombardment etching using Ar. This etching step is completely physical but is successful in removing the metal without damaging the rest of the sample or the active region.

Fig. 6.7 illustrates the openings in the resist mask used for the ion etch and how it aligns to the previous device layers. The mesa ridge is shown in blue and the top contact layer is shown in light purple. The dark pink box represents and area with no metal, direction on top of the isolation trench. The openings in the resist mask where the top contact connections were etched are shown in red. Following DFB ICL mask design, space with no metal is placed between the contact pads to provide clear separation in the next

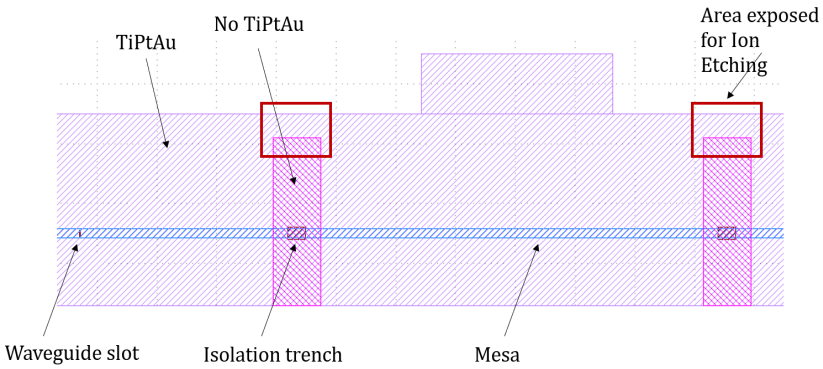

Figure 6.7: The ion etch mask layout with respect to the SVT ICL device layers.

electroplated Au layers and to help cleaving. After the ion etch, the samples were cleaned and ready to be cleaved. Fig. 6.8A shows an image of an isolation trench between two contact pads in the test section. Etching abnormalities are observed at the trench-mesa overlap. Fig. 6.8B shows an overview image of the SVT sample. The dark areas indicate sections that have not been electroplated in Au and the separation between the sections on the SVT ICL devices is clear. During electroplating bubbles formed in the Au layer of the process, which made it difficult to properly contact with the probes for current injection. It was observed that the phase section was fabricated to be one slot period from M1 instead of twice the slot period. The shorter phase section will not pose a problem but could limit the continuity of tuning achieved.

These samples needed to be cleaved carefully in order to maintain the design length. The marks for cleaving are numbered in Fig. 6.5. First, the horizontal cleaves, 1 and 2, separated the sample into thirds. Next, vertical cleaves separated the sections and defined the final lengths of the lasers (and their facets). The final step was facet coating: the sections for B and C devices had AR coatings applied to both facets while the two-section slotted ICLs had an AR coating applied to the facet near the slots and an HR coating applied to the facet near the gain.

6.4 SVT ICL performance

SVT1 and SVT3 were successfully fabricated but SVT2 was damaged during the process run and no devices could be salvaged for testing. The tests and results obtained from the isolation trench section, the FP ICL test section, the two-section slotted ICL section and the SVT ICL section will be discussed below.

6.4.1 Isolation trench test section

The resistance was measured between the two sections by contacting the pads or mesa with the probes connected to a Fluke multimeter. During cleaving, the devices for trench widths of 10 µm and 15 µm were damaged on SVT3. In Fig. 6.9A the resistance with respect to the trench widths on SVT1 with a trench depth of 1.4 µm is plotted. A linear fit for these points gives a slope of $m = 20\,\Omega\,\mu\text{m}^{-1}$. Meanwhile,

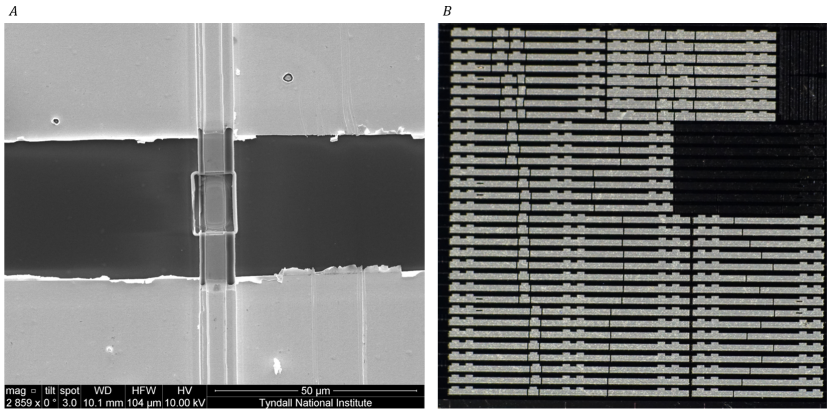

Figure 6.8: *A:* An SEM image depicting an isolation trenches after fabrication. *B:* An overview image of the SVT sample before cleaving.

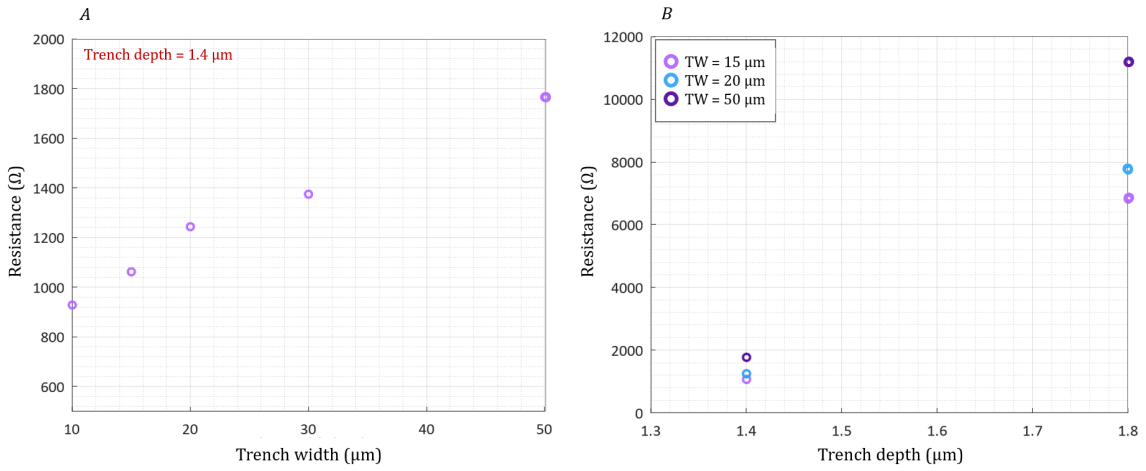

Figure 6.9: The resistance measurements for the isolation trenches. *A:* The measurements from SVT1 are shown as the slot width increases. *B:* The measurements are shown as the etch depth increases, i.e. for SVT1 and SVT3.

the linear fit for the SVT3 sample have a slope of $m = 121\,\Omega\,\mu m^{-1}$. In Fig. 6.9B, the resistance with respect to the trench depth is shown. These trench depths were assumed to be the same as the slot depths. More statistics are needed to make a better statement about the trend for the trench depth. As expected, increasing the depth has a stronger effect on the resistance. The SVT1 sample had isolation at the anticipated required level of $\approx$1 kΩ while the SVT3 sample had isolation an order of magnitude higher at a level of $\approx$10 kΩ.

6.4.2 FP ICL test section

The FP ICL test section was tested before facet coating to determine whether or not the process was normal. This involved measuring the spectra and the PIV performance for 3 mm devices, as shown in Fig. 6.10 for the SVT3 sample. Fig. 6.10A shows the PIV measurements for some of the devices at 10 °C in CW mode. The two best devices, FP12 and FP14, had I_{thr} $\approx$80 mA, R_s of 5.5 Ω and V_{OC} of 2.7 V. FP10 and FP11 illustrate typical defects observed through this fabrication run: FP10 looks as if there was a short and FP11 appears to have leakage current and subsequently failed around the threshold at 80 mA. Fig. 6.10B shows a typical spectrum measured with an OSA at 10 °C and with a current of 130 mA. There are two peaks observed spaced by 13 nm likely due to a higher order transverse mode appearing from the 8 nm ridge. C_{FSR} was measured to be 1.67 nm although it was anticipated to be around 0.6 nm and significant ASE is observed.

The short of FP10 likely originates from a defect that occurred during the process. There are no wings that can be formed, but pinholes can occur in the isolation layer and lead to shorts. The breakdown of FP11 could originate from the process or from the growth. While the leakage current and drop in voltage indicates a parasitic resistance from the isolation layer or contact depositions, the surface defects observed on the sample indicate "spitting" from the gas cells that could result in shorts if this occurred in the layers below the active region[169]. The larger C_{FSR} measured in the spectra would come from a smaller cavity length than what was physically measured; around 1 mm rather than 3 mm, or a much larger n_g than

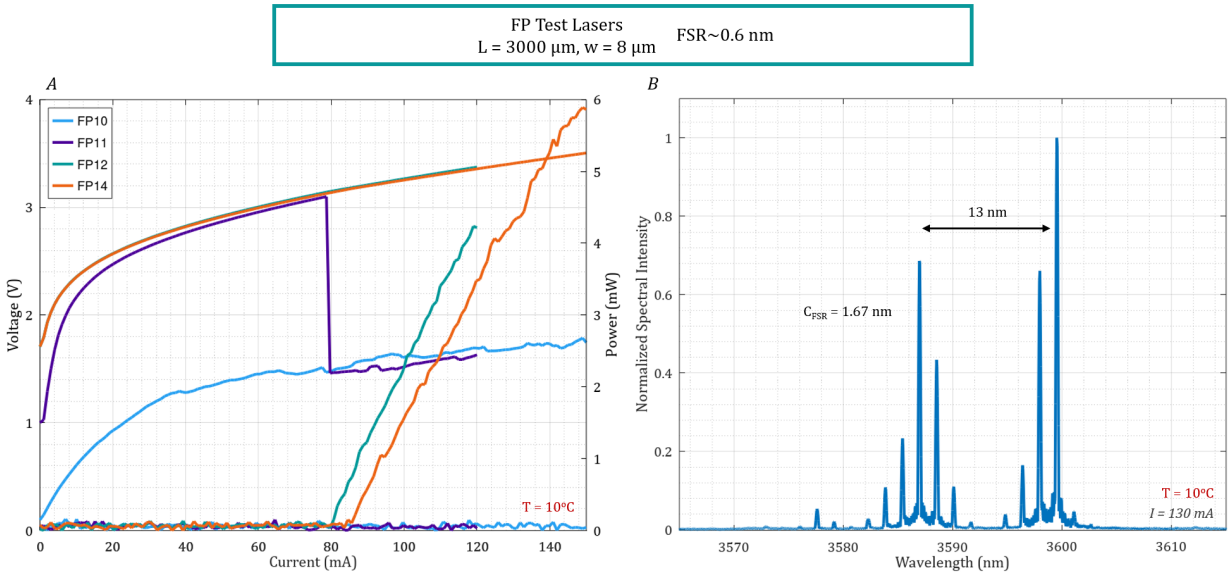

Figure 6.10: The spectra and PIV from the FP ICL test section are shown for L=3000 µm (w=8 µm) and uncoated facets. *A:* The PIV characteristics are presented for all the FP ICLs of the section. *B:* The spectra are presented for two of the lasers well above threshold.

anticipated. It should also be noted that although the output power of FP12 was above 4 mW where the spectra was measured, the signal coupled into the OSA was very low suggesting a broad divergence angle of these devices and likely there are weaker modes unresolved in the ASE.
The PIV results suggest there were some problems during the processing step that resulted in local defects: shorts and leakage current are observed for some of the devices. The large amount of ASE observed in the spectra of the devices points towards a non-optimal growth. SVT1 and SVT3 did not give a high yield of working devices so decoupling the growth/process issues from design issues will be challenging. However, the SVT process proceeded with facet coating since the FP ICLs lased. The FP ICL spectra will be used as a platform to understand if any suppression or interaction is happening from the slots in the multi-section devices and an FTIR will be used rather than an OSA in order to accommodate the low signal.

6.4.3 Two-section slotted ICLs

The goal of this section was to diagnose whether the further steps of the process worked and verify the design choices for the slotted waveguides, such as which slot period was well matched to the material, and how the gain section affected the performance. The PIV characteristics of the slotted ICLs were measured by placing the laser bars directly on a TEC and collecting the output from the AR coated facet. Either as a propagation of the processing irregularity seen with the FP ICLs or from the electroplated contact, many of the devices were shorted and many gain sections didn't lase. This presented itself in the IV curves as failures that would occur past 100 mA. The section did not lase and so the injection current was increased to over 200 mA in some cases, searching for threshold behaviour, and this lead to device failure.

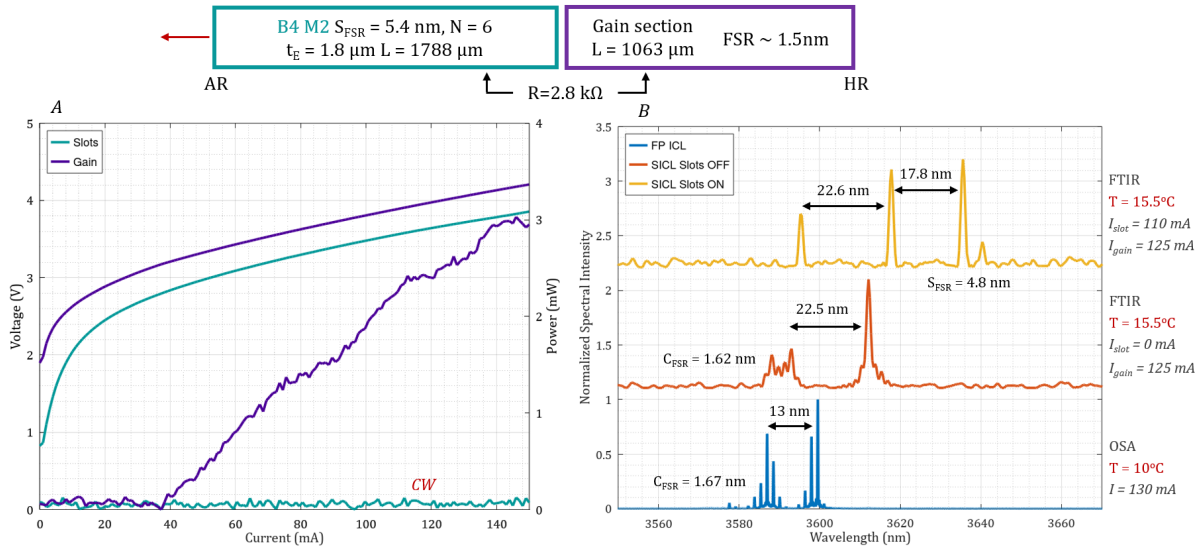

Figure 6.11: Electro-optical characteristics from the two-section slotted ICL test lasers mounted epi-up in CW mode. *A:* The PIV curves for each section pumped independently are shown at 10 °C in CW. *B:* The spectra are shown for the slotted ICLs at 15.5 °C with the slots pumped (ON) and not pumped (OFF) with the FP ICL spectra plotted for comparison.

There were some devices whose gain section lased that demonstrate encouraging performance on the SVT3 sample, with t_E =1.8 µm. Fig. 6.11 illustrates the electro-optical characteristics of a B design with d =294 µm, $N = 6$, and gain section length of 1063 µm. The total length was 2.88 mm after cleaving. Fig. 6.11A shows the PIV in CW mode at 10 °C. The resistance between the two sections was 2.1 kΩ. The gain section demonstrates typical performance; I_{thr} is 37 mA, V_{OC} is 3.0 V and R_s is 8.2 Ω. The slot section does not lase in CW and the IV curve reveals current leakage that lowers V_{OC} to 2.5 V while R_s remains the approximately the same at 7.6 Ω.

Fig. 6.11B illustrates the efficacy of the slotted waveguide on the spectra. The FP ICL laser operated at 10 °C at 130 mA is shown for reference in the bottom spectrum. The middle spectrum was measured at 15.5 °C with gain current of 125 mA and the slots "OFF" with no current. There are two bunches of peaks observed spaced by 22.5 nm and the C_{FSR} was measured to be an average of 1.62 nm although it was anticipated to be around 1.5 nm. Laser emission is still observed and looks similar to the FP ICLs, but with a lower signal. This indicates that even if the slotted section doesn't lase, significant absorption isn't occurring. The top spectrum was measured at 15.5 °C with gain current of 125 mA and the slots "ON" with 110 mA. The spectra is modified: there are three groups of peaks observed spaced by 22.6 nm and 17.8 nm, respectively. In the third group, it appears the slots spacing is observed and a S_{FSR} of 4.8 nm was measured, although the targeted value was 5.4 nm. The spacing of the group of peaks could be from a convolution of the FP spectra and the S_{FSR}. At a higher temperature, the spacing between the bunches of peak increases with temperature (App. 7). One of the modes in these groups may then overlap with an integer multiple of the S_{FSR}. These results demonstrate a long slotted section does not absorb all of the light generated by the gain section and that even with sub-threshold pumping, the slots interact with the cavity modes.

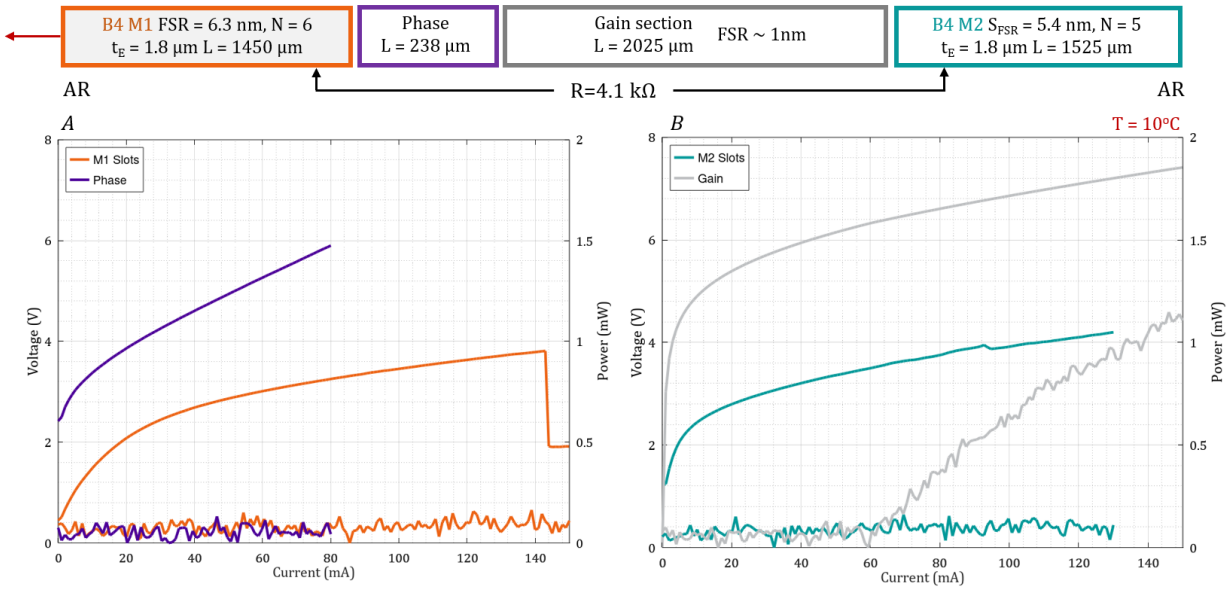

Figure 6.12: The PIV from the SVT ICL fabricated with the B4 design with each section pumped individually is shown at 10 °C in CW mode, as measured out of the facet on the M1 slot section. *A:* The M1 slot section and the phase section are presented. *B:* The gain section and the M2 slot section are presented.

The PIV performance is not as expected and the processing defect was worse on the slots. However, the current and temperature shift the spectra from the gain section indicating that we control the emission wavelength as we would with a FP ICL. The interaction of the slotted waveguide with the output when pumped suggests we may be able to observe mode suppression and some tuning in the SVT ICLs.

6.4.4 SVT ICL section

Unfortunately, none of the devices were fully operational which means all 4 sections did not have normal IV curves. Many of gain and slotted sections from the devices did not lase. On SVT3 the B4 design had a gain section that lased and delivered promising results.

Fig. 6.12 illustrates the PIV characteristics of the semi-functional *B4*, with a total device length was 5.1 mm after cleaving measured in CW mode at 10 °C. The resistance between the slotted sections was 4.1 kΩ. Fig. 6.12A shows the measurements of the M1 slotted section and the phase section. No lasing is observed in either section and the IV curves are not optimal. For the phase section the voltage is expected to be higher since the section length is very short, and a V_{OC} of 3.4 V is reasonable but an R_s of 32 Ω will be difficult for the section to support and leads to the high voltage of 6 V at 80 mA. For the M1 slotted section, there is a short which creates parasitic resistance from typical diode behaviour. The voltage is also quite low until a further breakdown occurs at around 140 mA. The measured V_{OC} was 2.6 V and was R_s of 8.7 Ω. Fig. 6.12B shows the measurements of the gain section and the M2 slotted section. No lasing is observed for the slots but lasing is observed in the gain section. The PI characteristics from the gain section are typical with an I_{thr} of 57 mA and a P_{Max} of 1.1 mW, but the IV characteristics show extremely high voltage. V_{OC} is 5.7 V and R_s is normal with 11 Ω. This indicates poor contacts creating an extra voltage barrier to

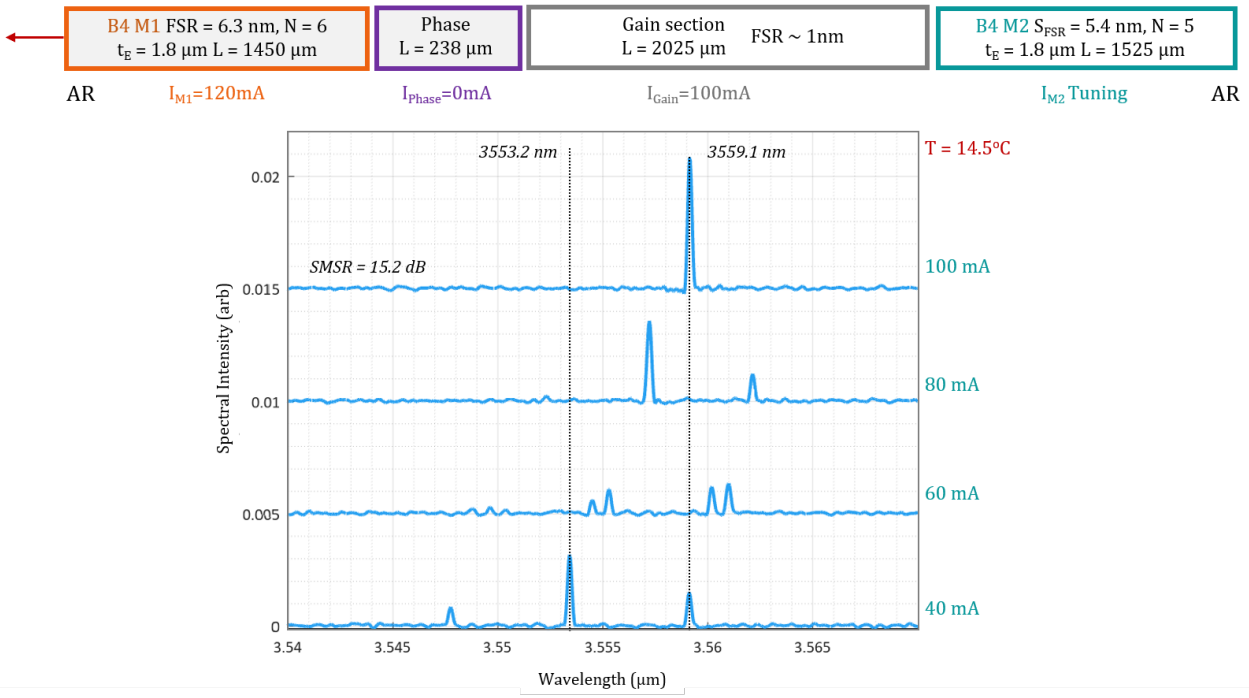

Figure 6.13: The spectral emission after tuning the M2 slotted section with currents of 40 mA, 60 mA, 80 mA, and 100 mA. The other sections had fixed currents with the M1 slots at 120 mA, the phase at 0 mA, and the gain at 100 mA at a heat sink temperature of 14.5 °C.

overcome before alignment of the cascade in the active region can occur. In the M2 slotted section, less leakage current is observed and the voltage is lower than the gain section, closer to the FP ICLs, with a V_{OC} of 3.1 V, and a R_s of 8.7 Ω. Current pumping was stopped before 140 mA for this section.

From these results, it is unlikely the full tuning range targeted will be able to be achieved since it relies on the ability to shift the S_{FSR} of both waveguides. Without lasing, the ability to shift the mode is likely limited. With a fault in one section, it is unclear how the emission will be affected. The M1 slotted section was treated as a passive section and therefore a less adjustable S_{FSR}. Measuring the emission from the facet near M1 ensured interaction with the M1 slots. A comparison of the emission from each output is shown in App. 7.

Fig. 6.13 illustrates operating conditions where different aspects of the design can be measured by tuning the current from the M2 slotted section, I_{M2}, between 40 mA to 100 mA in increments of 20 mA at 14.5 °C. This was done with the other sections at fixed currents: the current for the M1 slots, I_{M1}, was 120 mA, the current for the phase, I_{Phase}, was 0 mA, and the current for the gain, I_{Gain}, was 100 mA. At I_{M2} =40 mA and 80 mA the S_{FSR} can be measured and is 5.69 nm. At I_{M2} =60 mA the C_{FSR} can be estimated from the modes appearing within the slot reflectivity peak and was measured to be 0.79 nm. The fact that two can be supported under the peaks allows the FWHM of the S_{FSR} to be estimated as well, and this indicates a width around 1.6 nm. The central peak from I_{M2} =40 mA at λ =3353.2 nm appeared to shift from multi-mode to single-mode at I_{M2} =100 mA with emission of 3559.1 nm and an SMSR of 15.2 dB. This represents a electrical tuning rate of 0.1 nm mA^{-1} and a total shift of $\Delta\lambda$ =5.9 nm, which is the S_{FSR} from M2. These results demonstrate the concept of Vernier tuning is viable on ICLs since the peak can be

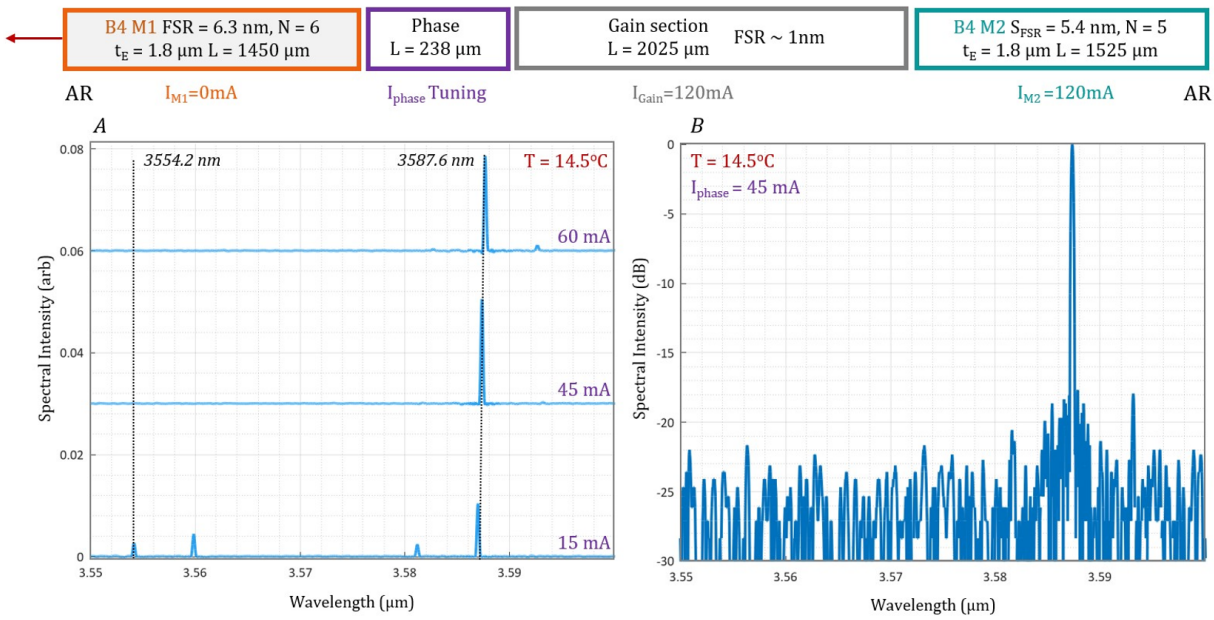

Figure 6.14: *A:* The spectral emission after tuning the Phase section with currents of 15 mA, 45 mA, and 60 mA. The other sections had fixed currents with I_{M1} =0 mA, I_{Gain} =120 mA, and I_{M2} =120 mA at a heat sink temperature of 14.5 °C. *B:* The spectra for the I_{Phase} =45 mA measurement plotted in the log scale to highlight the SMSR.

shifted by the full S_{FSR}. The SMSR can be adjusted by improving the FWHM of the slots and increasing the ΔS_{FSR}. From the measured C_{FSR} we can also estimate the effective cavity length is 2060 µm, which will correspond to the length of gain section and the penetration depth into the M2 slot section.

Fig. 6.14A shows operating conditions that extend the range of accessible emission wavelengths from the Vernier tuning concept. Overlap of the two S_{FSR} is changed by tuning of I_{Phase} between 15 mA to 60 mA in increments of 15 mA at 14.5 °C. This was done with the other sections at fixed currents: I_{M1} was set to 0 mA, I_{Gain} was set to 120 mA and I_{M2} was set to 120 mA. At I_{Phase} =15 mA multi-mode emission is observed, likely due to the partial overlap of the slotted waveguides. This becomes single-mode at I_{Phase} =45 mA when the slots are perfectly overlapped and moves back to multi-mode at I_{Phase} =60 mA as they move past optimal overlap. Between the lowest wavelength for I_{Phase} =15 mA at λ =3554.2 nm and the wavelength measured at I_{Phase} =60 mA at λ =3587.6 nm there is 33.4 nm. The wavelength 3587.6 nm can be accessed because of Vernier tuning. Single-section devices can not tune between 3554.2 nm using current injection alone. Measuring these two wavelengths at the same temperature demonstrates the use of Vernier tuning, albeit with a low SMSR. Fig. 6.14B depicts the best SMSR recorded for this device at I_{Phase} =45 mA with 17.7 dB.

Conclusion

This chapter presented the design, fabrication, and testing of the first ICLs implementing the Vernier tuning principle via slotted waveguides. Simulations of the various waveguide geometries were conducted to determine feasible device configurations to fabricate using standard UV photolithography and dry

etching.

Because of the low yield of this process run, it would be best to repeat since we could not during this project due to time constraints. There appear to be abnormalities during the isolation layer and/or contact layer depositions that resulted in leakage current and shorting across the samples. The electroplated contact had additional defects as well. The process could also be repeated on a different growth that can handle higher currents and that has less ASE in the spectra.

Nevertheless, performance of the SVT ICLs demonstrated the design was successfully implemented and Vernier tuning was realized. The accessible wavelength range was increased to 36 nm and single-mode emission was achieved over this range with a SMSR of 13 dB to 18 dB, although the tuning was not continuous. The material could successfully shift one mode by the S_{FSR} using electrical tuning and close to the targeted S_{FSR} of 5.7 nm was measured in the spectra with 5.4 nm. Finally, the isolation trenches successful met their targeted resistance with at least 1 kΩ between sections. Despite the many open questions remaining, the results are encouraging and the concept was successfully demonstrated.

CHAPTER 7

Conclusion

This thesis has presented a comprehensive exploration of the fabrication of slotted waveguides on GaSb based ICLs with emission between 3 µm to 4 µm for the realization of widely tunable mid-infrared semiconductor lasers. Single-section lasers were fabricated that coupled slots with a gain section for single-mode emission, two-section lasers were fabricated that decoupled these sections allowing for single-mode emission and independent section pumping, and four-section lasers were fabricated that coupled two different slotted waveguides together and employed Vernier tuning for a wider tuning range of single-mode emission. The research was divided into several chapters, each addressing a key step towards developing SVT ICLs.

Chapter 2 provided the foundation for the project and outlined the challenges faced by different types of semiconductor lasers in realizing emission in the mid-infrared range. ICLs are an efficient performer because of the interband cascade configuration employing type-II QWs to address the increasing Auger absorption. Techniques for single-mode waveguide designs were presented that introduce periodic modulation to the refractive index of the waveguide to create interference that can suppress unwanted cavity modes. Coupling multiple waveguides together can extend the tuning range using the concept of Vernier tuning. DFB gratings having been used for single-mode emission and applying Vernier tuning to ICLs, but slotted waveguides and slotted Vernier tuned designs have never been developed for ICLs. The state-of-the-art for slotted waveguide lasers, Vernier tuned devices, FP ICLs, and DFB ICLs was presented to provide context for development of novel slotted waveguide ICLs.

Chapter 3 introduced the complete technological process in place at the start of this thesis for fabricating FP ICLs. This included a description of the ICL structure design and growth as well as the microfabrication steps for making FP ICLs. We grew five different ICLs for this thesis with emission between 3.3 µm to 3.6 µm that demonstrated near state-of-the-art performance with threshold current densities between 150 $\mathrm{A\,cm^{-2}}$ to 350 $\mathrm{A\,cm^{-2}}$ as measured from narrow ridge FP ICLs that I used for characterization. These growths and the FP ICL process would serve as my starting point for the development of slotted waveguides on ICLs that were described in the remaining chapters.

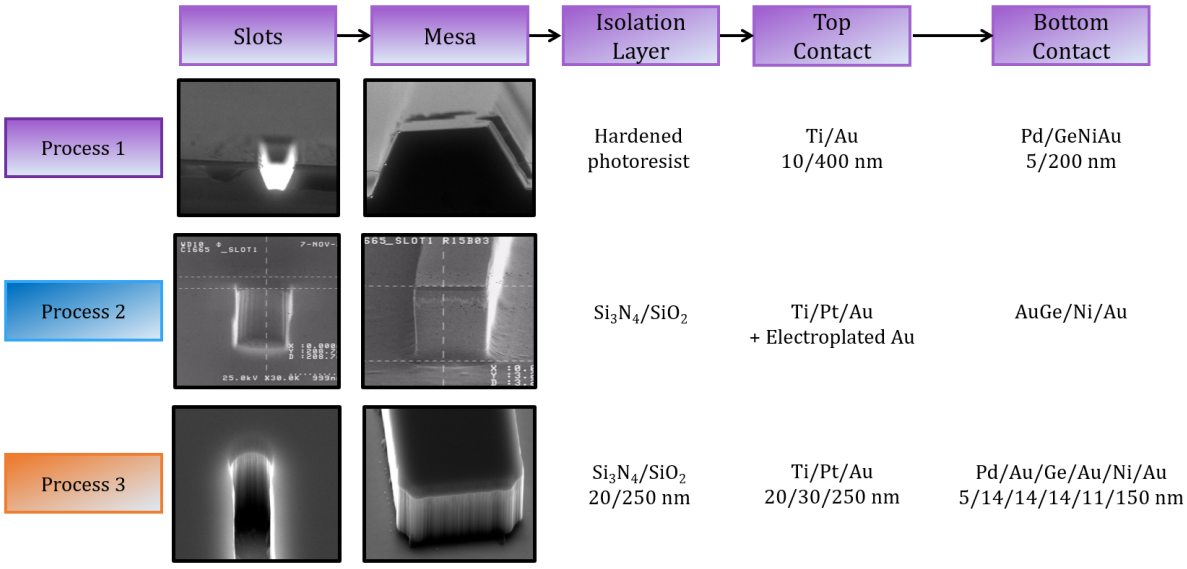

Figure 7.1: Overview of the steps and fabrication achievements from the three processes explored to fabricate single-section slotted ICLs.

Single-section slotted ICLs

Chapter 4 and 5 delved into the design and fabrication of slotted waveguides placed in the upper cladding of a FP ICL. Chapter 4 described the complete process for the first slotted ICL including the simulations, mask design, process development, and electro-optical characterization. The emphasis in this chapter was establishing an empirical link between simulations and single-mode emission that would serve as the foundation for further optimization. In Chapter 5 I pursued the optimization of single-mode performance by improving the fabrication of the slots. This included exploring different photolithography techniques and optimizing the dry etching recipe. In total, I developed three processes that are summarized in Fig. 7.1. Each process followed the same flow beginning with definition of the slots, definition of the mesa, deposition of the isolation layer, deposition of the top contact, substrate thinning, and finally deposition of the bottom contact. The goal of optimizing the process to have a vertical etch profile was achieved.

Two of the three process runs yielded slotted ICLs that demonstrated single-mode emission. The characterization of these devices was then used in the design of the SVT ICLs. The main objective for each process was to test a different slotted waveguide geometry to improve the SMSR and increase the continuous single-mode wavelength shift, $\Delta\lambda$, measured. The improvements/changes I made to the fabrication allowed narrower and deeper slots to be etched which helped ensure the targeted slot period was implemented on the growth. The optimizations explored resulted in the increase of the SMSR from 13 dB to 22.3 dB and an increase of $\Delta\lambda$ from 2 nm to 2.7 nm. There is still room for improvement in the process development: slots are partially filled with dielectric leading to non-uniform metal coverage that could be inducing losses. Thermal management also remains a necessary avenue to explore for epi-up devices. A thinner top contact in process 3 was used with respect to process 1; 200 nm vs 400 nm, which could have been the cause of relatively low rollover points observed for the third slotted ICLs. Electroplating was employed in process 2 but the performance enhancement could not be observed. A

Parameter	Slotted ICL 1	Slotted ICL 2	Slotted ICL 3
Growth	C1661	C1665	E802A
Emission λ	3.51 µm	3.39 µm	3.43 µm
d	6.68 µm	12.8 µm	13.1 µm/39.1 µm
w	8 µm	6.6 µm	8 µm
L	1.8 mm	1.2 mm	1.2 mm
λ tuning	0.1 nm/mA	–	0.2 nm/mA
Cont. $\Delta\lambda$	2 nm	–	2.7 nm
Max SMSR	13 dB	–	22.3 dB
I_{thr}	88 mA	–	54 mA
I_{max}	145 mA	–	100 mA
P_{max}	2 mW/facet	–	>1 mW/facet
T	20 °C	–	17 °C
d_s	1.2 µm	1.0 µm	0.74 µm
t_E	0.8 µm	1.0 µm	1.1 µm
N	269	94	34
n_{eff}	3.6781	*3.6025*	3.6656
Δn	0.00011 /mA	–	0.00021 /mA

Table 7.1: Summary of electro-optical parameters of the best slotted ICLs from each process run mounted epi-up. **Note: n_{eff} for C1665 was calculated from a* DFB *fabrication.*

summary of the characteristics of the best performers from process 1 and process 3 are listed in Table 7.1.

Part of the challenge of introducing a new waveguide design to a new materials system was developing a model that gave an accurate representation of the indices of refraction and their dispersive properties. ICL structures are difficult to model due to the many layers in the structure and because III-V-Sb materials have not been extensively characterized. The indices of refraction of the binary compounds are well described, but the differential laser gain and optical losses are not extensively characterized [170, 171]. From the experimental results with the slotted ICLs, the material model used for the FIMMWAVE simulations of the waveguide design was verified to yield working devices. This starting point paves the way for future optimization by shrinking the parameter space that needs to be explored.

The performance of these lasers can be optimized for single-mode operation without considering their use for designing SVT ICLs. For example, the output power can be significantly increased by mounting epi-down, as shown in Fig. 7.2, but was not explored in this thesis because of the difficulty pumping multiple sections epi-side down. Fig. 7.2A presents the PIV characteristics of slotted ICLs from process 3 mounted epi-down in comparison to their counterparts mounted epi-up in Fig. 7.2B (Sec. 5.2.5). Mounting epi-down results in more effective heat transfer away from the active region which shifts the gain curve and likely caused these devices to be multi-mode from a subsequent mismatch with the slot period. However, LP3 was not lasing in the epi-up configuration and becomes the device with the highest output power in the epi-down configuration. This suggests the opportunity for slots with higher reflectivity strength, and therefore more suppression strength, without compromising on the power.

The next steps to explore to improve the design would be to decouple the length from the number of slots. This would allow an independent optimization of each parameter and for the link between the number of slots, the etch depth, and the FWHM to be characterized. A simulation parameter could be

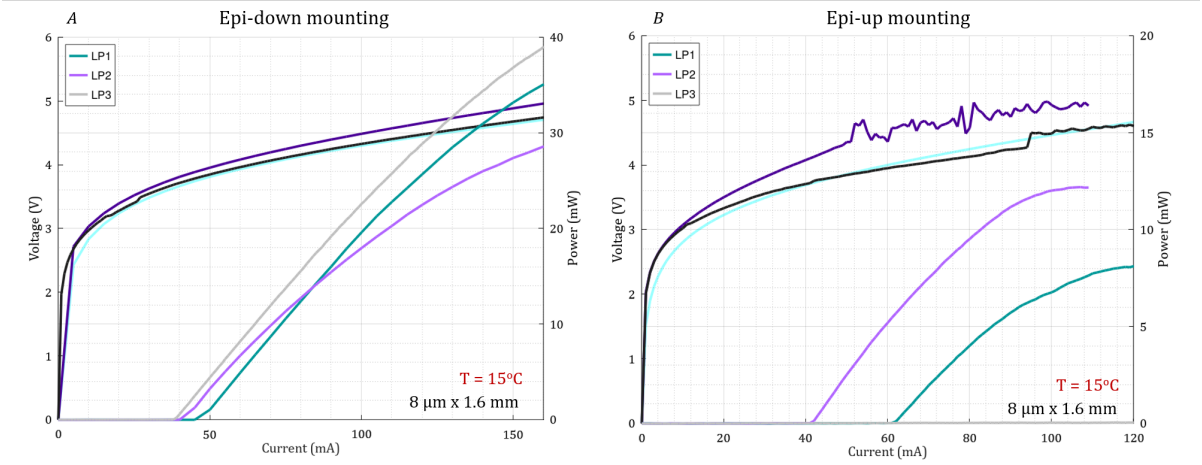

Figure 7.2: PIV from the LP samples E802A, with LP1 t_E =0.8 µm, LP2 t_E =1.1 µm, LP3 t_E =1.0 µm, w =8 µm and L =1.6 mm. *A:* The etch series for the SICLs mounted epi-down. *B:* Comparison of the etch series mounted epi-up. Both measurements are shown for 15 °C The noise in the IV curve is just due to poor contact with the probe needle.

investigated that represents the process to process variation since it was difficult to target specific etch depths for systematic study. Perhaps a parameter such as the slot aspect ratio, a ratio of the etch depth to the slot width, would be suitable since it allows the fluctuation of both the slot width and etch depth. Now that the etch profile is vertical, the targeted mesa ridge width also needs to be decreased from 8 µm in order to ensure transverse single-mode operation.

Multi-section ICLs

Chapter 6 presented a diverse range of device configurations used to assess and understand the design challenges in fabricating Vernier tuned lasers. In order to pump sections independently, isolation trenches were added to the lasers which were new features that needed to provide electrical isolation. Since these were not designed and fabricated for ICLs before, especially for those with a SL cladding layer that has significant current spreading, a test section was included to characterize the isolation achieved as the trench geometry was altered. In the test section, the non-electroplated 15 µm wide trenches met this requirement for with resistances of 1.1 kΩ and 10.4 kΩ for trench depths of 1.4 µm and 1.8 µm, respectively. In order to assess the process quality, FP ICLs were fabricated without Au electroplating for reference. Their PIV performance revealed leakage current and problems with the isolation layer/contact depositions, indicating shorts and low voltage measured in the multi-section devices were due to an issue with the process rather than the design. The growth was not optimized and the gain profile resulted in more broadly spaced cavity modes than expected. For this process, the ridge widths were 8 µm and supported higher order transverse modes. Some devices still lased with typical threshold currents, suggesting there was still an opportunity to study the emission from the multi-section devices.
Two-section slotted ICLs were fabricated as an intermediate stepping stone between the single-section slotted ICLs and the development of the four-section SVT ICLs. These lasers were necessary to evaluate the new slotted waveguide designs efficacy with the growth and to characterize the impact of decoupling

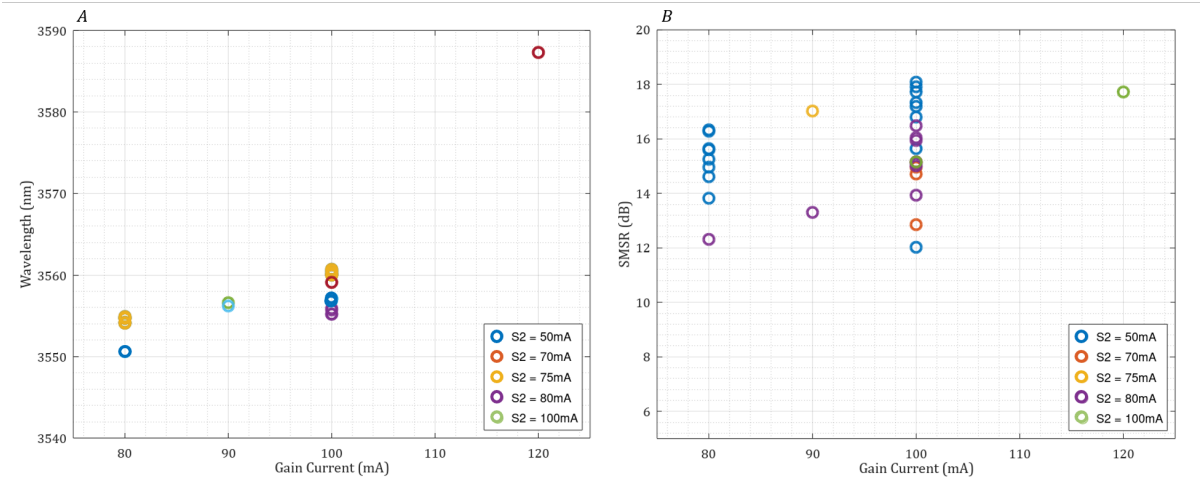

Figure 7.3: Summary of single-mode emission measured over I_{Gain} and I_{S2} currents at 14.5 °C. I_{Phase} and I_{S1} are not shown. *A:* The wavelengths measured for the given operating conditions. *B:* The corresponding SMSR for the given operating conditions.

the two sections on emission. The issues with the process were observed in this section of devices as well and many of the sections did not lase due to leakage current and low voltage. Some devices had a gain section that did lase, with a threshold current similar to that of the FP ICL reference, and the spectra could be measured and the emission wavelength predictably shifted through the slotted section. This suggested significant absorption did not occur at this wavelength though the slotted section still interacted with the modes created in the gain section and some mode suppression was observed.

The four-section SVT ICLs designed explored two different slotted waveguide combinations with variations included that aimed to pinpoint the optimal FWHM for Vernier tuning. A significant practical challenge was designing the mask to accommodate these variations of long lasers. The emphasis on this process run was to investigate the initial design choices for the SVT ICLs, so minimal changes were made to the process. None of the lasers had two slotted sections that were free of the process issues, therefore the SVT ICLs were characterized with one "passive" slotted section and one "active" slotted section. This limited the device's tuning continuity and range. Fig. 7.3A illustrates the wavelengths achieved while Fig. 7.3B illustrates the corresponding SMSR. A comprehensive current-tuning map was not created, these measurements just present the operating conditions that were explored.

The convolution of problems with the process, a non-optimal growth, and unknowns about the efficacy of the design make the results difficult to interpret. However, we established a starting point for the development of the design and process which is a crucial step towards realizing SVT ICLs. The summary of the single-mode emission illustrated in Fig. 7.3 are encouraging results in terms of the range of accessible wavelengths and SMSR achieved and demonstrate a proof of concept for SVT ICLs.

Perspectives

The SVT ICLs demonstrated the potential for achieving widely tunable mid-infrared lasers, addressing the need for spectral coverage, precision, and flexibility in various applications. The tunability and single-mode operation of the slotted ICLs hold promise for applications in spectroscopy and gas sensing

in remote packaged sensors because of their low power threshold and long lifetime[101].
The Si integration of photonics is an important field of research that can offer solutions to the increasing global energy and data demands addressing the limitations faced by electronics [172]. The use of Si wafers provides an order of manitude reduction in cost in terms of price per area and allows for the processing of Si-based photonic integrated circuits with ultra-high volume and low cost. Due to the indirect band structure of the group IV elements, Si photonics often requires the integration of III–V lasers for efficient light generation. Both SVT and slotted ICLs can be fabricated on non-native wafers, such as Si and GaAs, which allow them to be used with other photonic integrated circuits[173]. One step towards this would be to develop ICLs with Si_3N_4 waveguides as was done for diode lasers in another OPTAPHI project[174]. Another interesting prospect for ICLs is their long lifetimes in monolithically integrated devices, despite defects that can arise due to lattice mismatch [175]. Therefore pursuing the development of SVT and slotted ICLs could yield the first widely tunable sources on Si.
Meanwhile, optical frequency combs have found a multitude of applications across various scientific and technological fields due to their unique properties. Optical frequency combs generate uniformly spaced spectral modes that have a known phase relation. Comb spectroscopy offers the possibility to directly map the optical spectrum to the radio-frequency domain and offer a chip solution without losing spectral resolution. However in the MIR, frequency comb generation is still limited to external pump lasers. Recently, ICLs have revealed the possibility of generating frequency-modulated combs based on gain-induced four-wave mixing indicating their ability to play a role in monolithic dual-comb spectroscopic applications[176]. At telecommunications wavelengths of around 1.55 µm, monolithically integrated photonic integrate circuits have used to generate tunable combs by gain switching one section of the two section slotted laser[177]. Continuing the developed of the multi-section slotted ICLs could allow a similar platform to be employed in generating MIR combs.
In conclusion, this thesis has contributed valuable insights into the development of widely tunable mid-infrared semiconductor lasers, opening avenues for further research and practical applications in the field of photonics and sensing.

List of Publications

Publications

J. A. M. Fordyce, D. A. Diaz-Thomas, L. O'Faolain, A. N. Baranov, T. Piwonski, L. Cerutti; Single-mode interband cascade laser with a slotted waveguide. Appl. Phys. Lett. 21 November 2022; 121 (21): 211102. doi.org/10.1063/5.0120460

J. A. M. Fordyce, D. A. Diaz-Thomas, T. Piwonski, A. N. Baranov, L. O'Faolain, L. Cerutti; Continuous-wave single-mode slotted interband cascade lasers emitting at 3.5 µm. In Novel In-Plane Semiconductor Lasers XXII. March 2023; Vol. 12440. SPIE. doi.org/10.1117/12.2648200

Conference Presentations

J. A. M. Fordyce, D. A. Diaz-Thomas, T. Piwonski, A. N. Baranov, L. O'Faolain, and L. Cerutti; Single-mode interband cascade lasers for petrochemical process monitoring. Mid-Infrared Optoelectronic Materials and Devices (MIOMD). September 2021. Online. *Winner of student presentation award*.

J. A. M. Fordyce, D. A. Diaz-Thomas, L. O'Faolain, A. N. Baranov, T. Piwonski, and L. Cerutti; Continuous-wave single-mode slotted interband cascade lasers emitting at 3.5 µm. Photonics West – Novel In-Plane Semiconductor Lasers XXII. January 2023.

J. A. M. Fordyce, J. Nauschutz, R. Weih, L. Cerutti, T. Piwonski, L. O'Faolain; Extended wavelength tuning of multi-section interband cascade lasers with slotted waveguides above 3 µm. Conference on Photonics for Advanced Spectroscopy and Sensing (CPASS) – Infrared Sources and Detectors. September 2023.

Bibliography

[1] Iouli Gordon, Laurence Rothman, Christian Hill, Roman Kochanov, Y Tan, Peter Bernath, Manfred Birk, V Boudon, Alain Campargue, and KV Chance. The hitran 2016 molecular spectroscopic database. *Journal of Quantitative Spectroscopy and Radiative Transfer*, 203:3–69, 2017.

[2] D. A. Diaz Thomas. *Design, fabrication and investigation of Interband Cascade structures for mid-IR VCSELs*. Ph.D. thesis, Université de Montpellier, 2020.

[3] Stephen J. Sweeney, Timothy D. Eales, and Igor P. Marko. 1 - the physics of mid-infrared semiconductor materials and heterostructures. In Eric Tournié and Laurent Cerutti, editors, *Mid-infrared Optoelectronics*, Woodhead Publishing Series in Electronic and Optical Materials, pages 3–56. Woodhead Publishing, 2020.

[4] Larry A. Coldren, G. A. Fish, Y. Akulova, J. S. Barton, L. Johansson, and C. W. Coldren. Tunable semiconductor lasers: A tutorial. *J. Lightwave Technol.*, 22, 2004.

[5] nanoplus nanosystems and technologies gmbh. Accessed on May 3, 2023.

[6] Thorlabs. Accessed on May 3, 2023.

[7] I. Vurgaftman, R. Weih, M. Kamp, J. R. Meyer, C. L. Canedy, C. S. Kim, M. Kim, W. W. Bewley, C. D. Merritt, J. Abell, and S. Hofling. Interband cascade lasers. *Journal of Physics D: Applied Physics*, 48(12), 2015.

[8] Mihaela Girtan. Is photonics the new electronics? *Materials Today*, 17(3):100–101, 2014.

[9] T. Aldhafeeri, M. K. Tran, R. Vrolyk, M. Pope, and M. Fowler. A review of methane gas detection sensors: Recent developments and future perspectives. *Inventions*, 5, 2020.

[10] Olivier Spitz, Shiyuan Zhao, Pierre Didier, Daniel Andres Díaz-Thomas, Laurent Cerutti, Alexei N Baranov, Hedwig Knötig, Robert Weih, Johannes Köth, Benedikt Schwarz, et al. Interband cascade technology for next-generation mid-ir communication and quantum applications. In *2022 IEEE Photonics Society Summer Topicals Meeting Series (SUM)*, pages 1–2. IEEE, 2022.

[11] Alexandre Delga and Luc Leviandier. Free-space optical communications with quantum cascade lasers. In *Quantum sensing and nano electronics and photonics XVI*, volume 10926, pages 140–155. SPIE, 2019.

[12] Ben Henderson, Amir Khodabakhsh, Markus Metsälä, Irène Ventrillard, Florian M Schmidt, Daniele Romanini, Grant AD Ritchie, Sacco te Lintel Hekkert, Raphaël Briot, Terence Risby, et al. Laser spectroscopy for breath analysis: towards clinical implementation. *Applied Physics B*, 124:1–21, 2018.

[13] Michael von Edlinger, Julian Scheuermann, Robert Weih, Lars Nähle, Marc Fischer, Johannes Koeth, Sven Höfling, and Martin Kamp. Interband cascade lasers for applications in process control and environmental monitoring. In *Optics and Photonics for Energy and the Environment*, pages EM2A–5. Optica Publishing Group, 2015.

[14] Lorenzo Cocola, Massimo Fedel, Giuseppe Tondello, and Luca Poletto. Tunable diode laser absorption spectroscopy for gas sensing in the agri-food industry. In *Imaging and Applied Optics 2016*, page JW1F.3. Optica Publishing Group, 2016.

[15] Optaphi homepage. Accessed September 2023.

[16] Chenyu Yao, Shoufei Gao, Yingying Wang, Pu Wang, Wei Jin, and Wei Ren. Mir-pump nir-probe fiber-optic photothermal spectroscopy with background-free first harmonic detection. *IEEE Sensors Journal*, 20(21):12709–12715, 2020.

[17] M. J. Wallace, Gaurav Jain, Robert Mckenna, Frank Bello, and J. F. Donegan. Tuning behaviour of slotted vernier widely tunable lasers. *Opt. Express*, 27(12), 2019.

[18] DS Baer, RK Hanson, ME Newfield, and NKJM Gopaul. Multiplexed diode-laser sensor system for simultaneous h 2 o, o 2, and temperature measurements. *Optics letters*, 19(22):1900–1902, 1994.

[19] M. von Edlinger, R. Weih, J. Scheuermann, L. Nahle, M. Fischer, J. Koeth, and M. Kamp. Monolithic single mode interband cascade lasers with wide wavelength tunability. *Applied Physics Letters*, 109:201109, 2016.

[20] Q. Lu, W.H. Guo, D. Byrne, and J.F. Donegan. Design of slotted single-mode lasers suitable for photonic integration. *IEEE Photonics Technology Letters*, 22, 2010.

[21] J. P. Englestadter. *Laser Diodes for Photonic Integrated Circuits*. Ph.D. thesis, University College Cork, 2009.

[22] David Caffey, Timothy Day, Chul Soo Kim, Mijin Kim, Igor Vurgaftman, William W Bewley, J Ryan Lindle, Chadwick L Canedy, Joshua Abell, and Jerry R Meyer. Performance characteristics of a continuous-wave compact widely tunable external cavity interband cascade lasers. *Optics express*, 18(15):15691–15696, 2010.

[23] A.N. Chryssis, Dagenais Mario, John Bruno, and John Bradshaw. Tunable external cavity interband cascade laser. pages 701 – 702, 11 2007.

[24] Alfred Perot and Charles Fabry. On the application of interference phenomena to the solution of various problems of spectroscopy and metrology. *Astrophysical Journal, vol. 9, p. 87*, 9:87, 1899.

[25] Arnold B Arons and MB Peppard. Einstein's proposal of the photon concept—a translation of the annalen der physik paper of 1905. *American Journal of Physics*, 33(5):367–374, 1965.

[26] Martin J. Klein. Max planck and the beginnings of the quantum theory. *Archive for History of Exact Sciences*, 1(5):459–479, 1962.

[27] J. P. Gordon, H. J. Zeiger, and C. H. Townes. The maser—new type of microwave amplifier, frequency standard, and spectrometer. *Phys. Rev.*, 99:1264–1274, Aug 1955.

[28] NG Basov and AM Prokhorov. Theory of the molecular generator and molecular power amplifier. *Sov. Phys. JETP*, 3(3):426–429, 1956.

[29] T.H. Maiman. Stimulated optical radiation in ruby. *Nature*, 187:493–494, 1960.

[30] Photonics Spectra. A history of the laser: 1960 - 2019, 2019.

[31] R. N. Hall, G. E. Fenner, J. D. Kingsley, T. J. Soltys, and R. O. Carlson. Coherent light emission from gaas junctions. *Phys. Rev. Lett.*, 9:366–368, Nov 1962.

[32] LA Coldren. Multi-section tunable laser with differing multi-element mirrors. Technical report, 1990.

[33] Jerome Faist, Federico Capasso, Deborah L. Sivco, Carlo Sirtori, Albert L. Hutchinson, and Alfred Y. Cho. Quantum cascade laser. *Science*, 264(5158):553–556, 1994.

[34] Rui Q. Yang. Interband cascade laser target the mid-infrared. *Compound Semiconductor*, 2019.

[35] M. Kim, C. L. Canedy, W. W. Bewley, C. S. Kim, J. R. Lindle, J. Abell, I. Vurgaftman, and J. R. Meyer. Interband cascade laser emitting at 3.75 um in continuous wave above room temperature. *Appl. Phys. Lett.*, 92, 2008.

[36] Orazio Svelto. *Principles of Lasers*. Springer, 5 edition, 2010.

[37] Larry A. Coldren, Scott W. Corzine, and Milan L. Masanovic. *Diode Lasers and Photonic Integrated Circuits*. John Wiley and Sons, 2 edition, 2012.

[38] Jens Buus, Markus-Christian Amann, and Daniel J. Blumenthal. *Tunable Laser Diodes and Related Optical Sources*. John Wiley and Sons, 2 edition, 2005.

[39] Q. Durlin, J.P. Perez, L. Cerutti, J.B. Rodriguez, T. Cerba, T. Baron, E. Tournié, and P. Christol. Midwave infrared barrier detector based on ga-free inas/inassb type-ii superlattice grown by molecular beam epitaxy on si substrate. *Infrared Physics & Technology*, 96:39–43, 2019.

[40] Laura Monge Bartolome. *Toward mid-infrared semiconductor lasers on silicon photonic integrated circuits*. Ph.D. thesis, Université de Montpellier, 2021.

[41] D. A. Diaz-Thomas, O. Stepanenko, M. Bahriz, S.Calvez, E. Tournié, A. N. Baranov, G. Almuneau, and L. Cerutti. Interband cascade lasers with algaassb cladding layers emitting at 3.3 um. *Optics Express*, 27, 2019.

[42] Zhores I. Alferov. Nobel lecture: The double heterostructure concept and its applications in physics, electronics, and technology. *Rev. Mod. Phys.*, 73, Oct 2001.

[43] G.A. Sai-Halasz, R. Tsu, and L. Esaki. A new semiconductor superlattice. *Applied Physics Letters*, 30(12):651 – 653, 1977.

[44] J. R. Meyer, C. A. Hoffman, F. J. Bartoli, and L. R. Ram-Mohan. Type-ii quantum-well lasers for the mid-wavelength infrared. *Appl. Phys. Lett*, 67(6), 1995.

[45] M. W. Prairie and R. M. Kolbas. A general derivation of the density of states function for quantum wells and superlattices. *Superlattices and Microstructures*, 7(4), 1990.

[46] KS Gadedjisso-Tossou, S Belahsene, MA Mohou, E Tournié, and Y Rouillard. Recombination channels in 2.4–3.2 μm gainassb quantum-well lasers. *Semiconductor Science and Technology*, 28(1):015015, 2012.

[47] J. Hader, J. V. Moloney, S. W. Koch, L. Fan, and M. Fallahi. Carrier recombination in semiconductor lasers: Beyond the abc. In *2006 International Conference on Numerical Simulation of Semiconductor Optoelectronic Devices*, pages 39–40, 2006.

[48] J. Hader, J.V. Moloney, and S.W. Koch. Supression of carrier recombination in semiconductor lasers by phase-space filling. *Applied Physics Letters*, 87(20), 2005.

[49] G. Bourdon, Ikwera Robert, Isabelle Sagnes, and I. Abram. Spontaneous emission in highly excited semiconductors: Saturation of the radiative recombination rate. *Journal of Applied Physics*, 92:6595–6600, 12 2002.

[50] P.T. Landsberg and D.J. Robbins. The first 70 semiconductor auger processes. *Solid-State Electronics*, 21(11):6595–6600, 1978.

[51] A.R. Beattie and P.T. Landsberg. Auger effect in semiconductors. *Proc. R. Soc. Lond. A*, 249, 1959.

[52] H.K Choi and G.W. Turner. Antimonide-based strained quantum-well diode lasers. *Physica Scripta T*, 69, 1997.

[53] GG Zegrya and VA Kharchenko. New mechanism of auger recombination of nonequilibrium current carriers in semiconductor heterostructures. *Soviet physics, JETP*, 74(1), 1992.

[54] I. Vurgaftman, J. R. Meyer, and L. R. Ram-Mohan. Band parameters for iii–v compound semiconductors and their alloys. *Journal of Applied Physics*, 89(11), 2001.

[55] Scott D Sifferman, Hari P Nair, Rodolfo Salas, Nathanial T Sheehan, Scott J Maddox, Adam M Crook, and Seth R Bank. Highly strained mid-infrared type-i diode lasers on gasb. *IEEE Journal of Selected Topics in Quantum Electronics*, 21(6):1–10, 2015.

[56] Sprengel Stephan, Demmerle Frederic, and Amann Markus-Christian. Novel inp-and gasb-based light sources for the near to far infrared. *Semiconductor Science and Technology*, 31(11):113005, 2016.

[57] N Bandyopadhyay, Y Bai, S Tsao, S Nida, S Slivken, and M Razeghi. Room temperature continuous wave operation of λ 3-3.2 μm quantum cascade lasers. *Applied Physics Letters*, 101(24), 2012.

[58] Y. Yao, A. Hoffman, and C. Gmachl. Mid-infrared quantum cascade lasers. *Nature Photon*, 6, 2012.

[59] Andre Slonopas and David Tomkinson. Study of the natural auger suppression mechanism in heterostructures through heteroboundary engineering. *J. Phys. Chem. A*, 121(40), 2017.

[60] C. H. Grein, M. E. Flatte, J. T. Olesberg, S. A. Anson, L. Zhang, and T. F. Boggess. Auger recombination in narrow-gap semiconductor superlattices incorporating antimony. *Journal of Applied Physics*, 92(12), 2002.

[61] GG Zegrya and AD Andreev AF. Theory of the recombination of nonequilibrium carriers in type-ll heterostructures. *semiconductors*, 2:3, 1996.

[62] R.Q. Yang. 12 - interband cascade (ic) lasers. In Alexei Baranov and Eric Tournié, editors, *Semiconductor Lasers*, Woodhead Publishing Series in Electronic and Optical Materials, pages 487–513. Woodhead Publishing, 2013.

[63] Jerry R. Meyer, Chadwick L. Canedy, Mijin Kim, Chul Soo Kim, Charles D. Merritt, William W. Bewley, and Igor Vurgaftman. Comparison of auger coefficients in type i and type ii quantum well midwave infrared lasers. *IEEE Journal of Quantum Electronics*, 57(5):1–10, 2021.

[64] Kedong Zhang, Yuzhe Lin, Wanhua Zheng, Rui Q. Yang, Hong Lu, and Yan-Feng Chen. Low threshold inas-based interband cascade lasers grown by mbe. *Journal of Crystal Growth*, 586:126618, 2022.

[65] Jerry R. Meyer, William W. Bewley, Chadwick L. Canedy, Chul Soo Kim, Mijin Kim, Charles D. Merritt, and Igor Vurgaftman. The interband cascade laser. *Photonics*, 7(3), 2020.

[66] J.T. Getty, E.J. Skogen, L.A. Johansson, and L.A. Coldren. Cw operation of 1.55-um bipolar cascade laser with record differential efficiency, low threshold, and 50-/spl omega/ matching. *IEEE Photonics Technology Letters*, 15(11), 2003.

[67] I. Vurgaftman, W.W. Bewley, C.L. Canedy, C.S. Kim, M. Kim, C.D. Merritt, J. Abell, J.R. Lindle, and J.R. Meyer. Rebalancing of internally generated carriers for mid-infrared interband cascade lasers with very low power consumption. *Nat Commun*, 2(585), 2011.

[68] Igor Vurgaftman, William W. Bewley, Chadwick L. Canedy, Chul Soo Kim, Mijin Kim, J. Ryan Lindle, Charles D. Merritt, Joshua Abell, and Jerry R. Meyer. Mid-ir type-ii interband cascade lasers. *IEEE Journal of Selected Topics in Quantum Electronics*, 17(5):1435–1444, 2011.

[69] Hedwig Knötig, Josephine Nauschütz, Nikola Opačak, Sven Höfling, Johannes Koeth, Robert Weih, and Benedikt Schwarz. Mitigating valence intersubband absorption in interband cascade lasers. *Laser & Photonics Reviews*, 16(9), 2022.

[70] D.A. Kozlowski, J.S. Young, J.M.C England, and R.G.S Plumb. Longitudinal mode control in 1.3pm fabry-perot lasers by mode suppression. Number 143. IEE Proc.-Optoelectron, 1996.

[71] V.N. Luk'yanov, A.T. Semenov, N.V. Shelkov, and S.D. Yakubovich. Lasers with distributed feedback (review). *J. Quantum Electronics*, 5(11), 1975.

[72] Jochen Seufert, Merlind Fischer, Marg Legge, K. Roessner, R. Werner, Jürgen Hildenbrand, J. Herbst, Armin Lambrecht, and Johannes Koeth. Dfb laser diodes and quantum cascade lasers for sensors in safeguard applications. 10 2008.

[73] H Kogelnik and C Vo Shank. Coupled-wave theory of distributed feedback lasers. *Journal of applied physics*, 43(5):2327–2335, 1972.

[74] Hedwig Knotig. *Interband cascade lasers and detectors: From active region design to devices*. PhD thesis, Technischen Universitat Wien, 2022.

[75] Richard M. De La Rue. *Waveguide Optoelectronics*. Springer Netherlands, 5 edition, 1992.

[76] F. Grillot. On the effects of an antireflection coating impairment on the sensitivity to optical feedback of ar/hr semiconductor dfb lasers. *Journal of Quantum Electronics*, 45(6), 2009.

[77] H. C. Casey, S. Somekh, and M. Ilegems. Room-temperature operation of low-threshold separate-confinement heterostructure injection laser with distributed feedback. *Applied Physics Letters*, 57(5), 08 1975.

[78] Quentin Gaimard, Laurent Cerutti, R. Teissier, and Aurore Vicet. Distributed feedback gasb based laser diodes with buried grating. *Applied Physics Letters*, 104, 03 2014.

[79] M Carras, M Garcia, X Marcadet, O Parillaud, A De Rossi, and S Bansropun. Top grating index-coupled distributed feedback quantum cascade lasers. *Applied physics letters*, 93(1), 2008.

[80] Jerome Faist, Claire Gmachl, Federico Capasso, Carlo Sirtori, Deborah L Sivco, James N Baillargeon, and Alfred Y Cho. Distributed feedback quantum cascade lasers. *Applied Physics Letters*, 70(20):2670–2672, 1997.

[81] R. Weih, L. Nahle, S. Hofling, J. Koeth, and M. Kamp. Single mode interband cascade lasers based on lateral metal gratings. *Applied Physics Letters*, 105(071111), 2014.

[82] RD Martin, S Forouhar, S Keo, RJ Lang, RG Hunsperger, RC Tiberio, and PF Chapman. Cw performance of an ingaas-gaas-algaas laterally-coupled distributed feedback (lc-dfb) ridge laser diode. *IEEE photonics technology letters*, 7(3):244–246, 1995.

[83] M Hummer, K Rossner, A Benkert, and A Forchel. Gainassb-algaassb distributed feedback lasers emitting near 2.4 μm. *IEEE Photonics Technology Letters*, 16(2):380–382, 2004.

[84] C. S. Kim, M. Kim, W. W. Bewley, J. R. Lindle, C. L. Canedy, I. Vurgaftman, and J. R. Meyer. Single-mode distributed-feedback interband cascade laser for the midwave infrared. *Applied Physics Letters*, 88, 2006.

[85] John Patchell, Dewi Jones, Brian Kelly, and James O'Gorman. Specifying the wavelength and temperature tuning range of a fabry perot laser containing refractive index perturbations. Number 5825 in Opto-Ireland 2005. Proc. of SPIE, 2005.

[86] I. Mathews, A. Abdullaev, S. Lei, R. Enright, M. J. Wallace, and J. F. Donegan. Reducing thermal crosstalk in ten-channel tunable slotted-laser arrays. *Opt. Express*, 23(18), 2015.

[87] D.C. Byrne, J.P.Engelstaedter, W.H. Guo, Q.Y. Lu, B. Corbett, B. Roycroft, J. O'Callaghan, F.H. Peters, and J.F. Donegan. Discretely tunable semiconductor lasers suitable for photonic integration. *Quantum Electronics*, 15(3), 2009.

[88] Robert Weih, Martin Kamp, and Sven Höfling. Interband cascade lasers with room temperature threshold current densities below 100 a/cm2. *Applied Physics Letters*, 102(23), 2013.

[89] Chadwick L. Canedy, Joshua Abell, Charles D. Merritt, William W. Bewley, Chul Soo Kim, Mijin Kim, Igor Vurgaftman, and Jerry R. Meyer. Pulsed and cw performance of 7-stage interband cascade lasers. *Opt. Express*, 22(7), 2014.

[90] Jeremy A Massengale, Yixuan Shen, Rui Q Yang, Samuel D Hawkins, and John F Klem. Long wavelength interband cascade lasers. *Applied Physics Letters*, 120(9), 2022.

[91] Yixuan Shen, JA Massengale, Rui Q Yang, SD Hawkins, and AJ Muhowski. Pushing the performance limits of long wavelength interband cascade lasers using innovative quantum well active regions. *Applied Physics Letters*, 123(4), 2023.

[92] Julian Scheuermann, Robert Weih, Michael von Edlinger, Lars Nähle, Marc Fischer, Johannes Koeth, Martin Kamp, and Sven Höfling. Single-mode interband cascade lasers emitting below 2.8 μm. *Applied Physics Letters*, 106(16), 2015.

[93] J Koeth, R Weih, J Scheuermann, M Fischer, A Schade, M Kamp, and S Höfling. Mid infrared dfb interband cascade lasers. In *Infrared Remote Sensing and Instrumentation XXV*, volume 10403, pages 46–52. SPIE, 2017.

[94] J. Koeth, R. Weih, J. Scheuermann, M. Fischer, A. Schade, M. Kamp, and S. Höfling. Mid infrared dfb interband cascade lasers. *Proc. SPIE*, 1040308(10403), 2017.

[95] C. Merritt, W. Bewley, C. Canedy, Chul Soo Kim, Myungsub Kim, M. Warren, I. Vurgaftman, and Jerry Meyer. Distributed feedback interband cascade lasers with reduced contact duty cycles. *Proc. SPIE 9855, Next-Generation Spectroscopic Technologies IX*, 98550C, 2016.

[96] Igor Vurgaftman, William W. Bewley, Chadwick L. Canedy, Chul Soo Kim, Mijin Kim, Charles D. Merritt, Joshua Abell, and Jerry R. Meyer. Interband cascade lasers with low threshold powers and high output powers. *IEEE Journal of Selected Topics in Quantum Electronics*, 19(4):1200210–1200210, 2013.

[97] C. S. Kim, M. Kim, J. Abell, W. W. Bewley, C. D. Merritt, C. L. Canedy, I. Vurgaftman, and J. R. Meyer. Mid-infrared distributed-feedback interband cascade lasers with continuous-wave single-mode emission to 80c. *Applied Physics Letters*, 101(6), 08 2012.

[98] W. Sun, Z. Gongyuan, Z. Pengfei, M. Wallace, F. Bello, Q. Lu, W. Guo, and J. F. Donegan. Design of 1.3-um high-performance directly modulated lasers based on high-order slotted surface gratings. *Quantum Electronics*, 53(5), 2017.

[99] eblana photonics. Accessed on May 3, 2023.

[100] Xuefeng Jia, Lijun Wang, Ning Zhuo, Zhiwei Jia, Jinchuan Zhang, Fengqi Liu, Junqi Liu, Shenqiang Zhai, and Zhanguo Wang. Single-mode quantum cascade laser at 5.1 um with slotted refractive index modulation. *IEEE PHOTONICS TECHNOLOGY LETTERS*, 29(22), 2017.

[101] M. Nawrocka, Q. Lu, W. H. Guo, A. Abdullaev, F. Bello, J. O'Callaghan, T. Cathcart, and J. F. Donega. Widely tunable six-section semiconductor laser based on etched slots. *Optics Express*, 22(16), 2014.

[102] B. Meng, Y. Q. Zeng, G. Liang, J. Tao, X. N. Hu, E. Rodriguez, and Q. J. Wang. Broadly continuously tunable slot waveguide quantum cascade lasers based on a continuum to continuum active region design. *Applied Physics Letters*, 107(11), 2015.

[103] Jane Hodgkinson and Ralph P Tatam. Optical gas sensing: a review. *Measurement science and technology*, 24(1):012004, 2012.

[104] Maximilian Lackner. Tunable diode laser absorption spectroscopy (tdlas) in the process industries–a review. *Reviews in Chemical Engineering*, 23(2):65–147, 2007.

[105] James D Ingle Jr and Stanley R Crouch. Spectrochemical analysis. 1988.

[106] M. von Edlinger, J. Scheuermanna, L. Nählea, C. Zimmermanna, L. Hildebrandta, M. Fischera, J. Koetha, R. Weihb, S. Höflingb, and M. Kamp. Dfb interband cascade lasers for tunable laser absorption spectroscopy from 3 to 6 um. Number 8993 in Quantum Sensing and Nanophotonic Devices XI. Proc. of SPIE, 2014.

[107] Angelo Sampaolo, Pietro Patimisco, Marilena Giglio, Andrea Zifarelli, Hongpeng Wu, Lei Dong, and Vincenzo Spagnolo. Quartz-enhanced photoacoustic spectroscopy for multi-gas detection: A review. *Analytica Chimica Acta*, 1202:338894, 2022.

[108] Y.D. Premchand, A. Bieberle-Hütter, and L.J. Gauckler. Fuel cells – solid oxide fuel cells | micro cells. In Jürgen Garche, editor, *Encyclopedia of Electrochemical Power Sources*, pages 148–157. Elsevier, 2009.

[109] C. J. Hill and R. Q. Yang. Mbe growth optimization of sb-based interband cascade lasers. *Journal of Crystal Growth*, 278, 2005.

[110] Robert Weih, Adam Bauer, M. Kamp, and Sven Höfling. Interband cascade lasers with algaassb bulk cladding layers. *Optical Materials Express*, 3:1624–1631, 10 2013.

[111] nextnano software for semiconductor nanodevices. Accessed on August 8, 2023.

[112] H. Abid, M. Rezki, and H. Aourag. Electronic structure and optical properties of the quaternary alloy gaalassb. *Materials Science and Engineering: B*, 41(3):314–321, 1996.

[113] Claude L. Alibert, Mohammed Skouri, Andre F. Joullie, M. Ghali Benouna, and Shatha Sadiq. Refractive indices of alsb and gasb-lattice-matched algaassb in the transparent wavelength region. *Journal of Applied Physics*, 69:3208–3211, 1991.

[114] W. W. Bewley, J. R. Lindle, C. L. Canedy, M. Kim, C. S. Kim, D. C. Larrabee, I. Vurgaftman, and J. R. Meyer. Gain, loss, and internal efficiency in interband cascade lasers emitting at $\lambda = 3.6$–4.1um. *Journal of Applied Physics*, 103(1), 2008.

[115] Dr. M. Kamp from University of Wurzburg. Lasim is a simulation program developed used by nanoplus. email martin.kamp(at)physik.uniwuerzburg.de.

[116] I. Vurgaftman, R. Weih, M. Kamp, J. R. Meyer, C. L. Canedy, C. S. Kim, M. Kim, W. W. Bewley, C. D. Merritt, J. Abell, and S. Hoefling. Interband cascade lasers. *Journal of Physics D : Applied Physics*, 48(12), 2015.

[117] C. Zhou, B. Cui, I. Vurgaftman, C. L. Canedy, C. S. Kim, M. Kim, W. W. Bewley, C. D. Merritt, J. Abell, J. R. Meyer, and M. Grayson. Thermal conductivity tensors of the cladding and active layers of interband cascade lasers. *Applied Physics Letters*, 105:261905, 2014.

[118] C. Zhou, I. Vurgaftman, C. L. Canedy, C. S. Kim, M. Kim, W. W. Bewley, C. D. Merritt, J. Abell, J. R. Meyer, A. Hoang, A. Haddadi, M. Razeghi, and M. Grayson. Thermal conductivity tensors of the cladding and active layers of antimonide infrared lasers and detectors. *Optical Material Express*, 3(10), 2013.

[119] W.W. Bewley, C.L. Canedy, C.S. Kim, I. Vurgaftman, M. Kim, and J.R. Meyer. Antimonide type-ii "w" lasers: growth studies and guided-mode leakage into substrate. *Physica E: Low-dimensional Systems and Nanostructures*, 20(3):466–470, 2004.

[120] S Roux, L Cerutti, E Tournie, B Gérard, G Patriarche, A Grisard, and E Lallier. Low-loss orientation-patterned gasb waveguides for mid-infrared parametric conversion. *Optical Materials Express*, 7(8):3011–3016, 2017.

[121] C. L. Canedy, J. Abell, W. W. Bewley, E. H. Aifer, C. S. Kim, J. A. Nolde, M. Kim, J. G. Tischler, J. R. Lindle, E. M. Jackson, I. Vurgaftman, and J. R. Meyer. Molecular beam epitaxial growth effects on type-ii antimonide lasers and photodiodes. *Journal of Vacuum Science Technology B*, 28, 2010.

[122] K. Y. Cheng. Development of molecular beam epitaxy technology for iii–v compound semiconductor heterostructure devices. *Journal of Vacuum Science & Technology A*, 31(050814), 2013.

[123] A. Y. Cho and J. E. Arthur. *Progress in Solid State Chemistry*, volume 10. Pergamon, New York, 1975.

[124] Christophe Charpentier. *Molecular beam epitaxial growth of high-quality Sb-based III/V semiconductor heterostructures*. PhD thesis, ETH Zurich, 2014.

[125] J.H. Neave, B.A. Joyce, and P.J. Dobson. Dynamics of film growth of gaas by mbe from rheed observations. *Appl. Phys. A*, 31(8), 1968.

[126] J.J. Harris, B A. Joyce, and P.J. Dobson. Oscillations in the surface structure of sn-doped gaas during growth by mbe. *Surface Science*, 103(1), 1981.

[127] P. M. Thibado, B. R. Bennett, B. V. Shanabrook, and L. J. Whitman. A rheed and stm study of sb-rich alsb and gasb (0 0 1) surface reconstructions. *Journal of Crystal Growth*, 175/176:317–322, 1997.

[128] AS Bracker, MJ Yang, BR Bennett, JC Culbertson, and WJ Moore. Surface reconstruction phase diagrams for inas, alsb, and gasb. *Journal of crystal growth*, 220(4):384–392, 2000.

[129] Hédi Fitouri, Mohamed Mourad Habchi, and Ahmed Rebey. High-resolution x-ray diffraction of iii–v semiconductor thin films. In Alicia Esther Ares, editor, *X-ray Scattering*, chapter 7. IntechOpen, 2017.

[130] Mateusz Dyksik, Marcin Motyka, Grzegorz Sek, Jan Misiewicz, Matthias Dallner, Robert Weih, Martin Kamp, and Sven Hofling. Submonolayer uniformity of type ii inas/gainsb w-shaped quantum wells probed by full-wafer photoluminescence mapping in the mid-infrared spectral range. *Nanoscale Res. Lett.*, 10(402), 2015.

[131] J. R. Arthur. Interaction of ga and as2 molecular beams with gaas surfaces. *Journal of Applied Physics*, 39(8), 1968.

[132] Rui Q. Yang, Cory J. Hill, Baohua Yang, and John K. Liu. Room-temperature type-ii interband cascade lasers near 4.1 um. *Applied Physics Letters*, 83(11), 2003.

[133] Microchemicals hmds. Aug. 15, 2023.

[134] José M. Quero, Francisco Perdigones, and Carmen Aracil. 11 - microfabrication technologies used for creating smart devices for industrial applications. In Stoyan Nihtianov and Antonio Luque, editors, *Smart Sensors and MEMs (Second Edition)*, Woodhead Publishing Series in Electronic and Optical Materials, pages 291–311. Woodhead Publishing, second edition edition, 2018.

[135] Regina Luttge. Chapter 2 - basic technologies for microsystems. In Regina Luttge, editor, *Microfabrication for Industrial Applications*, Micro and Nano Technologies, pages 13–54. William Andrew Publishing, Boston, 2011.

[136] S. Manakasettharn, J.A. Taylor, and T. Krupenkin. 4.13 - superhydrophobicity at micron and submicron scale. In David L. Andrews, Gregory D. Scholes, and Gary P. Wiederrecht, editors, *Comprehensive Nanoscience and Technology*. Academic Press, 2011.

[137] Katarzyna Racka-Szmidt, Bartłomiej Stonio, Jaroslaw Żelazko, Maciej Filipiak, and Mariusz Sochacki. A review: Inductively coupled plasma reactive ion etching of silicon carbide. *Materials*, 15(1), 2022.

[138] L. Zhang, L. F. Lester, R. J. Shul, C. G. Willison, and R. P. Leavitt. Inductively coupled plasma etching of iii–v antimonides in bcl 3 /ar and cl 2 /ar. *Journal of Vacuum Science and Technology B*, 17, 1999.

[139] T. A. Nilsen, A. Martinez, L. F. Lester, and B. O; Fimland. High aspect ratio etching of gasb/algaassb for photonic crystals. Number 891 in Materials Research Society Symposium. Materials Research Society, 2006.

[140] S. S. Cooperman, H. K. Choi, H. H. Sawin, and D. F. Kolesar. Reactive ion etching of gaas and algaas in a bcl3–ar discharge. *Journal of Vacuum Science and Technology B*, 7, 1989.

[141] P MORIARTY and G HUGHES. Preliminary studies on the rate of native oxide growth on iii-v semiconductor surfaces by scanning tunnelling microscopy. *L'Actualité chimique*, (2):180–183, 1992.

[142] J.A Robinson and S.E Mohney. An improved in-based ohmic contact to n-gasb. *Solid-State Electronics*, 48(9):1667–1672, 2004.

[143] Thorlabs s180c power meter. Aug. 12, 2023.

[144] I. E. Trofimov, C. L. Canedy, C. S. Kim, M. Kim, W. W. Bewley, C. L. Merritt, I. Vurgaftman, J. R. Meyer, and L. T. Le. Interband cascade lasers with long lifetimes. *Appl. Opt.*, 54(32):9441–9445, 2015.

[145] Photon design, 2021. June 23, 2023.

[146] Wayne D Kimura. *Electromagnetic Waves and Lasers (Second Edition)*. 2053-2563. IOP Publishing, 2020.

[147] Photon Design. Fimmwave and fimmprop training course, December 2020.

[148] Aritra Roy, Saroj K. Patra, and Tomasz Piwonski. Tunable semiconductor slotted lasers for near-infrared optical coherence tomography. *IEEE Photonics Technology Letters*, 33, 2021.

[149] J. Parasuraman, A. Summanwar, F. Marty, P. Basset, D.E. Angelescu, and T. Bourouina. Deep reactive ion etching of sub-micrometer trenches with ultra high aspect ratio. *Microelectronic Engineering*, 113, 2014.

[150] Hiroshi Ito. Chemical amplification resists for microlithography. *Microlithography· Molecular Imprinting: -/-*, pages 37–245, 2005.

[151] S. Keller, G. Blagoi, M. Lillemose, D. Haefliger, and A. Boisen. Processing of thin su-8 films. *Journal of Micromechanics and Microengineering*, 18(125020), 2008.

[152] K.H. Rasmussen, S.S. Keller, F. Jensen, A.M. Jorgensen, and O. Hansen. Su-8 etching in inductively coupled oxygen plasma. *Microelectronic Engineering*, 112, 2013.

[153] H.W. Park and H.J. Kim. Simple and cost-effective method for edge bead removal by using a taping method. *Journal of the Korean Physical Society*, 73(10), 2018.

[154] J.A.M Fordyce, D.A. Diaz-Thomas, L. O'Faolain, A.N. Baranov, T. Piwonski, and L. Cerutti. Single-mode interband cascade laser with a slotted waveguide. *Appl. Phys. Lett.*, 121(21), 2022.

[155] Tyndall national institute homepage, 2023.

[156] Heidelberg mla. Accessed October 2023.

[157] H. B. Andagana and X. A. Cao. Fast and smooth etching of indium tin oxides in bcl3/cl2 inductively coupled plasmas. *Journal of Vacuum Science & Technology A*, 28(2), 2010.

[158] Alexander R Giehl, Matthias Kessler, Axel Grosse, Norbert Herhammer, and Henning Fouckhardt. Deep reactive ion etching of gasb in cl2/ar-plasma discharges using single-layer soft mask technologies. *Journal of Micromechanics and Microengineering*, 13(2):238, 2003.

[159] nanoplus team. Private communication.

[160] C. M. Silvestre, V. Nguyen, H. Jansen, and O. Hansen. Deep reactive ion etching of 'grass-free' widely-spaced periodic 2d arrays, using sacrificial structures. *Microelectronic Engineering*, 223(111228), 2010.

[161] JL Bradshaw, NP Breznay, JD Bruno, JM Gomes, JT Pham, FJ Towner, DE Wortman, RL Tober, CJ Monroy, and KA Olver. Recent progress in the development of type ii interband cascade lasers. *Physica E: Low-dimensional Systems and Nanostructures*, 20(3-4):479–485, 2004.

[162] Wei-Hua Guo, Qiaoyin Lu, Marta Nawrocka, Azat Abdullaev, James O'Callaghan, Michael Lynch, Vincent Weldon, and John F Donegan. Integrable slotted single-mode lasers. *IEEE Photonics Technology Letters*, 24(8):634–636, 2012.

[163] C.S. Kim, M. Kim, W.W. Bewley, J.R. Lindle, C.L. Canedy, J. Abell, I. Vurgaftman, and J.R. Meyer. Corrugated-sidewall interband cascade lasers with single-mode midwave-infrared emission at room temperature. *Appl. Phys. Lett.*, 95(231103), 2009.

[164] Microposit s1805/s1813, 2023.

[165] PB Vigneron, François Joint, Nathalie Isac, R Colombelli, and E Herth. Advanced and reliable gaas/algaas icp-drie etching for optoelectronic, microelectronic and microsystem applications. *Microelectronic Engineering*, 202:42–50, 2018.

[166] Robert J Hoekstra, Mark J Kushner, Valeriy Sukharev, and Phillipe Schoenborn. Microtrenching resulting from specular reflection during chlorine etching of silicon. *Journal of Vacuum Science & Technology B: Microelectronics and Nanometer Structures Processing, Measurement, and Phenomena*, 16(4):2102–2104, 1998.

[167] Jingli Gong, Rui Q Yang, Zhanyi Wang, and Jian-Jun He. Single-mode tunable interband cascade laser emitting at 3.4 μm with a wide tuning range over 100 nm. *IEEE Photonics Technology Letters*, 35(6):309–312, 2023.

[168] Tyndall team. Private communication.

[169] nanomir team. Private communication.

[170] S. Adachi. Optical dispersion relations for gap, gaas, gasb, inp, inas, insb, algaas, and ingaasp. *Journal of Applied Physics*, 66(6030), 1989.

[171] Sergey Suchalkin, David Westerfeld, Gregory Belenky, John D Bruno, John Pham, Fred Towner, and Richard L Tober. Measurement of semiconductor laser gain by the segmented contact method under strong current spreading conditions. *IEEE Journal of Quantum Electronics*, 44(6):561–566, 2008.

[172] Zhican Zhou, Xiangpeng Ou, Yuetong Fang, Emad Alkhazraji, Renjing Xu, Yating Wan, and John E Bowers. Prospects and applications of on-chip lasers. *Elight*, 3(1):1–25, 2023.

[173] Eric Tournié, Laura Monge Bartolome, Marta Rio Calvo, Zeineb Loghmari, Daniel A Díaz-Thomas, Roland Teissier, Alexei N Baranov, Laurent Cerutti, and Jean-Baptiste Rodriguez. Mid-infrared iii–v semiconductor lasers epitaxially grown on si substrates. *Light: Science & Applications*, 11(1):165, 2022.

[174] Andres Remis, Laura Monge-Bartolome, Michele Paparella, Audrey Gilbert, Guilhem Boissier, Marco Grande, Alan Blake, Liam O'faolain, Laurent Cerutti, Jean-Baptiste Rodriguez, et al. Unlocking the monolithic integration scenario: optical coupling between gasb diode lasers epitaxially grown on patterned si substrates and passive sin waveguides. *Light: Science & Applications*, 12(1):150, 2023.

[175] Laurent Cerutti, Daniel A. Diaz-Thomas, Jean-Baptiste Rodriguez, Marta Rio-Calvo, Gilles Pariarche, Alexei N. Baranov, and Eric Tournié. Quantum well interband semiconductor lasers highly tolerant to dislocations. In *Optica*, volume 8. Optical Society of America, OSA Publishing, 2021.

[176] Benedikt Schwarz, Johannes Hillbrand, Maximilian Beiser, Aaron Maxwell Andrews, Gottfried Strasser, Hermann Detz, Anne Schade, Robert Weih, and Sven Höfling. Monolithic frequency comb platform based on interband cascade lasers and detectors. *Optica*, 6(7):890–895, Jul 2019.

[177] John McCarthy and Frank H. Peters. On-chip gain switched frequency comb generation using a two sectioned single cavity laser without additional optical injection. *Opt. Express*, 31(18):29619–29626, Aug 2023.

Initial FP ICL characterization of the growths

Five different ICL wafers that were grown with the MBE at the beginning of the project were characterized by fabricating FP ICLs as described in Chapt. 3. Changes were made to the structures during the growth campaigns based on the PL signal to tune the central emission wavelength around the 3.3 µm needed to detect methane. A summary of the threshold current densities measured on the samples is shown in Fig. 4.

Material model used in FIMMWAVE

A table of values was generated and then used for the waveguide design, as summarized in Table 3, including the refractive index for the superlattice assuming equal amounts of AlSb and InAs.

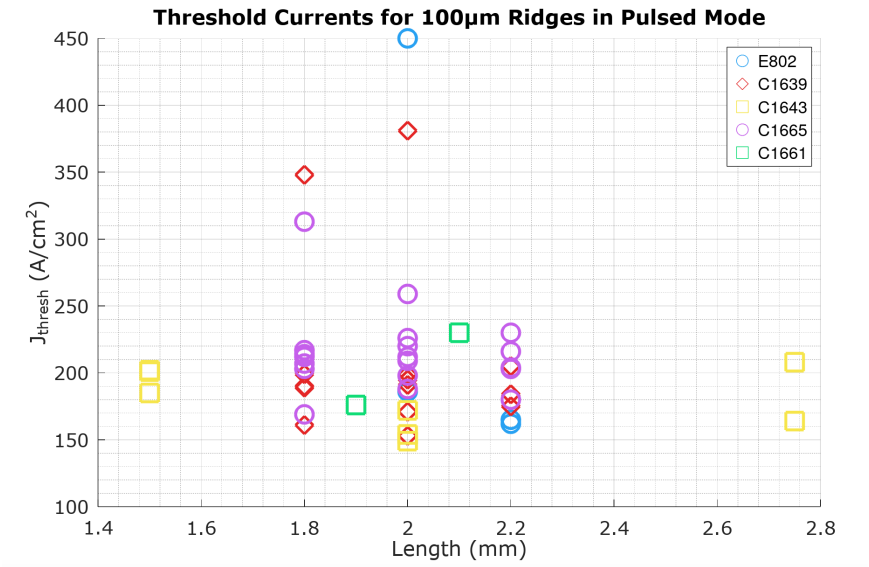

Figure 4: Threshold current density measurements of various growths characterized for this project

Growth	Center λ Envelope	Tuning	Avg. J_{Thr} Pulsed 0.1% DC	Avg. I_{Thr}, P_{max} CW	Slot process Device
E802A	3.34 µm 14 nm	0.11 nm/mA 1.4 nm/^{o}C	158 A/cm^2	70 mA 5.5 mW	Process 3 Slotted ICL 3
C1639	3.46 µm 16 nm	0.07 nm/mA N/A	352 A/cm^2	N/A N/A	N/A N/A
C1643	3.59 µm 15 nm	0.09 nm/mA 0.5 nm/^{o}C	191 A/cm^2	55 mA 10 mW	Process 2 SVT ICL
C1665	3.39 µm 7 nm	0.11 nm/mA 5.2 nm/^{o}C	231 A/cm^2	69 mA 5.5 mW	Process 2 Slotted ICL 2, DFB
C1661	3.53 µm 14 nm	0.08 nm/mA 0.3 nm/^{o}C	315 A/cm^2	50 mA 13 mW	Process 1 Slotted ICL 1

Table 2: Summary of the FP ICL characterization for the growths and their subsequent use in the investigation of slotted waveguides.

λ	n_{GaSb}	n_{AlSb}	n_{InAs}	n_{GaInSb}	n_{SL}	n_{AR}
2.9	3.7411	3.2006	3.5300	3.7934	3.3653	3.4844
3.1	3.7303	3.1696	3.5526	3.7858	3.3611	3.4823
3.3	3.7305	3.1700	3.5965	3.7889	3.3832	3.5019
3.5	3.7265	3.1710	3.5795	3.7875	3.3752	3.4940
3.7	3.7195	3.1591	3.5260	3.7828	3.3425	3.4652
3.9	3.7188	3.1603	3.5095	3.7841	3.3349	3.4583
4.1	3.7206	3.1600	3.5097	3.7876	3.3349	3.4588
4.3	3.7210	3.1600	3.5052	3.7894	3.3326	3.4571
4.5	3.7195	3.1602	3.4988	3.7901	3.3295	3.4541
4.7	3.7161	3.1591	3.4942	3.7902	3.3267	3.4512

Table 3: Calculated refractive indices

A2 Laser microfabrication

This section is meant to provide more details, general comments, and observations on each step of the process that I found were crucial but were too specific for the main body of the thesis.

Mask cleaning and photolithography quality

Between UM and Tyndall, a more strict procedure was followed regarding cleaning the masks. In Tyndall an acid bath at 90 °C was available to clean the masks after each use. Following this, the acetone/H2O/IPA rinses were done, similar as to what is done in UM. It became apparent that it was necessary to clean the masks after each exposure since the quality of the features degraded after repeated exposures in vacuum contact mode. In an attempt to avoid this, the mask-sample alignment was changed to use a "fresh part" of the mask for each each exposure but this lead to non-uniform sample-mask pressure in many cases. This would cause the feature size to be non-uniform over the sample. Wiping the mask between exposures was not sufficient to clean the masks, and could make the problem worse. This is because, although clean room wipes were used, the sharp metal edges of the mask could pull off fibers. Although time consuming, it is very important to clean the mask completely after at most 2 exposures.

Cleaning and surface treatment

The first crucial step in the process is to ensure the surface is sufficiently free of contamination, oxide layers, or water in order to improve the photoresist adhesion. This step has not been satisfactorily optimized. For the $SU-8$ etch mask deposition, the sample is dipped into a bath of diluted HCl ($1:4$ HCl:H_2O) to remove an native oxide layers to InAs. After the normal cleaning routine, Omnicoat was deposited on the surface (a commercially available mixture of cyclopentanone and 1-methoxy-2-propanol). It promoted adhesion and facilitated stripping after etching since it acted like a sacrificial layer.
For the processes that utilized a dielectric hard mask, it was crucial that the surface was free of debris. In Tyndall, HDMS was then used to improve resist adhesion.

Spin coating

The biggest problem in this step is eliminating the edge bead that forms at the boundaries of the substrate and minimizing non-uniformity problems from spinning non-circular substrates. An edge bead forms because of the boundary with the air and substrate. At this boundary, there is increased friction and

air turbulence which causes the fluid to dry faster than in the middle of the substrate. This change in evaporation rate changes the concentration and as fluid continues to flow over the edge bead, a step or bump forms. This is the reason for photoresist build up in the corners of rectangular substrates.
The best improvement made in the photolithography step of the process came from standardizing the sample size and shape. At the beginning of the project, different sizes were cleaved from the wafer to accommodate different studies and be conservative with the material. This was learnt from nanoplus and Tyndall. Nanoplus dice their wafers into rectangles and has the added benefit of having the mesa aligned closer to the crytal axes. Tyndall uses quarters of the wafers for every process and has the added benefit of a more uniform thickness due to the increased size.
Edgebead removal is crucial for high resolution and this is a practical detail that is often overlooked and not discussed. In this thesis, I taped the samples to a carrier wafer, used blank samples for flood exposures, used UV-film on the sample, and tried to wipe away the edge bead. Taping the edge of the samples to a carrier wafer and the UV-film were useful techniques for irregularly shaped samples, but doing a flood exposure was best. This was only convenient for samples with a consistent size, since cleaving Si blanks for irregular shapes proved difficult. A better idea is to use a photolithography mask to print a blank that can be used so that no contamination of the resist occurs with a dirty Si blank.

Soft Bake

The soft bake, exposure dose, and post exposure bake parameters influence the film stress, stability, and resolution for negative photoresists. It is important to reduce stress because this can partially develop the photoresist before exposure. In general, the changes are made to allow more solvent to remain in the film to facilitate cross linking with a low post exposure bake temperature. More solvent allows the monomers to be more mobile and diffuse throughout the film while the low post exposure bake temperature reduces film stress.
For both positive and negative resists, it is important to allow the samples to rest in ambient conditions before exposure. This allows the water that was removed to be deposited in the film.

SU-8 slot process

In the development of the first process, I spent too much time focused on trying to achieve 1 µm sized features with the photolithography only. My goal was to use a negative photoresist $SU-8$ as the dry etching mask because of the well known vertical sidewalls. This will summarize the final recipe that was developed.
$SU-8$ is a negative epoxy-like photoresist that is typically used to make structures on substrates in the areas of microfluidics or for mold creation[151]. The structures are normally quite thick, on the order of 100 µm, and can pattern features in films with aspect ratios of up to 20 that have an extremely vertical sidewalls. It was with these types of achievements in mind that this photoresist was thought to be a good candidate to be used for slot processing, since the shape of the photoresist can be a limiting factor in etching problems.
A thin film below 5 µm was required and this meant very different processing considerations before the etching step. This is because the more thin film would have different photo-acid diffusion and solvent

Substrate Preparation	HCl:H_2O 1:4 bath 30 s Acetone/Ethanol/IPA bath 30 s Dry sample with N_2
Sacrificial Layer Deposition	Dehydrate 5 min @200 °C Spin omnicoat First step: 200 min/5 s/5 s Second step: 500 min/5 s/5 s Third step: 3000 min/3 s/20 s Bake: 1 min @200 °C
SU-8 Deposition	Tape sample with thermal adhesive tape to Si wafer First step: 500 min/5 s/5 s Second step: 5000 min/3 s/30 s
Soft Bake	Ambient Conditions 96 min Hot Plate 40 °C 20 min Rehydrate and let rest 20 min
Exposure	Vacuum Contact and 85 s Set Pre/Full Vacuum Time to 10 s Ensure WEC pressure is at max $\approx$ 0.19 Before exposure increase WEC by 10
Post Exposure Bake	10 min @80 °C
Development	SU − 8 Developer for 30 s Rinse with IPA the dry with N2 Fully developed when no white film
Hard Bake	4 min @110 °C

Table 4: SU-8 Recipe optimized for vertical sidewalls for the slot definition.

evaporation properties. By looking at the size of the cross section in the center of the 100 µm slots and the angle of the sidewalls in the SEM, the process was optimized and is summarized in Table 4.

The preliminary tests done on a GaSb substrated indicated very positive results. The pattern developed with SU − 8 imprinted slots on the substrate that were much larger than intended at approximately 2.5 µm versus the exposed 1.2 µm but the hard mask opening had vertical walls. Subsequent etching of the substrate with the first etching recipe yielded slots between 87°and 92°both when the photoresist was removed prior to the dry etching and when it was left on. When etching on the practice ICL material an angle of <110°was not observed even when the photoresist angle being between 90°and 95°. This, and because the deposition process took a long time is why the first slotted ICL process was finalized with a dielectric hard mask.

Alternative dry etching masks

During the optimization of process 2 (at nanoplus) an option explored to reduce the wing formation was to use a metal mask. This was proposed to address an alternative explanation to the formation of the wings, which would be due to a non-uniform photoresist layer on top of the slots. We posited that the development of the photoresist resulted in an angle and the wing formation actually began during the hard mask opening of the Si_3N_4 etch.

The metal mask is formed by lifting off the photoresist to create the pattern, as opposed to dry etching.

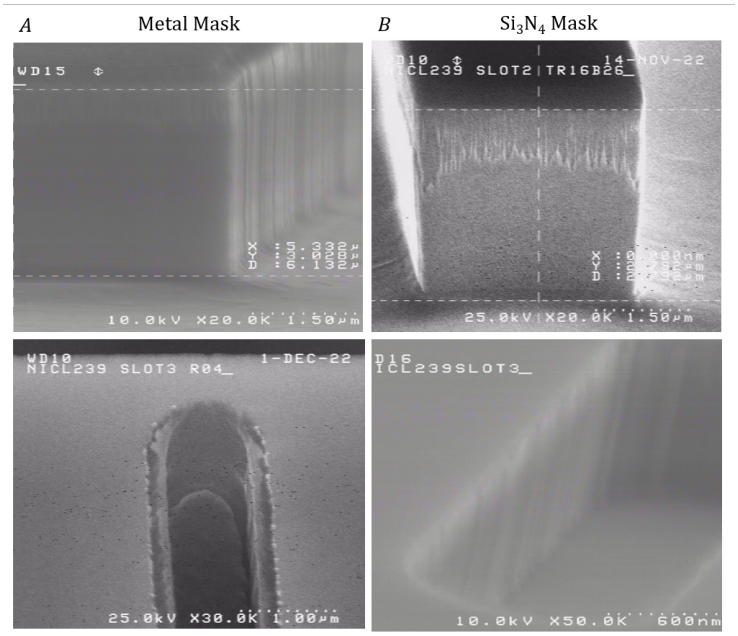

Figure 5: *A:* Dry etching using the N+ recipe and a metal mask. *B:* Again, the original recipe but with the dielectric hard mask. The top row shows the mesa profile. The bottom row shows the slots after the masks should be removed.

The inverse image of the mesa mask is exposed for this, so that the metal stack $Ti/Pt/BaF_2/Cr$ can coat what will become the top of the mesa. The remaining area will be on top of photoresist, and will be lifted off so that this area can be etched. BaF_2 is used in the metal stack because it is soluble in water and can be used to lift-off the metal after the etch is completed.
Fig. 5 shows the results of dry etching the mesa profile *(top)* and the slot profile *(bottom)* using *A* a metal mask and *B* the dielectric mask. The mesa profile looks qualitatively the same, which highlights that the dielectric mask is sufficient to have vertical sidewalls. The slots show a vertical profile for both masks, but it appears that the metal mask is not successful removed from inside the slot. If some metal remains from the hard mask, it is okay because it will become part of the top contact. But from the slot SEM of Fig. 5A it was not clear if there was partial removal of the mask and what the outline around the slot was. Although the wings looked more transparent for the samples etched with the metal mask and were shorter in general they were not completely removed. Continuing with the dielectric hard mask was more straightforward since the mask was fully removed from the slots.

Slot-mesa photolithography mask design

A mask designed to investigate the formation of the wings during dry etching and included two main features: slot width variation and slot length variation. The widths of the slots were varied to see if the wing formation was size dependent. The length of the slots were varied, with respect to the mesa width, to be smaller, the same, and larger. The wings were expected to form for the slot lengths that were larger than the mesa width, but they could also form for the slot lengths that were the same as the mesa width depending on the alignment accuracy. The slot lengths smaller than the mesa width were included to see

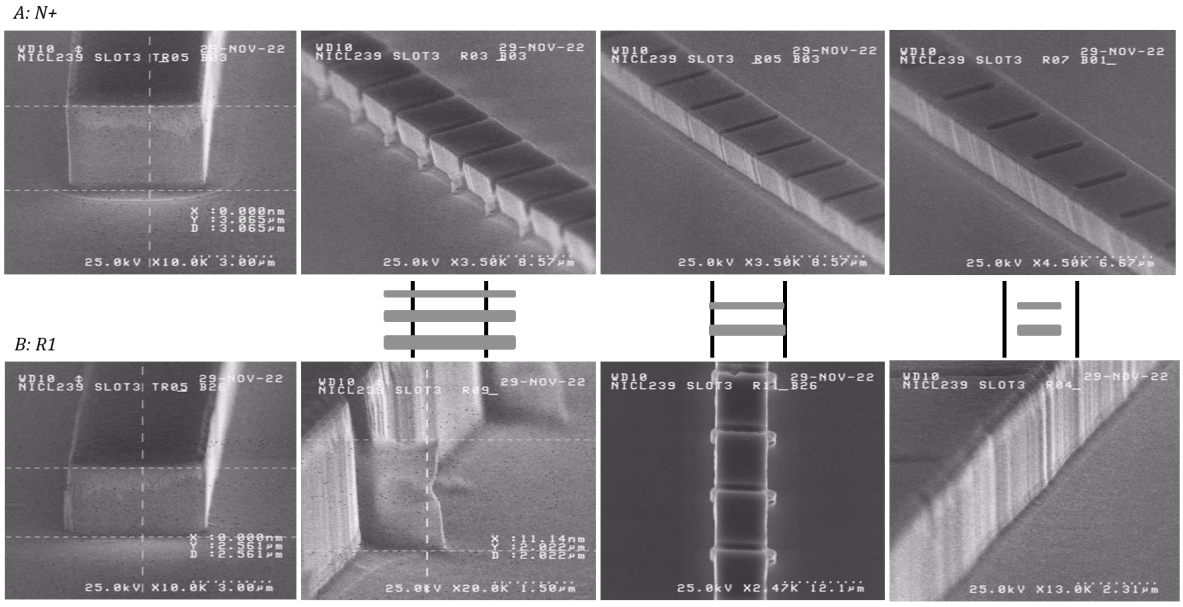

Figure 6: SEM images from the mesa cross section, slots > mesa width, slots = mesa width, and slots < mesa width profiles are shown, from left to right. *A:* The resulting etching profiles and wings observed from the N+ recipe. *B:* The resulting etching profiles and wings after implementing recipe 1 and increasing the Ar flow rate.

if they were a feasible option from the alignment accuracy that could be achieved. This test was done in conjuction with changing the dry etching recipe.

Fig. 6 shows the result from the N+ recipe and from increasing the Ar flow rate for the different slot-mesa configurations investigated. Wings were observed when the slots were larger than the mesa for both recipes and when the slots should be the same size as the mesa width with the increased Ar flow rate. In Fig. 6*A*, the sidewalls look a bit rougher in the mesa sidewall where the slots are located. Wings were not observed when the slots were smaller, and there were no obvious defects with that etch. The mesa height was 3.1 µm and the wing height was 2.7 µm. In Fig. 6*B*, the mesa height was 2.6 µm and the height of the wings was 2.0 µm. The relative height of the wing with respect to the mesa did not decrease with the lower etch rate. However; qualitatively, the wings appear to be less solid.

There were no obvious defects for when the slot length < mesa ridge, therefore, for future process runs this slot-mesa geometry would be used.

For other slotted waveguides, the slots and the ridges are etched at the same time and defects can occur they refer to as eyelashes [168]. The slot and ridge etching is separated in this thesis since ICLs must be etched through the active region. Changing the order of the etch may fix this problem, but at the cost of the resolution and difficulties during the slot photolithography.

Dielectric dry etching study

During the optimization of process 3 (at Tyndall), different dielectric hard masks were explored in order to improve the slot etch. The deposition of SiO_2 and Si_3N_4 using PECVD and sputtered SiO_2 was considered. This would test if the density of the dielectric had any effect on the smoothness of the mask opening. The

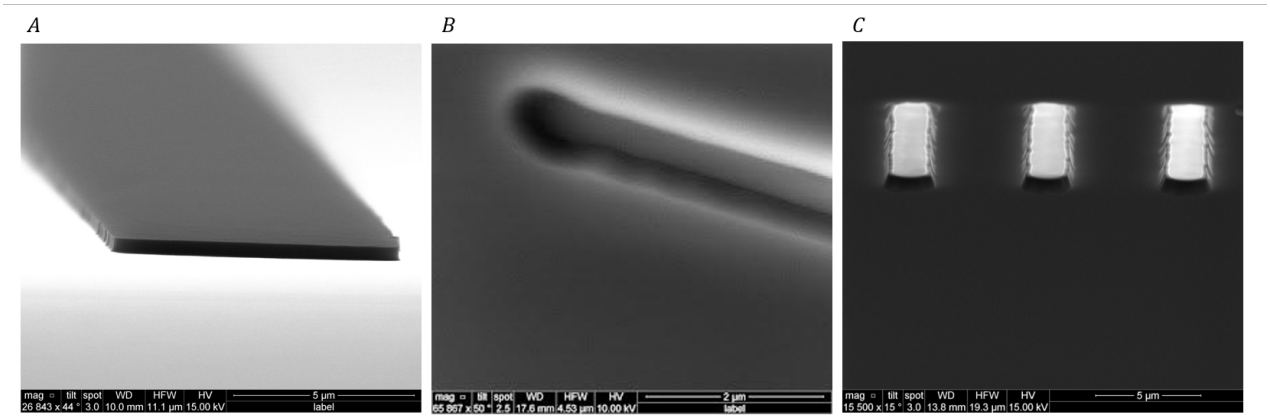

Figure 7: A few different F-based dry etching recipes to open/remove the hard mask from Tyndall. *A* shows a SF_6 recipe, *B* shows the slot/mesa mask opening recipe in process 3 ($SF_6/C_4F_8/H_2/He$), and *C* shows the contact window opening recipe of process 3 (C_4F_8/He).

photolithography and hard mask opening improved to the point that it seemed the photolithography mask defects were being transferred to the sample. In most trials, the PECVD masks gave the smoothest features and as a result Si_3N_4 using PECVD was used as a hard mask though this could be investigated further for applications in facet etching and improvement to the smoothness of the slot/mesa.

The dry etching recipe used to open the hard mask was investigated after the first observation of the hard mask remaining in the slot after mesa etching, as shown in Fig. 5.13. Fig. 5.13A depicts the results from a high pressure recipe with SF_6 that was isotropic. This is observed from the pronounced lateral etch of the hard mask. Fig. 5.13B shows the results from a recipe with $SF_6/C_4F_8/H_2/He$ that was originally used to open the hard mask in process 3. Fig. 5.13C shows the second variant of the recipe with just C_4F_8/He at a lower temperature from the contact window opening in process 3.

The recipe shown in Fig. 5.13B opens the slot and mesa etching mask very well but does not remove the isolation layer from inside the slots well, as shown in Fig. 5.13. The recipe shown in Fig. 5.13C is what was used to try and remove the isolation layer from the slots. It is unclear how to best monitor this, since overetching could be a concern that degrades the surface. When time permits, the sample needs to be viewed with a SEM but this is extremely inconvenient. I describe these results because I just had one reference sample that was processed slightly ahead of the LP samples in process 3. This dry etching recipe change was made as a result of this one test study and should be explored further.

A3 DFB cross comparison study

The other objective during the secondment at nanoplus (N+) was to compare the commercial DFB ICL process on the material grown at the University of Montpellier (UM) to the material grown by N+. The comparison would not be apples to apples since the ICL designs are different, but the goal was to get some insight into what could be improved. In general, the expectation was that the threshold currents of the N+ material will be lower but the UM material should be able to output more power with the extra stages, if the growth is optimal in both cases. In order to target methane detection, two epitaxies were chosen from UM and N+ that had FP devices previously fabricated on them, emitting around λ =3.3 µm; this was C1665 from UM and N120 from N+. Note, part of this study was to compare the slotted ICL process on the two structures but the shorts occurred on both C1665 and NICL120.
The process flow is similar to what is used to create the slotted ICLs in Sec. 5.1 with a few notable exceptions:

- The mesa step is first and both the mesa and grating is defined using e-beam lithography instead of UV photolithography
- The mesa etch occurs to the bottom of the active region (instead of through the bottom SCL) in order to bring the grating closer to improve coupling
- The grating is not etched, the metal is deposited and the grating is formed using a lift-off with the photoresist

The structures are different because of many potential ways for optimizations concerning output power, threshold current, and series resistance. For this study, the N+ epitaxy used 5 stages with symmetric 370 nm SCLs grown on each side. The top and bottom cladding layers consisted of a AlSb/InAs superlattice with Si doping at levels that were a compromise between minimizing mode interaction and improving electron injection. They were 2100 nm and 3700 nm thick, respectively. A doped InAs cap of 25 nm completed the 7000 nm thick structure. This structure is presented on the left of Fig. 8. Meanwhile, the UM epitaxy used 7 stages with thicker, symmetric SCLs of 490 nm grown on each side. Similarly, the top and bottom cladding layers were AlSb/InAs superlattices but with different thicknesses of 1900 nm and 3300 nm, respectively, and a slightly different Si doping gradient. The UM epitaxy is topped with a slightly thinner 20 nm InAs cap and the entire 6800 nm structure is summarized on the right of Fig. 8.
The differences in the structure results in slight changes to the shape of the zeroth order mode in the



Figure 8: The materials used to make a performance comparison based on the DFB process developed at nanoplus. These were chosen because the SCLs were symmetric and the expected wavelength was similar. Both epitaxies represent an optimization for emission near λ =3.3 µm

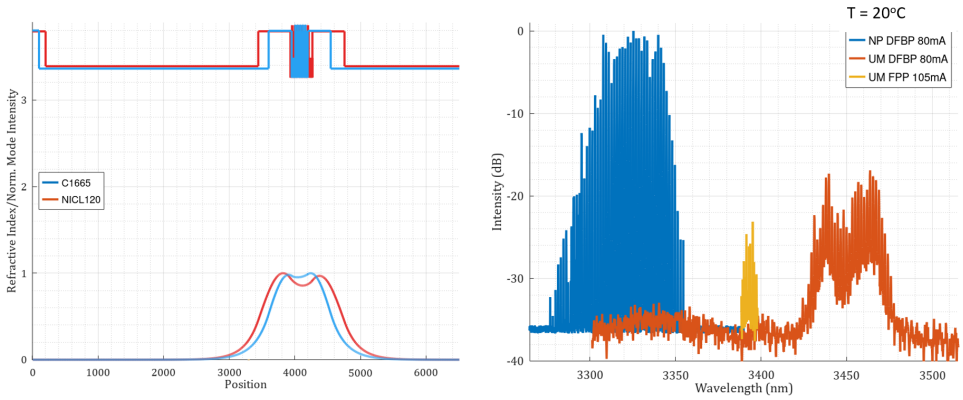

Figure 9: *Left:* Resulting optical modes predicted for the different ICL structures and their refractive index profile. *Right:* Comparison of the FP ICL performance between material from N+ and UM, and to the UM FP process (FPP). Taken at 20 °C and I_{thr} ≈30 mA.

structure and its overlap with the active region and other layers. The higher the overlap in the active region, the more the gain can amplify the mode. However, the material losses of the active region are higher than in the SCL so this also results in higher internal losses. Minimizing the overlap in the cladding layers, also lowers the overall internal losses but this will also decrease our ability to interfere with the mode to create a single mode laser [68]. For these two structures, the mode was simulated using lasim[115]. The refractive index profile and the simulated mode is shown below on the left of Fig. 9. The modes are shown for a normalized intensity, and the real active region confinement factors are 0.199 and 0.164 for C1665 and NICL120, respectively.

The right of Fig. 9 shows the performance of the reference FP ICLs created on the DFB laser samples

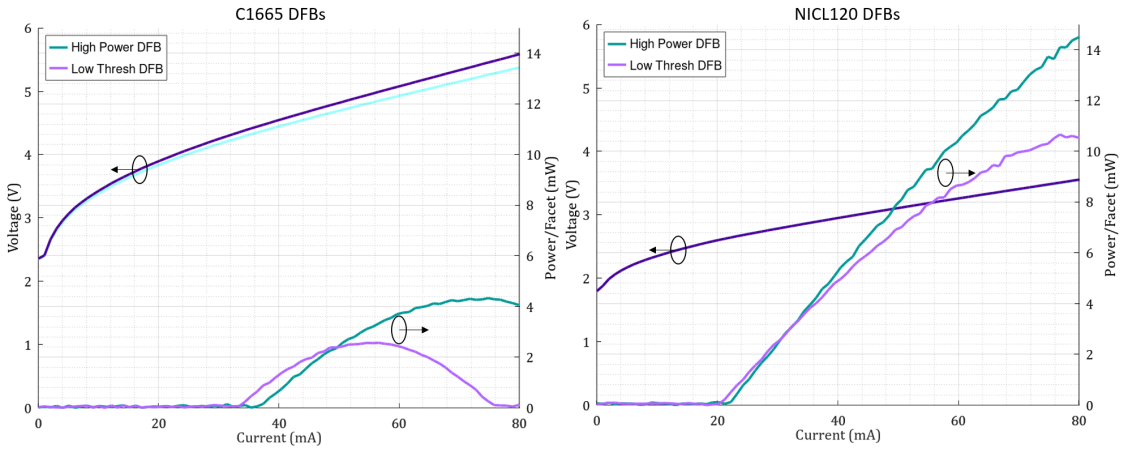

Figure 10: PIV measurements of DFB ICLs with uncoated facets and L =900 µm at T =10 °C. *Left:* The results from C1665 are presented and achieved I_{thr} ≈38 mA and P_{out} ≈4 mW. *Right:* The results from NICL120 are presented and achieved I_{thr} ≈21 mA and P_{out} ≈14 mW, though the rollover point was not reached yet.

(DFBP). There is approximately 150 nm of difference between the central emission of the two growths at the same operating conditions of 20 °C and 80 mA. For reference, the spectra from a broad area FP ICL fabricated at UM is shown as well (FPP), but at different conditions: 20 °C and 105 mA. The DFBP lasers are the same size w =5 µmx$L$ =900 µm whereas the FPP laser is w =100 µmx$L$ =2000 µm. The DFBP lasers were measured on the same thermoelectric cooler and with an OSA, while the FPP laser was measured at a different set up and with a grating spectrometer and so the sensitivity is quite different. There is more ASE with respect to the cavity modes in the UM DFBP laser and the gain bandwidth is narrower than the NP DFBP. The signal is a lot weaker from the UM material, despite the extra 7 stages, but the local active region temperature could be higher due higher resistance and subsequent heating. Between FPP and DFBP on C1665, there seems to have been an improvement since the width of the envelope of the spectral emission is broader though this could be because of the sensitivity of the different measurements and a low or diverging output beam. These measurements give us a good idea of how the different characterization set ups compare and how the material compares.

The NICL120 outperforms the the C1665 growth in this process in all the metrics. The extra active stages in the UM growth do no compensate a higher I_{thr} and with higher output power. This may be because of extra losses that come from the higher overlap with the active region. R_s is higher as well, indicating the doping levels need to be recalibrated during the growth as they must be too low. As well, the thermal management should be improved to increase the rollover point. This can be done with thinner cladding layers to reduce the amount of material with a low thermal resistance.

The facet coatings help to protect the surface from oxidation and enhance the cavity feedback (with an AR/HR combination). As expected, almost a factor of 2 is gained in the output power, as the max goes from ≈4 mW to ≈7.5 mW for the highest performer. The spectra are used to determine what the optimal grating period was and where the highest SMSR/broadest single mode wavelength tuning range can be found. The measurements from a few different operating currents past the threshold are shown in Fig. 11. Based on the spectra measured, the calculated refractive index is n_{eff} =3.6056.

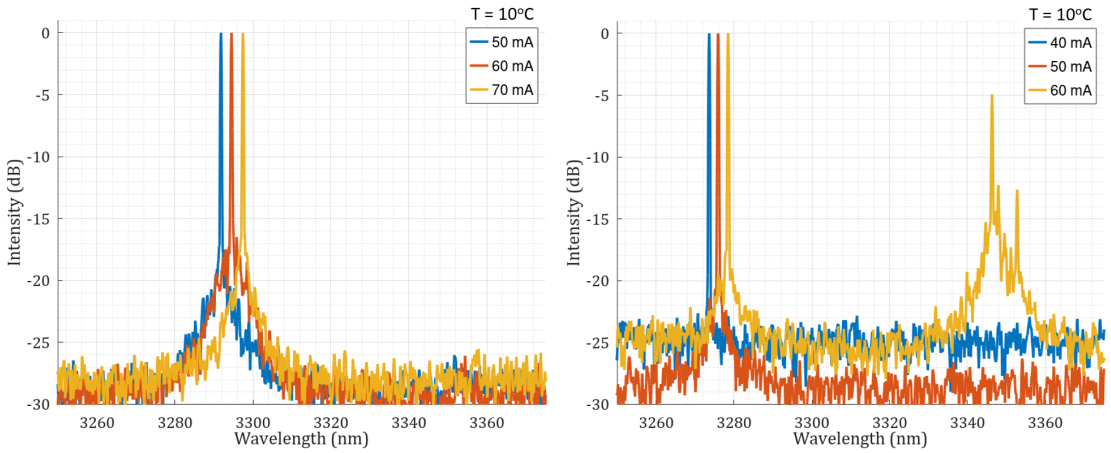

Figure 11: *Left:* The laser with the best single-mode tuning range and SMSR. *Right:* The laser with the lowest threshold.

Now that it is shown that the facet coating worked, the sample can be tested to find a laser that has high SMSR and a wavelength with the highest power at a wavelength appropriate for the detection of methane. These lasers will be cleaved off the the bar and mounted epi side up on a heat spreader. Ideally, it is better since the laser is separated and soldered to a metal so the power output should increase. For interest and for use in different set ups, a few of the DFB ICLs mounted to heat spreaders were additionally packaged and capped in a TO 66 can. A laser was chosen that had λ =3315 nm and P_{out} ≈7 mW at 20 °C. Another laser was chosen for this wavelength and had P_{out} ≈5 mW at 20 °C.

A4 Slotted ICL performance

This section presents additional measurements regarding the LP samples from process 3 in both epi-down and epi-up mounting configurations. The PIV characteristics improved for all when the lasers were mounted epi-down, but this doesn't discriminate against multi-mode operation. There did not appear to be any mode suppression in LP1 and LP3 - the emission profile looked like that from a FP cavity. The spectra are depicted in Fig. 12. LP1 is shown in Fig. 12A and it appears the emission has a higher order transverse mode due to the presence of two bunches of cavity modes. LP3 is shown in Fig. 12B and the emission appears to be single-mode in the transverse direction.

The spectra for LP2 mounted epi-down was also multi-mode, but there was clearly some mode suppression. Fig. 13 summarizes these observations for LP1, LP2, and LP3 from *left* to *right* at various conditions. The top panel for LP1 and LP3 shows the weighted average from the modes measured by the grating spectrometer. The middle panel is a plot for the width of the spectral emission envelope. The bottom panel plots the C_{FSR} of the modes as the current changes at a constant 15 °C and 35 °C for LP1 and LP3, respectively. For LP2, the top panel plots the wavelength of the highest mode, the middle panel plots the SMSR, and the bottom panel plots the shift of the highest mode with respect to changing temperature at a

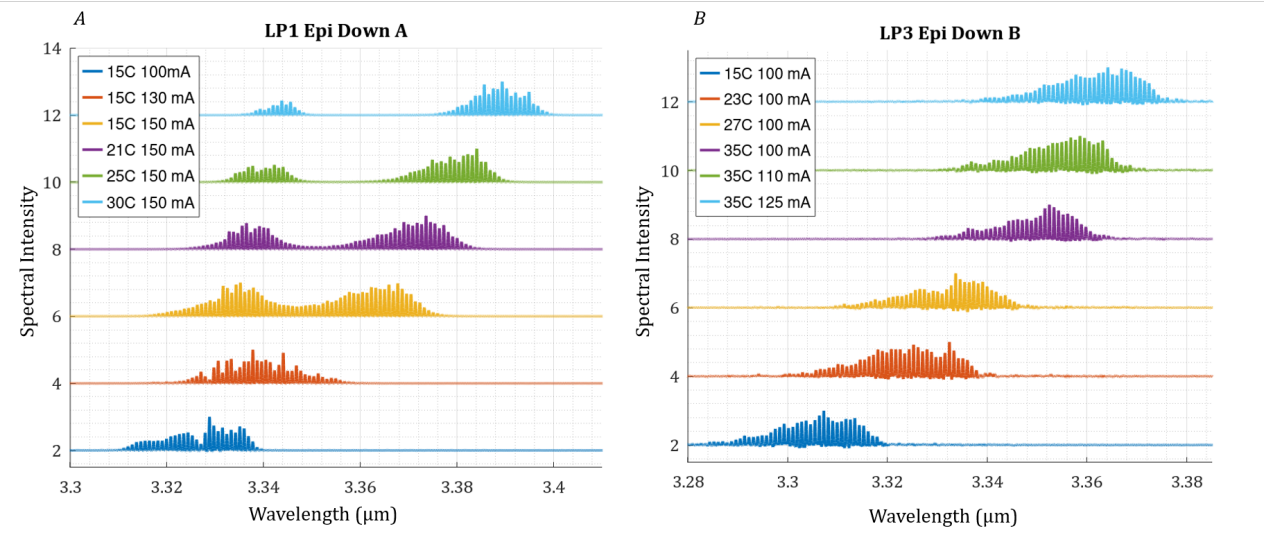

Figure 12: Summary of the emission measured from 8 µmx1.6 mm lasers mounted in the epi-down configuration. *A:* LP1 and *B:* LP3.

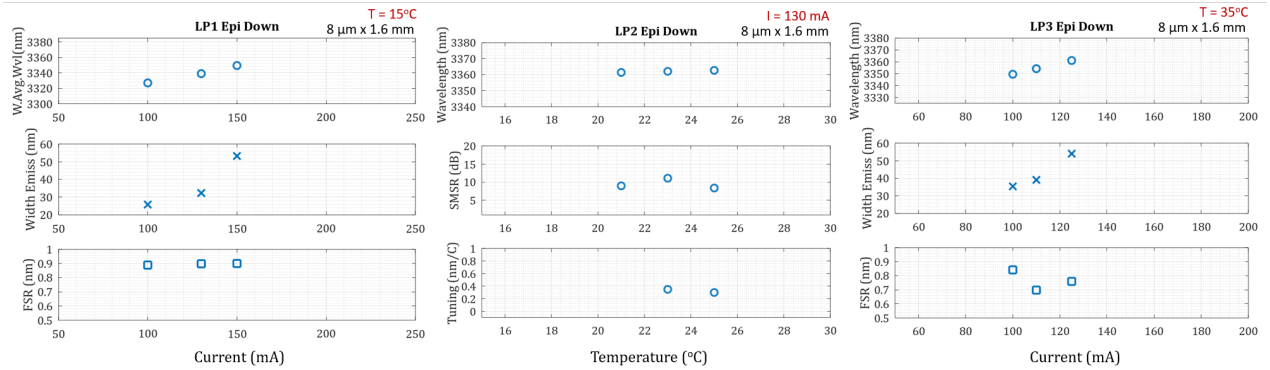

Figure 13: Summary of the emission measured from the devices mounted in the epi-down configuration. *Left:* LP1 performance is shown at 15 °C. *Middle:* LP2 performance is shown for an injected current of 130 mA as the temperature is changed. *Right:* LP3 performance is shown at 35 °C.

constant current of I =130 mA. Note, lasers aren't typically described as single-mode until the SMSR is at least 20 dB but this depends on the application requirements.

For LP1 and LP2 mounted epi-up, there were some conditions where single mode behaviour was observed. Fig. 14 highlights the most single-mode emission for lasers from LP1 and LP2 with L =1.6 mm and a laser from LP2 with L =1.2 mm (described in the main body), respectively from *left* to *right*. Two temperatures are shown for LP1 with the 23 °C emission illustrating what it looks like when a laser is single mode until the gain becomes too high while increasing the injected current. The 25 °C tuning meanwhile shows a mode hop as the current is increased. For LP1 the highest SMSR recorded was 19.5 dB, with λ =3.37 µm at 23 °C and 85 mA. The middle panel shows the L =1.6 mm laser from LP2. Single mode emission was observed at 25 °C and 70 mA with SMSR of 20.7 dB and λ =3.39 µm using an FTIR. No tuning is observed with the injected currents measured as the SMSR drops sharply after this point. From simulations, it was predicted that shorter lasers would be more single mode so another laser was cleaved from LP2 with L =1.2 mm and these results are shown in the right panel at 17 °C. A large tuning range between 3.28 µm to 3.43 µm (89 mA to 103 mA) with an average SMSR of 18 dB in this range and 0.2 nm mA^{-1}. The highest SMSR is 22.3 dB at 17 °C and 90 mA. At other temperatures, some of the emission was single mode but not for as broad of a range as presented.

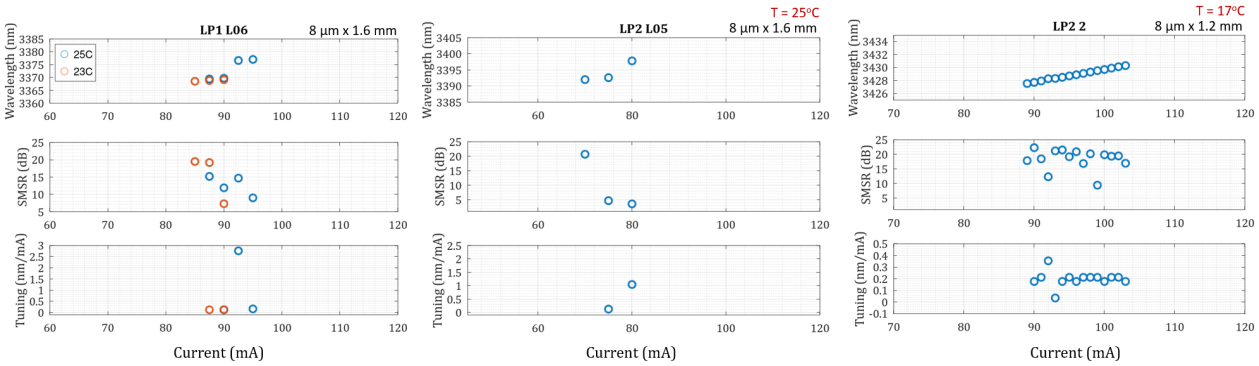

Figure 14: Summary of the emission measured from the devices mounted in the epi up configuration that lased. *Left:* LP1 performance is shown at 23 °C and 25 °C for a laser with L =1.6 mm, with some single mode emission observed. *Middle:* LP2 performance is shown for a laser with L =1.6 mm at 25 °C with an operating point for single mode emission. *Right:* LP2 performance is shown again for a laser with L =1.2 mm at 17 °C with a large tuning range of single mode emission.

This section includes extra design considerations and additional measurements from devices that are included here to support the analysis of the main section.
The measured C_{FSR} can originate from into a few different categories:

- facet - facet reflections
- trench - trench reflections (full sections)
- facet - slot/slot - slot reflections (slot subcavities)

The facet - facet reflections result in the smallest C_{FSR} that are <0.6 nm. For the trench - trench reflections, it depends on the specific design and section in question, but the range for both the B and C design result C_{FSR} of ≈0.8 nm to 2.5 nm. The phase section from the B design has a narrower range of 3.5 nm to 4 nm and the C design has 4.7 nm to 5.3 nm. The slot sub-cavities result in the largest C_{FSR} that are 4 nm to

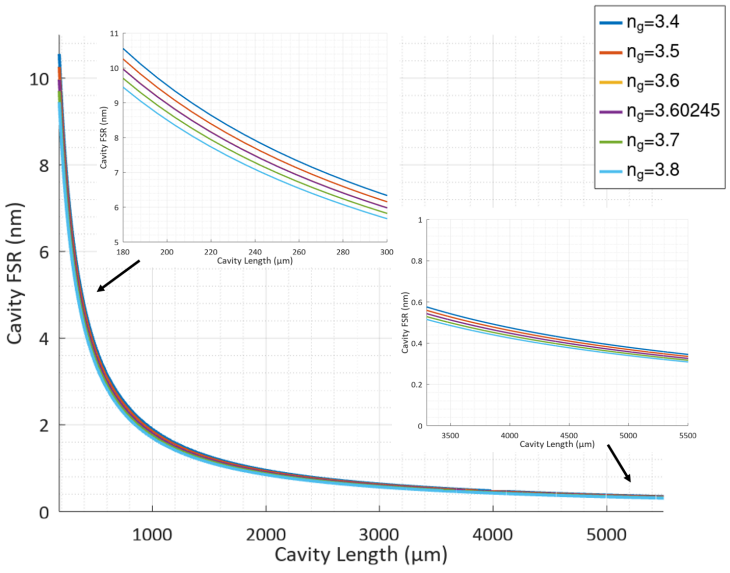

Figure 15: The C_{FSR} is calculated for different values of n_g that are possible from the material. The range of lengths shown covers the single slot period up to the full facet to facet length of the different designs. The inset highlights the C_{FSR} from the range of the single slot periods implemented in the designs.

Parameters	A1	A2	D11	D12
M1 N	7	7	6	6
M2 N	6	6	5	6
M1 Length (μm)	1754	1754	1647	1647
M2 Length (μm)	1875	1875	1563	1875
M1+M2 Length (μm)	3629	3629	3209	3522
M1 L_{eff} (μm)	751.88	751.88	549	686
M2 L_{eff} (μm)	781.25	781.25	625	781
M1+M2 L_{eff} (μm)	1533	1533	1174	1467
M1 HWHM (nm)	0.395	0.395	0.4	0.4
M2 HWHM (nm)	0.40	0.4	0.45	0.45
Half ΔFSR (nm)	0.6	0.6	0.35	0.35
Cavity FSR (nm)	0.65	0.55	0.3	0.3
Calc L_{eff} (μm)	2597	3069	5626	5626
Req Gain Length (μm)	565	1037	3906	3616
Total Device Length (μm)	4693	5165	7662	7681
Adjusted Device Length (μm)	4878	5251	7656	7656
New Gain Length (μm)	750	1123	3900	3588
New Cavity FSR (nm)	0.61	0.54	0.30	0.30

Table 5: Summary of the design parameters and calculations implemented for the first development of SVT ICLs 3.

11 nm. This is useful for record keeping and analyzing the resultant spectra.

Additional designs; the A and D series, that were simulated but could not be included on the photolithography mask are presented here. These designs focused on changes that were made to the C_{FSR} and the FWHM from the S_{FSR}. Their parameters are summarized in Table 5.

Fig.16 depicts two lasers from the FP ICL spectra on SVT3 plotted on the logarithmic scale to better illustrate the ASE and the modes. The difference in the spectra illustrates some of the difficulty in detecting weak modes.

Fig. 17 illustrates the PIV characteristics of each section of the slotted ICL pumped individually at 10 °C. Fig. 17*A* shows the PIV in pulsed mode operation with a 1% duty cycle at 10 kHz and Fig. 17*B* shows the PIV in CW mode. The resistance between the two sections from the isolation trench was 2.8 kΩ, which is sufficient for independent section pumping. The gain section lases in both pulsed and CW mode demonstrating typical performance; I_{Thr} is 31 mA, V_{OC} is 3.5 V and R_s is 7.6 Ω in CW while I_{Thr} is 3 mA. The slot section does not lase in CW but does in in pulsed mode a I_{Thr} of 100 mA. The IV curve in CW mode points to problems during the fabrication due to the current leakage shifting the knee of the diode to about 10 mA. In pulsed mode, the output power reaches a maximum of 5 µW at 250 mA which points to losses leading to heating that prevent room temperature lasing.

Fig. 18 illustrates the electro-optical characteristics from the slotted ICL in CW mode with both sections

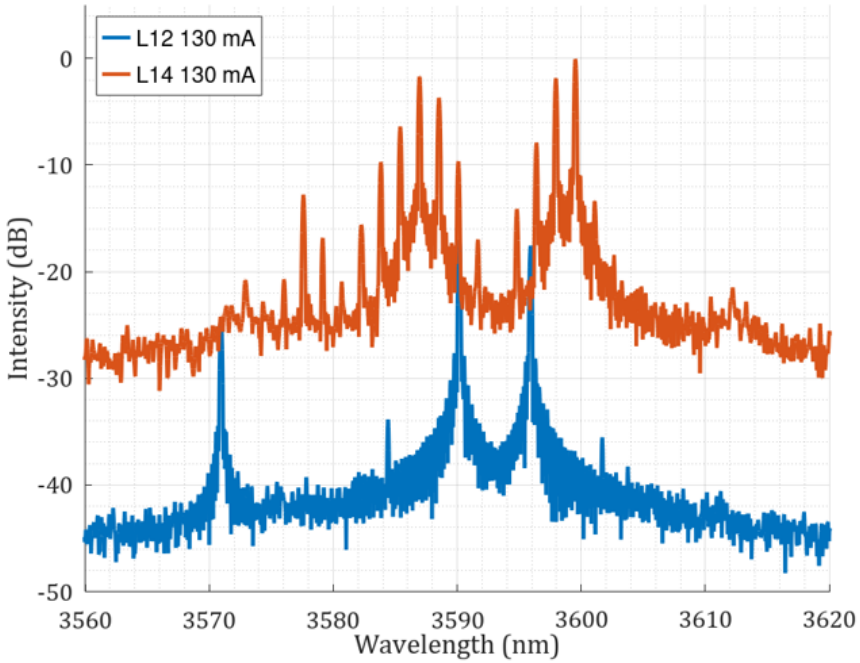

Figure 16: PIV characteristics from the two-section slotted ICL test lasers mounted epi-up in CW mode are shown at 10 °C for devices with a ridge width of 7 µm and length of 1.6 mm. *B:* The temperature dependence of the PI curves from LP1 are shown.

pumped. Fig. 18*A* shows the PIV at 10 °C with I_{Slot} at 0 mA and 150 mA as the gain current is swept. Fig. 18*B* shows the spectra at 16 °C with I_{Gain} set to 110 mA as I_{Slot} is increased. The measured mode spacing corresponds to the S_{FSR} for M2: for 0 mA and 90 mA the mean spacing is 5.5 nm and for 110 mA and 125 mA the mean spacing is 5.8 nm.

There is absorption occurring when the light travels through the slot section from the decrease in power in the PIV, which is not what was expected. Pumping the section should increase the gain and decrease the losses travelling through the section. However, the light generated by the gain section may be blue shifted with respect to the gain bandwidth of the slot section due to difference in local active region temperatures. This would explain why the signal is not amplified but the S_{FSR} is observed in the spectra, even with 0 mA for this device. The slots are acting as a passive grating.

Fig. 19 presents the spectra measured as I_{M2} is increased between 0 mA to 100 mA with I_{Gain} set to 140 mA and I_{M1}/I_{Phase} set to 0 mA. The blue curve shows the output measured near the M1 slotted section, similar to what was presented in the main body of the thesis. The purple curve shows the output measured near the M2 slotted section. There appears to be partial overlap between the S_{FSR} from the two slotted waveguides. This also illustrates how the separate waveguides interact with the cavity modes. Near the red arrow there is overlap and therefore enhancement when viewing from the second output

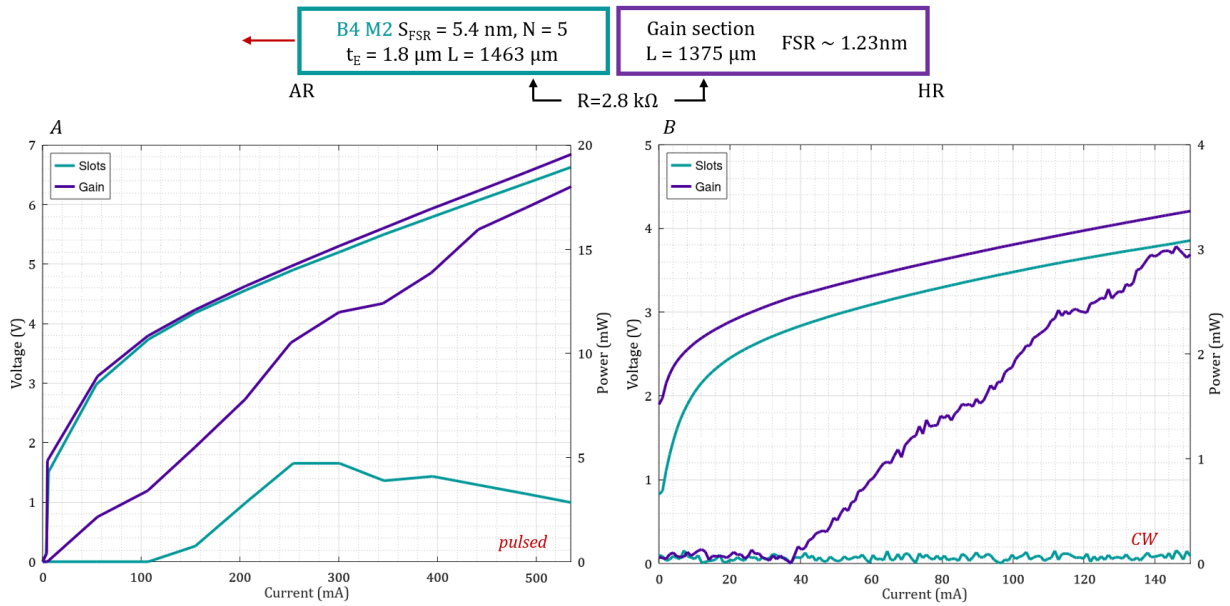

Figure 17: PIV characteristics from the two-section slotted ICL test lasers mounted epi-up in CW mode are shown at 10 °C for devices with a ridge width of 8 µm and length of 1.6 mm. *A:* Testing done in pulsed mode. *B:* Testing done in CW mode.

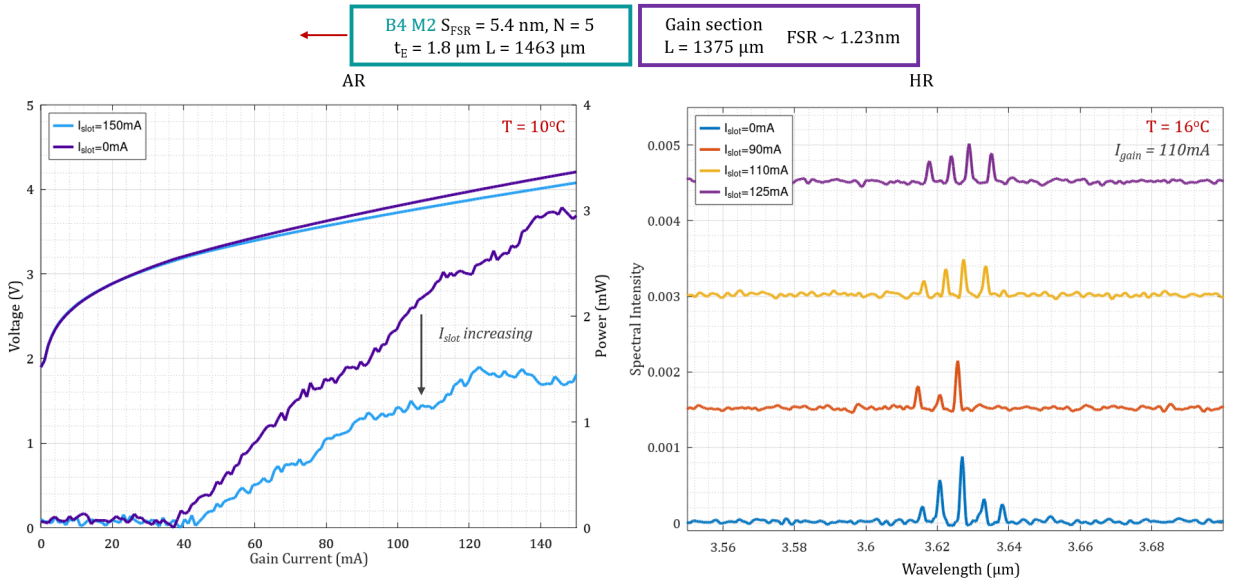

Figure 18: PIV and spectra from the two-section slotted ICL with both sections pumped. *A:* The PIV at in CW mode at 10 °C with I_{Slot} at 0 mA and 150 mA. *B:* The spectra are shown at 16 °C with I_{Gain} at 110 mA as I_{Slot} is increased between 0 mA to 125 mA.

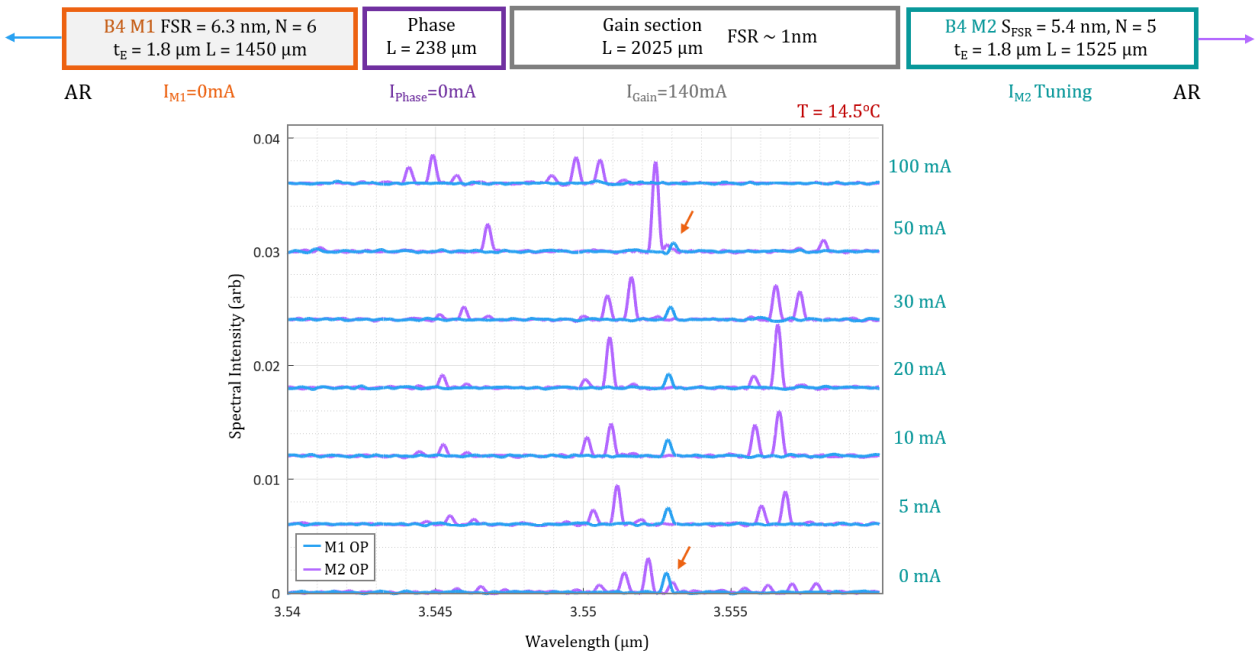

Figure 19: The spectra measured from both outputs of the SVT ICL are shown as I_{M2} is increased with only the gain section pumped at 140 mA at 14.5 °C.

Declaration

This thesis is entirely the candidate's own work, except where otherwise accredited.

The research has complied with the University's Code of Good Practice in Research.

Author's signature:
Jordan Fordyce



24/01/2024

Supervisor's signature:
Dr. Laurent Cerutti, UM



24/01/2024

Supervisor's signature:
Dr. William Whelan-Curtin (Liam O'Faolain), MTU



24/01/2024

Abstract

Interband cascade lasers (ICLs) provide sources for the mid-infrared spectral range between 3 µm to 6 µm with low power consumption and efficient performance. This spectral range is of particular interest to the detection of gases involved with petrochemical processing, such as methane, ethane, and carbon dioxide due to their strong absorption in this range. Correct identification of a gas present in a sample requires single-mode emission and some tuning to match the absorption line, depending on the environmental conditions. Increasing the tuning range possible with one laser source opens up new possibilities in spectroscopic applications. An economical design alternative to what is currently commercially available can be realized through the use of slotted waveguides, which can be fabricated using photolithography, reducing the cost of fabrication. Two new types of ICLs have been designed, fabricated, and studied in this thesis: a single-section slotted ICL and a multi-section slotted Vernier tuned (SVT) ICL. An extensive study of the fabrication step and in particular dry etching was carried out to achieve vertical etching of the materials constituting the ICLs. First, the slotted ICLs were fabricated demonstrating single-mode emission in continuous wave operation at room temperature with emission close to 3.4 µm. Building from this foundation, the SVT ICL was fabricated to extend the tuning range and demonstrate that Vernier tuning could be implemented on this material system.

Résumé

Les lasers à cascade interbandes (ICL) fournissent des sources pour la gamme spectrale du moyen infrarouge compris entre 3 µm to 6 µm particulièrement efficaces en termes de consommation d'énergie. Cette gamme spectrale est particulièrement intéressante pour la détection des gaz impliqués dans l'industrie pétrochimique, car des gaz tels que le méthane, l'éthane et le dioxyde de carbone présentent une forte absorption dans cette gamme de longueur d'onde. L'identification correcte d'un gaz présent dans un échantillon nécessite des lasers avec une émission monomode et une certaine accordabilité en longueur d'onde. L'amélioration de cette plage de réglage possible avec une source laser offre de nouvelles opportunités dans des applications liées à la spectroscopie. Une alternative à ce qui est actuellement disponible dans le commerce peut être réalisée grâce à l'utilisation de guides d'ondes à fente, qui peuvent être fabriqués en utilisant de la photolithographie conventionnelle, réduisant ainsi le coût de fabrication. Deux nouveaux types d'ICL ont été conçus, fabriqués, et étudiés dans le cadre de cette thèse : un ICL à fentes à section unique et un ICL à fentes multiples accordé par Vernier (SVT). Une étude approfondie des étapes de fabrication et en particulier de la gravure sèche a été réalisée pour obtenir une gravure verticale des matériaux constituants les ICLs. Les premiers ICLs à fentes ont été fabriqués démontrant un e une émission monomode en régime continu à température ambiante avec une émission proche de 3.4 µm. Sur cette base, l'ICL SVT a été fabriqué pour étendre la plage d'accord et démontrer que l'accord par effet Vernier pouvait être mis en œuvre sur ce système de matériaux.